ONSETS OF LIQUID AND GAS ENTRAINMENT DURING DISCHARGE FROM A STRATIFIED AIR-WATER REGION THROUGH TWO HORIZONTAL SIDE BRANCHES WITH CENTERLINES FALLING IN AN INCLINED PLANE

by

Marcus R. Maier

A thesis
presented to the University of Manitoba
in partial fulfillment of the
requirements for the degree of
Master of Science
in
Mechanical Engineering

Winnipeg, Manitoba, Canada 1998

THE UNIVERSITY OF MANITOBA

FACULTY OF GRADUATE STUDIES

*****

COPYRIGHT PERMISSION PAGE

ONSETS OF LIQUID AND GAS ENTRAINMENT DURING DISCHARGE FROM A STRATIFIED AIR-WATER REGION THROUGH TWO HORIZONTAL SIDE BRANCHES WITH CENTERLINES FALLING IN AN INCLINED PLANE

BY

MARCUS R. MAIER

A Thesis/Practicum submitted to the Faculty of Graduate Studies of The University of Manitoba in partial fulfillment of the requirements of the degree of

MASTER OF SCIENCE

ABSTRACT

In recent years, considerable effort has been placed on understanding two-phase flow in small branches discharging from large pressure vessels that contain a two-phase mixture. This effort is due to the importance of the geometrical flow arrangement to industry. One particular application is to the CANDU nuclear reactor. The header/feeder arrangement in the reactor is a similar geometry and during a postulated Loss-of-Coolant Accident, or LOCA, the feeders can experience two-phase flow which is detrimental to the safety of the reactor.

Experimental investigations of single-branch discharge have been conducted. These investigations have examined the onsets of gas and liquid entrainment for branch orientations of bottom, side, and top. As well, theoretical investigations of the onset of liquid entrainment for single and dual side-oriented branches have also been performed. These investigations have treated the branch or branches as point sinks or circular geometry with a finite diameter. Further, for the case of dual-branch discharge, experimental studies into the onsets of gas and liquid entrainment have been performed for two side-oriented branches with centerlines falling in a vertical plane only. To date, there does not exist a theoretical model for the onset of liquid entrainment that considers two branches of finite dimensions discharging horizontally with centerlines falling in an inclined plane. Further, experimental data do not exist for the onsets of liquid and gas entrainment for two side-oriented branches with centerlines falling in an inclined plane.

An experimental study was conducted on the onsets of gas and liquid entrainment for dual, horizontal discharge from two, 6.35 *mm* diameter branches with centerlines falling in an inclined plane located on the side of a large pressure vessel that contained a stratified two-phase air-water mixture. A test apparatus was utilized that permitted measurement of the test-section pressure, branch separation distance, an-

gle of inclination of the branches, branch flow rates, and the critical height at the onset. The system pressure was fixed at 310 kPa and 510 kPa for the onsets of liquid entrainment and gas entrainment, respectively. The onset was measured as the distance from the center of the primary branch to the flat air-water interface. It was detected visually as the moment the entrainment became continuous; i.e., a liquid stream or gas cone was entraining into at least one branch. The primary branch was defined as the branch located closest to the air-water interface. The distance between the branches was controlled as well as the angle of inclination. Further, the flow rates in the branches were measured using the Froude number. For the present investigation for both gas and liquid entrainment onsets, experimental data were collected for branch separation distances of l/d = 1.5, 2.0, and 8.0. For separation distances of l/d = 1.5 and 2.0, experimental data were collected for angles of inclination, α, of 0°, 10°, 30°, and 60°. For l/d = 8.0, data were collected for α = 0°, 10°, and 30°. For each l/d and α combination, four Froude numbers at the secondary branch, Fr_2, were established. For the onset of liquid entrainment, Fr_2's of 9.5, 19.0, 28.5, and 38.0 were specified and for the onset of gas entrainment, Fr_2's of 14.0, 28.5, 42.5, and 56.6 were set. Within the experimental matrix just described, data were generated for as wide a range of primary branch Froude numbers, Fr_1, as possible. For the onset of liquid entrainment, the Fr_1 range was 0 to 38.0 and for the onset of gas entrainment, the Fr_1 range was 0 to 70.0.

The critical height corresponding to the onsets of gas and liquid entrainment were found to be dependent upon the two branch discharge rates, the separation distance between the orifices, and the angular orientation. Further, the data collected were placed into five categories corresponding to five distinct modes of entrainment. The categorization scheme developed is analogous for gas and liquid entrainment.

The onset of liquid entrainment was analyzed theoretically for dual discharge through two side-oriented square branches of finite dimension d with centerlines falling

in an inclined plane; these branches discharge from a large reservoir containing a stratified mixture of two immiscible fluids. The theoretical analysis assumes constant-property, incompressible flow under steady-state conditions. Further, the effects of viscosity and surface tension are neglected. The flow is assumed to be irrotational such that potential flow theory applies. A closed-form solution is given that can be solved iteratively for the critical height at the onset. The theoretical model was in excellent agreement with the experimental data for the onset of liquid entrainment.

ACKNOWLEDGMENTS

I would like to extend sincere appreciation to my advisors, Dr. H.M. Soliman and Dr. G.E. Sims, for their continuous encouragement, guidance, and support.

The financial support of Atomic Energy of Canada Limited, The Whiteshell Laboratories is gratefully acknowledged. As well, the financial support of the University of Manitoba Department of Mechanical and Industrial Engineering in the form of Sessional Lecturer and Teaching Assistantship positions is acknowledged.

I would like to thank my wife, Margaret, for her patience and encouragement throughout my graduate research.

TABLE OF CONTENTS

LIST OF FIGURES

LIST OF TABLES

NOMENCLATURE

A	cross sectional area of branch, m^2
$ALPM$	Actual Litres Per Minute
b_1, b_2	constants in Equation (2.1)
Bo	Bond number as given in Equation (2.9)
C_P	constant pressure specific heat, $J/kg.K$
d	branch diameter, 6.35 mm, or dimension of square branch side, m
D	linear distance, m
DPT	differential pressure transducer reading, $volts$
Fr	Froude number as given by Equation (3.28)
Fr^*	modified Froude number as given by Equation (2.25)
g	gravitational acceleration, 9.81 m/s^2
h	height of interface measured relative to the flat interface, m
$H = h/l$	nondimensional height of interface
k	ratio of specific heats
l	separation distance of branches, m
$L = l/d$	nondimensional separation distance of the branches
$\dot{m}$	mass flow rate, kg/s
N_Γ	Circulation number as given in Equation (2.6)
N_μ	Viscosity number as given in Equation (2.10)
P	pressure, Pa
Q	parameter in uncertainty analysis
$\dot{Q}$	volume flow rate, $SLPM$
R	universal gas constant, $J/kg.K$
Re	Reynolds number

s	distance between the tip of the deflected interface and the branch or slot centerline, m
s/d	nondimensional distance between the tip of the deflected interface and the branch or slot centerline
$S = s/l$	nondimensional distance between the tip of the deflected interface and the branch or slot centerline
$SCALE$	flow meter scale reading, %
$SLPM$	Standard Litres Per Minute
t	distance between a point on the deflected interface and the flat interface, m
T	temperature, K
$T^* = t/l$	nondimensional distance between a point on the deflected interface and the flat interface
v	mean velocity of fluid in the main pipe, m/s
v_d	mean velocity through the branch, m/s
V	local velocity, m/s
W	micromanometer reading, m
x, y, z	Cartesian coordinate system
X	nondimensional density given by Equation (B.17)
Greek	
α	angle of inclination of branches, *degrees*
μ	viscosity, $kg/s.m$
ρ	density, kg/m^3
$\Delta\rho$	density difference between heavy and light phases, $kg/m.s$
σ	surface tension, N/m
ϕ	scalar potential flow function

Subscripts

act	actual
atm	atmosphere
B	linking point
cal	calibration
f	flat interface
fm	flow meter
g	gauge
G	gas
i	branch inlet
L	liquid
m	meniscus
S	system
SS	stainless steel float in rotameters
ST	standard temperature and pressure
o	test section
1	primary branch
2	secondary branch

CHAPTER 1

INTRODUCTION

In recent years the nuclear power industry has become increasingly concerned with accident scenarios that involve the loss of reactor cooling fluid. Such an accident scenario is termed a Loss-of-Coolant Accident or LOCA. In a LOCA simulation, one objective is to determine the distribution of the cooling fluid throughout the reactor core. Of primary importance to the simulation is the configuration of the piping network that distributes the cooling fluid to the core.

CANDU reactors use a piping network that consists of large manifolds (or headers) and feeder tubes. A typical header/feeder tube arrangement consists of two headers situated on either side of the reactor core and the feeder tubes that connect to each header and travel through the core. The feeders are spaced at regular intervals along the header length. As shown in Figure 1.1, at a given cross section, five feeder tubes branch away from the header, two exit horizontally, two exit inclined at 45°, and one exits vertically downwards.

With the fixed geometrical arrangement of the header and feeder tubes, two distinct flow phenomena may emerge during LOCA. Imagine that the liquid level in the header has dropped to the point where it is just above the two horizontal feeders. For certain conditions in the header, gas cones can get pulled down into the horizontal feeder tubes as shown in Figure 1.2. This is similar to what one observes when one drains a sink. The phenomenon is called gas pull-through or gas entrainment. Conversely, if the liquid level drops further to the point where feeder tubes are situated above the vapour-liquid interface, the flow of vapour out of the feeder

can pull the liquid up the wall and into the tube. This is depicted in Figure 1.3 and the phenomenon is termed liquid entrainment. For the situation shown in Figure 1.3, it is possible to have liquid entrainment in the feeders above the interface and gas entrainment in the feeders below the interface. Now, depending upon the proportion of each phase (vapour and liquid) that is present in the feeder tube, the cooling of the reactor core can range from adequate to insufficient. Thus, the understanding of gas and liquid entrainments is of major importance to the nuclear industry. At the University of Manitoba, over the past several years, experimental and theoretical investigations have taken place that are providing insights into the phenomena of gas and liquid entrainments (a detailed literature review is given in Chapter 2).

In order to study these phenomena, simplifications were made to the CANDU header/feeder geometry. The diameter of the header was assumed to be large enough, such that when compared to the feeder diameter, the header wall curvature is essentially flat and can be ignored. In addition, the feeder tubes or branches to be studied were situated in the horizontal orientation only. As a result, the complex header/feeder geometry of the CANDU reactor was approximated by a plane vertical wall with branches oriented horizontally. The simplified geometry is depicted in Figure 1.4. The number of branches was also reduced in order to simplify the problem further. Initial experiments and theoretical analyses examined only one branch. Building on the success of single-discharge studies, later works examined the case of two branches. Another simplification was the use of a smooth stratified interface which may not be the case in the real header. Finally, the gas and liquid entrainment phenenoma were initially limited to studying the onsets only.

The onset of gas or liquid entrainment is the point when single-phase flow in the branch just becomes two-phase. With the liquid level or interface sufficiently above the branch, only single-phase liquid is flowing out the branch as shown in Figure 1.4. As the interface drops, the flow of liquid out the branch has the effect of forming a

depression in the interface. As the interface continues to drop, the depression becomes larger to the point where, at a critical interface level, a gas cone is pulled into the orifice. At this moment the flow in the branch changes from single-phase liquid flow to two-phase gas-liquid flow and is termed the onset of gas entrainment. The opposite of the onset of gas entrainment is the onset of liquid entrainment. In the situation shown in Figure 1.5, the gas-liquid interface is sufficiently below the branch that only single-phase gas is exiting the branch. As the liquid level is raised, the flow of gas out the branch has the effect of raising the interface below the branch. As the liquid level rises further, the liquid is pulled up the wall higher and higher. Eventually, a critical interface level is reached where the liquid just begins entraining into the branch. At this moment, the flow out the branch changes from single-phase gas to two-phase gas-liquid flow. This instance is termed the onset of liquid entrainment and defines the boundary between single-phase gas flow and two-phase vapour-liquid flow. Thus, the onsets of gas and liquid entrainment define the upper and lower interface levels or boundaries at which the flow out the branch is either single-phase or two-phase. Outside the boundaries the flow is single-phase and within the boundaries the flow is two-phase.

With the above concepts and simplifications established, the relevant experimental variables were identified. In order to establish the upper and lower boundaries of two-phase flow by studying two onsets, the interface elevation or critical height, h, was identified as the dependent variable. The number of independent variables varies with the number of active branches. At first, single discharge or one-active-branch studies were conducted. With single discharge experiments, the independent variables are the branch diameter, d, the density of the gas phase, ρ_G, the density of the liquid phase, ρ_L, and the mass flow rate, $\dot{m}$, in the branch. Their effects on the critical height, h, were examined. When a second branch was introduced, more independent variables were added. The mass flow rate in the second branch, $\dot{m}_2$, was added as

an independent variable. The distance that separates the branches, l, can vary and it became an independent variable. Finally, the angle of inclination, α, formed by the horizontal and the straight line that passes through the centers of the branches became the last independent variable (see Figure 1.6). Therefore the experimental variables are as follows:

h	interface critical height	dependent variable
d	branch diameter	independent variable
ρ_G	gas density	independent variable
ρ_L	liquid density	independent variable
$\dot{m}_1$	mass flow rate in the primary branch	independent variable
$\dot{m}_2$	mass flow rate in the secondary branch	independent variable
l	separation distance between branches	independent variable
α	angle of inclination	independent variable

In previous experimental studies involving two branches, the separation distance, l, and the mass flow rates, $\dot{m}_1$ and $\dot{m}_2$, were varied. Extensive data were collected with the angle of inclination fixed at $\alpha = 90°$. Limited data were collected at $\alpha = 0°$ and need to be supplemented. It is the objective of this work to perform experimental studies that determine the onsets of gas and liquid entrainment for various angles of inclination between $\alpha = 0°$ and $\alpha = 90°$. In addition, a theoretical analysis will be performed to predict the liquid height at the onset of liquid entrainment for the conditions covered experimentally.

While the preceding discussion has focused on the application of the onsets of gas and liquid entrainment to the nuclear industry and, in particular, the LOCA simulation, the problem presented is applicable to any application where the geometrical and flow conditions are similar. As long as the geometrical situation consists of a large pressure vessel containing a two-phase mixture with branches discharging mass

horizontally from the vessel, the preceding discussion is applicable.

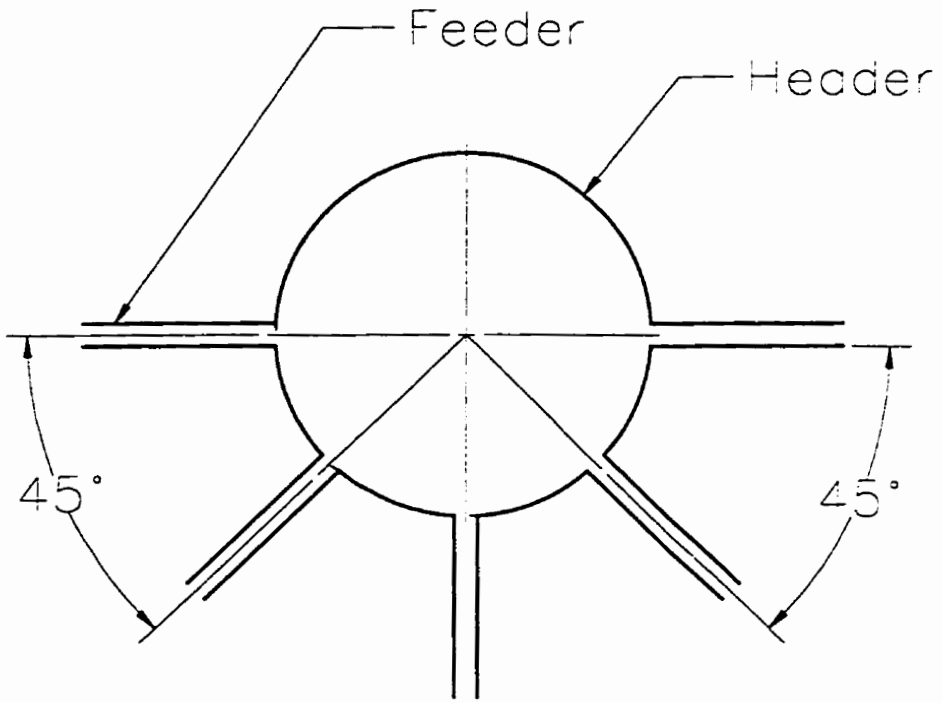

Figure 1.1: CANDU nuclear reactor header cross section

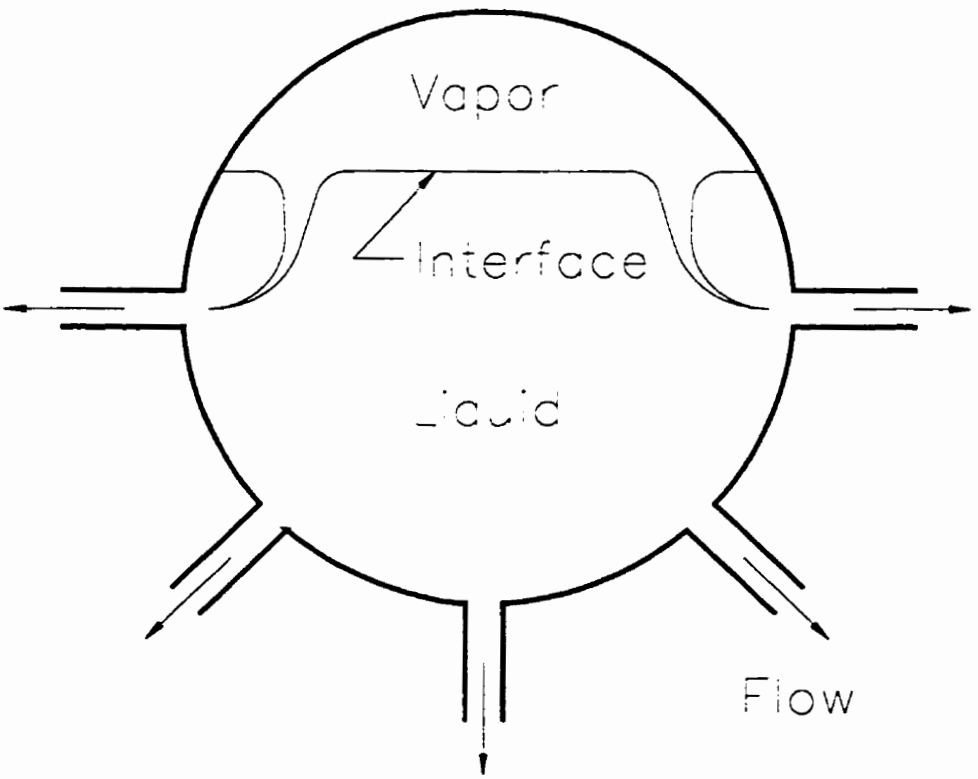

Figure 1.2: An example of the onset of gas entrainment in the header

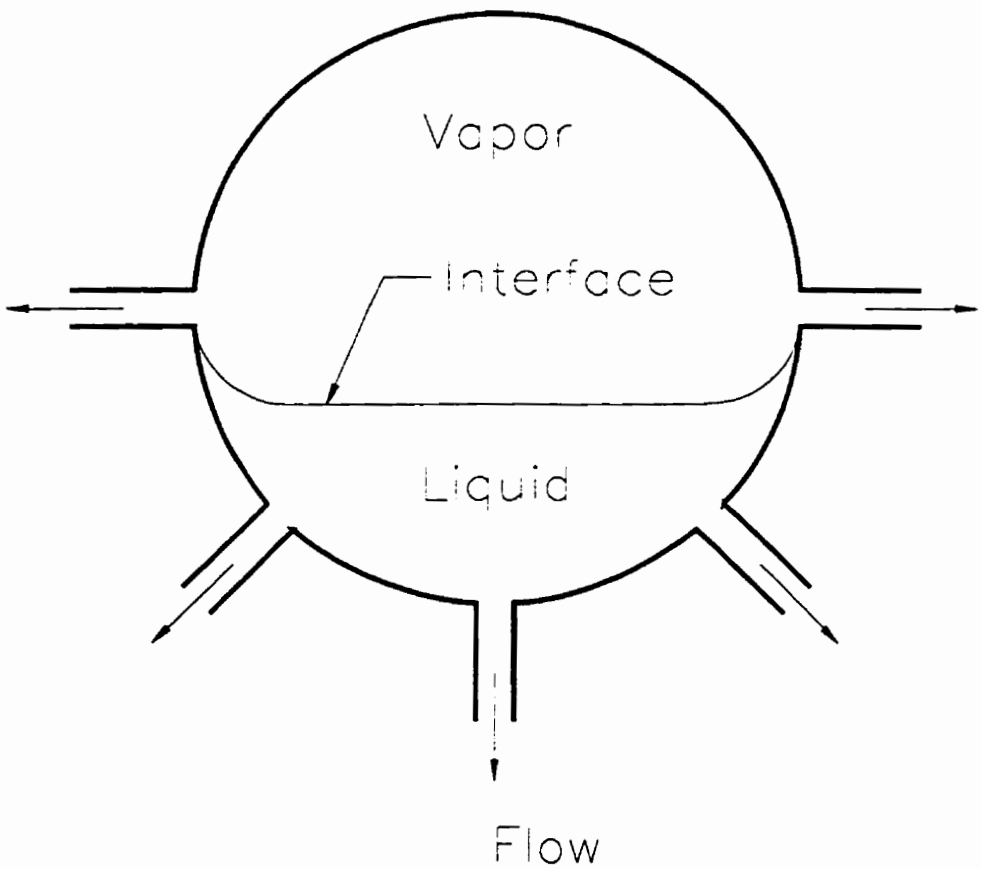

Figure 1.3: An example of the onset of liquid entrainment in the header

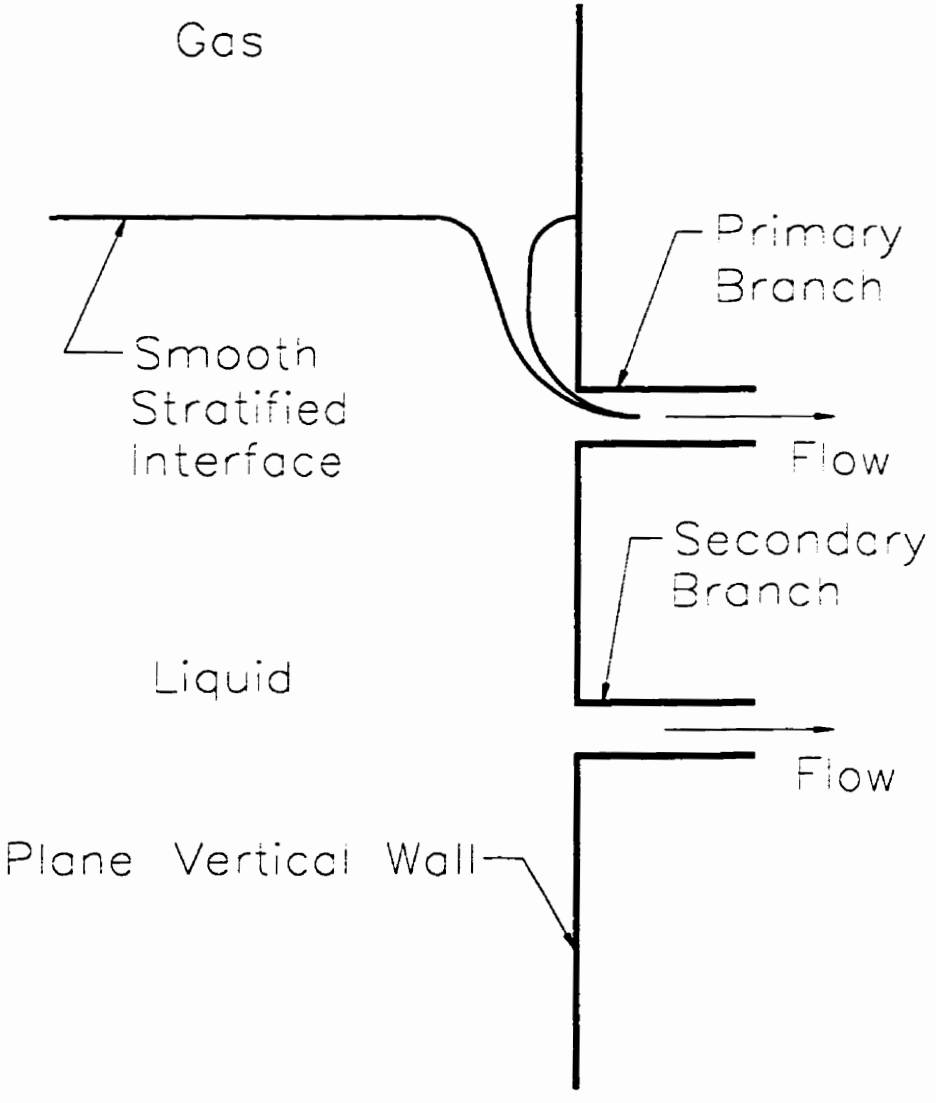

Figure 1.4: Simplified geometry used in previous studies

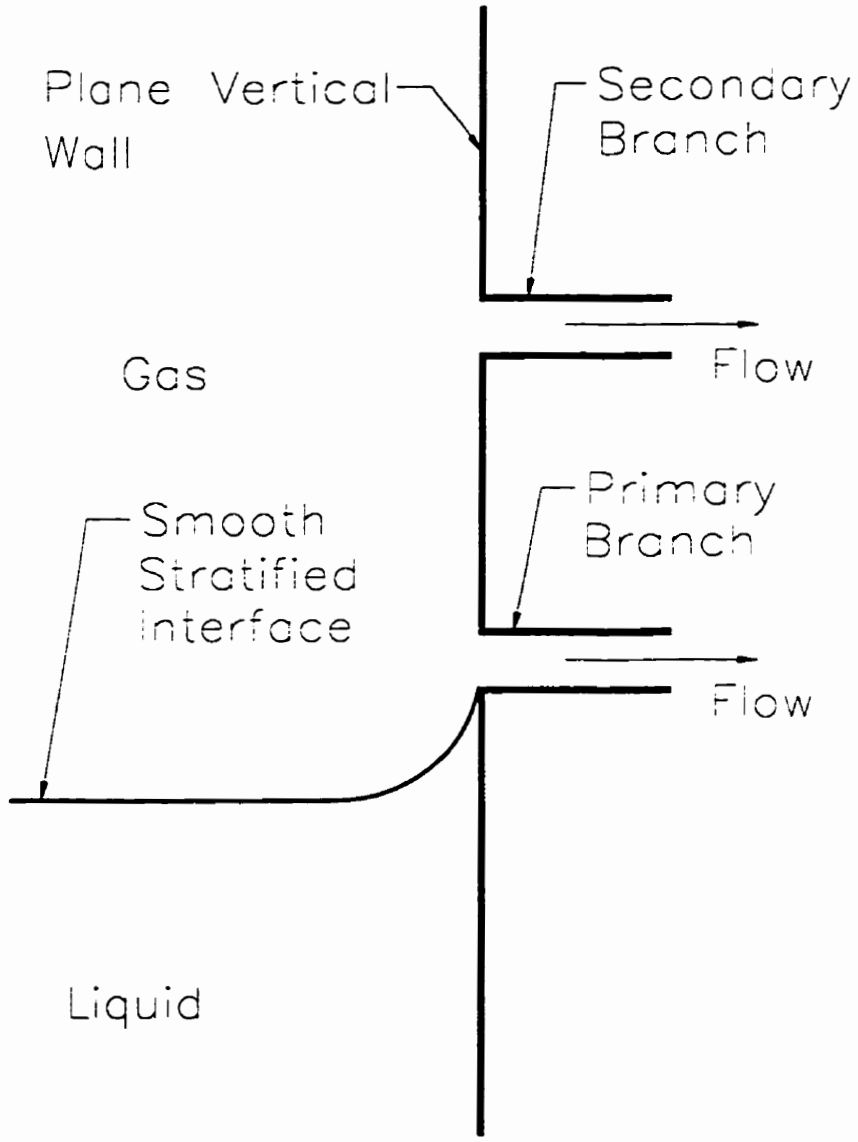

Figure 1.5: Onset of liquid entrainment for dual discharge from a plane vertical wall

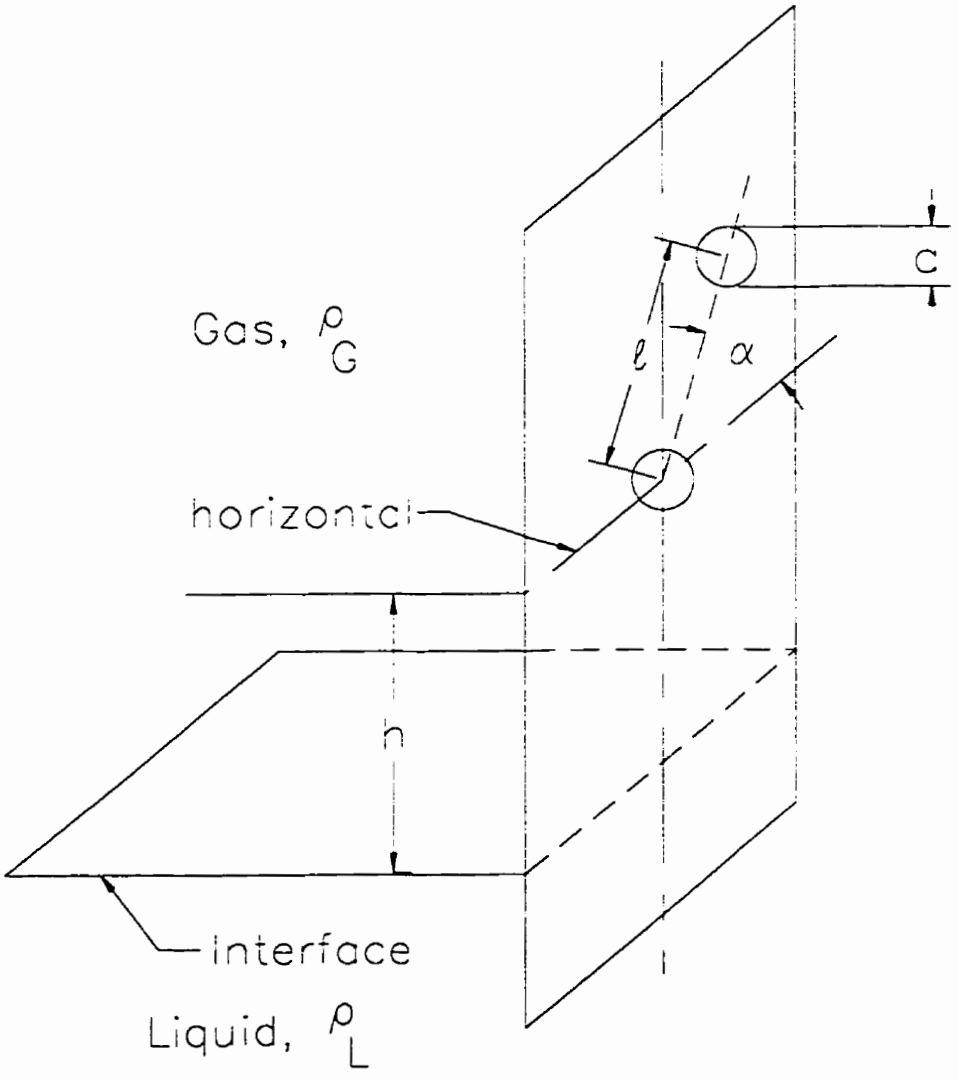

Figure 1.6: Geometry under consideration

CHAPTER 2

LITERATURE REVIEW

2.1 Introduction

This chapter contains a review of the publications related to the onsets of gas and liquid entrainment in small breaks. First, a review of literature prior to 1980 is given. Then, all relevant publications after 1980 pertaining to single breaks are reviewed. Finally, works that studied the onset phenomena in multiple breaks are presented. The words "break" and "branch" are used synonymously in this review.

2.2 Early Literature

Zuber (1980) published a report in which he presented the topic of two-phase flow through small breaks from the perspective of the nuclear industry. In this fundamental report, Zuber described the onset phenomena that may occur in the event of a LOCA. As well, he reviewed existing publications that examined the phenomena of the onsets of liquid and gas entrainment. He concluded from his literature review that both onsets of liquid and gas entrainment may be correlated by an equation of the form

$$h/d = b_1(Fr)^{b_2} \tag{2.1}$$

where h is the vertical distance from the flat interface to the centerline of the break, d is the diameter of the branch simulating the break, and b_1 and b_2 are constants whose

values depend on the type of phenomenon and geometrical arrangement, while Fr is the Froude number given by

$$Fr = \frac{v_d}{\sqrt{\frac{\Delta\rho}{\rho} gd}} \tag{2.2}$$

where v_d is the velocity of the continuous phase through the branch (which is gas during liquid entrainment and liquid during gas entrainment), ρ is the density of the continuous phase, $\Delta\rho$ is the density difference between the two phases, and g is the gravitational acceleration. In his report, Zuber was able to identify the relevant phenomena, define the parametric dependence of liquid and gas entrainment, and spark the curiousity of the research community. A summary of the publications he reviewed is presented in Table 2.1.

Table 2.1: Summary of publications reported in Zuber (1980)

Phenomenon	Authors	Geometry	Equation (2.1)	
			b_1	b_2
Liquid Entrainment	Craya (1949) & Gariel (1949)	Withdrawal from a large reservoir through a side branch	0.625	0.400
		Withdrawal from a large reservoir through a side slot	0.756	0.667
	Rouse (1956)	Withdrawal through a large reservoir through a vertical pipe	0.419	0.500
Gas Entrainment	Lubin and Hurwitz (1966)	Vortex-free withdrawal from a tank through a bottom branch		
		$h/d < 1$	0.574	0.667
		$h/d > 1$	0.624	0.400

Craya (1949) presented a theoretical paper which examined the flow phenomenon of liquid entrainment through a branch or a slot. The break was located on the side of a large reservoir containing an infinite vertical extent of two immiscible fluids of densities ρ and $\rho + \Delta\rho$ with the interface a distance h from the center of the break. Gariel (1949) experimentally verified the correlations derived analytically by Craya. In Craya's analysis he used Bernoulli's equation to describe the fluid motion along the interface and the potential flow theory to analyze the motion along the wall. As well, he neglected the effects of viscosity and surface tension. The branch and the slot were approximated as a point sink and a line sink, respectively. Craya's (1949) model for the onset of liquid entrainment yielded the first expression of the form of Equation (2.1). With respect to Equation (2.1), Craya obtained a value of b_1 of 0.625 and b_2 of 0.4 for a side branch and of b_1 of 0.699 and b_2 of 0.667 for a side slot. Despite the simplifications made in developing Equation (2.1), it proved to yield results which agreed remarkably well with the experimental data reported by Gariel (1949). However, in order to satisfy reservations about using these correlations, Craya performed a more detailed two-dimensional analysis for a slot which involved transformations and complex algebra. The resulting analytical expression for predicting the onset of liquid entrainment through a side slot was of the form of Equation (2.1) with b_1 equal 0.756 and b_2 equal 0.667. The new value of b_1 is only 8% higher than his first estimate. The new correlation proved to predict the experimental data of Gariel with high accuracy.

Rouse (1956) investigated the development of a non-circulatory waterspout both experimentally and theoretically. He measured the critical height for the onset of liquid entrainment into a vertical pipe. This publication is analogous to LOCA investigations simulating a top break. In the experimental investigation the apparatus consisted of an open tank with suction pipes of 12.7, 38.1, and 76.2 *mm* inner diameter mounted above the interface. Tests were performed in water under air and

saline water under fresh water. In the theoretical investigation, viscous and surface tension effects were neglected. Based on his theoretical and experimental work, Rouse suggested an experession of the form of Equation (2.1) with $b_1 = 0.419$ and $b_2 = 0.5$. The comparison between the theory and the experimental results yielded remarkable agreement suggesting that the assumptions made are valid. However, he noted that the results are limited to fluids of low viscosity.

Lubin and Springer (1967) considered the drainage of a cylindrical tank with a circular branch pipe located at the bottom of the tank. They investigated the critical height for the formation of a dip at the surface. In order to examine the effects of viscosities and densities of the water and the fluid above it, experiments were performed with air-water, water-turpentine, water-silicone oil, water-corn oil, and water-kerosene. As well, the tank was open to atmospheric pressure. In addition to performing an experimental investigation, the authors developed a theoretical expression to predict the critical height when the dip will form. The following assumptions were made in the analysis: 1) the effect of viscosity of the lighter and heavier fluid is negligible; 2) the effect of surface tension at the interface of the lighter and heavier fluid is negligible; 3) the pressure at the interface is due to the hydrostatic pressure only; 4) the flow is steady at the instant prior to the formation of the dip; and 5) the initial dip at the interface reaches the drain instantaneously. The correlation developed is of the form of Equation (2.1) with $b_1 = 0.625$ and $b_2 = 0.4$. The theoretical predictions were found to be in very good agreement with the experimental results which lead the authors to conclude that for a system similar to the one examined, the assumptions made in developing the theoretical correlation were valid.

Daggett and Keulegan (1974) studied vortex formation theoretically and experimetally. They established the parametric dependence of the critical height for vortex formation. The experimental apparatus consisted of two vortex tanks. The first tank was 1676 *mm* in diameter and 460 *mm* in depth. Drain branches of 25, 51, 76, and

100 *mm* were used. The second tank had a 343 *mm* diameter test area and was 240 *mm* in depth. Drain holes of 9.5, 19.29, and 38 *mm* were used in the second tank. The flow entered both tanks horizontally through a set of vanes to induce vortex flow. The authors tested several types of fluids in conjunction with one another in order to investigate the effects of viscous and surface tension forces on the formation of vortices. It was concluded that for the range of values tested, surface tension did not apprear to influence the flow. However, viscosity and initial circulation did affect the flow. The empirical correlations developed to predict the critical height for the onset of gas entrainment by a vortex type flow are as follows:

$$\frac{h}{d} = 17.5 \times 10^{-3} N_\Gamma Re, \qquad Re < 5 \times 10^4 \tag{2.3}$$

$$\frac{h}{d} = 75 N_\Gamma, \qquad Re \geq 5 \times 10^4 \tag{2.4}$$

where Re and N_Γ are the Reynolds number and circulation number given by the following equations:

$$Re = \frac{vd\rho}{\mu} \tag{2.5}$$

$$N_\Gamma = \frac{Vd}{2UH} \tag{2.6}$$

where, in Equation (2.6), V is the initial tangential velocity, U is the initial radial velocity, and H is the inital depth of fluid in the tank. Equations (2.3) and (2.4) represented the experimental data satisfactorily.

2.3 Recent Literature on Single Branches

Crowley and Rothe (1981) studied the onsets of liquid and gas entrainment for a stratified air-water flow in a horizontal pipe of 76.2 *mm* diameter with a branch pipe of 6.4 *mm* diameter oriented at the top, side and bottom of the main pipe. As well, they performed tests with a 6.4 *mm* diameter nozzle for the side orientation only. The operating pressure in the apparatus was 0.3 *MPa* and the flow was discharged directly to the atmosphere. Experimental values for the critical height at the onset of liquid entrainment through the top branch, side branch, and side nozzle geometries were measured. As well, the critical heights at the onset of gas pull-through were collected for the side branch, bottom branch, and side nozzle. These results were compared with the predicted critical heights from previously published correlations. A summary of their findings is presented in Table 2.2, where the percentage deviation refers to the deviation between experimental values and predictions.

Reimann and Smoglie (1983) performed experiments studying the onset of liquid entrainment through a branch located at the top of a main pipe containing a stratified air-water flow. The apparatus used was the same as that used by Reimann and Khan (1984), see below. They noted that at the onset of liquid entrainment, only a small fraction of the water spout reached the branch because of the large vorticity of the air flow. The theoretical correlation developed assumed negligible viscosity and surface tension effects. The resulting expression is of the form of Equation (2.1) with b_1=1.099 and b_2=0.25. They found that when superimposed velocities were introduced into Equation (2.1) the influence on b_1 was small. Finally, break mass flux and quality correlations after the onsets of liquid and gas entrainment were given with comparison to experimental results.

Table 2.2: Summary of the comparisons between the data of Crowley and Rothe (1981) and previous correlations

Geometry	Phenomenon	Correlation Used	h/d		Deviation (%)
			Measured	Calculated	
Top Branch	Liquid Entrainment	Rouse (1956)	3.60	3.00	20
Side Branch	Liquid Entrainment	Craya (1949) and Gariel (1949)	2.00	3.00	-33
Side Branch	Liquid Entrainment	Craya (1949) and Gariel (1949)	2.5	3.00	-17
Bottom Branch	Gas Entrainment	Lubin and Springer (1967)	3.96	3.00	32
Side Branch	Gas Entrainment	Lubin and Springer (1967)	2.52	3.00	-16
Side Nozzle	Gas Entrainment	Lubin and Springer (1967)	3.54	3.24	9.3

Reimann and Khan (1984) studied the critical height for the onset of gas entrainment using an air-water mixture with a bottom break only. The apparatus consisted of a horizontal main pipe of 206 mm diameter and circular branches of 6, 12, and 30 mm. The system pressure was 0.5 MPa and the flow through the branch was regulated by a valve. In addition to examining the critical heights, the break mass flux and break quality were also measured. Three different stratified air-water flows were tested. For symmetrical inflow from both ends of the main pipe, the onset of gas entrainment always occurred through a vortex-free mechanism and their data

agreed well with Equation (2.1) with values of b_1 and b_2 as reported by Lubin and Springer (1967). The second type of flow condition studied was that of flow supplied from one end of the main pipe with the other end closed. For this condition, the onset of gas entrainment always occurred by a vortex-induced mechanism and the data were best correlated by Equation (2.1) with values of b_1 and b_2 of 1.9 and 0.4, respectively. Finally, the third flow condition studied was a stratified cocurrent flow through the main pipe. A vortex-free onset of gas entrainment was always observed here and the data agreed well with Equation (2.1) with b_1 and b_2 equal 1.025 and 0.4, respectively.

Hardy and Richter (1984) studied the onset of gas entrainment from a stratified steam-water mixture through side and bottom nozzles. The apparatus consisted of a 178 mm diameter pressure vessel, 254 mm in height with the break located in the end flange. The vessel could be rotated 90° to simulate a bottom or a side break. For both bottom and side orientations, nozzles of 6.35 and 12.7 mm diameters were tested. The initial system pressure was varied between 2.7 Pa and 0.3 MPa. They used the Reimann and Khan (1984) correlation for symmetrical inflow (i.e., b_1=0.625 and b_2=0.4) to predict the onset of gas entrainment for both bottom and side nozzle orientations. The authors assumed that for the side orientation no liquid entrainment would occur if the liquid level was below the nozzle as long as one accounted for the swelling of the flashing mixture. Good agreement was found between the experimental results and the theoretical correlation. In addition, break entrance quality and mass flux analyses beyond the onsets of liquid and gas entrainment were performed and compared with experimental results.

Smoglie and Reimann (1986) performed air-water tests in a horizontal pipe with stratified flow to study the onsets of liquid and gas entrainment through top, side, and bottom branches. The apparatus was the same as that of Reimann and Khan (1984). The theoretical correlation used was of the form of Equation (2.1). However, based

on previous literature the authors suggested a value of b_2=0.4 should be used in Equation (2.1) for both onsets of liquid and gas entrainment and all orientations of the branch. The value of b_1 was obtained by comparison with the experimental results obtained. For liquid entrainment they suggested b_1=1.516 for the top branch and b_1=0.626 for the side branch. The latter is in excellent agreement with Craya (1949) and Gariel (1949). For gas entrainment, b_1 = 0.681 for the side branch correlated well with their results. Values of b_1 for gas entrainment for the bottom branch were 1.816 during vortex flow and 0.625 during vortex-free flow. The latter is in remarkable agreement with that of Lubin and Springer (1967). When results were presented for superimposed velocities, a significant influence was observed only for gas entrainment at the bottom branch. Therefore, the authors suggested that the correlations found experimentally for the top and side branches, having inflow from one end, may be applied to situations where the stratified mixture flows cocurrently through the pipe (i.e., superimposed velocities). Finally, correlations were presented for break quality and break mass flux for zero and non-zero superimposed velocities after the onsets of liquid and gas entrainment.

Schrock *et al.* (1986) studied the onset of liquid and gas entrainment for stratified two-phase flow in a horizontal main pipe (102 mm diameter) with branches (4, 6, and 10 mm diameter) oriented downwards, sideways and upwards. Both air-water and steam-water were studied at system pressures up to 1.07 MPa with flow regulated by a valve. For air-water and steam-water tests, the gas entrainment experimental results did not correlate well when presented in the form of Equation (2.1) for both bottom and side branch tests. By including the effects due to viscosity, μ, and surface tension, σ, they developed the following correlations which are functions of Bond number, viscosity number, and Froude number:

$$FrBo^2 N_\mu^{-0.5} = 19.4 \left(\frac{h}{\sqrt{\sigma/g\Delta\rho}} \right)^{2.2} \tag{2.7}$$

for gas entrainment at the bottom branch and

$$FrBo^2N_\mu^{-0.5} = 40.6\left(\frac{h}{\sqrt{\sigma/g\Delta\rho}}\right)^{2.1} \tag{2.8}$$

for gas entrainment at the side branch. In the above expressions, Bo is the Bond number given by,

$$Bo = \frac{d}{\sqrt{\sigma/g\Delta\rho}} \tag{2.9}$$

and N_μ is the viscosity number given by,

$$N_\mu = \mu\left(\frac{g\Delta\rho\sigma^3}{\rho^3}\right)^{0.25} \tag{2.10}$$

Equations (2.7) and (2.8) represented well the experimental results obtained. For liquid entrainment, the critical heights for both side and top branch orientations were found to be independent of surface tension and viscosity effects. Therefore, the experimental results for the side branch were represented well by Equation (2.1) with b_1 and b_2 agreeing with Craya (1949) and Gariel (1949). Lastly, for the top break, an expression of the form of Equation (2.1) well correlated the experimental results with $b_1 = 1.45$ and $b_2 = 0.4$. Finally, quality correlations were given.

Anderson (1987) performed similar studies with a single 34 mm diameter branch oriented at the side or bottom of a horizontal pipe of 284 mm diameter with stratified steam-water flow at system pressures of 3.4, 4.4, and 6.2 MPa. Anderson concluded from the high pressure experiments that for a side branch, the previous results of Smoglie and Reimann (1986) are valid for the onsets of liquid and gas entrainment, branch mass flow rate, and branch flow quality. In addition, for gas entrainment at the bottom branch orientation, Anderson found good agreement between the experimental results and the correlations of Reimann and Khan (1984). Therefore, fluid properties such as pressure do not seem to cause large deviations in the predictions for the onsets of liquid entrainment.

Yonomoto and Tasaka (1988) performed a theoretical and experimental study on the onsets of liquid and gas entrainment of a stratified two-phase flow through a branch. The theoretical analysis revealed a correlation of the form of Equation (2.1) with $b_1 = 0.555$ and $b_2 = 0.4$ for both top and bottom breaks, and $b_1 = 0.483$ and $b_2 = 0.4$ for a side break. These values disagree with Lubin and Springer (1967). The authors felt that this was because Lubin and Springer (1967) developed their model from the condition of stable existence of the interface without entrainment, whereas, the their model was derived from the stable entrainment condition. Further, the authors stated that they observed unstable and intermittent entrainment of a liquid droplet or a gas bubble before the stable entrainment condition. An air-water experiment was performed with branch orientations of upward, horizontal, and downward. The apparatus consisted of a 190 mm square, horizontal duct with branch diameters of 10 or 20 mm. The maximum system pressure was 0.7 MPa and discharge flow was controlled by a valve. Three types of experiments were performed similar to Reimann and Khan (1984): a) air and water supplied from one side and the outlet flow from the duct is not zero; b) the outlet flow of air or water is zero; and c) air, water, or air and water symmetrically flow from both sides of the duct. From the theoretical analysis, an expression of the form of Equation (2.1) was obtained with values of b_1 and b_2 summarized in Table 2.3. For top break, entrainment was measured when a continuous stream of liquid droplets entered the branch which accounts for the high value of b_1. If entrainment was taken to be the moment the first droplet entered the branch the value of b_1 would have been as shown by the results of Smoglie and Reimann (1984) and Schrock *et al.* (1986). For side liquid entrainment, b_1 was larger than Smoglie and Reimann (1984) but similar to Anderson (1987). The experimental results correlated well with the predicted data for top- and side-branch liquid entrainment and side- and bottom-branch gas entrainment when using Equation (2.1) with

the values of b_1 and b_2 given in Table 2.3[1].

Table 2.3: Experimental results of Yonomoto and Tasaka (1988) compared with previously published experimental results

Phenomenon	Branch		Yonomoto and Tasaka (1988)	Smoglie and Reimann (1986)	Schrock *et al.* (1986)		Anderson (1987)
			A-W	A-W	A-W	S-W	S-W
Liquid Entrainment	Top	b_1	0.626	1.516	1.440	1.440	—
		b_2	0.400	0.400	0.400	0.400	—
	Side	b_1	0.559	0.626	0.624	—	0.563
		b_2	0.400	0.400	0.400	—	0.400
Gas Entrainment	Side	b_1	0.681	0.681	0.674	0.917	0.745
		b_2	0.400	0.400	0.500	0.500	0.400
	Bottom	b_1	0.909	1.025	0.825	1.130	0.909
		b_2	0.400	0.400	0.500	0.500	0.400

Empirical modifications were made to their theoretical results which yielded values of $b_1 = 0.628$ and 0.860 for side and bottom gas entrainment, respectively. These values disagree with the values in Table 2.3. The authors felt that this occurred because the derivation of their model was based upon the stable entrainment condition without crossflow and vortex flow. Further, intermittent entrainment was not considered important because break flow may be considered single-phase flow. In addition

[1]In Table 2.3 A-W represents Air-Water and S-W represents Steam-Water.

to the correlations for the onsets of liquid and gas entrainment, Yonomoto and Tasaka developed correlations for break quality and flow rates. Yonomoto and Tasaka (1991) improved their existing empirical correlations for break quality and flow rates and acheived better agreement with their experimental results obtained in 1988.

Micaelli and Memponteil (1989) studied the onsets of liquid and gas entrainment for steam-water stratified flow in a horizontal pipe of 80 and 135 mm in diameter with branches of 12 and 20 mm oriented upwards, horizontally, and downwards. The system pressure was varied from 0.2 to 7 MPa and the branch discharge was controlled by a valve. One of the objectives of the study was to extend the range of flow conditions covered by previously published data for liquid and gas entrainment. The authors found that at liquid velocities near zero the trend for gas entrainment at the bottom branch was well represented by Equation (2.1) with values of b_1 and b_2 given by Smoglie and Reimann (1986). However, b_1 decreased significantly as the liquid velocity in the pipe increased. For example, b_1 was found to drop to 0.4 for a velocity of 3 m/s. Therefore, the authors suggested that the stability of gas entrainment may be controlled by a balance between horizontal and vertical inertia forces. If the liquid velocity is v and v_d in the branch, then the ratio of horizontal to vertical inertia forces is $(v/v_d)^2$. Using this ratio, a new correlation was developed to predict the onset of gas entrainment for the bottom branch:

$$\frac{h}{d} = 0.907 \left[1 - \left(\frac{v}{v_d} \right)^{0.4} \right] Fr^{0.4} \tag{2.11}$$

Their results for the onsets of liquid and gas entrainment at the side branch were in good agreement with those of Smoglie and Reimann (1986). However, the experimental results for liquid entrainment in the top branch and the results obtained by Smoglie and Reimann (1986) were best represented by Equation (2.1) with the new values of b_1=0.749 and b_2=0.667.

Soliman and Sims (1991) and Soliman and Sims (1992) analyzed theoretically

the onset of liquid entrainment during discharge from large reservoirs containing a stratified mixture of two immiscible fluids through a side slot of small finite width and side branch of small finite diameter, respectively. They pointed out that the investigation done by Craya (1949) simulating the slot as a two-dimensional line sink and the branch as a point sink does not approach appropriate limits as the discharge approaches zero. Craya developed the following correlations:

$$h/d = 0.699 Fr^{2/3} \tag{2.12}$$

and

$$s/d = (2/3)(h/d) \tag{2.13}$$

for a side slot and

$$h/d = 0.625 Fr^{0.4} \tag{2.14}$$

and

$$s/d = 0.8 h/d \tag{2.15}$$

for a side branch, where s is the distance between the tip of the deflected interface and the centerline of the slot or branch. From the above equations, as Fr goes to zero, h and s go to zero, while physically $h = s = d/2$ is a more appropriate limit for both the side slot and the side branch. Therefore, the authors wished to take into consideration the finite size of the slot and the branch to make the results more applicable to the whole range of Fr. The analysis follows Craya's (1949) approach neglecting the effects due to viscosity and surface tension. Only the correlations developed for a side slot are presented here:

$$\frac{h}{d} = \frac{s}{d} + \frac{1}{2}\left(\frac{Fr}{\pi}\right)^2 \left[\ln\left(\frac{s/d - 1/2}{s/d + 1/2}\right)\right]^2 \tag{2.16}$$

and

$$\ln\left(\frac{s/d+1/2}{s/d-1/2}\right)=\frac{(s/d)^2-1/4}{(Fr/\pi)^2} \tag{2.17}$$

Equation (2.17) can be solved iteratively for s/d which is then substituted into Equation (2.16) to solve for the critical height h/d. The authors note that both equations are functions of Fr as are Craya's. In addition, s/d and h/d both approach the limiting value of $1/2$ as Fr goes to zero and as Fr increases Equations (2.16) and (2.17) approach Craya's (1949) model. For discharge through a side branch, comparison with experimental data collected by Armstrong *et al.* (1992) revealed that for high values of Fr the experimental deviation from Craya's (1949) model was small. In addition, for low values of Fr the experimental results closely followed the trends suggested by the new model. They concluded that their model for a side slot or side branch closely approaches Craya's simplified model beyond $Fr = 10$; however, the authors recommended their model for $Fr < 10$.

Hassan *et al.* (1994) performed experiments studying the mass flow rates and quality of a two-phase discharge through a small branch located on the side of a large reservoir under stratified conditions. Good agreement was found when comparing their data for the critical height at the onset of liquid entrainment with previous results. The authors stated that the manner in which the experiment was performed influenced h at low discharge values. Deviations occurred between a slowly decreasing liquid level and a slowly increasing liquid level when measuring the critical height at the onset of liquid entrainment. For the critical height for the onset of gas pull-through, the data correlated best with Micaelli and Memponteil (1989). In addition, the mass flow rate and quality results also correlated best with Micaelli and Memponteil (1989). The authors suggest that one reason for the good agreement with Micaelli and Memponteil is that the correlation developed by Micaelli and Memponteil has the widest data base among all existing correlations.

2.4 Multiple Branches

Kowalski and Krishnan (1987) studied two-phase steam-water flow in a large manifold typical of a CANDU reactor header-feeder system. The authors reported flow phenomena of stratification in the manifold and flow stagnation followed by steam flushing in some of the feeders. It was reported that the correlations of Smoglie and Reimann (1986) did not predict well the onsets of liquid and gas entrainment of the complex geometry. One possible reason for the disagreement is that the CANDU header (see Figure 1.1) involves multiple discharge from the same cross-section while the correlations of Smoglie and Reimann correspond to single discharge. In addition to providing data for the onsets of liquid and gas entrainment, Krishnan and Kowalski obtained data for the void fraction in some feeders.

Parrott *et al.* (1991) performed experiments to investigate the onset of gas pull-through for simultaneous discharge from two branches (6.35 mm dia) located on the side of a high-pressure reservoir containing a stratified air-water mixture. The system pressure was maintained at 0.51 MPa and the separation distance between the branches, l, was varied centre-to-centre to yield tests at l/d=1.5, 2, 3, 4, and 6. In addition, the branches were vertically aligned for all tests and discharge through the branches, Fr_1 and Fr_2 , was controlled. The main objective of the study was to determine the influence of the separation distance and the rate of flow from the secondary or lower branch, Fr_2, on the onset of gas entrainment at the primary or upper branch, Fr_1. During the experiment, three possible onsets were observed depending on the system parameters. The onset of gas entrainment could occur at the upper branch only, lower branch only, or both branches simultaneously. In addition, it was noted that the critical height at the onset of gas entrainment could be reported as the distance between the flat interface to the branch centerline, h_f, or as the distance between the branch centerline and the meniscus created by the liquid at the

vessel wall, h_m. The meniscus height was approximately 3.3 mm which is significant compared to the size of the branch diameter (6.35 mm) and the height reported significantly influenced the results. For example, in the special case of extraction through the upper branch only (i.e., Fr_2=0) experimental results for h_m/d agreed quite well with the correlation suggested by Smoglie and Reimann (1986) while the results for h_f/d deviated significantly. Therefore, the authors recommended that the liquid height be specified more clearly in future studies. For h_f/d, Parrott *et al.* (1991) recommended Equation (2.1) with b_1=0.425 and b_2=0.529 if h_f/d is less than 1.15 and b_1=0.508 and b_2=0.435 otherwise. For all h_m/d, they recommended b_1=0.887 and b_2=0.334. For the onset of gas entrainment at the upper branch, it was found that the critical height increased as the discharge rate from the lower branch increased, with a larger effect at low values of Fr_1. In addition, the influence of Fr_2 on gas entrainment at the upper branch was enhanced as the distance between the branches was decreased. It was found that the influence of the second discharge, Fr_2, has little effect for $l/d > 6$. For the system analyzed and the experimental range covered, Parrott *et al.* (1991) developed the empirical correlation

$$\frac{h_f}{d} = 0.887 \left[Fr_1 + Fr_2 \exp\left\{ -2.52 \left(l/d\right)^{1.1} Fr_1^{-0.22} Fr_2^{-0.16} \right\} \right]^{0.334} \qquad (2.18)$$

to predict the onset of gas entrainment for two vertically aligned branches located on the side of a wall.

Armstrong (1991) examined theoretically the case in which two branches, located on the side of a large vessel containing a stratified two-phase mixture and with centerlines falling in an inclined plane, can be oriented at any angle. Armstrong made the following assumptions: a) the effects due to viscosity and surface tension were neglected, b) the flow was assumed to be steady, incompressible, and to have constant properties, and d) the flow was further assumed to be irrotational and potential flow theory was applied. The finite diameter branches were approximated by point sinks.

With these simplifications, a model was developed that predicted the onset of liquid entrainment. The approach was to establish a coordinate system centered on Sink 1 and obtain a model that predicted the onset with respect to Sink 1. Then, the coordinate system was shifted such that it was now centered on Sink 2 and the solution procedure repeated. Thus, two separate models were developed. The equations with respect to Sink 1 are as follows:

$$H_1 = T_1^* + \frac{1}{2}\left(\frac{Fr_1}{T_1^{*2}} + \frac{Fr_2\left[T_1^* + L\sin\alpha\right]}{\left[T_1^{*2} + L^2 + 2T_1^* L\sin\alpha\right]^{3/2}}\right) \div \left(\frac{2Fr_1}{T_1^{*3}} + \frac{Fr_2\left\{3\left[T_1^* + L\sin\alpha\right]^2 - \left[T_1^{*2} + L^2 + 2T_1^* L\sin\alpha\right]\right\}}{\left[T_1^{*2} + L^2 + 2T_1^* L\sin\alpha\right]^{5/2}}\right) \tag{2.19}$$

and

$$64 = \left(\frac{Fr_1}{T_1^{*2}} + \frac{Fr_2\left[T_1^* + L\sin\alpha\right]}{\left[T_1^{*2} + L^2 + 2T_1^{*2} L\sin\alpha\right]^{3/2}}\right) \times \left(\frac{2Fr_1}{T_1^{*3}} + \frac{Fr_2\left\{3\left[T_1^* + l\sin\alpha\right]^2 - \left[T_1^{*2} + L^2 + 2T_1^* L\sin\alpha\right]\right\}}{\left[T_1^{*2} + L^2 + 2T_1^* L\sin\alpha\right]^{5/2}}\right) \tag{2.20}$$

The equations with respect to Sink 2 are:

$$H_2 = T_2^* - L\sin\alpha + \frac{1}{2}\left(\frac{Fr_2}{T_2^{*2}} + \frac{Fr_1\left[T_2^* - L\sin\alpha\right]}{\left[T_2^{*2} + L^2 + 2T_2^* L\sin\alpha\right]^{3/2}}\right) \div \left(\frac{2Fr_2}{T_2^{*3}} + \frac{Fr_1\left\{3\left[T_2^* - L\sin\alpha\right]^2 - \left[T_2^{*2} + L^2 - 2T_2^* L\sin\alpha\right]\right\}}{\left[T_2^{*2} + L^2 - 2T_2^* L\sin\alpha\right]^{5/2}}\right) \tag{2.21}$$

and

$$64 = \left(\frac{Fr_2}{T_2^{*2}} + \frac{Fr_1\left[T_2^* - L\sin\alpha\right]}{\left[T_2^{*2} + L^2 - 2T_2^{*2} L\sin\alpha\right]^{3/2}}\right) \times \left(\frac{2Fr_2}{T_2^{*3}} + \frac{Fr_1\left\{3\left[T_2^* - L\sin\alpha\right]^2 - \left[T_2^{*2} + L^2 - 2T_2^* L\sin\alpha\right]\right\}}{\left[T_2^{*2} + L^2 - 2T_2^* L\sin\alpha\right]^{5/2}}\right) \tag{2.22}$$

where $T^* = t/l$. An iterative solution technique was employed to solve for T_1^* or T_2^* in Equations (2.20) and (2.22), respectively, where $T^* = t/l$. These solutions were then substituted into Equations (2.19) and (2.21) to solve for the critical heights H_1 and H_2, respectively. The critical heights, H_1 and H_2, were then compared and a procedure was employed to determine at which orifice liquid entrainment occurred. If H_1 was greater than H_2 then the phenomenon was said to have occurred at Sink 1 or branch 1. If the opposite is true, then the phenomenon occurred at Sink 2 or branch 2. Finally, if H_1 equals H_2, then entrainment was simultaneous.

Armstrong *et al.* (1992) performed a theoretical and experimental study on the onset of liquid entrainment for simultaneous discharge from two vertically aligned branches (6.35 mm dia) located on the side of a large pressure vessel containing a stratified air-water mixture. The apparatus was the same as that used by Parrott *et al.* (1991). The system was maintained at a pressure of 0.31 MPa. The main objective of the study was to determine the influence of the separating distance, l, and the discharge from the secondary or upper branch, Fr_2, on the critical height for liquid entrainment at the primary or lower branch, Fr_1. The separating distance was varied to yield tests at l/d=1.5, 2, 3, and 4. In their experiment, liquid entrainment occurred at the lower branch only. For the special case of Fr_2=0, the experimental data correlated well with Craya's (1949) model. However, the authors stated that at low discharge the data diverged from Craya's (1949) model due to the approximation of the branch as a point sink. Similar to Parrott *et al.* (1991), it was found that h/d increased as Fr_2 increased for all Fr_1 and was much more pronounced at low Fr_1 values. In addition, this influence of Fr_2 on h/d was enhanced as the separating distance, l, was decreased. It was concluded that the flow through the second or upper branch has a small effect on h/d for $L/d > 4$. The following correlations were

developed:

$$H = S + \frac{1}{4}\left[\frac{\frac{Fr_1^*}{S^2} + \frac{Fr_2^*}{(1+S)^2}}{\frac{Fr_1^*}{S^3} + \frac{Fr_2^*}{(1+S)^3}}\right] \tag{2.23}$$

and

$$\left[\frac{Fr_1^*}{S^2} + \frac{Fr_2^*}{(1+S)^2}\right]\left[\frac{Fr_1^*}{S^3} + \frac{Fr_2^*}{(1+S)^3}\right] = 32 \tag{2.24}$$

where

$$Fr^* = \frac{(4/\pi)\,\dot{m}}{\sqrt{g\frac{\Delta\rho}{\rho}l^5}}, \qquad H = h/l, \qquad \& \qquad S = s/l \tag{2.25}$$

and Fr^* is related to Fr and H to h/d by

$$Fr = Fr^*\left(\frac{l}{d}\right)^{2.5} \qquad \& \qquad \frac{h}{d} = H\left(\frac{l}{d}\right) \tag{2.26}$$

The model showed the same trend as the experimental results stated above. Overall, Armstrong *et al.* stated that the theory slightly overpredicted the experimental data most likely due to the assumptions made in the analysis but the deviation is small.

Armstrong *et al.* (1992) performed a theoretical study into the onset of liquid entrainment for simultaneous discharge from two horizontal slots located on the side of a large reservoir containing a stratified air-water mixture. Armstrong *et al.* followed Craya's approach and extended it to the case of two parallel slots. The effects of viscosity and surface tension were considered negligible. The analysis resulted in the following correlations:

$$H = S + \frac{1}{2}\left[\frac{\frac{Fr_1^*}{S} + \frac{Fr_2^*}{(1+S)}}{\frac{Fr_1^*}{S^2} + \frac{Fr_2^*}{(1+S)^2}}\right] \tag{2.27}$$

and

$$\left[\frac{Fr_1^*}{S}+\frac{Fr_2^*}{1+S}\right]\left[\frac{Fr_1^*}{S^2}+\frac{Fr_2^*}{(1+S)^2}\right]=\pi^2 \tag{2.28}$$

where

$$Fr^*=\frac{q}{\sqrt{g\frac{\Delta\rho}{\rho}l^3}}, \qquad H=h/l, \qquad \& \qquad S=s/l \tag{2.29}$$

where q is the discharge per unit length of the slot. The authors stated that for Fr_2^*=0, Equation (2.28) reduces to Craya's (1949) model and Equation (2.27) reduces to $s = 2h/3$. The trends are similar to those of two branches; as Fr_2^* increases or l decreases h/l increases for all Fr_1^* and the effect is more pronounced at low Fr_1^*.

Hassan (1995) performed an experimental investigation into the onsets of gas and liquid entrainment for two side branches (6.35 mm dia) with centerlines falling in the same horizontal and vertical planes located on the side of a high-pressure reservoir containing a stratified air-water mixture. An experimental apparatus was constructed and system pressures of 316 and 516 kPa were used. The separation distance of the branches examined were l/d=1.5, 2.0, 3.0, and 8.0. The Froude numbers of the branches were held equal by maintaining equal pressure drop and equal hydraulic resistance across the branches. The pressure drop across the branches was varied from 37 to 229 kPa and the hydraulic resistance ranged from 900 to 3000 $(kg.m)^{-0.5}$. Empirical correlations were given for both the horizontal orientation and the vertical orientation of the branches. The correlations for the onset of gas entrainment and the onset of liquid entrainment, respectively, for the horizontal orientation are as follows:

$$h/d = 0.57\,(AFr)^{0.4} \tag{2.30}$$

and

$$h/d = 0.87\,(BFr)^{0.31} \tag{2.31}$$

where constants A and B are given by:

$$A = 1.0 + exp\left[-0.613\frac{l}{d}^{1.5} Fr^{-0.4}\right] \tag{2.32}$$

and

$$B = 1.0 + exp\left[-2.06\frac{l}{d}^{2.54} Fr^{-1.2}\right] \tag{2.33}$$

For the vertical orientation, the data presented for the onset of gas entrainment were in excellent agreement with the data reported by Parrott *et al.* (1991) and the data presented for the onset of liquid entrainment were in good agreement with the theoretical model presented by Armstrong *et al.* (1992). As well, a theoretical model was developed for predicting the onset of liquid entrainment for dual discharge from a large vessel containing a stratified two-phase mixture. The branches were of square cross-section and of finite dimension d. The following assumptions used: a) the effects of viscosity and surface tension were neglected, b) the flow was assumed to be steady, incompressible, and to have constant properties, and d) the flow was further assumed to be irrotational and potential flow theory was applied. The plane wall on which the branches were located was permitted to incline (i.e., the wall orientation was not restricted to the vertical position but pivoted so that the orientation of the branches varied from horizontal above the interface to vertical, as previously described). The model was in very good agreement with Armstrong *et al.* (1992). Further, when the secondary branch was inactive, $Fr_2 = 0$, the model was in excellent agreement with the single-discharge model presented by Soliman and Sims (1992) for a circular branch. This suggested that the shape of the branch had little effect on the onset.

The previous literature review shows that considerable information is available for single discharge while limited information is available for dual discharge. In particular, two theoretical models were reviewed for predicting the onset of liquid entrainment during dual discharge in which the branches were approximated by point sinks and

squares. Further, only three experimental studies were found that give data for the onsets of liquid and gas entrainment during dual discharge from a large pressure vessel containing a stratified two-phase mixture with branches discharging horizontally. Parrott *et al.* (1991) and Armstrong *et al.* (1992) presented extensive data for the case of two branches with centerlines falling in a vertical plane. Hassan (1995) presented limited data for two branches with centerlines falling in a horizontal plane. There is a need to study the onsets of gas and liquid entrainment such that the branches can be aligned with centerlines falling in an inclined plane. This information would benefit the design of piping networks in which small branches are distributing mass from a large header.

CHAPTER 3

THEORETICAL ANALYSIS

3.1 Introduction

The theoretical studies of the onset of liquid entrainment have primarily concentrated on single-branch models. Only two studies reported in the literature review contained theoretical models to predict the onset of liquid entrainment during dual discharge (Armstrong 1991 and Hassan 1995). The inappropriate physical limits of the model by Armstrong (1991) at $Fr_1 = Fr_2 = 0$ suggest that an alternate approach is required to conform adequately with the physics of the problem. This can be accomplished by performing a three-dimensional analysis that eliminates the point-sink assumption. The present solution follows the solution technique of Craya (1949) and applies to any two immiscible fluids.

3.2 Analytical Approach

The configuration for the present analysis is shown in Figure 3.1. A stratified layer of two immiscible fluids of densities ρ and $(\rho + \Delta\rho)$ is contained in a large reservoir. The circular branches are approximated as square branches located on the plane vertical wall of the reservoir. In Figure 3.1, the squares are of dimension d and are separated by a distance l measured from center to center. The coordinate system (x, y, z) is centered on Square 1. The angle of inclination, increasing counterclockwise, is denoted by α and is measured from the horizontal x-axis to the straight line that passes

through the centers of the squares. The analysis assumes steady, incompressible flow with constant fluid properties. In addition, potential flow is assumed throughout the flow field. Viscosity and surface tension effects are neglected with gravity and inertia forces dominating. Following the Armstrong (1991) approach, the *system method* for determining the onset of liquid entrainment is utilized. The *system method* considers that the onset can occur at either square or both squares simultaneously. Therefore, a solution is required that predicts the onset or critical height at Square 1, h_1, and one that predicts the onset or critical height at Square 2, h_2. By comparing the predictions given by the two solutions, the onset is obtained as follows:

$$\begin{aligned} h_s &= h_1 && \text{if } h_1 > h_2 \\ h_s &= h_2 && \text{if } h_1 < h_2 \\ h_s &= h_1 = h_2 && \text{if } h_1 = h_2 \end{aligned}$$

Craya (1949) first proposed an analytical solution composed of three steps. The first part of the solution is accomplished by performing an equilibrium analysis along the interface using Bernoulli's equation. Next, the velocity field in the lighter fluid is determined by a potential flow analysis. Third, equality of the velocity along the interface and its gradient at linking point B, shown in Figure 3.1, are imposed as the conditions for the onset of liquid entrainment. Finally, following the *system method*, the coordinate system is relocated to the center of Square 2 and the analysis repeated to determine the onset of liquid entrainment at Square 2. Thus, a two-solution set is obtained and the *system method*, as discussed above, is utilized to determine the true onset.

3.3 Equilibrium Balance at the Interface

The equilibrium at the interface is controlled by a balance between gravity and inertia forces as shown in Figure 3.1. Therefore, by applying the Bernoulli equation along a streamline coincident with the interface, first on the lighter fluid side then on the heavier fluid side and equating, the following expression was obtained

$$\frac{V^2}{2} = \frac{\Delta\rho}{\rho} gt \tag{3.1}$$

where V is the velocity along the interface and t is the local deflection measured from the flat interface. The linking point between the reservoir wall and the interface is denoted point B which corresponds to $t = h - s$, which on substituting yields

$$\frac{V_B^2}{2} = \frac{\Delta\rho}{\rho} g\,(h_1 - s_1) \tag{3.2}$$

Linking point B is of interest since it is at this location that the equilibrium velocity along the interface is equated with the velocity of the lighter fluid.

3.4 Velocity Field in the Lighter Fluid

In this analysis the velocity field in the lighter fluid is obtained by ignoring the presence of the heavier fluid. The lighter fluid is considered as a semi-infinite medium with boundaries $-\infty \leq x \leq +\infty$, $-\infty \leq y \leq +\infty$, and $0 \leq z \leq +\infty$. The flow discharges through the two squares situated on the $x - y$ plane at $z = 0$. The flow out Square 1 is denoted by velocity $-v_{d,1}$ over the range $-d/2 \leq x \leq +d/2$ and $-d/2 \leq y \leq +d/2$. Similarily, the flow out Square 2 is denoted by $-v_{d,2}$ over the range $(l\cos\alpha - d/2) \leq x \leq (l\cos\alpha + d/2)$ and $(l\sin\alpha - d/2) \leq y \leq (l\sin\alpha + d/2)$. With the assumptions stated above, the velocity field is obtained from the continuity equation,

$$\frac{\partial V_x}{\partial x} + \frac{\partial V_y}{\partial y} + \frac{\partial V_z}{\partial z} = 0 \tag{3.3}$$

By introducing the scalar potential flow function, ϕ, such that

$$V_x = \frac{\partial \phi}{\partial x}, \quad V_y = \frac{\partial \phi}{\partial y}, \quad and \quad V_z = \frac{\partial \phi}{\partial z} \tag{3.4}$$

the well known Laplace equation is obtained

$$\frac{\partial^2 \phi}{\partial x^2} + \frac{\partial^2 \phi}{\partial y^2} + \frac{\partial^2 \phi}{\partial z^2} = 0 \tag{3.5}$$

Equation (3.5) is subject to the following boundary conditions

1. $x \to \pm\infty$, ϕ is finite
2. $y \to \pm\infty$, ϕ is finite
3. $z \to +\infty$, ϕ is finite
4. a) $z = 0$, $\frac{\partial \phi}{\partial z} = -v_{d,1}$, $-d/2 \leq x \leq +d/2$ and $-d/2 \leq y \leq +d/2$
   b) $z = 0$, $\frac{\partial \phi}{\partial z} = -v_{d,2}$, $(l\cos\alpha - d/2) \leq x \leq (l\cos\alpha + d/2)$ and $(l\sin\alpha - d/2) \leq y \leq (l\sin\alpha + d/2)$
   c) $z = 0$, $\frac{\partial \phi}{\partial z} = 0$ all other x and y

A solution following the method of separation of variables, Zill (1989), that satisfies boundary conditions 1, 2, and 3 is

$$\phi = \int_0^{+\infty} \int_0^{+\infty} [A(\lambda,\mu)\cos(\lambda x) + B(\lambda,\mu)\sin(\lambda x)]\,[C(\lambda,\mu)\cos(\mu y) + D(\lambda,\mu)\sin(\mu y)]\,F(\lambda,\mu)\exp^{-\sqrt{\mu^2+\lambda^2}z}\,d\lambda d\mu \tag{3.6}$$

where constants A, B, C, D, E, and F are constants of integration. Now all that remains is to satisfy boundary condition 4. First, by taking the partial derivative of Equation (3.6) with respect to z and setting $z = 0$, the following expression is

obtained

$$\left.\frac{\partial\phi}{\partial z}\right|_{z=0} = \int_0^{+\infty}\int_0^{+\infty} \left[A_F(\lambda,\mu)\cos(\lambda x) + B_F(\lambda,\mu)\sin(\lambda x)\right] \left[C(\lambda,\mu)\cos(\mu y) + D(\lambda,\mu)\sin(\mu y)\right]\left(-\sqrt{\mu^2+\lambda^2}\right) d\lambda d\mu \quad (3.7)$$

where $A_F = A \times F$ and $B_F = B \times F$. By setting

$$J(x,\lambda,\mu) = \int_0^{+\infty} \left[A_F(\lambda,\mu)\cos(\lambda x) + B_F(\lambda,\mu)\sin(\lambda x)\right]\left(\sqrt{\mu^2+\lambda^2}\right) d\lambda \quad (3.8)$$

and substituting into Equation (3.7), the following was obtained

$$\left.\frac{\partial\phi}{\partial z}\right|_{z=0} = \int_0^{+\infty} -J(x,\lambda,\mu)\left[C(\lambda,\mu)\cos(\mu y) + D(\lambda,\mu)\sin(\mu y)\right] d\mu \quad (3.9)$$

Equation (3.9) is a Fourier Integral. Multiplying constant $J(x,\lambda,\mu)$ into the square brackets of Equation (3.9), constants $J_C(x,\lambda,\mu)$ and $J_D(x,\lambda,\mu)$ result. Now, applying boundary conditions 4a), b), and c), constants $J_C(x,\lambda,\mu)$ and $J_D(x,\lambda,\mu)$ were determined using Fourier cosine and Fourier sine transforms, respectively. The resulting expressions are:

$$\begin{aligned} J_C(x,\lambda,\mu) &= \frac{2v_{d,1}}{\mu\pi}\sin(\mu\frac{d}{2}) \quad for \quad -\frac{d}{2} \le x \le \frac{d}{2} \\ &= \frac{v_{d,2}}{\mu\pi}\left[\sin\left\{\left(l\sin\alpha + \frac{d}{2}\right)\mu\right\} - \sin\left\{\left(l\sin\alpha - \frac{d}{2}\right)\mu\right\}\right] \\ &\quad for \quad (l\cos\alpha - \frac{d}{2}) \le x \le (l\cos\alpha + \frac{d}{2}) \\ &= 0 \quad for\ all\ other\ x \end{aligned} \quad (3.10)$$

and

$$\begin{aligned} J_D(x,\lambda,\mu) &= 0 \quad for \quad -\frac{d}{2} \le x \le \frac{d}{2} \\ &= \frac{v_{d,2}}{\mu\pi}\left[\cos\left\{\left(l\sin\alpha - \frac{d}{2}\right)\mu\right\} - \cos\left\{\left(l\sin\alpha + \frac{d}{2}\right)\mu\right\}\right] \\ &\quad for \quad (l\cos\alpha - \frac{d}{2}) \le x \le (l\cos\alpha + \frac{d}{2}) \\ &= 0 \quad for\ all\ other\ x \end{aligned} \quad (3.11)$$

Next, by referring back to Equation (3.7), it can be seen that by expanding out the brackets, constants A_FC, A_FD, B_FC, and B_FD result. To solve for these constants, Equation (3.8) was multiplied by C. This produced the following expression:

$$J_C(x,\lambda,\mu) = \int_0^{+\infty} [A_FC(\lambda,\mu)\cos(\lambda x) + B_FC(\lambda,\mu)\sin(\lambda X)\,]\left(\sqrt{\mu^2+\lambda^2}\right)d\lambda \quad (3.12)$$

which is a Fourier Integral. Constants A_FC and B_FC are solved using Fourier cosine and Fourier sine transforms, respectively. Recalling that J_C is given by Equation (3.10), the expressions for A_FC and B_FC are given by

$$\begin{aligned} A_FC(\lambda,\mu) = \frac{1}{\mu\lambda\pi^2\sqrt{\mu^2+\lambda^2}}\Bigg\{ & 4v_{d,1}\sin\left(\mu\frac{d}{2}\right)\sin\left(\lambda\frac{d}{2}\right) \\ & + v_{d,2}\sin\left[\left(l\sin\alpha+\frac{d}{2}\right)\mu\right]\sin\left[\left(l\cos\alpha+\frac{1}{2}\right)\lambda\right] \\ & - v_{d,2}\sin\left[\left(l\sin\alpha-\frac{d}{2}\right)\mu\right]\sin\left[\left(l\cos\alpha+\frac{1}{2}\right)\lambda\right] \\ & - v_{d,2}\sin\left[\left(l\sin\alpha+\frac{d}{2}\right)\mu\right]\sin\left[\left(l\cos\alpha-\frac{d}{2}\right)\lambda\right] \\ & + v_{d,2}\sin\left[\left(l\sin\alpha-\frac{d}{2}\right)\mu\right]\sin\left[\left(l\cos\alpha-\frac{d}{2}\right)\lambda\right]\Bigg\} \end{aligned} \quad (3.13)$$

and

$$\begin{aligned} B_FC(\lambda,\mu) = \frac{v_{d,2}}{\mu\lambda\pi^2\sqrt{\mu^2+\lambda^2}}\Bigg\{ & \sin\left[\left(l\sin\alpha+\frac{d}{2}\right)\mu\right]\cos\left[\left(l\cos\alpha-\frac{d}{2}\right)\lambda\right] \\ & - \sin\left[\left(l\sin\alpha-\frac{d}{2}\right)\mu\right]\cos\left[\left(l\cos\alpha-\frac{d}{2}\right)\lambda\right] \\ & - \sin\left[\left(l\sin\alpha+\frac{d}{2}\right)\mu\right]\cos\left[\left(l\cos\alpha+\frac{1}{2}\right)\lambda\right] \\ & + \sin\left[\left(l\sin\alpha-\frac{d}{2}\right)\mu\right]\cos\left[\left(l\cos\alpha+\frac{1}{2}\right)\lambda\right]\Bigg\}. \end{aligned} \quad (3.14)$$

Similarly, constants A_FD and B_FD were determined by multiplying Equation (3.8)

through by D. This yielded the following expression:

$$J_D(x,\lambda,\mu) = \int_0^{+\infty} [A_F D(\lambda,\mu)\cos(\lambda x) + B_F D(\lambda,\mu)\sin(\lambda x)]\left(\sqrt{\mu^2+\lambda^2}\right) d\lambda \quad (3.15)$$

which is, again, a Fourier Integral and the constants were calculated in the same manner as previously stated. Performing the steps yields,

$$\begin{aligned} A_F D(\lambda,\mu) = \frac{v_{d,2}}{\mu\lambda\pi^2\sqrt{\mu^2+\lambda^2}} \Bigg\{ &\cos\left[\left(l\sin\alpha - \frac{d}{2}\right)\mu\right]\sin\left[\left(l\cos\alpha + \frac{1}{2}\right)\lambda\right] \\ &- \cos\left[\left(l\sin\alpha + \frac{d}{2}\right)\mu\right]\sin\left[\left(l\cos\alpha + \frac{1}{2}\right)\lambda\right] \\ &- \cos\left[\left(l\sin\alpha - \frac{d}{2}\right)\mu\right]\sin\left[\left(l\cos\alpha - \frac{d}{2}\right)\lambda\right] \\ &+ \cos\left[\left(l\sin\alpha + \frac{d}{2}\right)\mu\right]\sin\left[\left(l\cos\alpha - \frac{d}{2}\right)\lambda\right]\Bigg\} \end{aligned} \quad (3.16)$$

and

$$\begin{aligned} B_F D(\lambda,\mu) = \frac{v_{d,2}}{\mu\lambda\pi^2\sqrt{\mu^2+\lambda^2}} \Bigg\{ &\cos\left[\left(l\sin\alpha - \frac{d}{2}\right)\mu\right]\cos\left[\left(l\cos\alpha - \frac{d}{2}\right)\lambda\right] \\ &- \cos\left[\left(l\sin\alpha + \frac{d}{2}\right)\mu\right]\cos\left[\left(l\cos\alpha - \frac{d}{2}\right)\lambda\right] \\ &- \cos\left[\left(l\sin\alpha - \frac{d}{2}\right)\mu\right]\cos\left[\left(l\cos\alpha + \frac{1}{2}\right)\lambda\right] \\ &+ \cos\left[\left(l\sin\alpha + \frac{d}{2}\right)\mu\right]\cos\left[\left(l\cos\alpha + \frac{1}{2}\right)\lambda\right]\Bigg\}. \end{aligned} \quad (3.17)$$

With all constants determined, the velocity field in the lighter fluid can now be obtained by substituting the constants given by Equations (3.13), (3.14), (3.16), and (3.17) into Equation (3.6). This yields an expression for ϕ. We are interested in the vertical component of the velocity field at the reservoir wall, i.e. $V_y|_{x=z=0}$. Thus,

using Equation (3.4), the value of V_y is given by

$$
\begin{aligned}
V_y|_{x=z=0} = \int_0^{+\infty}\int_0^{+\infty} \frac{1}{\lambda\pi^2\sqrt{\mu^2+\lambda^2}} \Bigg[& 4v_{d,1}\sin\left(\mu\frac{d}{2}\right)\sin\left(\lambda\frac{d}{2}\right)\sin(\mu y) \\
& + v_{d,2}\sin\left(l\sin\alpha - \frac{d}{2}\mu\right)\sin\left(l\cos\alpha + \frac{1}{2}\lambda\right)\sin(\mu y) \\
& - v_{d,2}\sin\left(l\sin\alpha + \frac{d}{2}\mu\right)\sin\left(l\cos\alpha + \frac{1}{2}\lambda\right)\sin(\mu y) \\
& + v_{d,2}\sin\left(l\sin\alpha + \frac{d}{2}\mu\right)\sin\left(l\cos\alpha - \frac{d}{2}\lambda\right)\sin(\mu y) \\
& - v_{d,2}\sin\left(l\sin\alpha - \frac{d}{2}\mu\right)\sin\left(l\cos\alpha - \frac{d}{2}\lambda\right)\sin(\mu y) \\
& + v_{d,2}\cos\left(l\sin\alpha - \frac{d}{2}\mu\right)\sin\left(l\cos\alpha + \frac{1}{2}\lambda\right)\cos(\mu y) \\
& - v_{d,2}\cos\left(l\sin\alpha + \frac{d}{2}\mu\right)\sin\left(l\cos\alpha + \frac{1}{2}\lambda\right)\cos(\mu y) \\
& - v_{d,2}\cos\left(l\sin\alpha - \frac{d}{2}\mu\right)\sin\left(l\cos\alpha - \frac{d}{2}\lambda\right)\cos(\mu y) \\
& + v_{d,2}\cos\left(l\sin\alpha + \frac{d}{2}\mu\right)\sin\left(l\cos\alpha - \frac{d}{2}\lambda\right)\cos(\mu y)\Bigg]\, d\lambda d\mu.
\end{aligned}
\tag{3.18}
$$

Equation (3.18) is solved in closed form using the tables of integral transforms by Bateman (1954). Making the necessary integrations yields

$$
\begin{aligned}
V_y|_{x=z=0} = \frac{v_{d,1}\Gamma^2\left(\frac{1}{2}\right)}{2\pi^2} \Bigg\{ & \frac{1}{\left(\frac{y}{d}+\frac{1}{2}\right)} {}_2F_1\left(\frac{1}{2},\frac{1}{2},\frac{3}{2};\frac{-1}{\left(\frac{2y}{d}+1\right)^2}\right) \\
& - \frac{1}{\left(\frac{y}{d}-\frac{1}{2}\right)} {}_2F_1\left(\frac{1}{2},\frac{1}{2},\frac{3}{2};\frac{-1}{\left(\frac{2y}{d}-1\right)^2}\right)\Bigg\} \\
& + \frac{v_{d,2}\Gamma^2\left(\frac{1}{2}\right)}{2\pi^2} \Bigg\{ \frac{\left(\frac{l}{d}\cos\alpha+\frac{1}{2}\right)}{\left(\frac{y}{d}-\frac{l}{d}\sin\alpha+\frac{1}{2}\right)} \\
& {}_2F_1\left(\frac{1}{2},\frac{1}{2},\frac{3}{2};\frac{-\left(\frac{l}{d}\cos\alpha+\frac{1}{2}\right)^2}{\left(\frac{y}{d}-\frac{l}{d}\sin\alpha+\frac{1}{2}\right)^2}\right) \\
& - \frac{\left(\frac{l}{d}\cos\alpha+\frac{1}{2}\right)}{\left(\frac{y}{d}-\frac{l}{d}\sin\alpha-\frac{1}{2}\right)} {}_2F_1\left(\frac{1}{2},\frac{1}{2},\frac{3}{2};\frac{-\left(\frac{l}{d}\cos\alpha+\frac{1}{2}\right)^2}{\left(\frac{y}{d}-\frac{l}{d}\sin\alpha-\frac{1}{2}\right)^2}\right) \\
& + \frac{\left(\frac{l}{d}\cos\alpha-\frac{1}{2}\right)}{\left(\frac{y}{d}-\frac{l}{d}\sin\alpha-\frac{1}{2}\right)} {}_2F_1\left(\frac{1}{2},\frac{1}{2},\frac{3}{2};\frac{-\left(\frac{l}{d}\cos\alpha-\frac{1}{2}\right)^2}{\left(\frac{y}{d}-\frac{l}{d}\sin\alpha-\frac{1}{2}\right)^2}\right) \\
& - \frac{\left(\frac{l}{d}\cos\alpha-\frac{1}{2}\right)}{\left(\frac{y}{d}-\frac{l}{d}\sin\alpha+\frac{1}{2}\right)} {}_2F_1\left(\frac{1}{2},\frac{1}{2},\frac{3}{2};\frac{-\left(\frac{l}{d}\cos\alpha-\frac{1}{2}\right)^2}{\left(\frac{y}{d}-\frac{l}{d}\sin\alpha+\frac{1}{2}\right)^2}\right)\Bigg\}
\end{aligned}
\tag{3.19}
$$

where Γ is the Gamma function and ${}_2F_1(a,b,c;w)$ is the complex hypergeometric function of variable w with the parameters a, b, and c. This function is the solution of the hypergeometric equation

$$
w(1-w)\frac{\partial^2({}_2F_1)}{\partial w^2} = ab({}_2F_1) - [c-(a+b+1)w]\frac{\partial_2 F_1}{\partial w} \tag{3.20}
$$

Equation (3.20) has three singular points at $w = 0$, 1, and ∞ which correspond to $y = \infty$, imaginary value, and $y = \pm(d/2)$ or $y = -l \pm d/2$, the edges of the two squares, repectively.

Now, the kinetic energy at linking point B, $V_B^2/2$, is determined from Equation (3.19) with $x = z = 0$ and $y = -s_1$ as

$$\begin{aligned}
\frac{V_B^2}{2} = \frac{1}{2}\Bigg[& \frac{v_{d,1}\Gamma^2\left(\frac{1}{2}\right)}{2\pi^2}\Bigg\{\frac{1}{\left(\frac{-s_1}{d}+\frac{1}{2}\right)}\,{}_2F_1\left(\frac{1}{2},\frac{1}{2},\frac{3}{2};\frac{-1}{\left(\frac{-2s_1}{d}+1\right)^2}\right) \\
& -\frac{1}{\left(\frac{-s_1}{d}-\frac{1}{2}\right)}\,{}_2F_1\left(\frac{1}{2},\frac{1}{2},\frac{3}{2};\frac{-1}{\left(\frac{-2s_1}{d}-1\right)^2}\right)\Bigg\} \\
& +\frac{v_{d,2}\Gamma^2\left(\frac{1}{2}\right)}{2\pi^2}\Bigg\{\frac{\left(\frac{l}{d}\cos\alpha+\frac{1}{2}\right)}{\left(\frac{-s_1}{d}-\frac{l}{d}\sin\alpha+\frac{1}{2}\right)} \\
& {}_2F_1\left(\frac{1}{2},\frac{1}{2},\frac{3}{2};\frac{-\left(\frac{l}{d}\cos\alpha+\frac{1}{2}\right)^2}{\left(\frac{-s_1}{d}-\frac{l}{d}\sin\alpha+\frac{1}{2}\right)^2}\right) \\
& -\frac{\left(\frac{l}{d}\cos\alpha+\frac{1}{2}\right)}{\left(\frac{-s_1}{d}-\frac{l}{d}\sin\alpha-\frac{1}{2}\right)}\,{}_2F_1\left(\frac{1}{2},\frac{1}{2},\frac{3}{2};\frac{-\left(\frac{l}{d}\cos\alpha+\frac{1}{2}\right)^2}{\left(\frac{-s_1}{d}-\frac{l}{d}\sin\alpha-\frac{1}{2}\right)^2}\right) \\
& +\frac{\left(\frac{l}{d}\cos\alpha-\frac{1}{2}\right)}{\left(\frac{-s_1}{d}-\frac{l}{d}\sin\alpha-\frac{1}{2}\right)}\,{}_2F_1\left(\frac{1}{2},\frac{1}{2},\frac{3}{2};\frac{-\left(\frac{l}{d}\cos\alpha-\frac{1}{2}\right)^2}{\left(\frac{-s_1}{d}-\frac{l}{d}\sin\alpha-\frac{1}{2}\right)^2}\right) \\
& -\frac{\left(\frac{l}{d}\cos\alpha-\frac{1}{2}\right)}{\left(\frac{-s_1}{d}-\frac{l}{d}\sin\alpha+\frac{1}{2}\right)}\,{}_2F_1\left(\frac{1}{2},\frac{1}{2},\frac{3}{2};\frac{-\left(\frac{l}{d}\cos\alpha-\frac{1}{2}\right)^2}{\left(\frac{-s_1}{d}-\frac{l}{d}\sin\alpha+\frac{1}{2}\right)^2}\right)\Bigg\}\Bigg]^2
\end{aligned} \tag{3.21}$$

3.5 The Critical Height at the Onset of Liquid Entrainment

We now have two equations for the kinetic energy at linking point B, $V_B^2/2$, given by Equations (3.2) and (3.21). A graphical representation of Equations (3.2) and (3.21) is shown in Figure 3.2 for fixed values of V_{d_1}, V_{d_2}, α, l, d, g, ρ, and $\Delta\rho$. Thus, curves were generated in which s_1 and h_1 are the only parameters that vary. Equation (3.21) produces a single relation between $V_B^2/2$ and s_1, while Equation (3.2) produces a series of parallel, straight lines with negative slope.

For large values of h_1, there are two points of intersection. As h_1 decreases, a critical value is reached where the straight line forms a tangent to the curve with one point of intersection. As h_1 decreases further, no points of intersection are possible. The hypothesis in the analysis, first proposed by Craya (1949), is that the value of h_1, corresponding to the critical height for the onset of liquid entrainment at Square 1, is the value at which Equations (3.2) forms a tangent with Equation (3.21). Therefore, by equating the magnitudes of $V_B^2/2$ given by Equations (3.2) and (3.21) and their first derivatives with respect to s_1, the critical height, h_1, that corresponds to the onset of liquid entrainment with respect to Square 1 is obtained. Equating Equations (3.2) and (3.21) yields,

$$\frac{\Delta\rho}{\rho} g \left(\frac{h_1}{d} - \frac{s_1}{d} \right) = \frac{1}{2} \left[\frac{\Gamma^2\left(\frac{1}{2}\right)}{s_1 \pi^2} \left\{ v_{d,1} C_1 + v_{d,2} C_2 \right\} \right]^2 \tag{3.22}$$

and equating first derivatives with respect to s_1 yields,

$$\frac{-\Delta\rho}{\rho} g = \frac{1}{4\pi^2} \left[v_{d,1} C_1 + v_{d,2} C_2 \right] \left[v_{d,1} C_3 + v_{d,2} C_4 \right] \tag{3.23}$$

where

$$C_1 = \frac{1}{\left(\frac{s_1}{d}+\frac{1}{2}\right)}\,{}_2F_1\left(\frac{1}{2},\frac{1}{2},\frac{3}{2};\frac{-1}{\left(\frac{2s_1}{d}+1\right)^2}\right) - \frac{1}{\left(\frac{s_1}{d}-\frac{1}{2}\right)}\,{}_2F_1\left(\frac{1}{2},\frac{1}{2},\frac{3}{2};\frac{-1}{\left(\frac{2s_1}{d}-1\right)^2}\right) \tag{3.24}$$

$$\begin{aligned} C_2 = {} & \frac{\left(\frac{l}{d}\cos\alpha+\frac{1}{2}\right)}{\left(\frac{s_1}{d}+\frac{l}{d}\sin\alpha+\frac{1}{2}\right)}\,{}_2F_1\left(\frac{1}{2},\frac{1}{2},\frac{3}{2};\frac{-\left(\frac{l}{d}\cos\alpha+\frac{1}{2}\right)^2}{\left(\frac{s_1}{d}+\frac{l}{d}\sin\alpha+\frac{1}{2}\right)^2}\right) \\ & - \frac{\left(\frac{l}{d}\cos\alpha+\frac{1}{2}\right)}{\left(\frac{s_1}{d}+\frac{l}{d}\sin\alpha-\frac{1}{2}\right)}\,{}_2F_1\left(\frac{1}{2},\frac{1}{2},\frac{3}{2};\frac{-\left(\frac{l}{d}\cos\alpha+\frac{1}{2}\right)^2}{\left(\frac{s_1}{d}+\frac{l}{d}\sin\alpha-\frac{1}{2}\right)^2}\right) \\ & + \frac{\left(\frac{l}{d}\cos\alpha-\frac{1}{2}\right)}{\left(\frac{s_1}{d}+\frac{l}{d}\sin\alpha-\frac{1}{2}\right)}\,{}_2F_1\left(\frac{1}{2},\frac{1}{2},\frac{3}{2};\frac{-\left(\frac{l}{d}\cos\alpha-\frac{1}{2}\right)^2}{\left(\frac{s_1}{d}+\frac{l}{d}\sin\alpha-\frac{1}{2}\right)^2}\right) \\ & - \frac{\left(\frac{l}{d}\cos\alpha-\frac{1}{2}\right)}{\left(\frac{s_1}{d}+\frac{l}{d}\sin\alpha+\frac{1}{2}\right)}\,{}_2F_1\left(\frac{1}{2},\frac{1}{2},\frac{3}{2};\frac{-\left(\frac{l}{d}\cos\alpha-\frac{1}{2}\right)^2}{\left(\frac{s_1}{d}+\frac{l}{d}\sin\alpha+\frac{1}{2}\right)^2}\right) \end{aligned} \tag{3.25}$$

$$
\begin{aligned}
C_3 = \frac{1}{d}\Bigg[& \frac{4}{\left(\frac{2s_1}{d}+1\right)^2}\left\{\frac{1}{3\left(\frac{2s_1}{d}+1\right)^2}\,{}_2F_1\left(\frac{3}{2},\frac{3}{2},\frac{5}{2};\frac{-1}{\left(\frac{2s_1}{d}+1\right)^2}\right)\right. \\
& \left. - {}_2F_1\left(\frac{1}{2},\frac{1}{2},\frac{3}{2};\frac{-1}{\left(\frac{2s_1}{d}+1\right)^2}\right)\right\} \\
& - \frac{4}{\left(\frac{2s_1}{d}-1\right)^2}\left\{\frac{1}{3\left(\frac{2s_1}{d}-1\right)^2}\,{}_2F_1\left(\frac{3}{2},\frac{3}{2},\frac{5}{2};\frac{-1}{\left(\frac{2s_1}{d}-1\right)^2}\right)\right. \\
& \left. - {}_2F_1\left(\frac{1}{2},\frac{1}{2},\frac{3}{2};\frac{-1}{\left(\frac{2s_1}{d}-1\right)^2}\right)\right\}\Bigg]
\end{aligned}
\tag{3.26}
$$

and

$$
\begin{aligned}
C_4 = \frac{1}{d}\Bigg[& \frac{\left(\frac{l}{d}\cos\alpha+\frac{1}{2}\right)}{\left(\frac{s_1}{d}+\frac{l}{d}\sin\alpha-\frac{1}{2}\right)^2}\left\{\frac{-\left(\frac{l}{d}\cos\alpha+\frac{1}{2}\right)^2}{3\left(\frac{s_1}{d}+\frac{l}{d}\sin\alpha-\frac{1}{2}\right)^2}\,{}_2F_1\left(\frac{3}{2},\frac{3}{2},\frac{5}{2};\frac{-\left(\frac{l}{d}\cos\alpha+\frac{1}{2}\right)^2}{\left(\frac{s_1}{d}+\frac{l}{d}\sin\alpha-\frac{1}{2}\right)^2}\right)\right. \\
& \left. + {}_2F_1\left(\frac{1}{2},\frac{1}{2},\frac{3}{2};\frac{-\left(\frac{l}{d}\cos\alpha+\frac{1}{2}\right)^2}{\left(\frac{s_1}{d}+\frac{l}{d}\sin\alpha-\frac{1}{2}\right)^2}\right)\right\} \\
& + \frac{\left(\frac{l}{d}\cos\alpha+\frac{1}{2}\right)}{\left(\frac{s_1}{d}+\frac{l}{d}\sin\alpha+\frac{1}{2}\right)^2}\left\{\frac{\left(\frac{l}{d}\cos\alpha+\frac{1}{2}\right)^2}{3\left(\frac{s_1}{d}+\frac{l}{d}\sin\alpha+\frac{1}{2}\right)^2}\,{}_2F_1\left(\frac{3}{2},\frac{3}{2},\frac{5}{2};\frac{-\left(\frac{l}{d}\cos\alpha+\frac{1}{2}\right)^2}{\left(\frac{s_1}{d}+\frac{l}{d}\sin\alpha+\frac{1}{2}\right)^2}\right)\right. \\
& \left. - {}_2F_1\left(\frac{1}{2},\frac{1}{2},\frac{3}{2};\frac{-\left(\frac{l}{d}\cos\alpha+\frac{1}{2}\right)^2}{\left(\frac{s_1}{d}+\frac{l}{d}\sin\alpha+\frac{1}{2}\right)^2}\right)\right\} \\
& + \frac{\left(\frac{l}{d}\cos\alpha-\frac{1}{2}\right)}{\left(\frac{s_1}{d}+\frac{l}{d}\sin\alpha-\frac{1}{2}\right)^2}\left\{\frac{\left(\frac{l}{d}\cos\alpha-\frac{1}{2}\right)^2}{3\left(\frac{s_1}{d}+\frac{l}{d}\sin\alpha-\frac{1}{2}\right)^2}\,{}_2F_1\left(\frac{3}{2},\frac{3}{2},\frac{5}{2};\frac{-\left(\frac{l}{d}\cos\alpha-\frac{1}{2}\right)^2}{\left(\frac{s_1}{d}+\frac{l}{d}\sin\alpha-\frac{1}{2}\right)^2}\right)\right. \\
& \left. - {}_2F_1\left(\frac{1}{2},\frac{1}{2},\frac{3}{2};\frac{-\left(\frac{l}{d}\cos\alpha-\frac{1}{2}\right)^2}{\left(\frac{s_1}{d}+\frac{l}{d}\sin\alpha-\frac{1}{2}\right)^2}\right)\right\} \\
& + \frac{\left(\frac{l}{d}\cos\alpha-\frac{1}{2}\right)}{\left(\frac{s_1}{d}+\frac{l}{d}\sin\alpha+\frac{1}{2}\right)^2}\left\{\frac{-\left(\frac{l}{d}\cos\alpha-\frac{1}{2}\right)^2}{3\left(\frac{s_1}{d}+\frac{l}{d}\sin\alpha+\frac{1}{2}\right)^2}\,{}_2F_1\left(\frac{3}{2},\frac{3}{2},\frac{5}{2};\frac{-\left(\frac{l}{d}\cos\alpha-\frac{1}{2}\right)^2}{\left(\frac{s_1}{d}+\frac{l}{d}\sin\alpha+\frac{1}{2}\right)^2}\right)\right. \\
& \left. + {}_2F_1\left(\frac{1}{2},\frac{1}{2},\frac{3}{2};\frac{-\left(\frac{l}{d}\cos\alpha-\frac{1}{2}\right)^2}{\left(\frac{s_1}{d}+\frac{l}{d}\sin\alpha+\frac{1}{2}\right)^2}\right)\right\}\Bigg]
\end{aligned}
\tag{3.27}
$$

Now, with the mass flow rate for a square given by $\rho d^2 V_d$, the Froude number becomes

$$Fr = \frac{4V_d}{\pi\sqrt{gd\frac{\Delta\rho}{\rho}}} \tag{3.28}$$

Therefore, Equations (3.22) and (3.23) can be nondimensionalized by introducing the Froude number. Performing the appropriate algebra, we get

$$\frac{h_1}{d} = \frac{s_1}{d} + \frac{1}{128}\left\{Fr_1^2 C_1^2 + 2Fr_1 Fr_2 C_1 C_2 + Fr_2^2\right\} \tag{3.29}$$

and

$$-64 = Fr_1^2 C_1 C_3^* + Fr_1 Fr_2 [C_1 C_4^* + C_2 C_3^*] + Fr_2^2 C_2 C_4^* \tag{3.30}$$

where constants C_1 and C_2 are given by Equations (3.24) and (3.25), respectively, and C_3^* and C_4^* are given by

$$C_3^* = d \times C_3 \quad \textit{and} \quad C_4^* = d \times C_4. \tag{3.31}$$

Constants C_3 and C_4 in Equation (3.31) are given by Equations (3.26) and (3.27), respectively.

Equations (3.29) and (3.30) can be used to determine the critical height with respect to Square 1, h_1/d. Equation (3.30) is solved iteratively for s_1/d, then substituted into Equation (3.29) to find h_1/d.

The critical height for the onset with respect to Square 2, h_2/d, must now be determined. This could be accomplished using the same technique as for Square 1 following the situation described in Figure 3.3. However, an easier and much quicker solution can be found by transposing the appropriate parameters of Equations (3.29) and (3.30), as well as the appropriate constants, so that they are consistent with Figure 3.3. The resulting expressions are:

$$\frac{h_2}{d} = \frac{s_2}{d} - \frac{l}{d}\sin\alpha + \frac{1}{128}\left\{Fr_2^2 C_5^2 + 2Fr_1 Fr_2 C_5 C_6 + Fr_1^2\right\} \tag{3.32}$$

and

$$-64 = Fr_2^2 C_5 C_7^{\blacksquare} + Fr_1 Fr_2 [C_5 C_8^{\blacksquare} + C_6 C_7^{\blacksquare}] + Fr_1^2 C_6 C_8^{\blacksquare} \tag{3.33}$$

where constants C_5 and C_6 are given by Equations (3.35) and (3.36), respectively, and $C_7^{\blacksquare}$ and $C_8^{\blacksquare}$ are given by

$$C_7^{\blacksquare} = d \times C_7 \quad \textit{and} \quad C_8^{\blacksquare} = d \times C_8. \tag{3.34}$$

Constants C_7 and C_8 in Equation (3.34) are given by Equations (3.37) and (3.38), respectively. The equations for C_5, C_6, C_7, and C_8 are as follows.

$$\begin{aligned} C_5 = & \frac{1}{\left(\frac{s_2}{d} + \frac{1}{2}\right)} {}_2F_1\left(\frac{1}{2}, \frac{1}{2}, \frac{3}{2}; \frac{-1}{\left(\frac{2s_2}{d} + 1\right)^2}\right) \\ & - \frac{1}{\left(\frac{s_2}{d} - \frac{1}{2}\right)} {}_2F_1\left(\frac{1}{2}, \frac{1}{2}, \frac{3}{2}; \frac{-1}{\left(\frac{2s_2}{d} - 1\right)^2}\right) \end{aligned} \tag{3.35}$$

$$\begin{aligned} C_6 = & \frac{\left(-\frac{l}{d}\cos\alpha + \frac{1}{2}\right)}{\left(\frac{s_2}{d} - \frac{l}{d}\sin\alpha + \frac{1}{2}\right)} {}_2F_1\left(\frac{1}{2}, \frac{1}{2}, \frac{3}{2}; \frac{-\left(-\frac{l}{d}\cos\alpha + \frac{1}{2}\right)^2}{\left(\frac{s_2}{d} - \frac{l}{d}\sin\alpha + \frac{1}{2}\right)^2}\right) \\ & - \frac{\left(-\frac{l}{d}\cos\alpha + \frac{1}{2}\right)}{\left(\frac{s_2}{d} - \frac{l}{d}\sin\alpha - \frac{1}{2}\right)} {}_2F_1\left(\frac{1}{2}, \frac{1}{2}, \frac{3}{2}; \frac{-\left(-\frac{l}{d}\cos\alpha + \frac{1}{2}\right)^2}{\left(\frac{s_2}{d} - \frac{l}{d}\sin\alpha - \frac{1}{2}\right)^2}\right) \\ & + \frac{\left(-\frac{l}{d}\cos\alpha - \frac{1}{2}\right)}{\left(\frac{s_2}{d} - \frac{l}{d}\sin\alpha - \frac{1}{2}\right)} {}_2F_1\left(\frac{1}{2}, \frac{1}{2}, \frac{3}{2}; \frac{-\left(-\frac{l}{d}\cos\alpha - \frac{1}{2}\right)^2}{\left(\frac{s_2}{d} - \frac{l}{d}\sin\alpha - \frac{1}{2}\right)^2}\right) \\ & - \frac{\left(-\frac{l}{d}\cos\alpha - \frac{1}{2}\right)}{\left(\frac{s_2}{d} - \frac{l}{d}\sin\alpha + \frac{1}{2}\right)} {}_2F_1\left(\frac{1}{2}, \frac{1}{2}, \frac{3}{2}; \frac{-\left(-\frac{l}{d}\cos\alpha - \frac{1}{2}\right)^2}{\left(\frac{s_2}{d} - \frac{l}{d}\sin\alpha + \frac{1}{2}\right)^2}\right) \end{aligned} \tag{3.36}$$

$$
\begin{aligned}
C_7 = \frac{1}{d}\Bigg[& \frac{4}{\left(\frac{2s_2}{d}+1\right)^2}\left\{\frac{1}{3\left(\frac{2s_2}{d}+1\right)^2}\,{}_2F_1\left(\frac{3}{2},\frac{3}{2},\frac{5}{2};\frac{-1}{\left(\frac{2s_2}{d}+1\right)^2}\right)\right. \\
& \left. - {}_2F_1\left(\frac{1}{2},\frac{1}{2},\frac{3}{2};\frac{-1}{\left(\frac{2s_2}{d}+1\right)^2}\right)\right\} \\
& - \frac{4}{\left(\frac{2s_2}{d}-1\right)^2}\left\{\frac{1}{3\left(\frac{2s_2}{d}-1\right)^2}\,{}_2F_1\left(\frac{3}{2},\frac{3}{2},\frac{5}{2};\frac{-1}{\left(\frac{2s_2}{d}-1\right)^2}\right)\right. \\
& \left. - {}_2F_1\left(\frac{1}{2},\frac{1}{2},\frac{3}{2};\frac{-1}{\left(\frac{2s_2}{d}-1\right)^2}\right)\right\}\Bigg]
\end{aligned}
\tag{3.37}
$$

and

$$C_8 = \frac{1}{d}\left[\frac{\left(-\frac{l}{d}\cos\alpha+\frac{1}{2}\right)}{\left(\frac{s_2}{d}-\frac{l}{d}\sin\alpha-\frac{1}{2}\right)^2}\left\{\frac{-\left(-\frac{l}{d}\cos\alpha+\frac{1}{2}\right)^2}{3\left(\frac{s_2}{d}-\frac{l}{d}\sin\alpha-\frac{1}{2}\right)^2}\,{}_2F_1\left(\frac{3}{2},\frac{3}{2},\frac{5}{2};\frac{-\left(-\frac{l}{d}\cos\alpha+\frac{1}{2}\right)^2}{\left(\frac{s_2}{d}-\frac{l}{d}\sin\alpha-\frac{1}{2}\right)^2}\right)\right.$$
$$\left.+\,{}_2F_1\left(\frac{1}{2},\frac{1}{2},\frac{3}{2};\frac{-\left(-\frac{l}{d}\cos\alpha+\frac{1}{2}\right)^2}{\left(\frac{s_2}{d}-\frac{l}{d}\sin\alpha-\frac{1}{2}\right)^2}\right)\right\}$$
$$+\frac{\left(-\frac{l}{d}\cos\alpha+\frac{1}{2}\right)}{\left(\frac{s_2}{d}-\frac{l}{d}\sin\alpha+\frac{1}{2}\right)^2}\left\{\frac{\left(-\frac{l}{d}\cos\alpha+\frac{1}{2}\right)^2}{3\left(\frac{s_2}{d}-\frac{l}{d}\sin\alpha+\frac{1}{2}\right)^2}\,{}_2F_1\left(\frac{3}{2},\frac{3}{2},\frac{5}{2};\frac{-\left(-\frac{l}{d}\cos\alpha+\frac{1}{2}\right)^2}{\left(\frac{s_2}{d}-\frac{l}{d}\sin\alpha+\frac{1}{2}\right)^2}\right)\right.$$
$$\left.-\,{}_2F_1\left(\frac{1}{2},\frac{1}{2},\frac{3}{2};\frac{-\left(-\frac{l}{d}\cos\alpha+\frac{1}{2}\right)^2}{\left(\frac{s_2}{d}-\frac{l}{d}\sin\alpha+\frac{1}{2}\right)^2}\right)\right\}$$
$$+\frac{\left(-\frac{l}{d}\cos\alpha-\frac{1}{2}\right)}{\left(\frac{s_2}{d}-\frac{l}{d}\sin\alpha-\frac{1}{2}\right)^2}\left\{\frac{\left(-\frac{l}{d}\cos\alpha-\frac{1}{2}\right)^2}{3\left(\frac{s_2}{d}-\frac{l}{d}\sin\alpha-\frac{1}{2}\right)^2}\,{}_2F_1\left(\frac{3}{2},\frac{3}{2},\frac{5}{2};\frac{-\left(-\frac{l}{d}\cos\alpha-\frac{1}{2}\right)^2}{\left(\frac{s_2}{d}-\frac{l}{d}\sin\alpha-\frac{1}{2}\right)^2}\right)\right. \quad (3.38)$$
$$\left.-\,{}_2F_1\left(\frac{1}{2},\frac{1}{2},\frac{3}{2};\frac{-\left(-\frac{l}{d}\cos\alpha-\frac{1}{2}\right)^2}{\left(\frac{s_2}{d}-\frac{l}{d}\sin\alpha-\frac{1}{2}\right)^2}\right)\right\}$$
$$+\frac{\left(-\frac{l}{d}\cos\alpha-\frac{1}{2}\right)}{\left(\frac{s_2}{d}-\frac{l}{d}\sin\alpha+\frac{1}{2}\right)^2}\left\{\frac{-\left(-\frac{l}{d}\cos\alpha-\frac{1}{2}\right)^2}{3\left(\frac{s_2}{d}-\frac{l}{d}\sin\alpha+\frac{1}{2}\right)^2}\,{}_2F_1\left(\frac{3}{2},\frac{3}{2},\frac{5}{2};\frac{-\left(-\frac{l}{d}\cos\alpha-\frac{1}{2}\right)^2}{\left(\frac{s_2}{d}-\frac{l}{d}\sin\alpha+\frac{1}{2}\right)^2}\right)\right.$$
$$\left.\left.+\,{}_2F_1\left(\frac{1}{2},\frac{1}{2},\frac{3}{2};\frac{-\left(-\frac{l}{d}\cos\alpha-\frac{1}{2}\right)^2}{\left(\frac{s_2}{d}-\frac{l}{d}\sin\alpha+\frac{1}{2}\right)^2}\right)\right\}\right]$$

Equations (3.32) and (3.33) can be solved in the same iterative manner as Equa-

tions (3.29) and (3.30). Equations (3.29) and (3.30) together with Equations (3.32) and (3.33) determine the system critical height or the onset of liquid entrainment for the system.

3.6 Theoretical Results and Discussion

Equations (3.29) and (3.30) can predict the onset of liquid entrainment for a single square if we set $Fr_2 = 0$, $l/d = 0$, and $\alpha = 0$. The results generated are shown in Figure 3.4. As well, shown on Figure 3.4 are the solutions for the onset of liquid entrainment given by Soliman and Sims (1992) for a single circular branch of finite diameter and by Craya (1949) for a single point sink. As can be seen, the solution by Craya (1949) approaches $h/d = 0$ as Fr goes to zero. In contrast, the solution given in the present analysis is nearly identical to that given by Soliman and Sims (1992) asymptoting to the physical limit of $h/d = 0.5$ as Fr goes to zero. Further, the model from the present analysis collapses with the others for Fr greater than 10. Two important conclusions can be drawn from the above. One, the model developed in the present analysis asymptotes to the correct physical limits and two, the geometrical shape of the branch (square versus circle) has little effect on the prediction of the critical height. The use of the square shape simplified the present analysis and made possible the generation of a closed-form solution.

Figure 3.5 compares the models given by Armstrong (1991) and the present analysis. The figure shows the relationship between Fr_1 and the system critical height, h_s/d, at which the onset of liquid entrainment is predicted to occur. The discharge at branch 2, Fr_2, varies while l/d and α are fixed. As can be seen in Figure 3.5, the agreement between the models at low Fr_1 becomes better as Fr_2 increases until at $Fr_2 = 45$ the solutions are nearly identical. As well, as Fr_1 increases for any Fr_2 both models converge to nearly the same values. In addition, as Fr_2 decreases at low

Fr_1, the present analysis approaches the system critical height, h_s/d=0.5, while the Armstrong solution approaches h_s/d=0. Finally, for $\alpha = 90°$, the onset always occurs at branch 1, thus, $h_s = h_1$ for $\alpha = 90°$. The above observations from Figure 3.5 strengthens the main conclusion drawn from Figure 3.4.

By examining Figures 3.5 to 3.7, we see that the curves shift toward the single-discharge curve as α increases. For the range of Fr_1 shown, an increase in α from 30° to 60° reveals that for $Fr_2 = 15$, all entrainment occurs at branch 1. Further, the influence of branch 2 on the onset critical height is significant since the curves for all Fr_2 are not coincident with the single-discharge curve.

Figures 3.8 and 3.9 show the effect of α for $Fr_2 = 30$ and $l/d = 2$ and $l/d = 4$, respectively. As can be seen, in each figure as α increases, the theoretical curves shift toward the single-discharge curve. In Figure 3.9, an interesting trend predicted by the theory is revealed. As α increases, we see that, generally, the onset height decreases. However, when α increases from 40° to 90° degrees, the onset height increases (i.e., the trend reverses). This results is surprising; however, the analysis presented does not restrict the trend in the onset height for any of the independent parameters. Further discussion on the trend reversal is given below.

Figures 3.10 and 3.11 show the effect of l/d for $Fr_2 = 30$ and $\alpha = 30°$ and $\alpha = 60°$, respectively. In Figure 3.10, as the separation distance increases, the influence of the secondary branch diminishes. This can be seen by observing that the curves shift toward the single-discharge curve as l/d increases. At $l/d = 4$ the secondary branch has little effect on the onset height. At $l/d = 8$ the curve is nearly coincident with the single discharge curve indicating that the secondary branch is so far removed from the interface that it is unable to influence the onset height. In Figure 3.11, the curves, again, shift toward the single discharge curve as l/d increases. At $l/d = 4$, there is still an effect of the secondary branch on the onset height. But, at $l/d = 8$ the curve

is nearly coincident with the single discharge curve. Again, this illustrates that the secondary branch is so far removed from the interface to influence the onset height. Finally, the curves in Figure 3.11 approach lower onset heights at low Fr_1 than the same curves in Figure 3.10.

Figure 3.12 shows the effect of Fr_1 on h_s/d for $Fr_2 = 30$ and $l/d = 2$ with α on the x-axis. All predictions to the right of and to the left of the predicted simultaneous points are entrainment at branch 1 and branch 2, respectively. By examining the curves of constant Froude number from high values of Fr_1 to low values of Fr_1, a reversal in trend is found. First, examine $Fr_1 = 30$ from low values of α to high values of α. As can be seen, the curve shows a continuous drop in the onset height. For the Froude numbers presented, the above result holds for all $Fr_1 \geq 5.0$. Now, examine the curve for $Fr_1 = 1.0$ as α increases. To the right of the predicted simultaneous point, the theory predicts slightly larger values of the onset height as α continues to increase. Further, just to the left of the simultaneous point, the $Fr_1 = 0.1$ curve actually crosses the $Fr_1 = 0.0$ curve. This indicates a reversal in the onset height not only as α increases but as Fr_1 decreases for certain combinations of Fr_1 and α (i.e. low Fr_1 and mid to high α). In performing the theoretical analysis, at no point were any restrictions placed that specified the trend in onset height for values of Fr_1, Fr_2, l/d, and α except the physical boundary of $h/d = 0.5$ when $Fr_1 = Fr_2 = 0$. Therefore, the results presented in Figure 3.12 are valid.

Figure 3.13 is identical to Figure 3.12 except that the results obtained from the Armstrong (1991) model are shown for comparison. As can be seen, the Armstrong model also exhibits a reversal in the onset height for $Fr_1 = 1.0$ and $Fr_1 = 0.1$. In general, the two models are in very good agreement and it is primarily at low Fr_1 values when entrainment is occurring at branch 1 that the present analysis differs from Armstrong (1991).

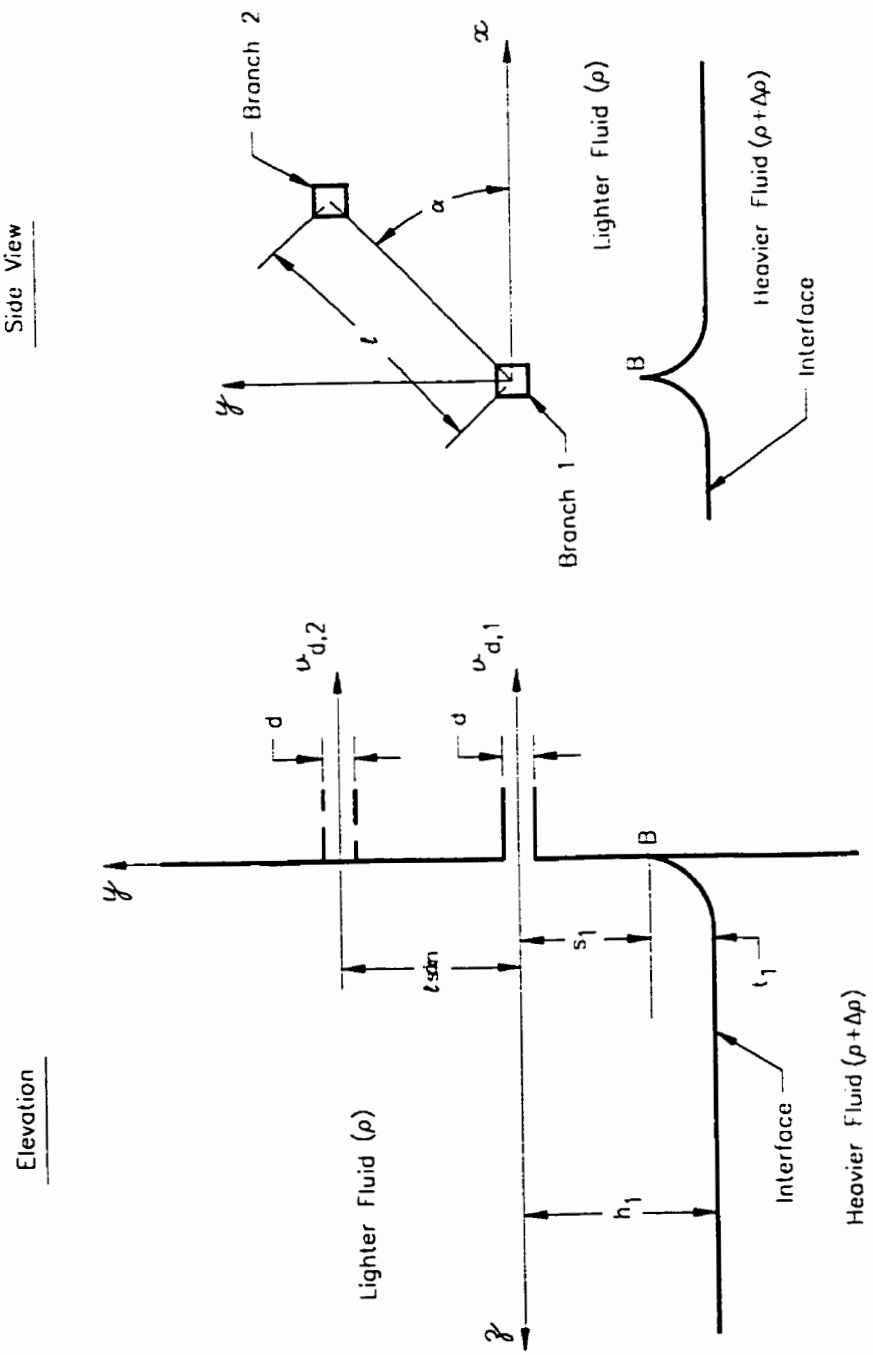

Figure 3.1: Coordinate system with relevant parameters and dimensions

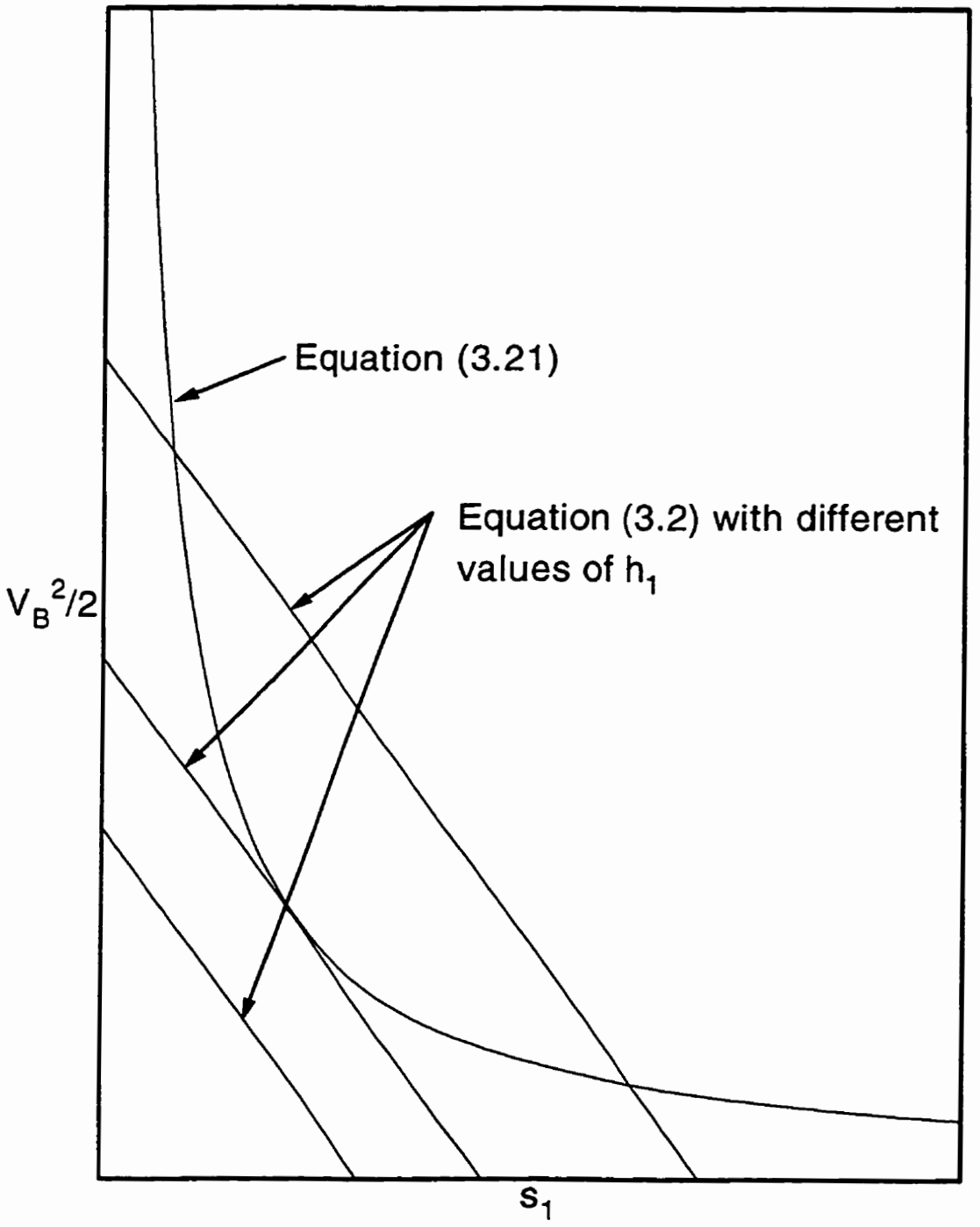

Figure 3.2: Relationship between $V_B^2/2$ and s_1

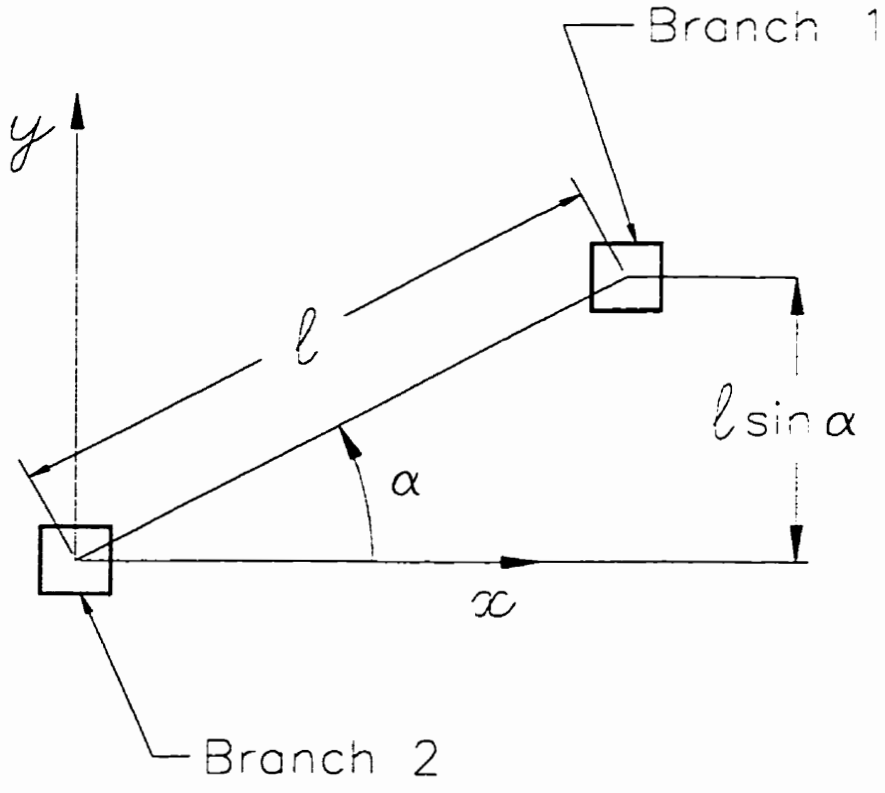

Figure 3.3: Coordinate system for analytical derivation with respect to branch 2

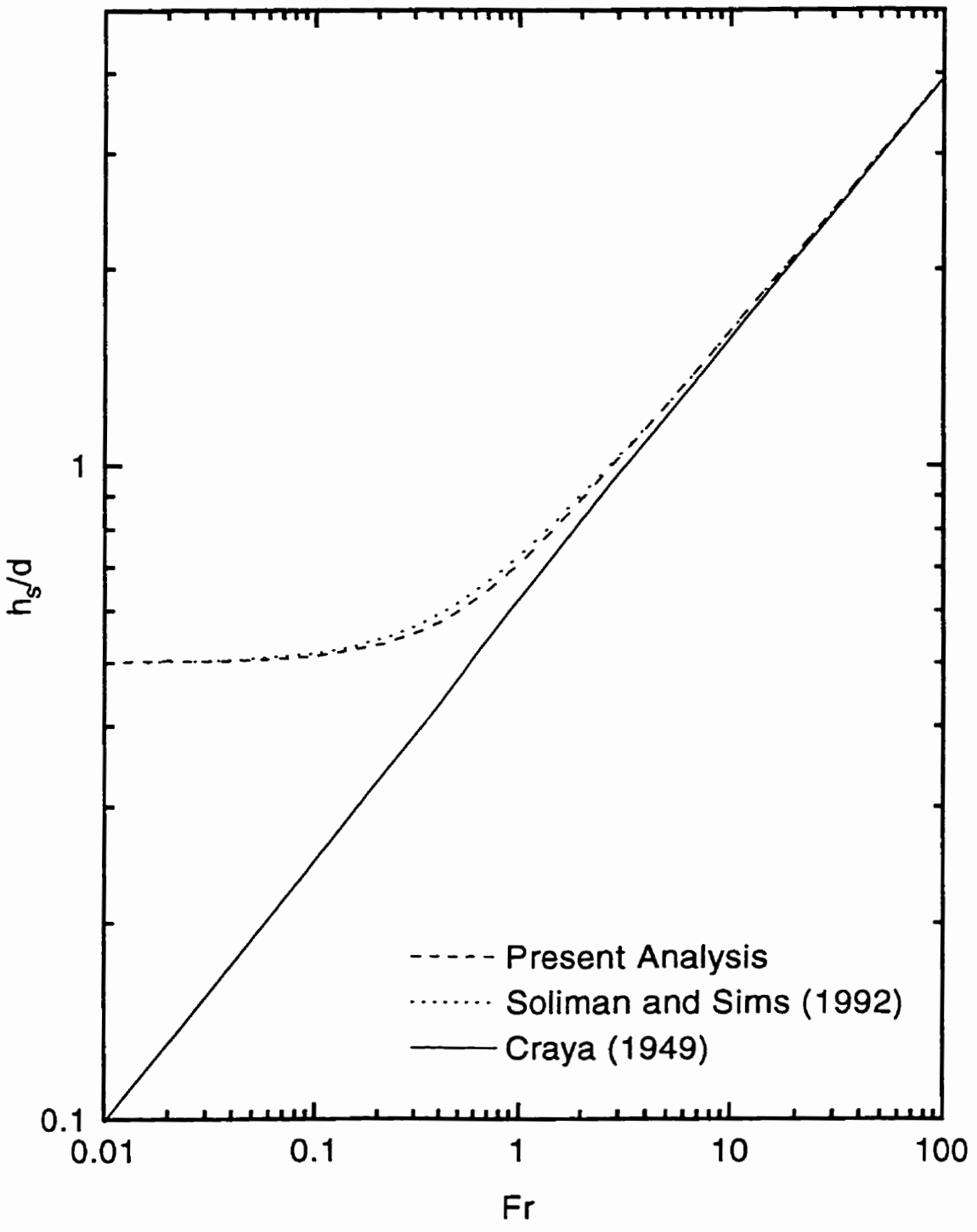

Figure 3.4: Theoretical prediction of the onset of liquid entrainment for single discharge

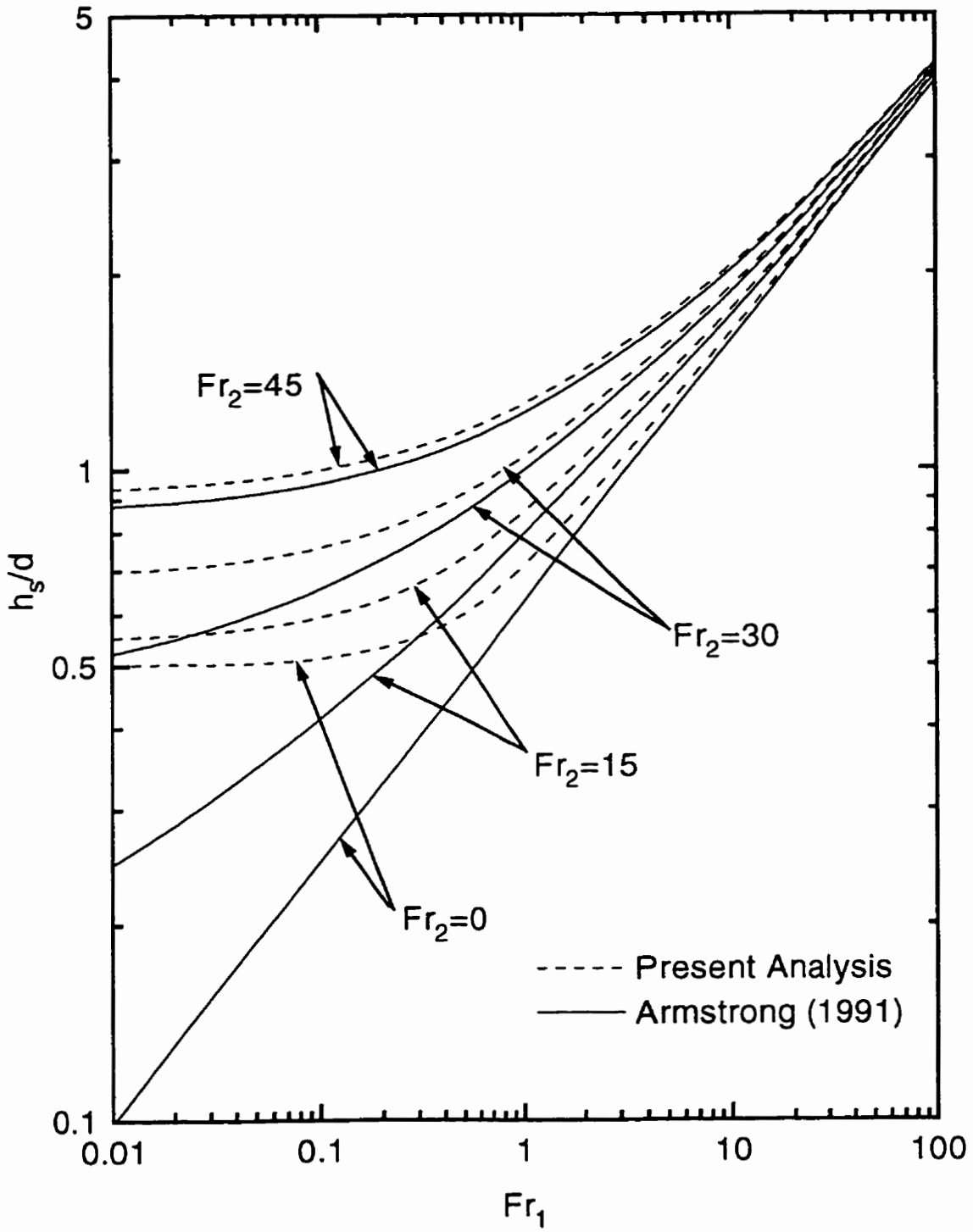

Figure 3.5: Influence of Fr_2 on h_s/d for $\alpha = 90°$ and $l/d = 2$

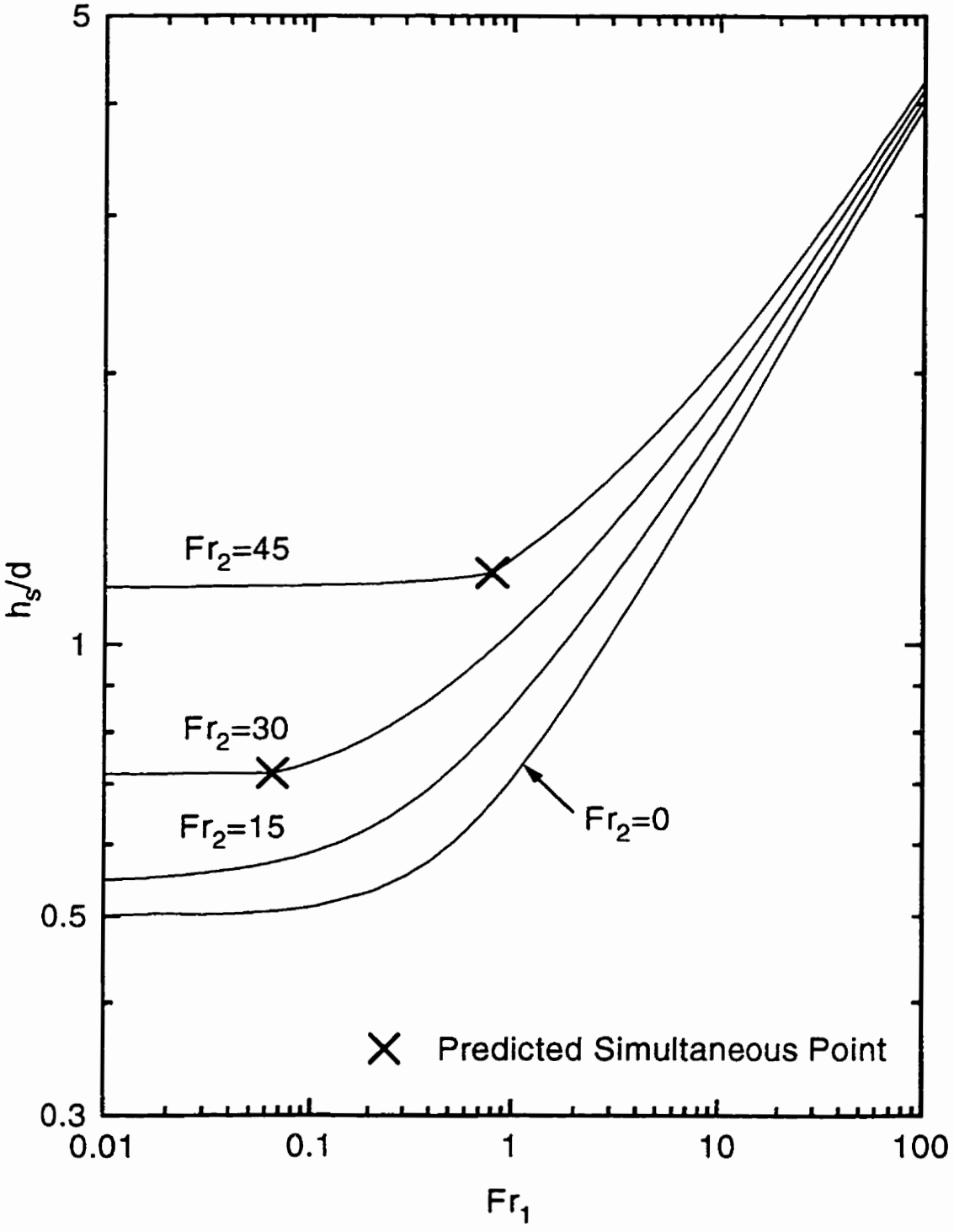

Figure 3.6: Influence of Fr_2 on h_s/d for $\alpha = 60°$ and $l/d = 2$

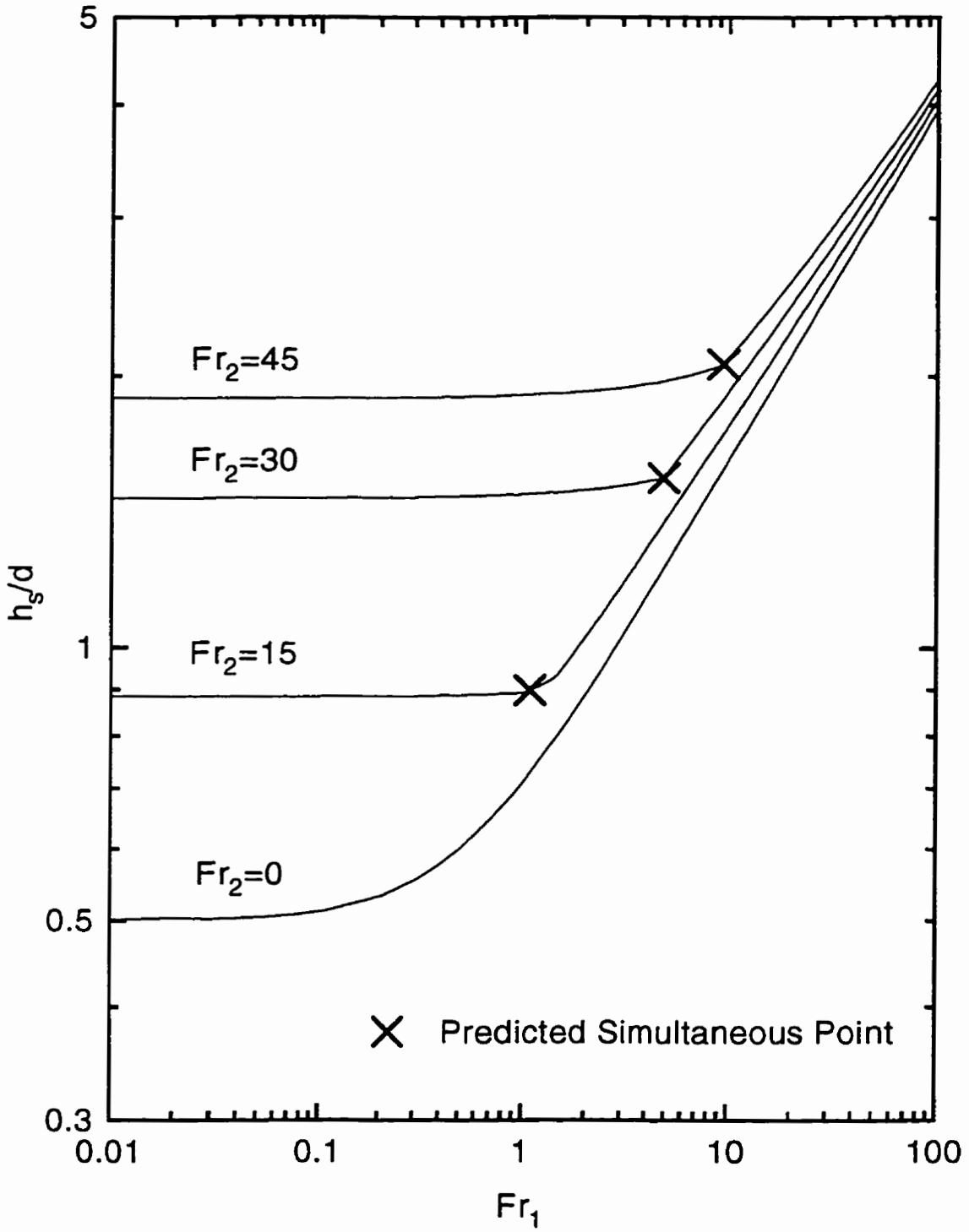

Figure 3.7: Influence of Fr_2 on h_s/d for $\alpha = 30°$ and $l/d = 2$

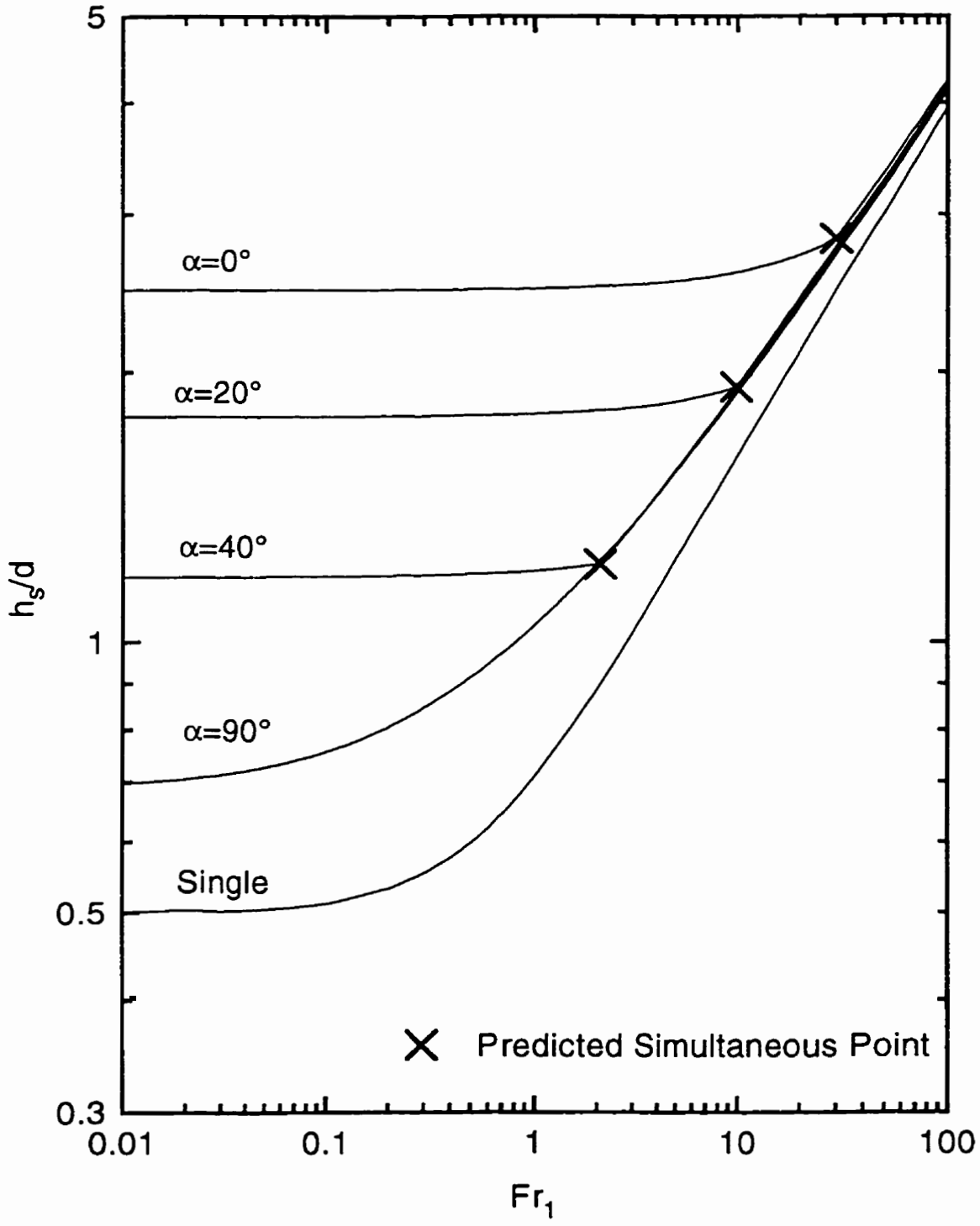

Figure 3.8: Influence of α on h_s/d for $Fr_2 = 30$ and $l/d = 2$

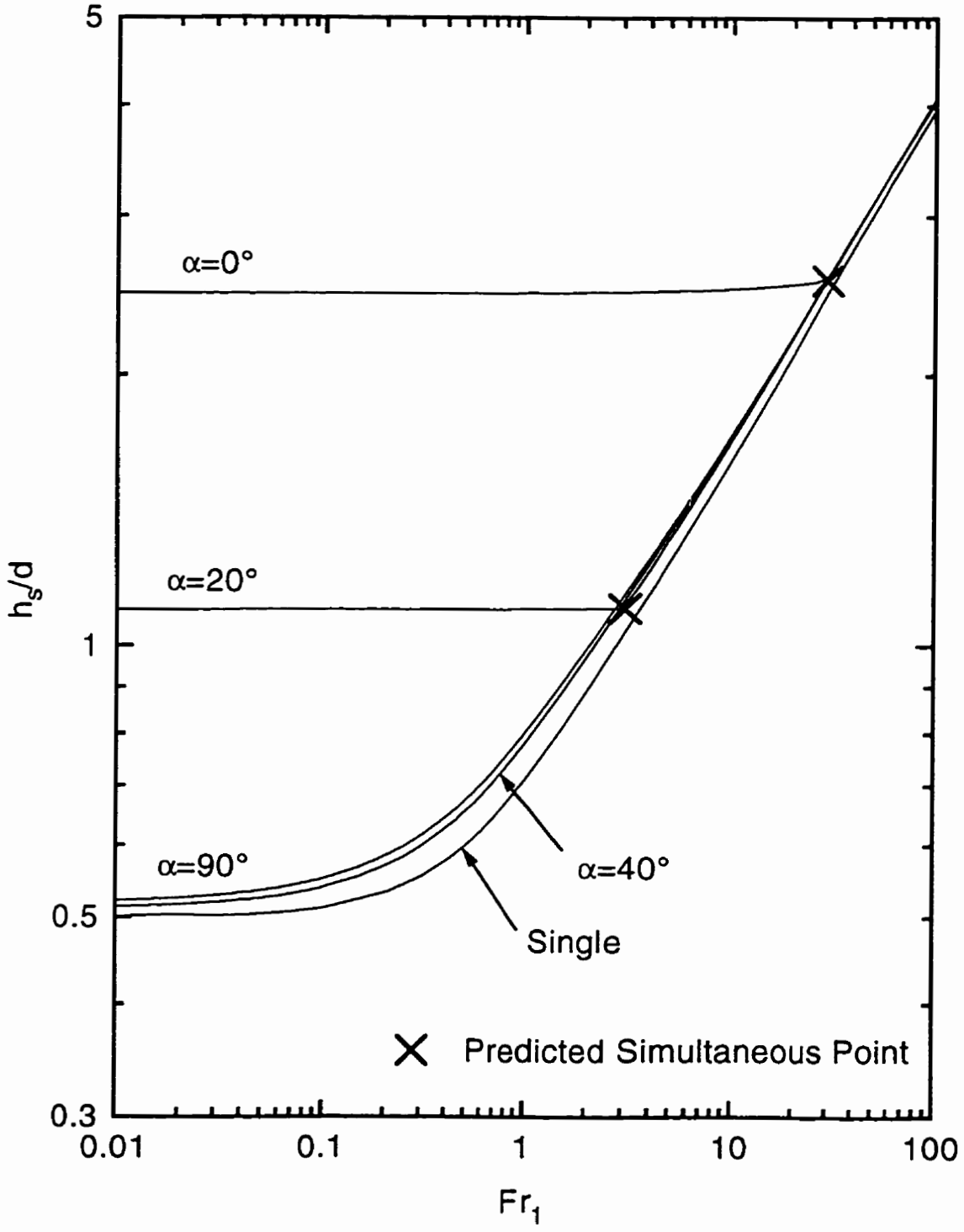

Figure 3.9: Influence of α on h_s/d for $Fr_2 = 30$ and $l/d = 4$

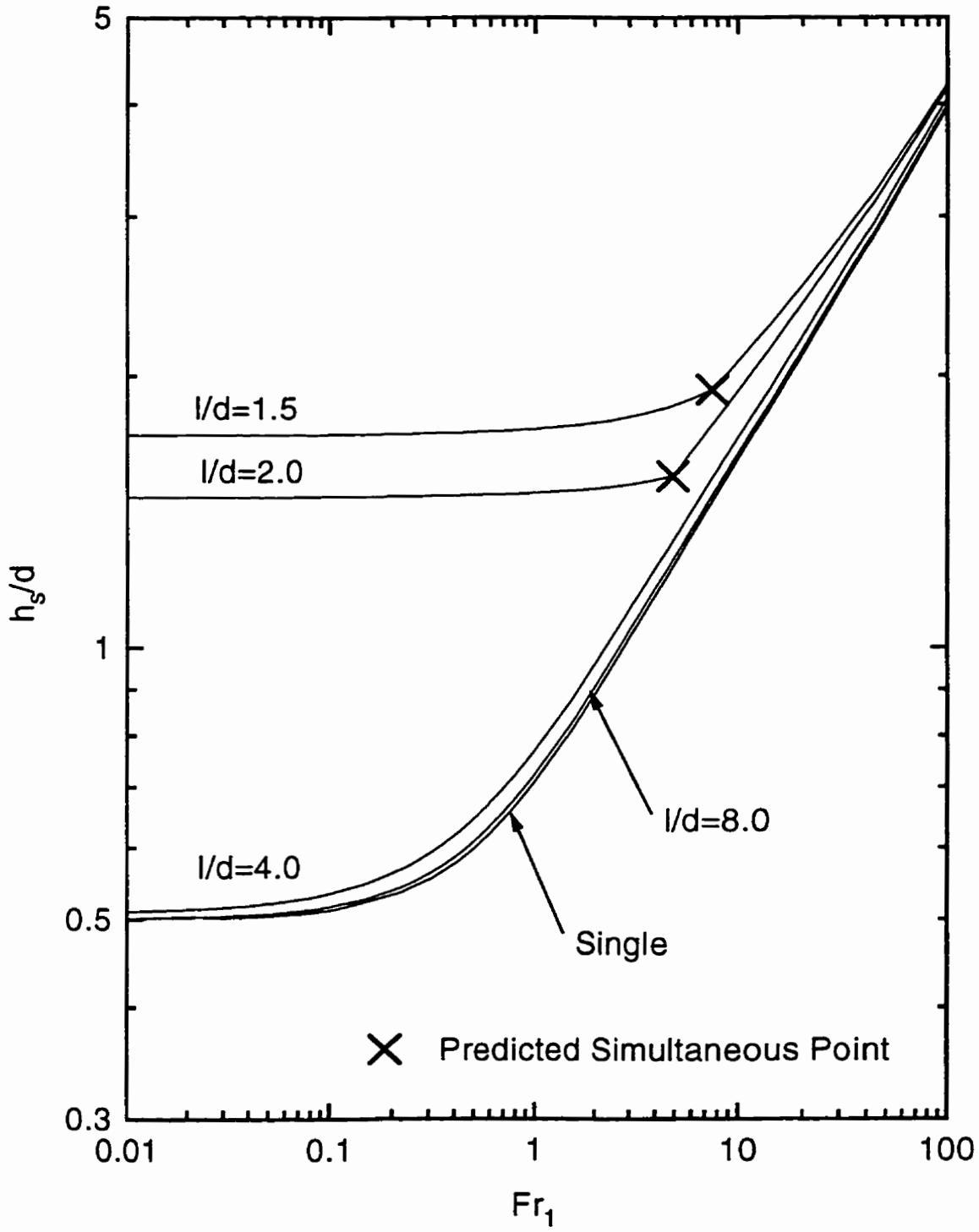

Figure 3.10: Influence of l/d on h_s/d for $Fr_2 = 30$ and $\alpha = 30°$

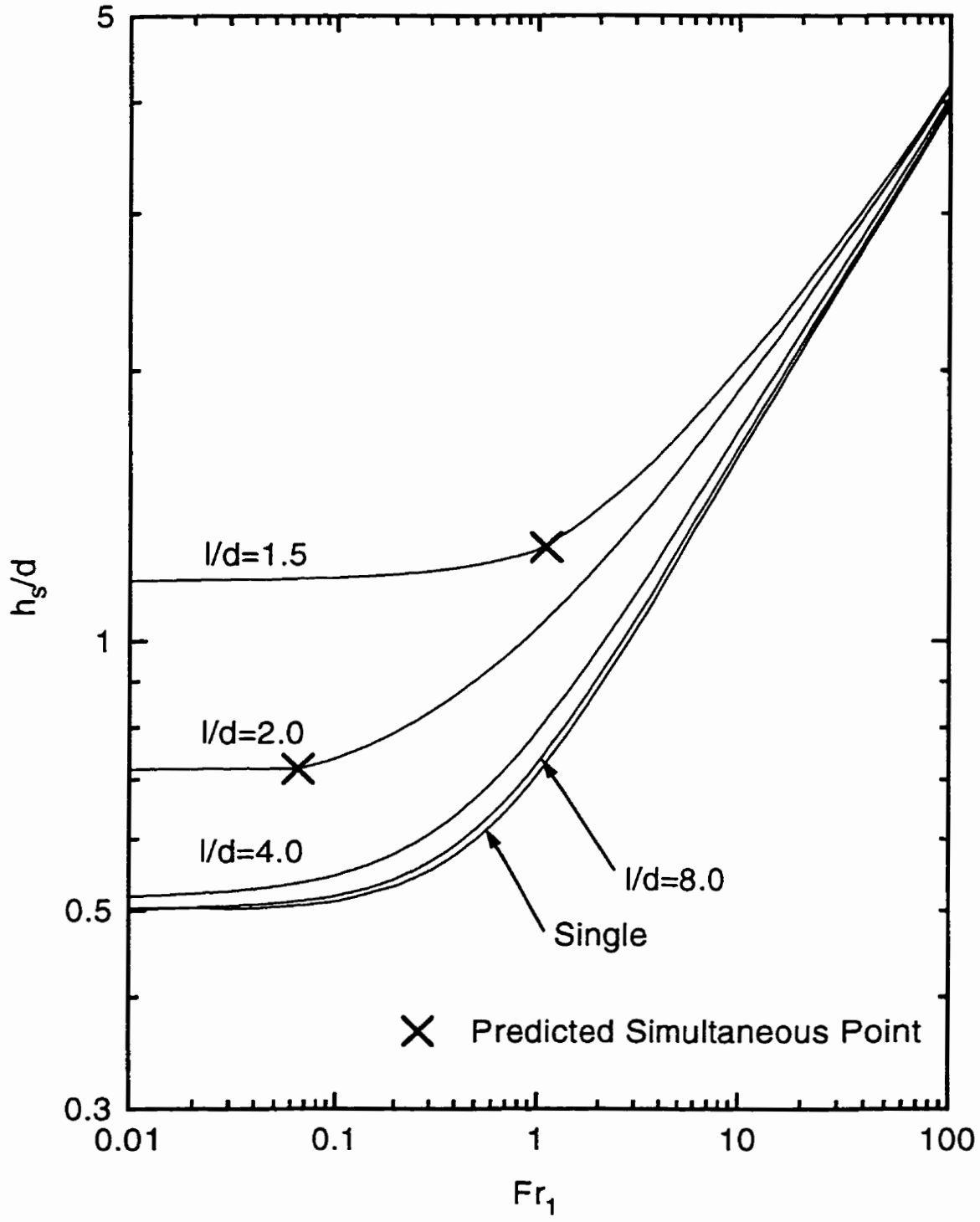

Figure 3.11: Influence of l/d on h_s/d for $Fr_2 = 30$ and $\alpha = 60°$

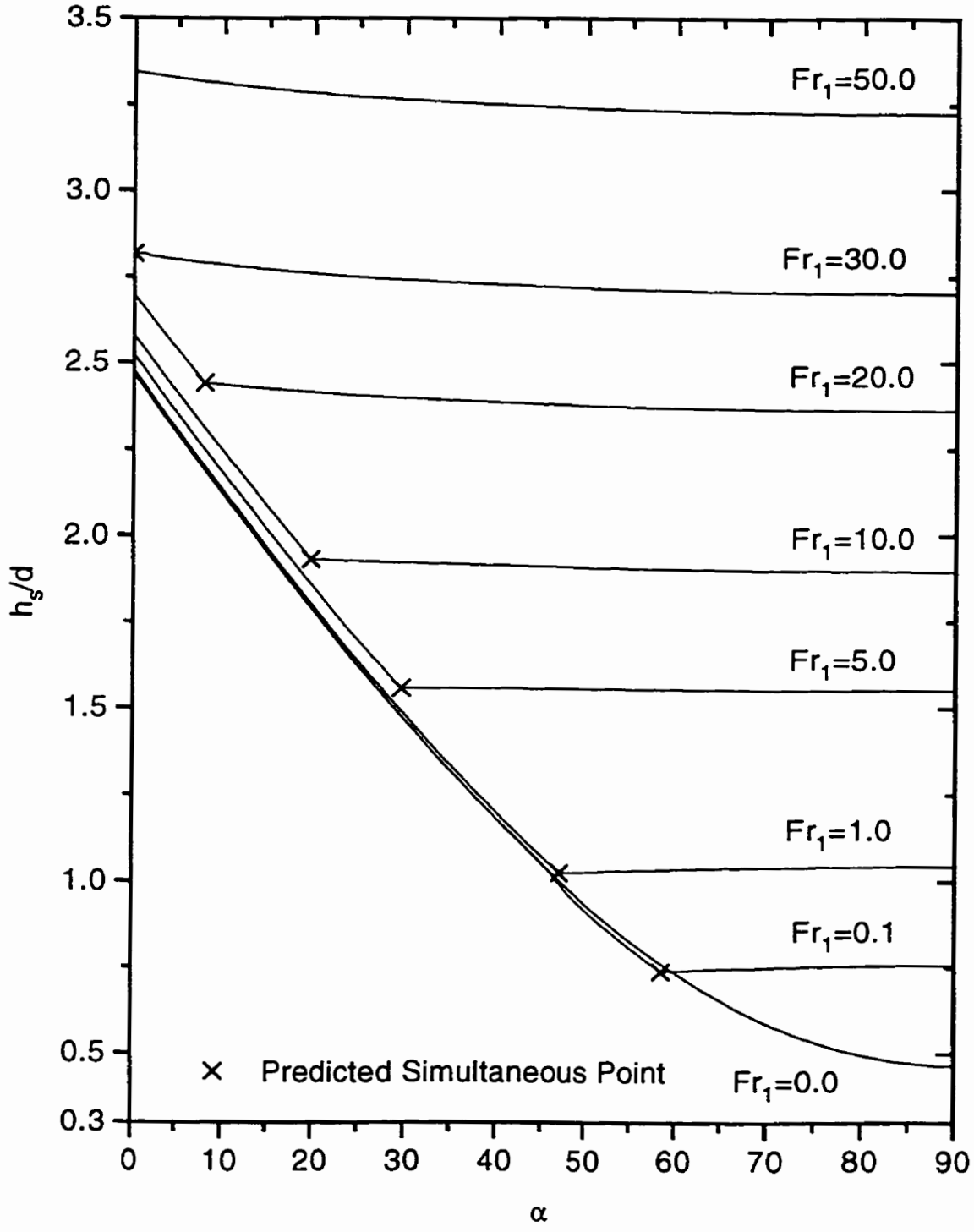

Figure 3.12: Influence of α on h_s/d for $Fr_2 = 30$ and $l/d = 2$

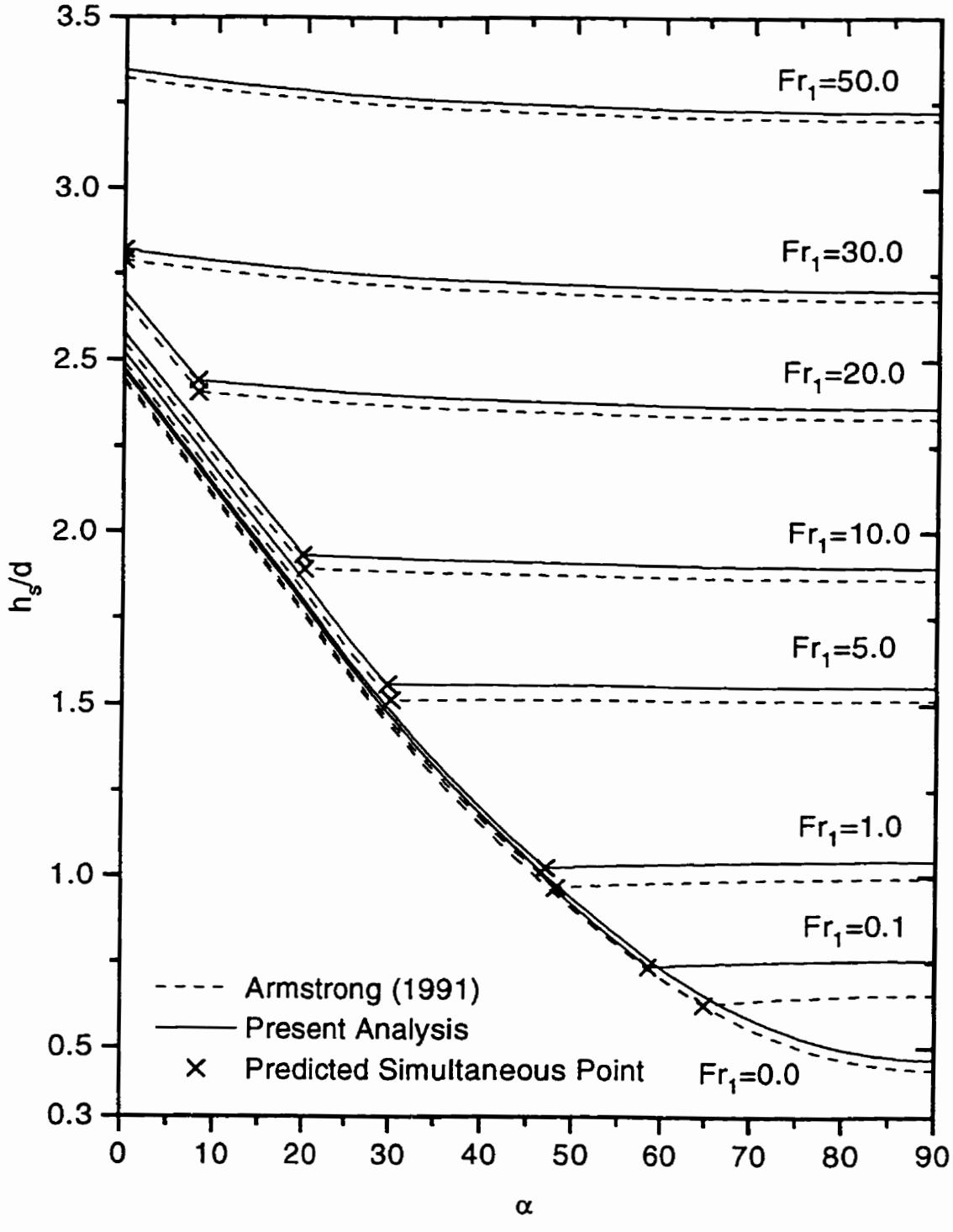

Figure 3.13: Influence of α on h_s/d for $Fr_2 = 30$ and $l/d = 2$

CHAPTER 4

EXPERIMENTAL INVESTIGATION

4.1 Introductory Remarks

As discussed in Chapter 1, the relevant experimental parameters were identified as the mass flow rates out each branch, $\dot{m}_1$ and $\dot{m}_2$, the separation distance between the branches, l, the angle of inclination of the plane containing the centerlines of the branches, α, and the critical height at the onset, h. Nondimensionalizing these parameters by utilizing the branch diameter, d, and neglecting the effects of viscosity and surface tension, the branch flow rates were transformed into corresponding Froude numbers, Fr_1 and Fr_2, the separation distance became l/d, and the critical height at the onset was expressed as h/d. Therefore, the four independent parameters were identified as Fr_1, Fr_2, l/d, and α. Their influences on the dependent parameter, h/d, is the focus of the experimental investigation. It should be noted that the experimental investigation was conducted at room temperature. Depending on the conditions of the day, the temperature of the air and water was maintained at 22 ± 5 $^{\circ}C$.

4.2 Experimental Apparatus

To determine the influence of the independent parameters on the dependent parameter, a test apparatus was constructed that was capable of measuring all parameters. The apparatus was constructed for previous studies, Parrott (1993) and Hassan

(1995). The construction of the test apparatus required a flow loop that provided a continuous, regulated supply of water and air and a means to measure the flow rates out from the branches, the angle of inclination, the separation distance between the branches, and the critical height at onset. The experimental apparatus consisted of a flow loop, a test section, discharge branches, and flow, temperature, and pressure measuring devices

4.2.1 Flow Loop

A schematic of the gas-entrainment flow loop is shown in Figure 4.1. It consists of a stainless steel test section in the shape of a tee. A supply of air was established using a model 4160K Fisher pressure controller. The air enters the test section through the air inlet flange (left side of tee). Distilled water was supplied by a submersible pump and entered the test section through the water inlet flange (bottom of tee). The rate of water supply was controlled by a by-pass line that emptied back to the distilled water tanks. The right flange of the tee was designated the outlet flange. The discharge branches were installed in the outlet flange and a clear acrylic visual section provided a clear view of the experimental flow phenomena. The rate of discharge through each of the branches was measured by variable-area flow meters with overlapping ranges. When performing gas-entrainment studies, the discharge water was returned to the holding tank. The air and water temperatures within the test section and at the flow meters was measured with copper-constantan thermocouples. An Omega (model TRC-III) ice point reference chamber served as the reference junction. The pressure in the test section was measured with a US Gauge bourdon pressure gauge. To remove excess heat generated by the submersible pump, a cooling coil was installed in the distilled water holding tanks in order to maintain the water supply temperature relatively constant. Figure 4.2 illustrates the flow loop for liquid entrainment. It

is essentially the same loop as for gas entrainment. An air-water separator was positioned between the branch discharge lines and the air flow meters to prevent any liquid entrained in the air flow from wetting the air flow meters. This was necessary in order to prevent an inaccurate reading from the flow meters. For liquid-entrainment studies, the discharge air was vented to the atmosphere. Finally, a mercury manometer provided the pressure reading at the air flow meters.

The test section was constructed of schedule 40 stainless steel and in the shape of a large tee section. It had a clear acrylic visual section at the outlet side for the purposes of viewing the experimental flow phenomena. As mentioned above, distilled water entered through the bottom flange or water inlet flange, air entered through the left or air inlet flange, and the discharge fluids exited through the right or outlet flange. The tee measured approximately 1.1 m in length from air inlet flange to discharge flange. The inner diameter was approximately 0.255 m in all sections expect the visual section which measured 0.280 m. The distance from the horizontal centerline of the tee to the water inlet flange was approximately 0.516 m. In order to attain a smooth, ripple-free interface, the water and air inlets had to be dispersed as they entered the test section. Thus, dispersion devices were installed on the two supplies. The dispersion devices forced the supply flows to make several 90° bends before venting into the test section. In this way the fluid velocity was dropped such that there was very little to no effect on the interface. A detailed cross-sectional view of the test section can be found in Hassan (1995).

The discharge branches required for this study were machined from two brass blocks. A sketch of the brass block with branch separation distances, l/d, of 2.0 and 8.0 is shown in Figure 4.3. The brass blocks were mounted in the test section by bolting them to the discharge flange. Each brass block had four branches 6.35 mm in diameter and 127 mm in length. Therefore, each branch had a straight downstream length of 20 diameters before any bends or area changes occurred. In order to accom-

plish measurement of the angle of inclination, a 203.2 *mm* outer diameter circular protractor was modified by machining the inner diameter such that a compression fit was achieved between the protractor and the brass-piece mounting flange. Further, the mounting flange slots were machined such that a rotation of approximately 40° was possible, with consideration given to the brass-block mounting bolts, permitting complete coverage of all angles between 0° and 90°.

4.2.2 Flow Rate Measurement

Gas Entrainment

The water flow rate from each branch was measured by two variable-area flow meters (Brooks model 1110). The flow capacity range of the meters overlapped such that a continuous flow range was achieved. For gas-entrainment experiments, the low-capacity flow meter range was 0.51 *kg/min* to 3.95 *kg/min* and the high-capacity flow meter range was 3.85 *kg/min* to 41.34 *kg/min*. The rate of discharge from each branch was controlled by throttling valves located just downstream of the flow meters. The calibration of the flow meters was verified by recording the elapsed time to collect a specified mass of water at a scale reading. This was done for several scale readings over the range of the flow meter. These points were then compared to the manufacturer's calibration data. The agreement was generally good for all water flow meters. However, calibration curves obtained in-house were available for each flow meter from previous work conducted on the experimental apparatus. Comparison between the flow rates predicted by these curves, at the corresponding scale readings as described above, and the calibration points collected revealed that the flow meter characteristics were unchanged; the maximum deviation was 3%. Therefore, it was decided to use (with confidence) the previously obtained in-house calibration curves. Appendix A, Section A.3.1 provides the complete flow meter calibration data.

Liquid Entrainment

As in the gas entrainment studies, the air flow rate from each branch was measured by two variable area flow meters (Brooks model 1110). The flow capacity range of the meters overlapped such that a continuous flow range was achieved. For liquid entrainment experiments the low-capacity flow meter range was 16.65 $SLPM$ to 166.51 $SLPM$ and the high-capacity flow meter range was 129.88 $SLPM$ to 1299.81 $SLPM$. The rate of discharge from each branch was controlled by throttling valves located just upstream of the flow meters. Calibration of the flow meters was performed in two ways. For low flow rates, up to 250 $SLPM$, the Elster Mainz wet test meters were utilized and for flow rates greater than 250 $SLPM$ venturi meters were required. Using these devices, several calibration points were taken over the range of each flow meter. For the air flow meters, manufacturer's calibration data were unavailable but calibration curves from previous work conducted on the experimental apparatus were available. A comparison between the flow rates predicted by these curves, at the corresponding scale readings of the above points, and the calibration points collected revealed that the flow meter characteristics were unchanged; the maximum deviation was 3%. Therefore, it was decided to use (with confidence) the previously obtained in-house calibration curves. Appendix A, Section A.3.2 provides the complete rotameter calibration data.

4.2.3 Interface Level Measurement

To determine the interface position, two pressure taps were installed on the outlet flange of the test section. These two taps were installed in vertical alignment; the top tap was exposed to the air in the test section and the bottom tap to the distilled water. They were then connected to the high and low sides of a Rosemount (model C1151DP) pressure transducer. This permitted measuring the height of the interface

which is related to the pressure difference across the transducer. Due to the changing interface level, the pressure transducer produced an electrial signal dependent upon the differential pressure created. Calibration of the transducer over the range of 2 to 10 volts permitted a measurement of 0 to 254 mm of water. The resolution on the voltmeter measuring the outlet signal from the transducer was 1 mV and the relationship between the differential pressure and voltage was linear. Therefore, a 1 mV increment corresponded to a differential pressure of 0.03505 mm of water. Appendix A provides the details of the calibration procedure.

With a method for determining the interface position in the test section established, a datum or reference position was required. It was decided to use as the datum the centerline of the primary branch. Recall that the primary branch was defined as the branch nearest to the interface. To characterize the centerline of the primary branch, the interface was first raised above it, then lowered slowly until the flat interface was even with the top edge and then the bottom edge of the primary branch. The "reflection method", described below, was used to determine when the interface was even with the top and bottom edges of the branch. The "reflection method" was developed by Parrott (1993). These readings were averaged to give the datum transducer reading corresponding to the alignment of the flat interface with the centerline of the primary branch. Then, to determine the critical height at the onset of either gas or liquid entrainment, the difference between this datum and the transducer reading at which entrainment occurred was evaluated. This difference was used to calculate h/d.

4.2.4 Angle of Inclination Measurement

The angle of inclination, α, of the branches was measured using the horizontal plane as a datum. A protractor with a resolution of 0.5° was sufficiently accurate since

it was expected that data sets collected within 1.0° of each other would not show any differences. In order to measure the desired angle of the two branches a datum was established. This was accomplished by orienting the branches in the horizontal alignment or $\alpha = 0°$. The procedure to ensure that the branches were horizontally aligned consisted of utilizing the "reflection method".

The reflection method consists of observing the interface from beneath or by looking up at it through the water. From this orientation, the interface served as a mirror and the image of the branches was seen reflected off the interface. When observing the reflected image, care was exercised not to view it through the curved meniscus that distorted the perspective. As well, observing the reflection as close to the interface as possible provided the most accurate result. The procedure was to lower the interface until the reflected image and the real branches just touched. As the distance between the reflection and the actual branches decreased, the distance between each branch and its reflection was compared for equality. If the distances were unequal the brass block was rotated and the process continued until the branches were horizontal. The horizontal orientation obtained with the "reflection method" was compared to the horizontal orientation achieved with a surveyor's transit. It was found the "reflection method" agreed to within less than one degree. Once horizontal alignment was achieved, the protractor reading was recorded as the datum. From this reference any angle was measured with high confidence.

4.3 Gas Entrainment Experiments

4.3.1 Experimental Procedure

The experimental matrix was designed to yield the influences of α, l/d, Fr_2, and Fr_1 on the critical height, h/d, at the onset of gas entrainment. The matrix procedure

was, for each l/d, to fix the outlet branches at a desired α and for each of the four Fr_2's, set at the secondary branch, cover the widest possible range of Fr_1. Then change the value of α and cover the Fr_2 and Fr_1 spectrum. Once all α, Fr_2, and Fr_1 combinations were covered, the next l/d was chosen. For each datum point the following procedure was employed.

1. The atmoshpheric pressure and room temperature were recorded.
2. For the current l/d, the discharge branches were positioned at the desired angle of inclination and the transducer reading corresponding to the reference datum for the critical height calculation was established.
3. The test section was filled with water far above both branches and the test section pressure set to a steady 510 kPa by pressurizing it with compressed air.
4. The water flow rates out from the branches were established by adjusting the float positions in the flow meters with the downstream throttling valves. The positions were set such that the float scale positions corresponded to the desired Fr_1 and Fr_2. The float positions were recorded.
5. The interface was lowered slowly by adjusting the by-pass line such that the rate of discharge slightly exceeded the rate of water supply. With the voltmeter reading changing by 1 mV approximately every 3 seconds, the interface dropped by less than 1 mm per minute.
6. When, by visual observation, a gas cone formed that was continuously entraining and not breaking off from the branch(es) the onset of entrainment was said to have occurred. At this moment the voltmeter reading was taken, which produced h/d, and the branch(es) at which entrainment occurred was recorded.

7. Other readings taken immediately after the onset were the test section pressure and the air and water temperatures inside the test section. The water temperature at the flow meters was assumed to be equal to the water temperature inside the test section.

For all experimental points the floats in the rotameters were very steady and the pressure transducer's signal free from noise. The above procedure applied to single or dual discharge. In the case of dual discharge, simultaneous gas entrainment was possible. Iteration of Fr_1 was required to determine the simultaneous point exactly. For all points the onset of gas entrainment was determined visually and/or by observing air bubbles in the flow meters. The surface of the brass block was cleaned on a regular basis with a 0.3 μm cleaning compound and alcohol to remove oxidation and ensure the surface was smooth.

4.3.2 Data Reduction

The experimental data collected were reduced to the experimental parameters of Fr_1, Fr_2, and h/d. This was accomplished by the use of a personal computer and a data-reduction program written in FORTRAN. The important calculations are as follows.

1. The mass flow rate, $\dot{m}$, through each branch was determined from the in-house calibration curves.
2. The test-section pressure, P_o, was corrected using the calibration chart for the pressure gauge.
3. The water in the test section was treated as a compressed liquid and the density, $\rho_{L,o}$, approximated as the density of a saturated liquid at the same temperature using standard steam tables.

4. The air density in the test section, $\rho_{G,o}$, was determined using the ideal gas law,

$$\rho_{G,o} = \frac{P_o}{RT_{G,o}} \tag{4.1}$$

5. The Froude numbers through each branch, Fr_1 and Fr_2, were calculated from Equation (3.28)
6. The critical height, h/d, was calculated using the differential pressure transducer reading. The details are provided in Appendix B.

4.4 Liquid-Entrainment Experiments

4.4.1 Experimental Procedure

The experimental matrix was designed to yield the influences of α, l/d, Fr_2, and Fr_1 on the critical height, h/d, at the onset of liquid entrainment. The matrix procedure was, for each l/d, to fix the discharge branches at a desired α and for each of the four Fr_2's set at the secondary branch cover the widest possible range of Fr_1. Then change the α and cover the Fr_2 and Fr_1 spectrum. Once all α, Fr_2, and Fr_1 combinations were covered the next l/d was chosen. For each datum point the following procedure was employed.

1. The atmoshpheric pressure and room temperature were recorded.
2. For the current l/d, the discharge branches were positioned at the desired angle of inclination and the reference datum for the critical-height calculation established.

3. The test section was filled with water far below both branches and the test section pressure set to a steady 310 kPa by pressurizing it with compressed air.
4. The air flow rates out the branches were established by adjusting the float positions in the flow meters with the upstream throttling valves. The positions were set such that the float scale positions corresponded to the desired Fr_1 and Fr_2. The float positions were recorded. The brass block was allowed to dry thoroughly by the air flow.
5. The interface was raised slowly by adjusting the by-pass line such that the rate of water supply into the test section caused the voltmeter reading to change by 1 mV approximately every 3 seconds. This corresponded to the interface rising by less than 1 mm per minute.
6. When, by visual observation, a liquid spout was pulled up the test piece and entrained continously into the branch(es), the onset of entrainment was said to have occurred. At this moment the voltmeter reading was taken, which corresponded to h/d, and the branch(es) at which entrainment occurred was recorded.
7. Other readings taken immediately after the onset were the test section pressure, the air and water temperatures inside the test section, the air temperature and manometer readings at the air flow meters.

For all experimental points the floats in the rotameters were very steady, the pressure transducer's signal free from noise, and the brass block thoroughly dried between points. The above procedure applied to single or dual discharge. In the case of dual discharge, simultaneous liquid entrainment was possible. Iteration of Fr_1 was required to determine the simultaneous point exactly. For all points the onset of liquid entrainment was determined visually. Finally, as in the gas-entrainment experiments,

the brass block surface was cleaned regularily to ensure its surface condition was controlled throughout the study.

4.4.2 Data Reduction

The experimental data collected was reduced to the experimental parameters of Fr_1, Fr_2, and h/d. This was accomplished by the use of a personal computer and a data reduction program written in FORTRAN. The important calculations were as follows:

1. The volumetric flow rate in $SLPM$ through each flow meter was determined from the in-house calibration curves.
2. The air density in the flow meters, $\rho_{G,fm}$, was calculated using the ideal gas law.

$$\rho_{G,fm} = \frac{P_{G,fm}}{RT_{G,fm}} \tag{4.2}$$

3. The actual flow rate in Actual Litres per Minute, $ALPM$, was determined using the following correction.

$$ALPM = SLPM \left[\frac{(\rho_{SS} - \rho_{G,fm})\,\rho_{G,ST}}{(\rho_{SS} - \rho_{G,ST})\,\rho_{G,fm}} \right]^{0.5} \tag{4.3}$$

where ρ_{SS} is the density of the stainless steel float in kg/m^3, $\rho_{G,ST}$ is the density of air at standard day conditions, 21.1 $^\circ C$ and 101.325 kPa, and $\rho_{G,fm}$ is the density of the air at the actual conditions of the flow meter in kg/m^3.

4. The mass flow rate of air was calculated as

$$\dot{m} = ALPM \times \rho_{G,fm} \tag{4.4}$$

5. To calculate the Froude numbers at each branch inlet, Fr_1 and Fr_2, the air velocity and density (temperature and pressure) were required. This was accomplished by the use of a nonlinear iterative technique to solve for the unknowns.

a) Treating the air as an ideal gas and applying an energy balance between the test section stagnation conditions and the branch inlet yields an expression for the inlet air temperature.

$$T_{G,i} = \frac{\left(C_P T_{G,o} + \frac{v_o^2}{2} - \frac{v_{G,i}^2}{2}\right)}{C_P} \tag{4.5}$$

b) Assuming isentropic expansion from the test section stagnation conditions to the branch inlet and treating the air as an ideal gas yields

$$P_{G,i} = P_o \left(\frac{T_{G,i}}{T_o}\right)^{k/(k-1)} \tag{4.6}$$

c) Using the mass flow rate of air through the branch, the velocity of the air at the branch inlet can be expressed as

$$v_{G,i} = \frac{4\dot{m}}{\rho_{G,i}\pi d^2} \tag{4.7}$$

where $\rho_{G,i}$ is the air density at the branch throat.

Equations 4.5, 4.6, and 4.7 were solved by starting with a guess value for one of the three unknowns and iterating until a converged solution was obtained.

6. The Froude number was calculated using Equation (3.28).
7. The critical height, h/d, was calculated using the differential pressure transducer reading. The details are provided in Appendix B.

4.5 Estimates of Uncertainty

An uncertainty analysis was performed for gas and liquid entrainment experiments. The uncertainty analysis was performed following the approach of Kline and McClintock (1949). Appendix E provides the procedure and results of the analysis. The uncertainty analysis was performed for six representative data sets; three for gas entrainment and three for liquid entrainment. The reason for performing an abbreviated uncertainty analysis stems from the fact that the experimental apparatus was used in previous studies. The uncertainty in the data obtained from the experimental rig has been established by Parrott (1993) and Hassan (1996).

The uncertainty in the Froude number for gas entrainment for the data sets examined ranged from $\pm 3.26\%$ to $\pm 4.77\%$. The uncertainty in the branch diameter and the uncertainty in the volumetric flow rate through the flowmeter were the dominant

uncertainties in the Froude number.

The uncertainty in the Froude number for liquid entrainment for the data sets examined ranged from ±3.99% to ±8.67%. The uncertainty in the branch air-inlet density and the uncertainty in the volumetric flow rate through the flowmeter dominated the uncertainty in the Froude number.

The uncertainty in the critical height for gas entrainment for the data sets examined ranged from ±1.86% to ±5.36%. The uncertainty in the critical height for liquid entrainment for the data sets examined ranged from ±1.85% to ±3.09%.

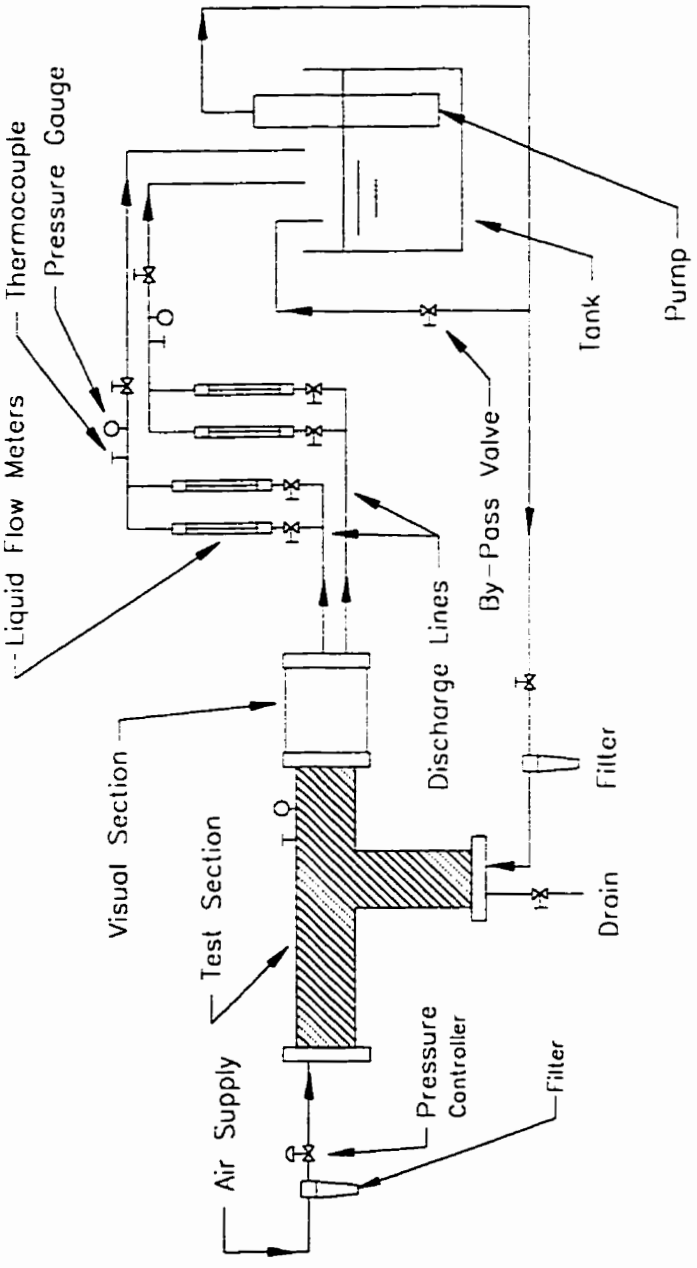

Figure 4.1: Schematic of experimental flow loop for gas-entrainment studies

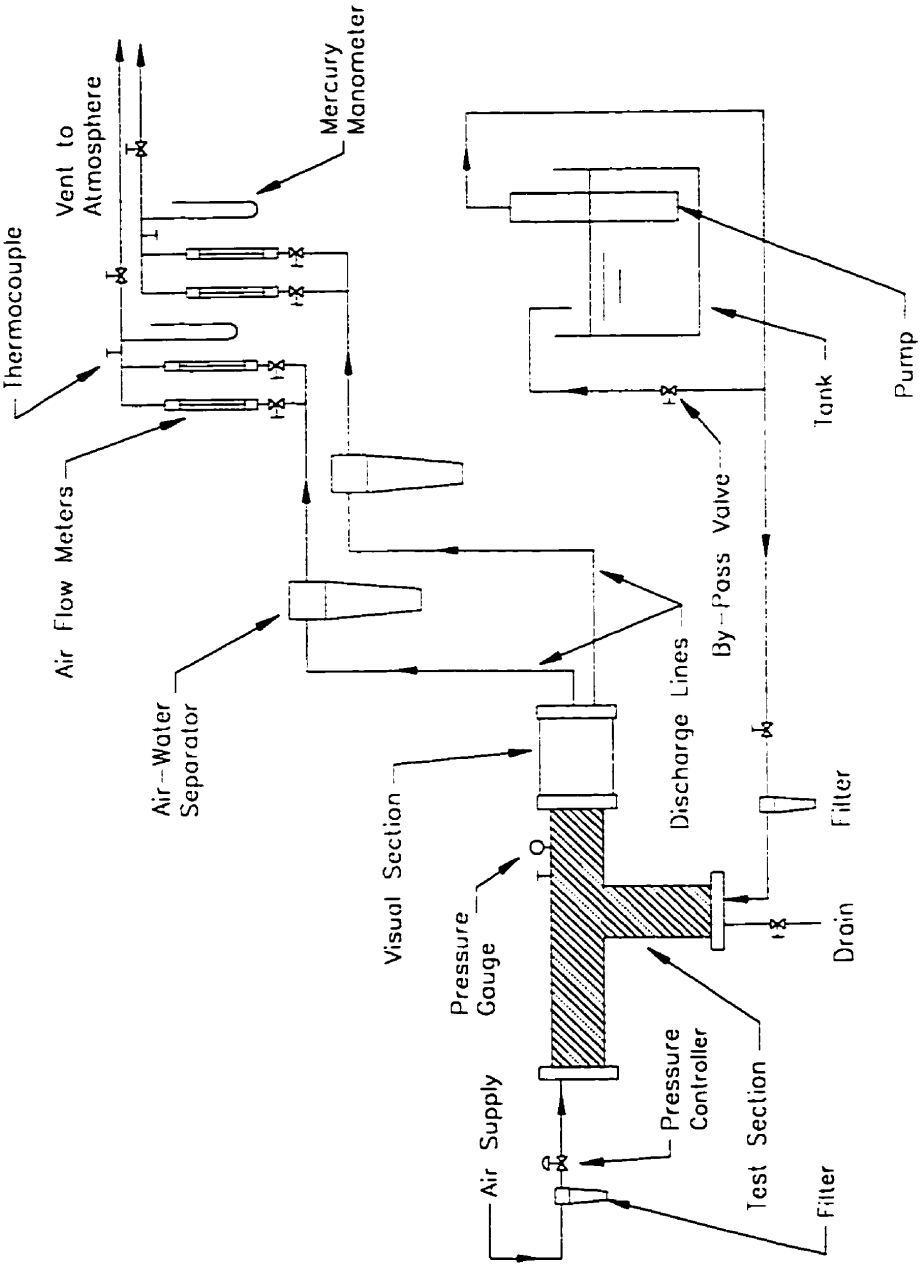

Figure 4.2: Schematic of experimental flow loop for liquid-entrainment studies

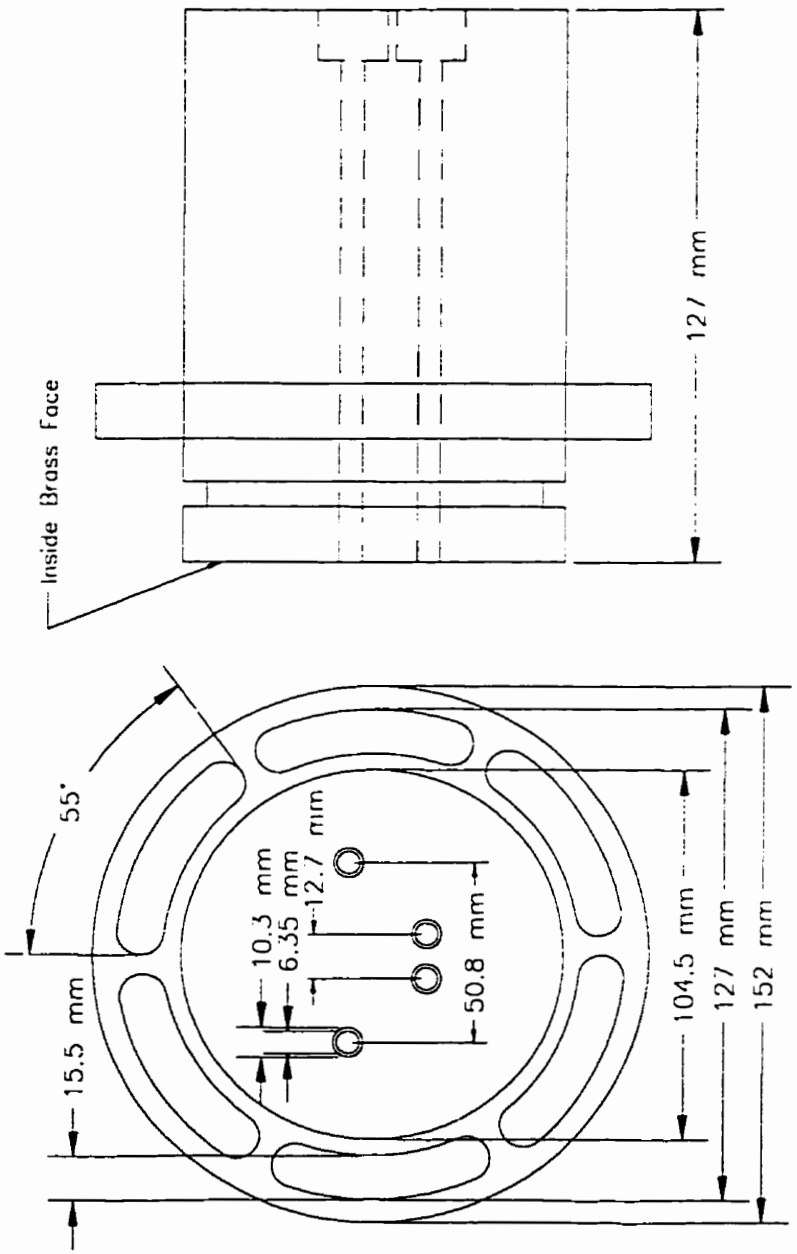

Figure 4.3: Branch layout for $l/d = 2.0$ and 8.0.

CHAPTER 5

EXPERIMENTAL RESULTS AND DISCUSSION

5.1 Introduction

There were two parts to the experimental investigation that was conducted. The first part was the investigation into the onset of gas entrainment and the second part was the investigation into the onset of liquid entrainment. The experimental results for the onset of liquid entrainment are compared with the analytical solution obtained in Chapter 4.

In collecting the experimental data, visual observations were made during each dataum point in order to describe the flow situation at the onset. These observations were recorded in detail for each data point collected and are presented below. The detailed observations were then used in grouping the data into categories to reduce the detail in presenting the data. The end result was that each dataum point was placed into one of five categories that were common to both gas and liquid entrainment.

During gas- or liquid-entrainment data collection, two modes of entrainment that occurred require preliminary mention before the results of each investigation are presented. These modes are continuous entrainment and intermittent entrainment. Continuous entrainment occurred when the entrained gas or liquid stream did not stop flowing into the branch but remained steadily entraining. Conversely, intermittent entrainment was characterized by the gas or the liquid jumping to the branch then breaking off in succession, without steadily entraining.

5.2 Gas Entrainment

5.2.1 Data Matrix

An extensive matrix of data was collected to ensure that the onset phenomena were well described. The matrix of parameters is as follows:

Test Section Pressure	$P_o = 510\ kPa$
Branch Diameter	$d = 6.35\ mm$
Angle of Inclination	$\alpha = 0°$, 10°, 30°, and 60°
Separation Distance	$l/d = 1.5$, 2.0, and 8.0
Primary-Branch Froude Number	$Fr_1 = 0.0$ to 70.0
Secondary-Branch Froude Number	$Fr_2 = 0.0$, 14.0, 28.5, 42.5, and 56.6

5.2.2 Flow Phenomena

As mentioned above, during the collection of each dataum point many observations were recorded. A complete description of these observations is presented below. The reader can refer to Appendix C for a complete listing of where in the experimental matrix these observations were recorded. In performing the gas-entrainment study, the method of data collection evolved after the initial experimental observations and results were analyzed. Initially, the onset was defined as the first instance of observable gas that was entrained. For some data points the first instance of entrainment corresponded to continuous entrainment and for others it corresponded to intermittent entrainment. After reviewing the initial results, the experimental method was revised such that all data points were collected for the continuous-entrainment condition. Thus, for gas entrainment, the interface was lowered slowly until continuous

entrainment occurred. As the interface was lowered all unique modes of gas entrainment that occurred at each branch from the first instance of entrainment to continuous entrainment were recorded. For gas entrainment there were four distinguishable modes of entrainment that occurred as given in Table 5.1.

Table 5.1: Descriptions of gas-entrainment modes

No.	Mode	Description
1.	IVE	Initial Vortex Entrainment, IVE, was the first observed gas entrained. It was characterized by a hair-thin, vortex, gas cone that originated from the flat interface over the branch(es) or the bottom of the depression in the interface formed over the branch(es). IVE was always intermittent. See Figure 5.1.
2.	CVE	Continuous Vortex Entrainment, CVE, was identical in appearance to IVE and formed in the same manner; however, CVE was continuous and always formed at the bottom of the depression. See Figure 5.2.

Descriptions of gas-entrainment modes

No.	Mode	Description
3.	IDE	Initial Depression Entrainment, IDE, was characterized by observing the first instance of the depression in the interface over the branch(es) becoming fully entrained. As the interface was lowered, the depression in the interface over the branch(es) deepened until it entrained. IDE was always intermittent and prior to its occurrence, vortex cones, much like IVE, may have occurred. IDE was either vortex or nonvortex in nature. See Figure 5.3.
4.	CDE	Continuous Depression Entrainment, CDE, was identical in appearance to IDE and formed in the same manner, however, CDE was continuous. See Figure 5.4.

In a typical gas-entrainment experiment, all four modes given above were normally observed as the interface was lowered. The order of appearance at branch as the interface was lowered was typically IVE, IDE, CVE, or CDE. Experimental data were recorded for each mode for later analysis. For some data points IDE and CVE

occurred in a reverse order. Also, it was possible for CVE not to occur when the other three were observed. In addition, CDE was sometimes the only entrainment mode observed, typically at low Froude numbers. Finally, with the interaction between the two branches, it was possible to observe CVE at one branch while IVE occurred at the other, i.e., a continuous form of entrainment at one branch, CVE or CDE, while intermittent or continuous entrainment occurred at the other.

Since the amount of gas entrained was insignificant for IVE and IDE and since these modes of entrainment showed poor repeatability, it was decided to classify the data based on establishing continuous entrainment at one branch and recording the condition at the other. This reduced the complexity of data presentation while maintaining a record of all observations. In this way, five categories emerged. as presented in Table 5.2.

Table 5.2: Experimental-data categorization scheme (gas entrainment)

No.	Category	Description
1.	**Entrainment at Branch 1**	The onset of continuous entrainment occurred at branch 1 only via CVE or CDE modes.
2.	**Entrainment at Branch 1 with Intermittence at Branch 2**	Continuous entrainment occurred at branch 1 (CVE or CDE) with intermittent entrainment at branch 2 (IVE or IDE).

Experimental-data categorization scheme (gas entrainment)

No.	Category	Description
3.	**Simultaneous Entrainment**	Continuous entrainment occurred at both branches at the same instance (CVE or CDE) and remained steadily entraining to both branches.
4.	**Entrainment at Branch 2 with Intermittence at Branch 1**	Continuous entrainment occurred at branch 2 (CVE or CDE) with intermittent entrainment at branch 1 (IVE or IDE).
5.	**Entrainment at Branch 2**	The onset of continuous entrainment occurred at branch 2 only (CVE or CDE).

5.2.3 Single Discharge

The experimental results for single discharge are shown in Figure 5.5. The data are in good agreement with the single-discharge data reported by Parrott (1993) measured from the flat interface from a horizontal branch. The experimental data are given in Appendix C.

5.2.4 Dual Discharge

The experimental results for dual discharge are shown in Figures 5.6 to 5.16. For each figure the separation distance, l/d, and the angle of inclination, α, are fixed while five

values of Fr_2 are shown for all Fr_1. A common legend scheme, shown in Table 5.4, is utilized for all plots and is based upon the data categories presented in Table 5.2. The reader should refer to Table 5.4 for a description of each symbol when examining Figures 5.6 to 5.16. A physical description of a typical curve given in these is required before conclusions are stated. The description of the entrainment phenomena follows from the categories presented in Table 5.2. In order to illustrate the categories given in Table 5.2, Figure 5.6 for $Fr_2 = 42.5$ should be examined. Following this curve from low Fr_1 to high Fr_1, several different categories of gas entrainment onset are encountered. First, at low Fr_1, solid symbols are given that correspond to entrainment at branch 2 (category 5). Thus, for Fr_1 between 1.0 and 26.0, the onset always occurs at branch 2. Notice, as well, that the curve exhibits a slightly increasing trend (h/d increases) due to the influence of branch 1. Next, at $Fr_1 = 34.0$, the onset phenomenon changes to category 4. At this point, Fr_1 is high enough to pull some of the entraining gas intermittently into branch 1. As Fr_1 increases further the onset phenomena passes into the simultaneous region (category 3). The simultaneous region for $\alpha = 0°$ is expected to occur at $Fr_1 = Fr_2$ since the branches are at equal distance from the interface. As Fr_1 increases past 42.5, branch 1 is now discharging more mass than branch 2 and therefore, exhibits a stronger influence on the onset. This is observed as a new region is encountered in Figure 5.6: entrainment according to category 2. In general, Categories 2, 3, and 4 occupy bands of finite widths on the Fr_1 scale, even though in Figure 5.6 they appear as single points. Finally, as Fr_1 increases further, the remaining data points are all open symbols indicating that the onset of gas entrainment occurred exclusively at branch 1 (category 1). Thus, as Fr_1 increases over its range five distinct onset regions are encountered. As will be shown, all five regions do not always occur. However, in general, the following conclusions can be drawn.

A general observation from Figures 5.6 to 5.16 is at low l/d, the curves for different

Fr_2 are smooth and gradually change slope. This results from the close interaction of the branches and their simultaneous influence on the onset. However, at $l/d = 8$, for each Fr_2 value, when the onset occurs at branch 2, it is essentially at a constant h/d value; i.e., the curve is flat in this section. At a specific (Fr_1,Fr_2) combination, the onset becomes simultaneous and this point falls on the single-discharge curve. Then, to the right of the simultaneous point, the onset always occurs at orifice 1 and these data points follow the single-discharge curve. An abrupt change in slope occurs at the simultaneous point. From the above statements it is concluded that for $l/d = 8$ the two branches act independently. This is further evidenced by observing that the h/d value, when the onset occurs at branch 2 for each Fr_2, is approximately equal to the same h/d that the single-discharge curve yields at the same Froude number.

Next, by comparing data for the same l/d but different α, for example Figures 5.6 to 5.9, it is observed that the data points change from mainly solid symbols at low α (Category 5) to mainly open symbols at high α (Category 1). In general, as α increases, the five regions given in Table 5.2 are observed to shift to lower Fr_1 values. In particular, an examination of the simultaneous region in Figures 5.6 through 5.9 for $Fr_2 = 56.6$ shows that it first occurs at $Fr_1 = 56.6$ in Figure 5.6 at $\alpha = 0°$ but shifts to $Fr_1 = 1.0$ in Figure 5.9 at $\alpha = 60°$. In addition, for Figures 5.14 and 5.15 in which $l/d = 8$ and $\alpha = 0°$ and $10°$, respectively, the simultaneous point for each Fr_2, falls on the single-discharge curve. This adds more strength to the conclusions stated above that the branches are acting independently of each other for $l/d = 8$. As well, entrainment categories 2 and 4 were not observed for any α when $l/d = 8$.

It can be seen from Figures 5.6 to 5.16 that for any Fr_1, h/d increases as Fr_2 increases. The percentage increase in h/d is more pronounced at low Fr_1 and drops monotonically as Fr_1 increases. For example, in Figure 5.14 at $Fr_2 = 56.6$, h/d is approximately 8 times the single-discharge value at $Fr_1 = 1.0$ but the two corresponding points are almost identical at $Fr_1 = 66$.

Next, as α increases for a fixed l/d, the data shift towards the single-discharge curve. As α increases, branch 2 moves farther away from the interface relative to branch 1. Therefore, its influence on h/d decreases and the entrainment phenomenon moves towards the single discharge curve. In Figures 5.6 to 5.9 where $l/d = 1.5$, the Fr_2 curves shift towards the single discharge curve as α increases. The shift is small but noticeable. The small shift is due to the close proximity of branch 2. For Figures 5.10 to 5.13 where $l/d = 2$, the data exhibit a greater shift towards the single discharge curve as α increases. Finally, for Figures 5.14 to 5.16 where $l/d = 8$, the Fr_2 curves dramatically collapse onto the single discharge curve as α increases from 0 to 30°. That is because branch 2 is sufficiently far removed from the interface in Figure 5.16 to have any effect on the entrainment phenomenon and the two branches are observed to act independently of each other.

5.2.5 Comparison with Previous Results

Figure 5.17 compares the present study with the results of Hassan (1995) for the case of $Fr_1 = Fr_2$, $\alpha = 0°$, and $l/d = 1.5$, 2.0, and 8.0. As can be seen, the present study agrees very well with the data reported by Hassan (1995) which strengthens the confidence in the present data.

5.3 Liquid Entrainment

5.3.1 Data Matrix

An extensive matrix of data was collected to ensure that the onset phenomena were well described. The matrix of parameters is as follows:

Test Section Pressure	$P_o = 310\ kPa$
Branch Diameter	$d = 6.35\ mm$
Angle of Inclination	$\alpha = 0°$, 10°, 30°, and 60°
Separation Distance	$l/d = 1.5$, 2.0, and 8.0
Primary-Branch Froude Number	$Fr_1 = 0.0$ to 38.0
Secondary-Branch Froude Number	$Fr_2 = 0.0$, 9.5, 19.0, 28.5, and 38.0

5.3.2 Flow Phenomena

As mentioned above, during the collection of each dataum point, observations were recorded. The experimental data is contained in Appendix C. For each experimental datum point, entrainment to a particular branch at a given h/d was either continuous or intermittent. For some data points, initially, the liquid entrained intermittently to a particular branch but changed to continuous entrainment at the same branch without a change in h/d. Therefore, these points were recorded as continuous.

It was necessary to place the above observations of onset modes into a small set so that the presentation of the data would be manageable and more coherent. This was accomplished by establishing a unique and necessary criterion that each datum point had to meet before it could be placed into the final categorization. For liquid entrainment, the criterion that signified to which category a data point belonged was the establishment of continuous entrainment at one or both branches. Table 5.3 provides a description of the five categories identified in this study.

Table 5.3: Experimental-data categorization scheme (liquid entrainment)

No.	Category	Description
1.	**Entrainment at Branch 1**	The onset of continuous entrainment occurred at branch 1 only.
2.	**Entrainment at Branch 1 with Intermittence at Branch 2**	Continuous entrainment occurred at branch 1 with intermittent entrainment at branch 2.
3.	**Simultaneous Entrainment**	Continuous entrainment occurred at both branches at the same instant and remained steadily entraining to both branches.
4.	**Entrainment at Branch 2 with Intermittence at Branch 1**	Continuous entrainment occurred at branch 2 with intermittent entrainment at branch 1.
5.	**Entrainment at Branch 2**	The onset of continuous entrainment occurred at branch 2 only.

5.3.3 Single Discharge

The experimental results for single discharge are shown in Figure 5.18. The data are in good agreement with the data reported by Parrott (1993) for single discharge from a horizontal branch. As well, the data are in excellent agreement with the data

reported by Hassan (1996) measured with the interface level increasing and with the theoretical prediction of Craya (1949). The tabulated data are given in Appendix C.

5.3.4 Dual Discharge

The experimental results for dual discharge are shown in Figures 5.19 to 5.29. In general, the same observations and comments made for gas entrainment studies apply to the results obtained for liquid entrainment. These comments are repeated below for completeness as well as remarks on the comparison with the theoretical results of Chapter 3.

In each figure the separation distance, l/d, and the angle of inclination, α, are fixed while five values of Fr_2 are shown for all Fr_1. A common legend scheme, shown in Table 5.5, is utilized for all plots and is based upon the data categories presented in Table 5.3. The reader should refer to Table 5.5 for a description of each symbol when examining Figures 5.19 to 5.29. A physical description of a typical curve given in these figures is required before conclusions are stated. In order to illustrate most of the categories given in Table 5.3, let us examine Figure 5.19 for $Fr_2 = 28.5$. Following this curve from low Fr_1 to high Fr_1, several different regions of liquid entrainment onset are noticed. First, at low Fr_1, solid symbols are given that correspond to entrainment at branch 2 (category 5). Thus as Fr_1 changes from 0.8 to 14.0 the onset always occurs at branch 2. Notice as well that the curve exhibits a slightly increasing trend (h/d increases) due to the influence of branch 1. Next, at $Fr_1 = 18.0$, the onset phenomenon changes to category 4. At this point, Fr_1 is strong enough to pull some of the entraining liquid intermittently into branch 1. As Fr_1 increases further the onset phenomenon passes into the simultaneous region (category 3). The simultaneous region for $\alpha = 0°$ is expected to occur at $Fr_1 = Fr_2$ since the branches are at equal distance from the interface. As Fr_1 increases past

28.5, branch 1 is now discharging more mass than branch 2 and therefore, exhibits a stronger influence on the onset. This is observed as a new region is encountered in Figure 5.19, category 2 entrainment. In general, all entrainment categories occupy bands of finite width on the Fr_1 scale even if some of them appear as a single point in Figures 5.19 to 5.29. The final region, entrainment at branch 1, did not appear as it lies outside the range of the Fr_1 values examined in the present study. Thus, as Fr_1 changes, five distinct onset regions are encountered. As will be shown, all five regions do not always occur.

A statement concerning the theoretical curves presented in Figures 5.19 to 5.29 is required for the comparisons shown. First, the theoretical study does not take into consideration the shape of the interface at the onset of entrainment. The assumption used was that of an infinitely narrow stream of entraining liquid. Therefore, entrainment categories 2 and 4 were not predicted by the theory and the simultaneous region is predicted as a single point indicated by an X on each theoretical curve. It can be inferred that all theoretical predictions to the left of the simultaneous point are entrainment at branch 2 and that all theoretical predictions to the right of the simultaneous point are entrainment at branch 1.

In general, the theoretical predictions are in excellent agreement with the experimental data. This indicates that the square-branch geometry assumed in performing the theoretical analysis is an acceptable approximation; there is little difference between a circular and square branch. Also, generally speaking, the theory predicts closely at which branch the onset will occur. As well, at $\alpha = 0°$ for all l/d the theory and experimental data are in excellent agreement for the simultaneous point. However, as α increases the theory over-predicts the value of Fr_1 at which simultaneous entrainment occurs.

A general observation from the Figures 5.19 to 5.29 is that at low l/d, the Fr_2

curves are smooth and gradually change slope. This results from the close interaction of the branches and their influence on the onset. However, at $l/d = 8$, for each Fr_2 value, when the onset occurs at branch 2, it is essentially at a constant h/d value; i.e., the curve is flat in this section. At a specific (Fr_1,Fr_2) combination, the onset becomes simultaneous and this point falls on the single discharge curve. Then, to the right of the simultaneous point, the onset always occurs at branch 1 and these data points follow the single discharge curve. An abrupt change in slope occurs at the simultaneous point. From the above statements it is concluded that for $l/d = 8$ the two branches act independently. This is further evidenced by observing that the h/d value, when the onset occurs at branch 2 for each Fr_2, is approximately equal to the same h/d that the single discharge curve yields at the same Fr. As well, entrainment Categories 2 and 4 were not observed for $l/d = 8$. Existence of Categories 2 and 4 is an indication that the branches are interacting closely to influence the onset.

Next, by comparing data of fixed l/d but varying α, for example Figures 5.19 to 5.22, it is observed that the data points change from mainly solid symbols (Category 5) at low α to mainly open symbols (Category 1) at high α. In general, as α increases, the five categories given in Table 5.3 are observed to shift to lower Fr_1 values. In particular, an examination of the simultaneous region in Figures 5.19 through 5.22 for $Fr_2 = 38.0$ shows that it first occurs at $Fr_1 = 30.0$ through $Fr_1 = 38.0$ in Figure 5.19 at $\alpha = 0°$, shifts to $Fr_1 = 3.0$ and $Fr_1 = 4.0$ in Figure 5.21 at $\alpha = 30°$, and did not occur in Figure 5.22. In addition, for Figures 5.27 and 5.28 in which $l/d = 8$ and $\alpha = 0°$ and 10°, respectively, the simultaneous point for each Fr_2, falls on the single-discharge curve. This adds more strength to the conclusions stated above that the branches are acting independently of each other for $l/d = 8$.

It can be seen on all figures that for any Fr_1, h/d increases as Fr_2 increases. The percentage increase in h/d is more pronounced at low Fr_1 and drops monotonically as Fr_1 increases. For example, in Figure 5.27 at $Fr_2 = 38.0$, h/d is approximately 4

times the single discharge value at $Fr_1 = 0.8$ but the two corresponding points are almost identical at $Fr_1 = 38.0$.

Next, as α increases for a fixed l/d, the data shift towards the single-discharge curve. As α increases branch 2 moves farther away from the interface relative to branch 1. Therefore, its influence on h/d decreases and the entrainment phenomenon moves towards the single-discharge curve. In Figures 5.19 to 5.22 where $l/d = 1.5$, the Fr_2 curves shift towards the single-discharge curve as α increases. The total shift of all Fr_2 curves by Figure 5.22 does not completely fall onto the single-discharge curve. This can be attributed to the influence of branch 2. For Figures 5.23 to 5.26 where $l/d = 2$, the data exhibit a greater shift towards the single discharge curve as α increases. Finally, for Figures 5.27 to 5.29 where $l/d = 8$, the Fr_2 curves dramatically collapse onto the single-discharge curve as α increases from 0 to 30°. That is because branch 2 is sufficiently far removed from the interface in Figure 5.29 so as to have no effect on the entrainment phenomenon and the two branches are observed to act independently of each other.

5.3.5 Comparison with Previous Results

Figure 5.30 compares the present study with the results of Hassan (1995) for the case of $Fr_1 = Fr_2$, $\alpha = 0°$, and $l/d = 1.5$, 2.0, and 8.0. As can be seen, the present study agrees very well with the data reported by Hassan (1995) which lends confidence to the present data. In Hassan (1995), the experimental method was to lower the interface during experimental data collection. Therefore, the method of Hassan (1995) resulted in a wet surface of the brass block during experimental data collection. In sharp contrast, in the present experiments, the experimental method was thoroughly to dry the interface before the commencement of a experimental datum point and to raise the interface. However, as can be seen in Figure 5.30, there is not a significant

difference in the reported experimental data to indicate a difference in experimental methods.

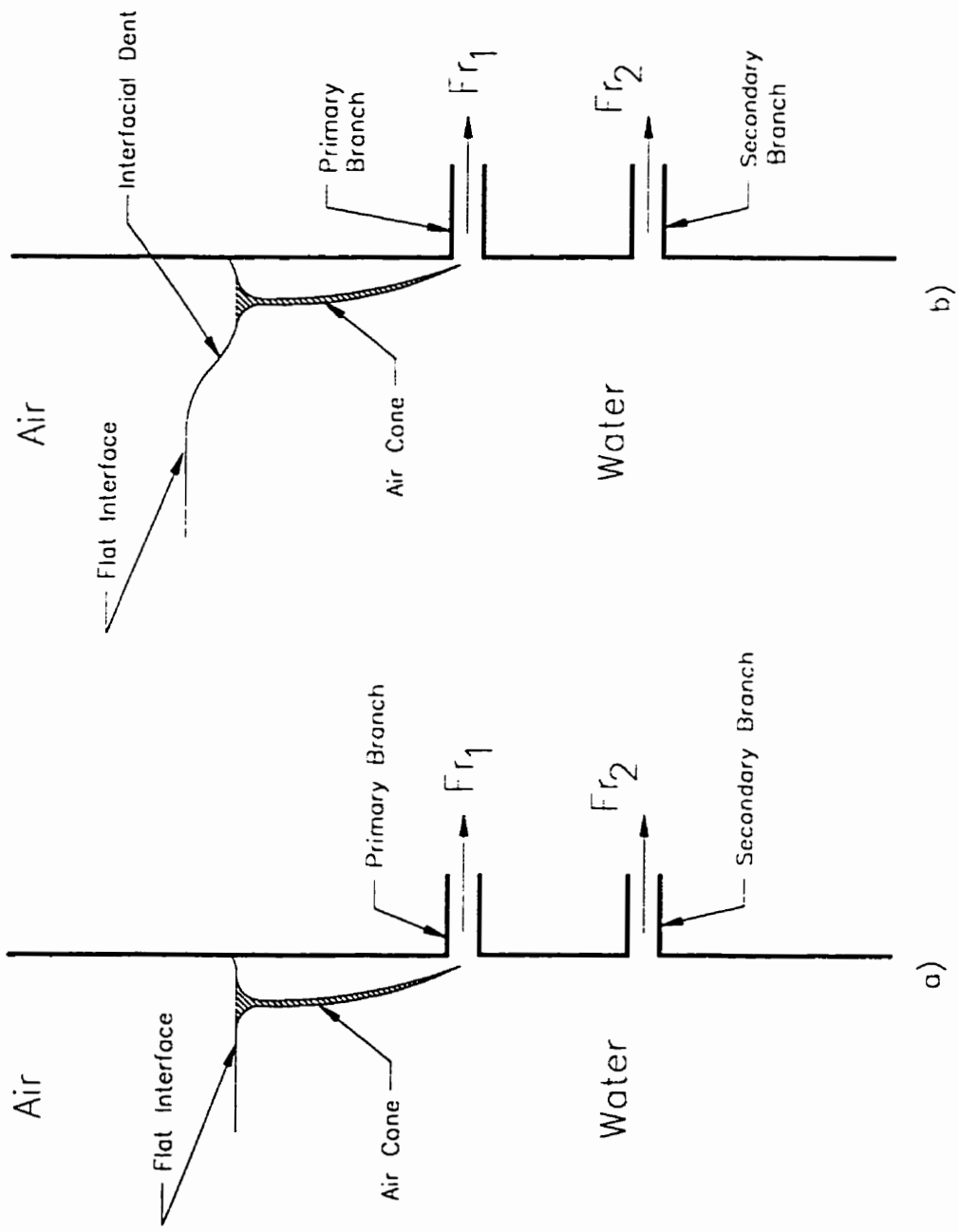

Figure 5.1: Sketch of the IVE entrainment mode

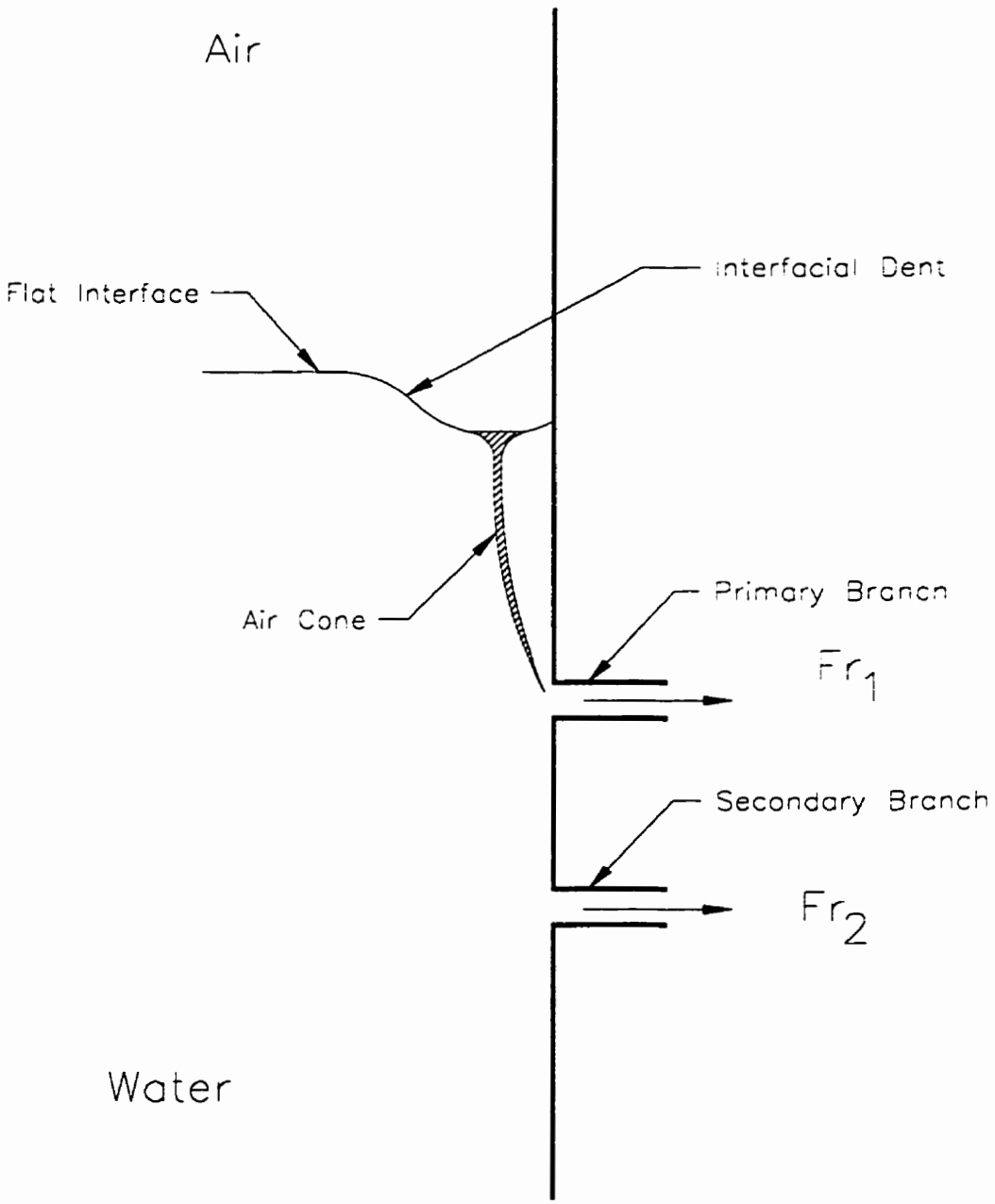

Figure 5.2: Sketch of the Gas CVE entrainment mode

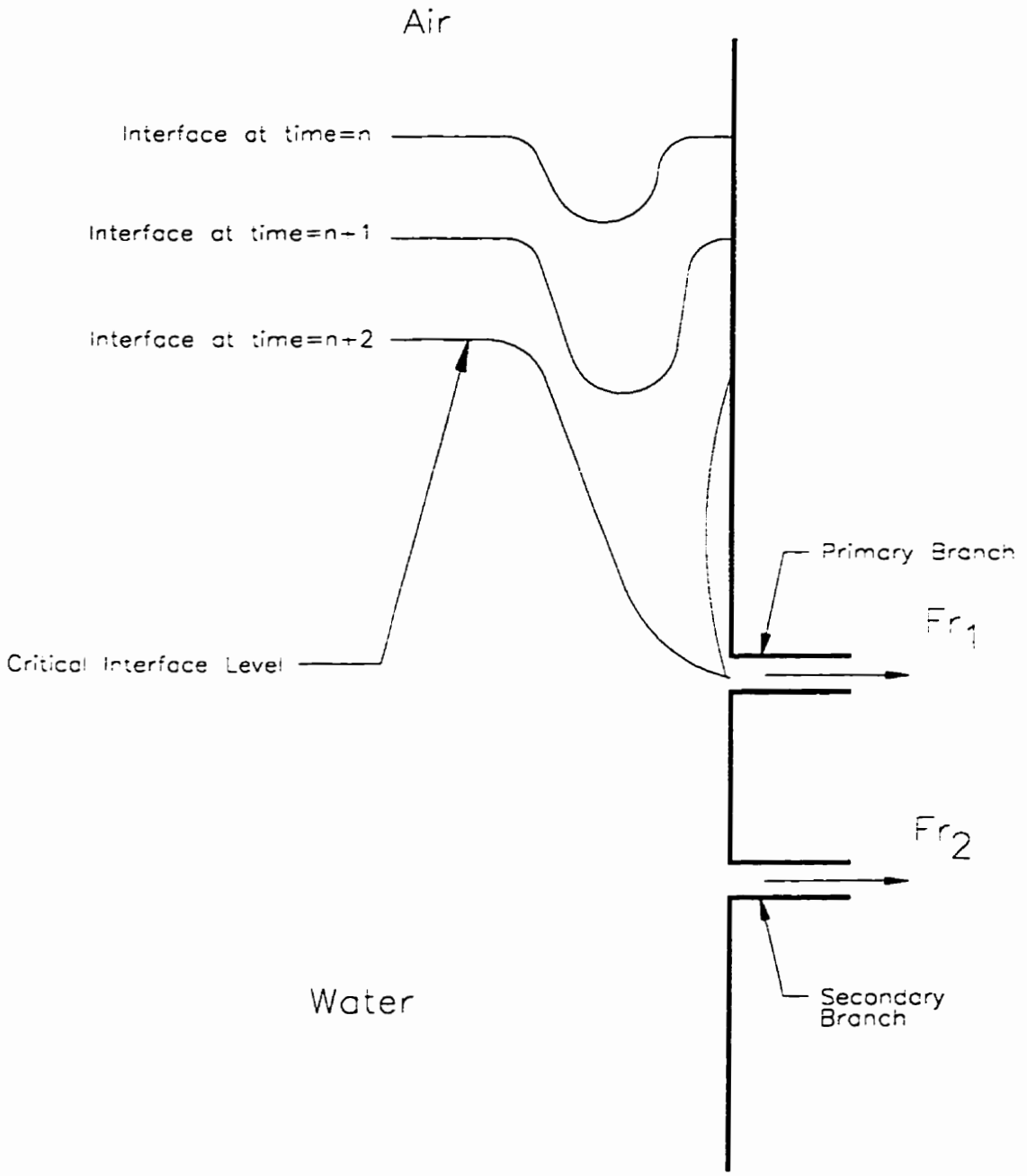

Figure 5.3: Sketch of the IDE entrainment mode

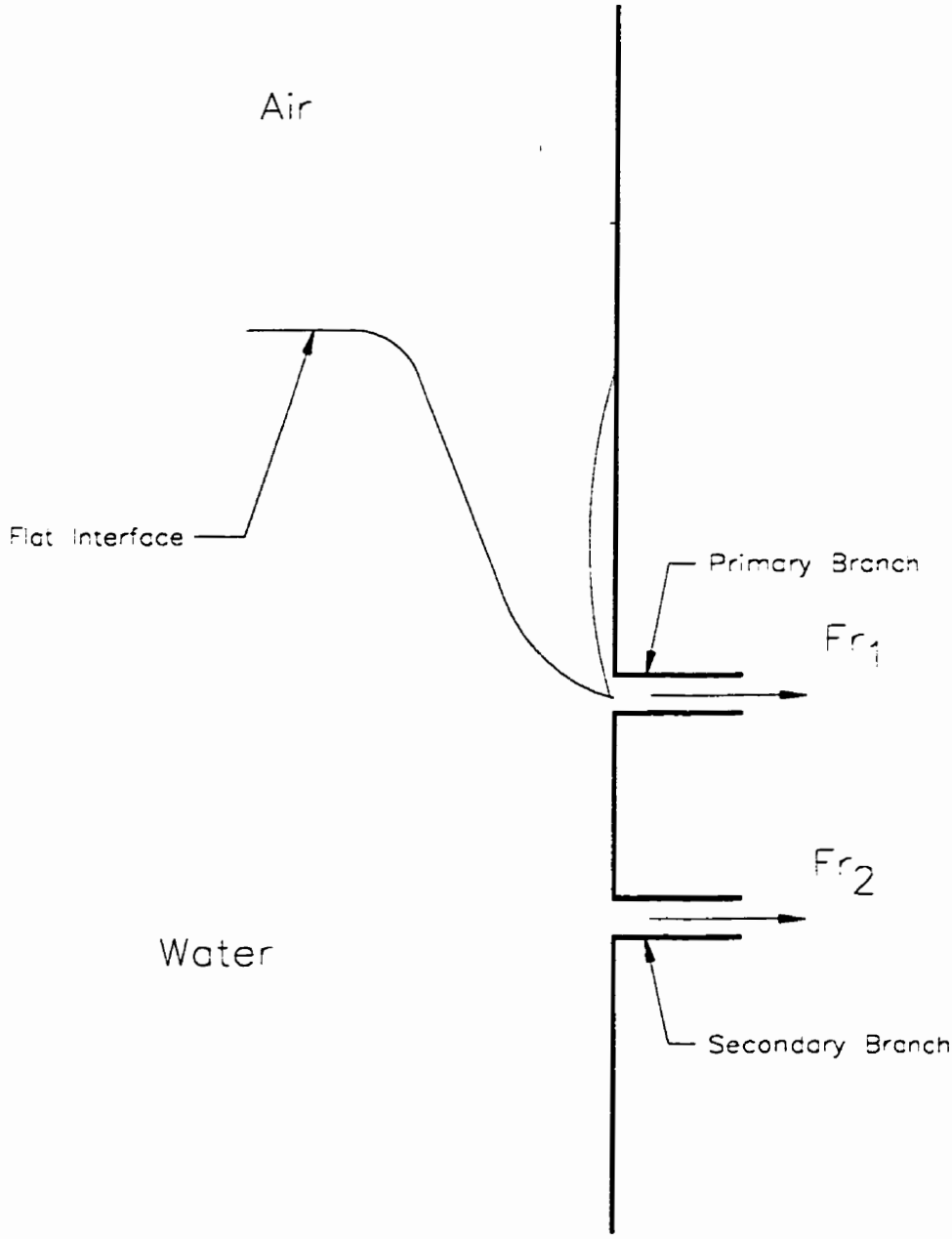

Figure 5.4: Sketch of the CDE entrainment mode

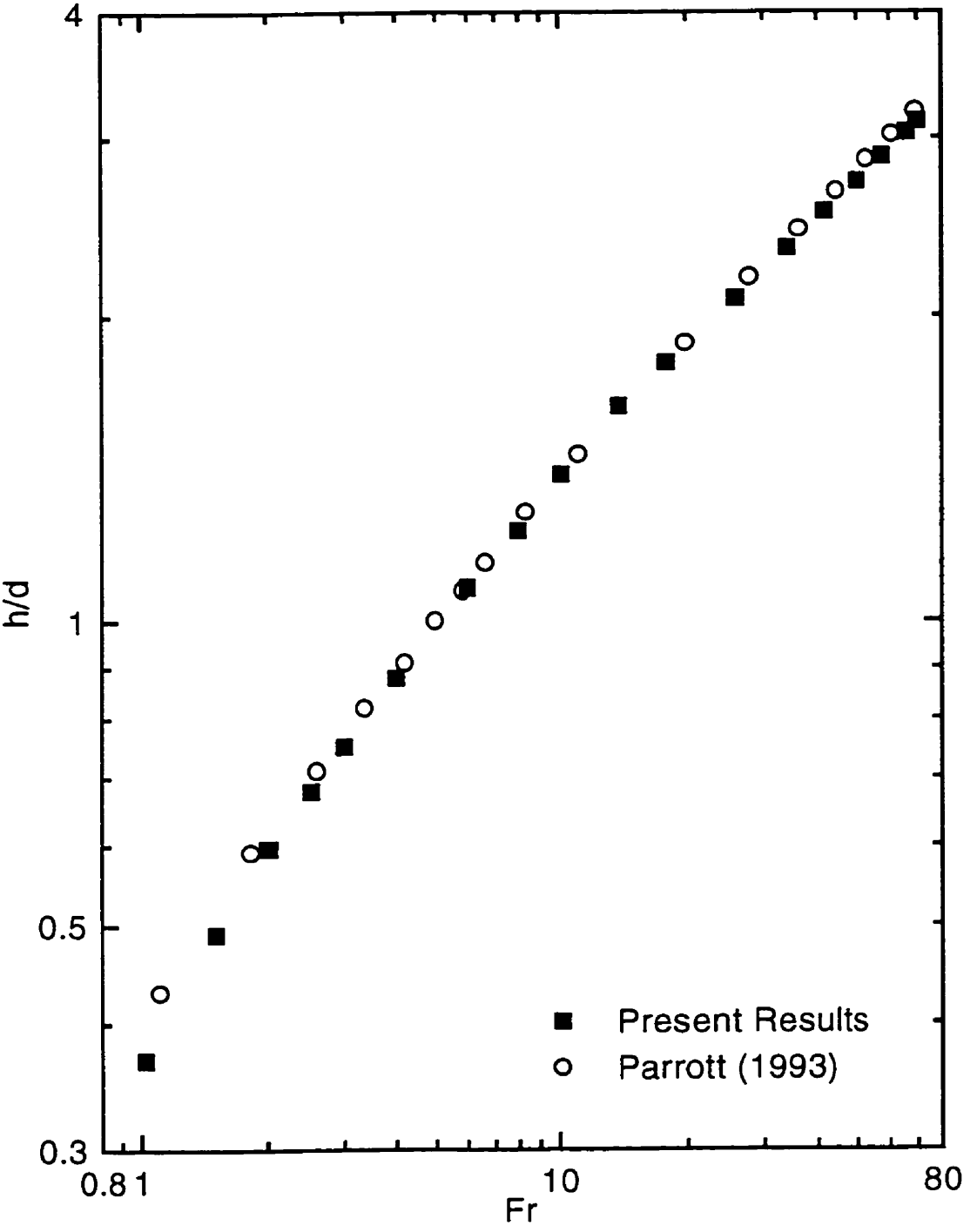

Figure 5.5: Experimental data of gas entrainment for single discharge

Table 5.4: Gas-entrainment-data symbols used in Figures 5.6 to 5.16

Fr_2	Symbol	Category
0.0	✳	
14.9	○	1
	⊙	2
	⊕	3
	⊖	4
	●	5
28.5	△	1
	◬	2
	⧋	3
	⧊	4
	▲	5
42.5	□	1
	⊡	2
	⊞	3
	⊟	4
	■	5
56.6	◇	1
	◈	2
	⧫	3
	⧫	4
	◆	5

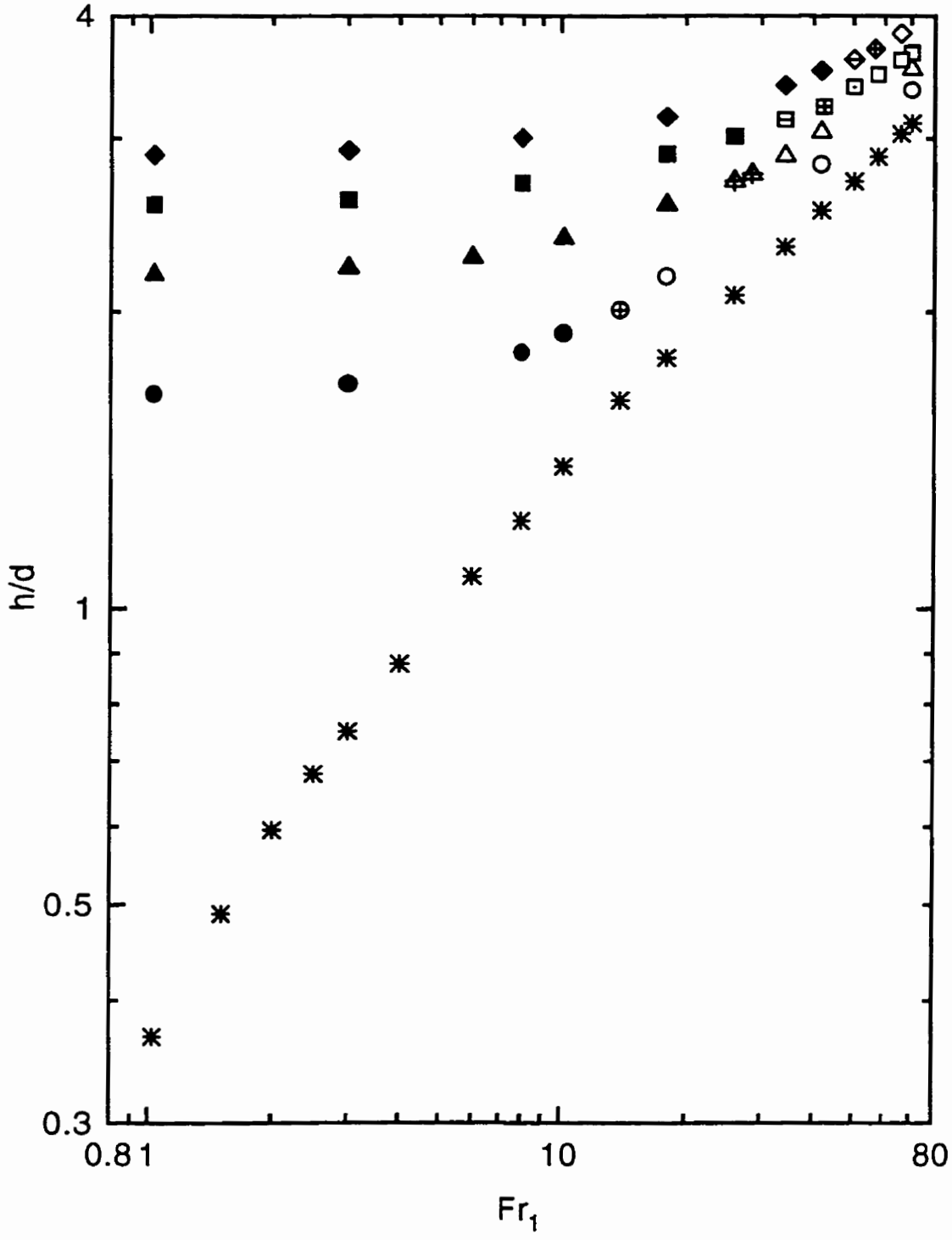

Figure 5.6: Dual-discharge gas entrainment, $l/d = 1.5$ and $\alpha = 0°$; refer to Table 5.4 for symbol notation

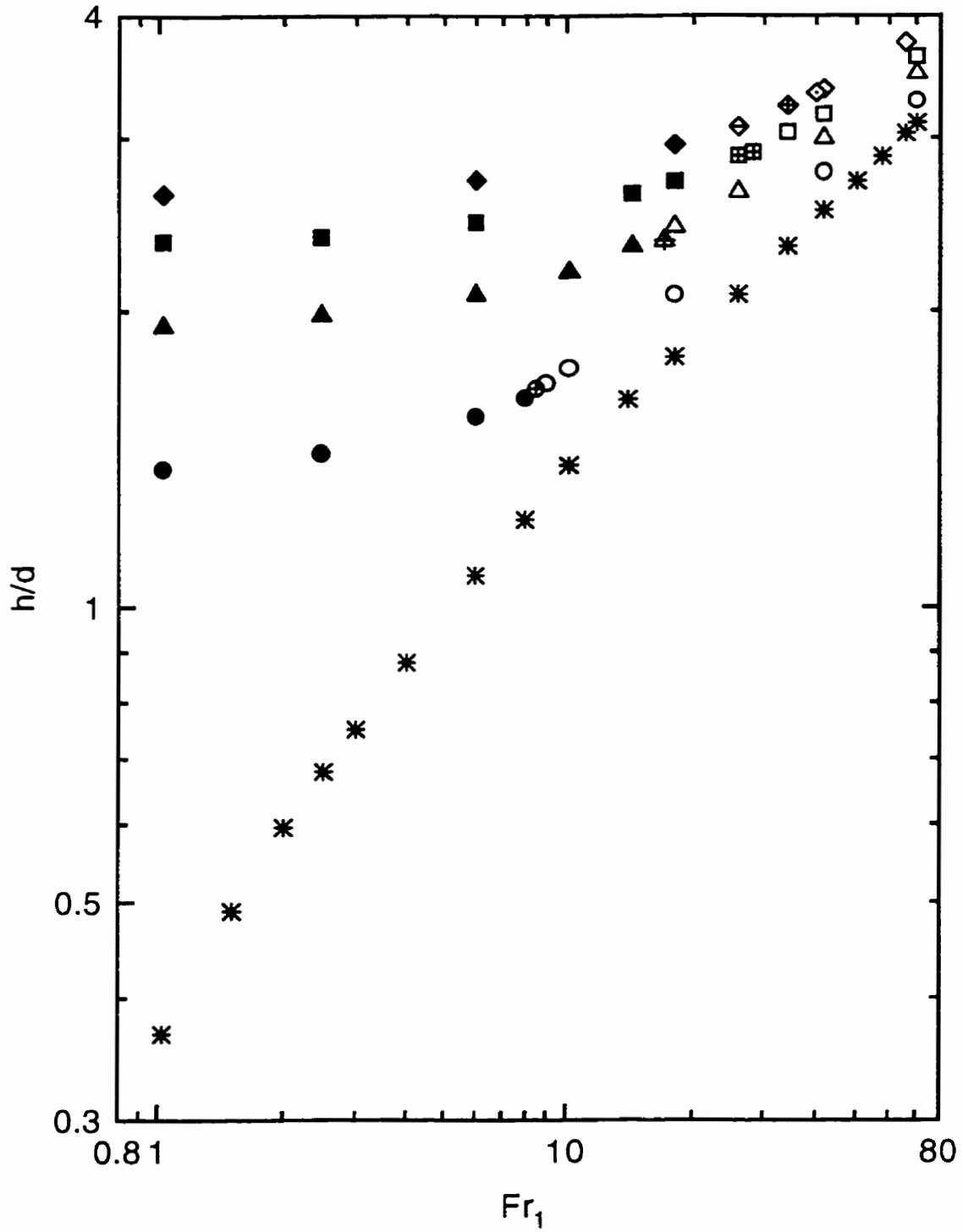

Figure 5.7: Dual-discharge gas entrainment, $l/d = 1.5$ and $\alpha = 10°$; refer to Table 5.4 for symbol notation

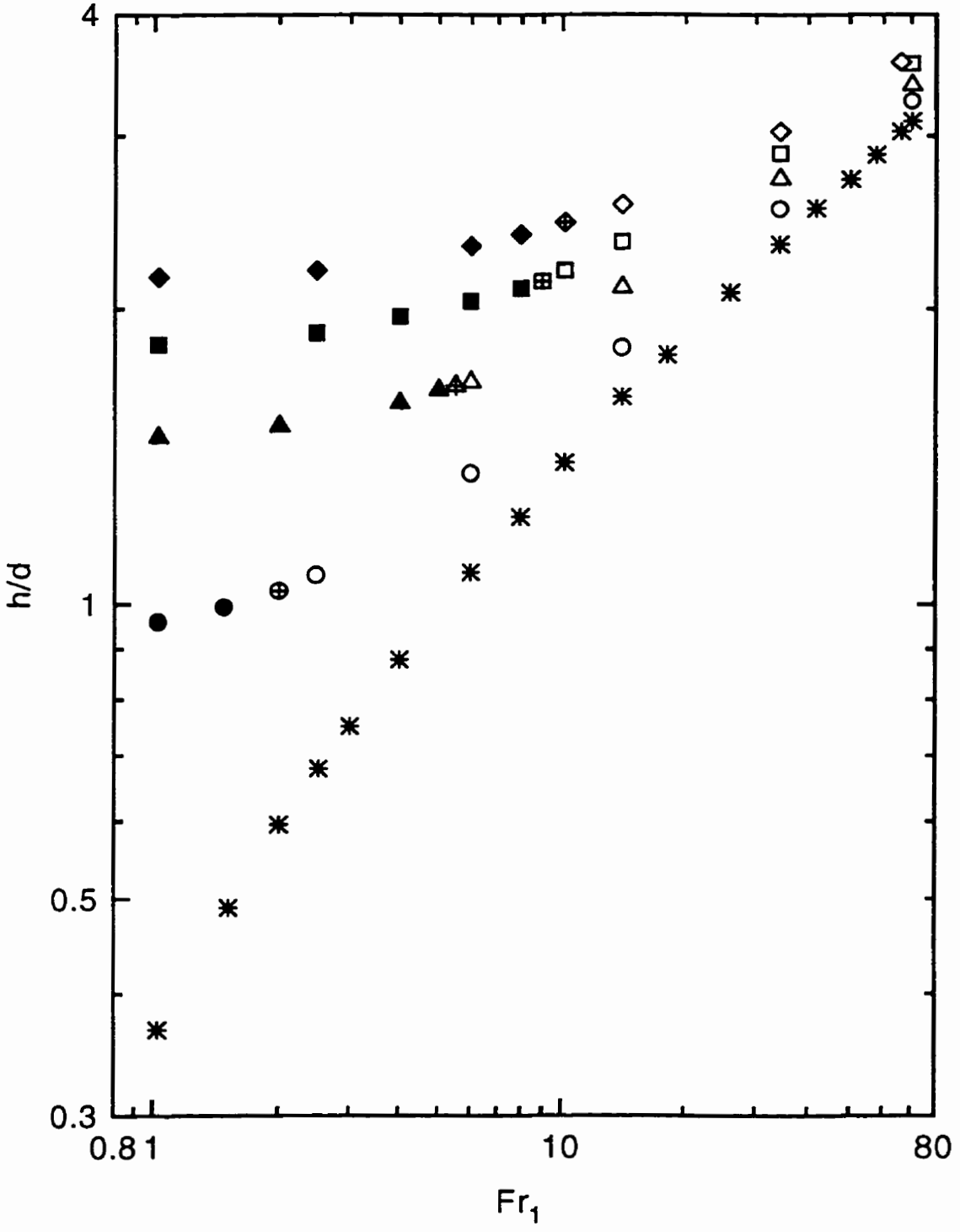

Figure 5.8: Dual-discharge gas entrainment, $l/d = 1.5$ and $\alpha = 30°$; refer to Table 5.4 for symbol notation

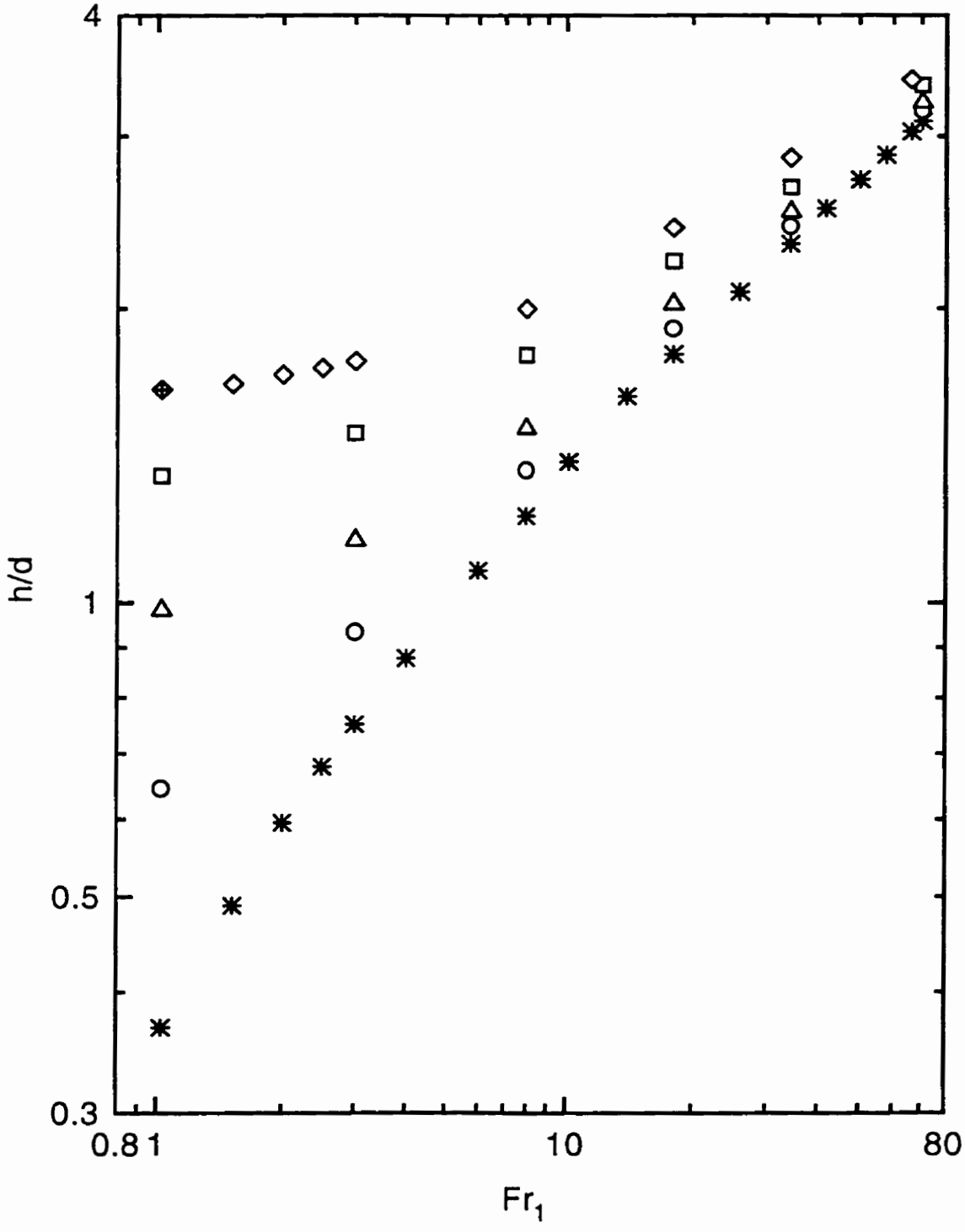

Figure 5.9: Dual-discharge gas entrainment, $l/d = 1.5$ and $\alpha = 60°$; refer to Table 5.4 for symbol notation

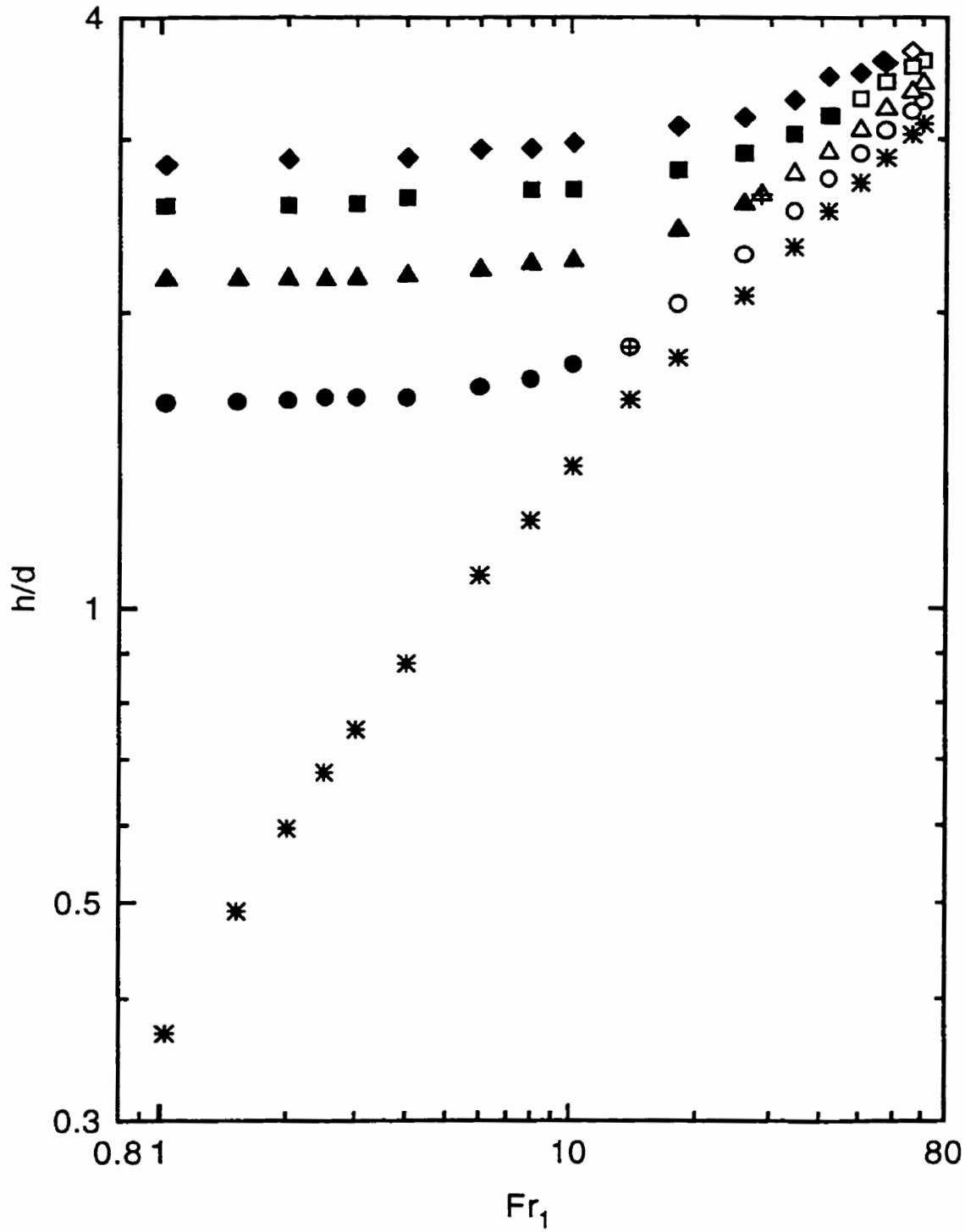

Figure 5.10: Dual-discharge gas entrainment, $l/d = 2.0$ and $\alpha = 0°$; refer to Table 5.4 for symbol notation

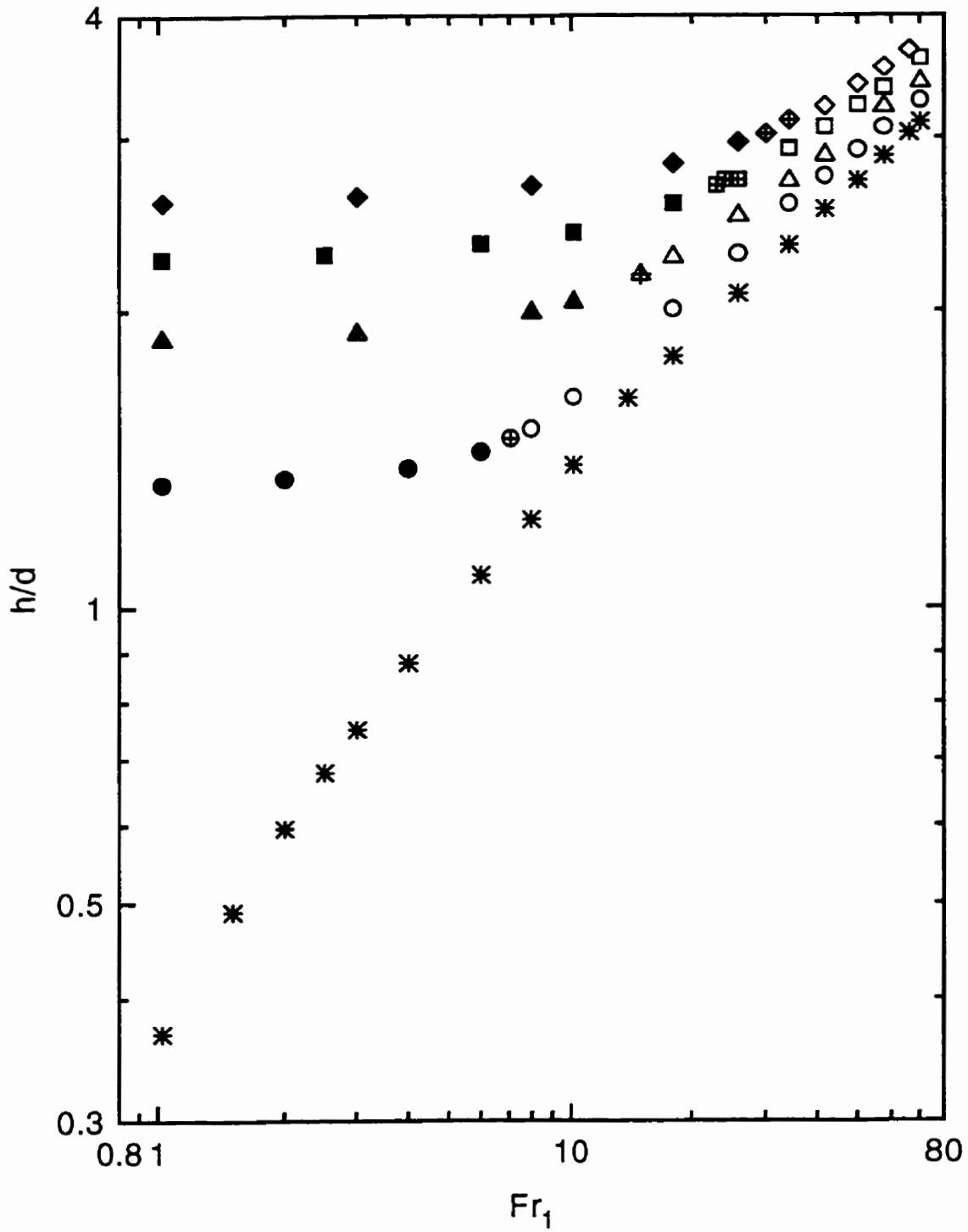

Figure 5.11: Dual-discharge gas entrainment, $l/d = 2.0$ and $\alpha = 10°$; refer to Table 5.4 for symbol notation

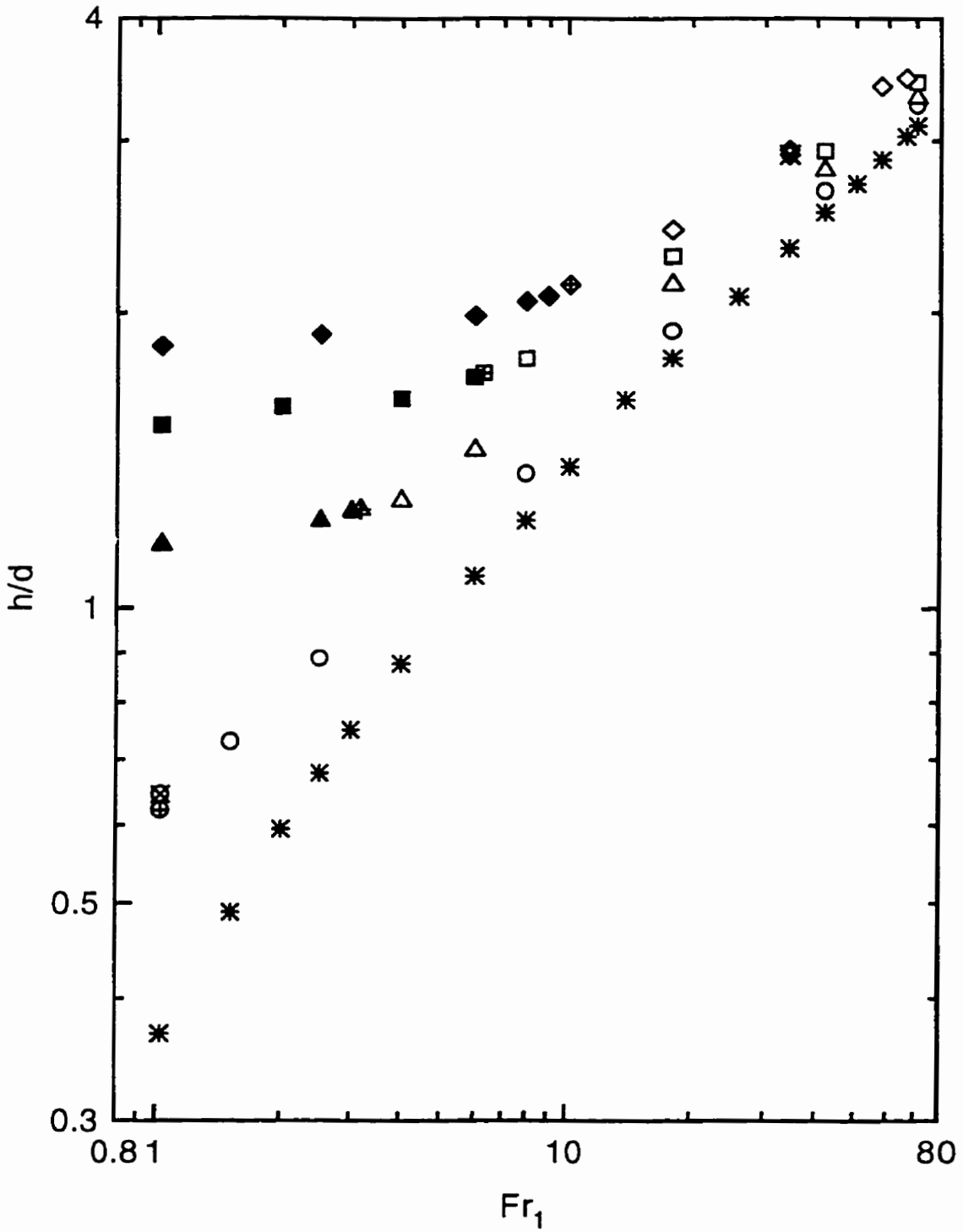

Figure 5.12: Dual-discharge gas entrainment, $l/d = 2.0$ and $\alpha = 30°$; refer to Table 5.4 for symbol notation

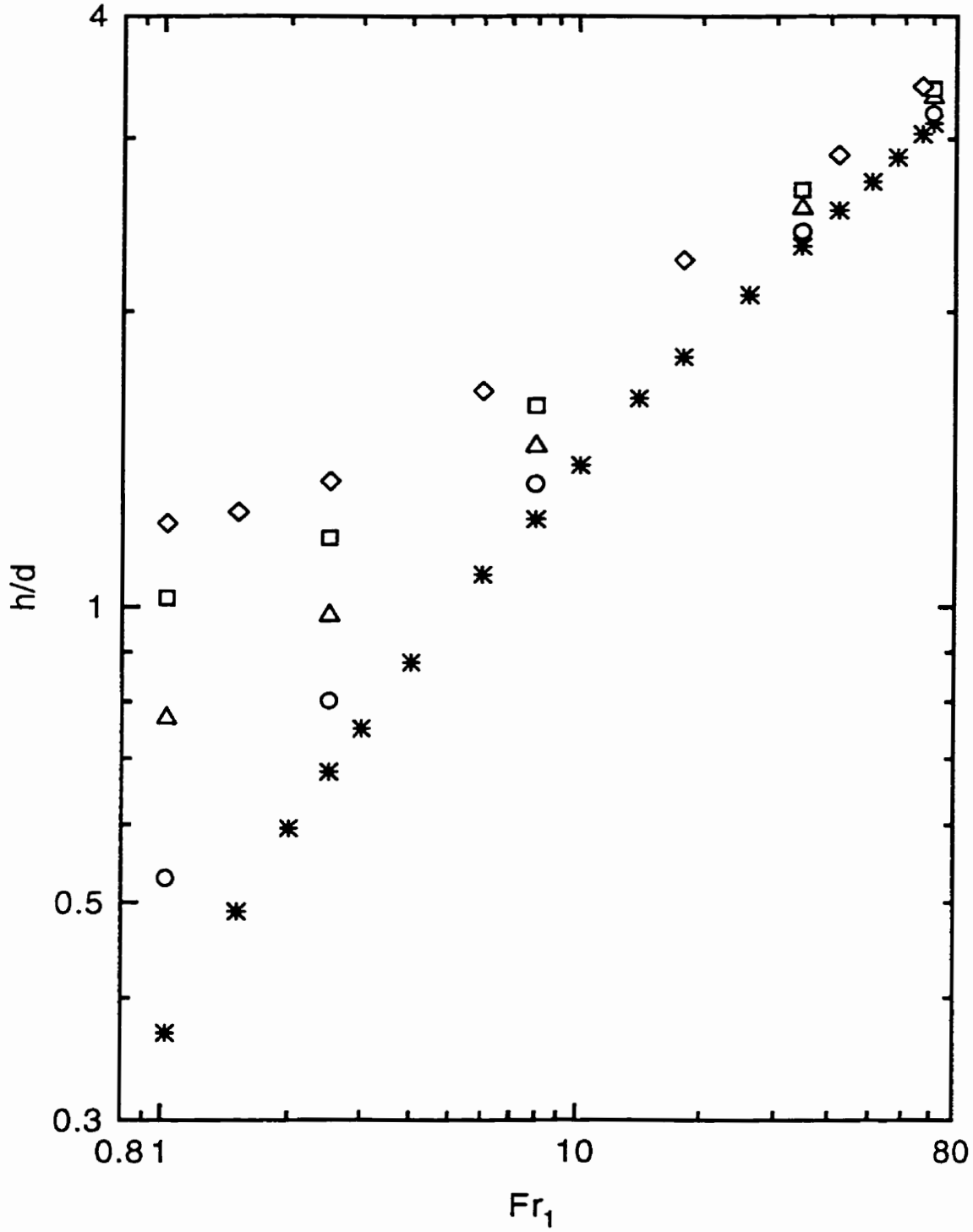

Figure 5.13: Dual-discharge gas entrainment, $l/d = 2.0$ and $\alpha = 60°$; refer to Table 5.4 for symbol notation

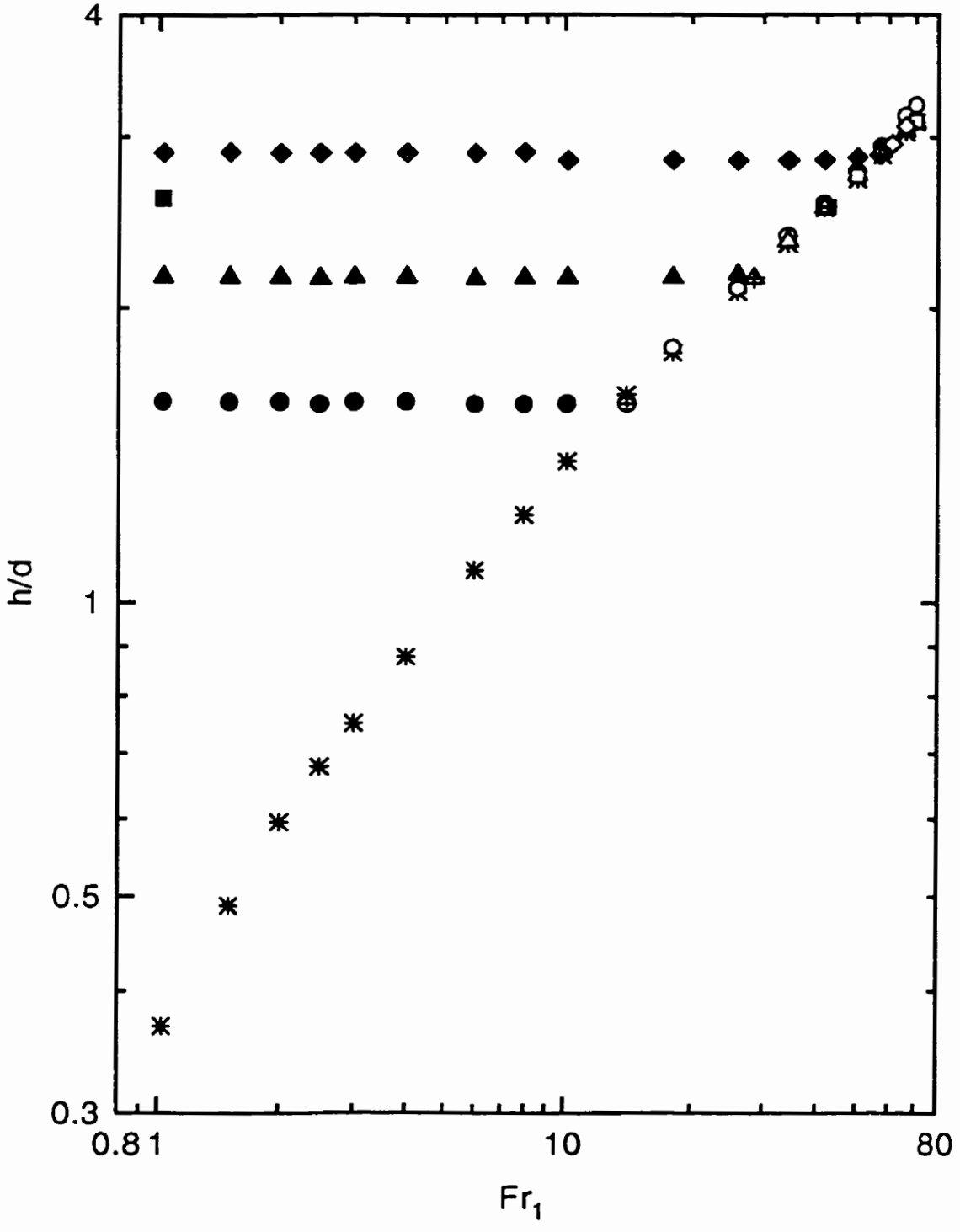

Figure 5.14: Dual-discharge gas entrainment, $l/d = 8.0$ and $\alpha = 0°$; refer to Table 5.4 for symbol notation

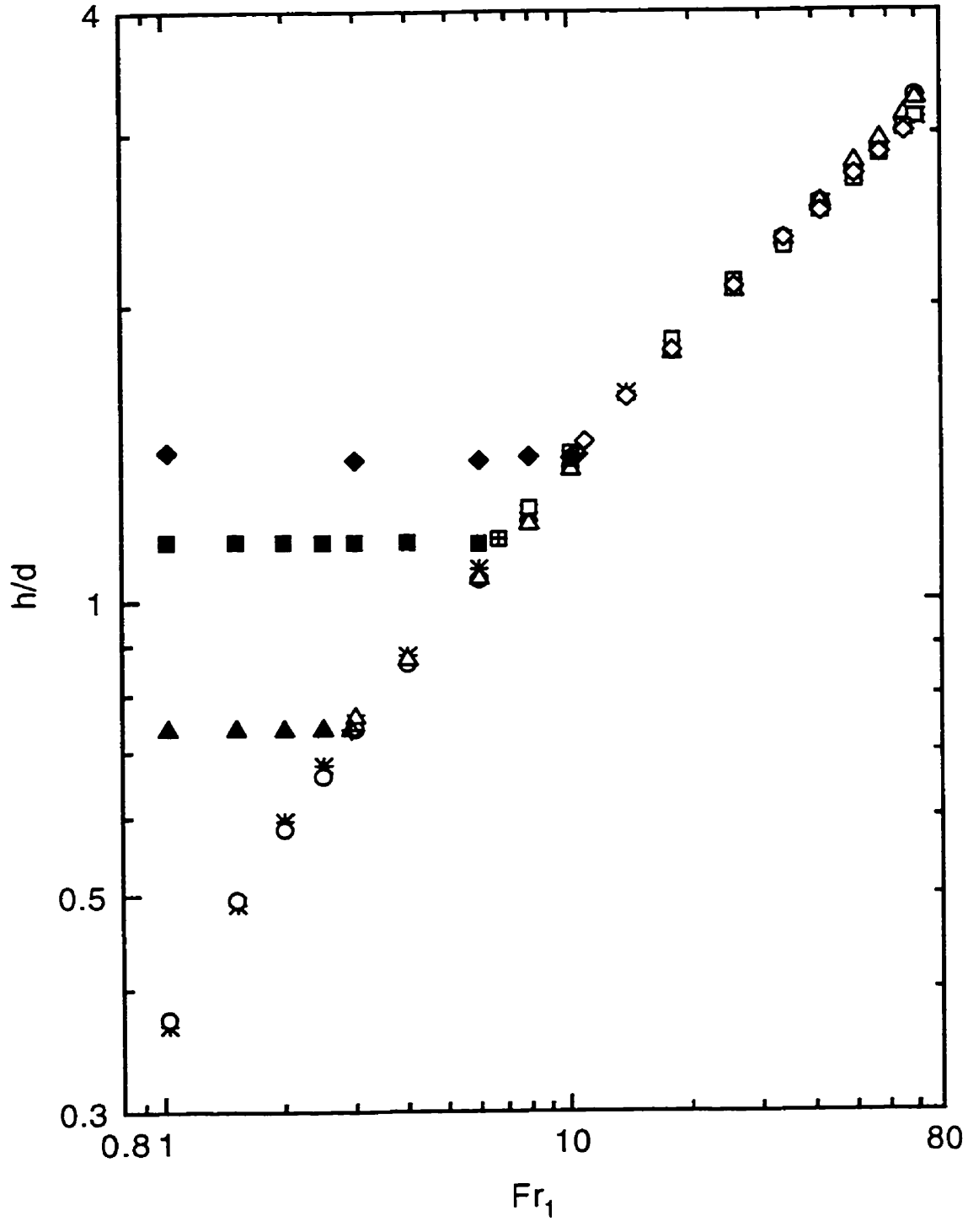

Figure 5.15: Dual-discharge gas entrainment, $l/d = 8.0$ and $\alpha = 10°$; refer to Table 5.4 for symbol notation

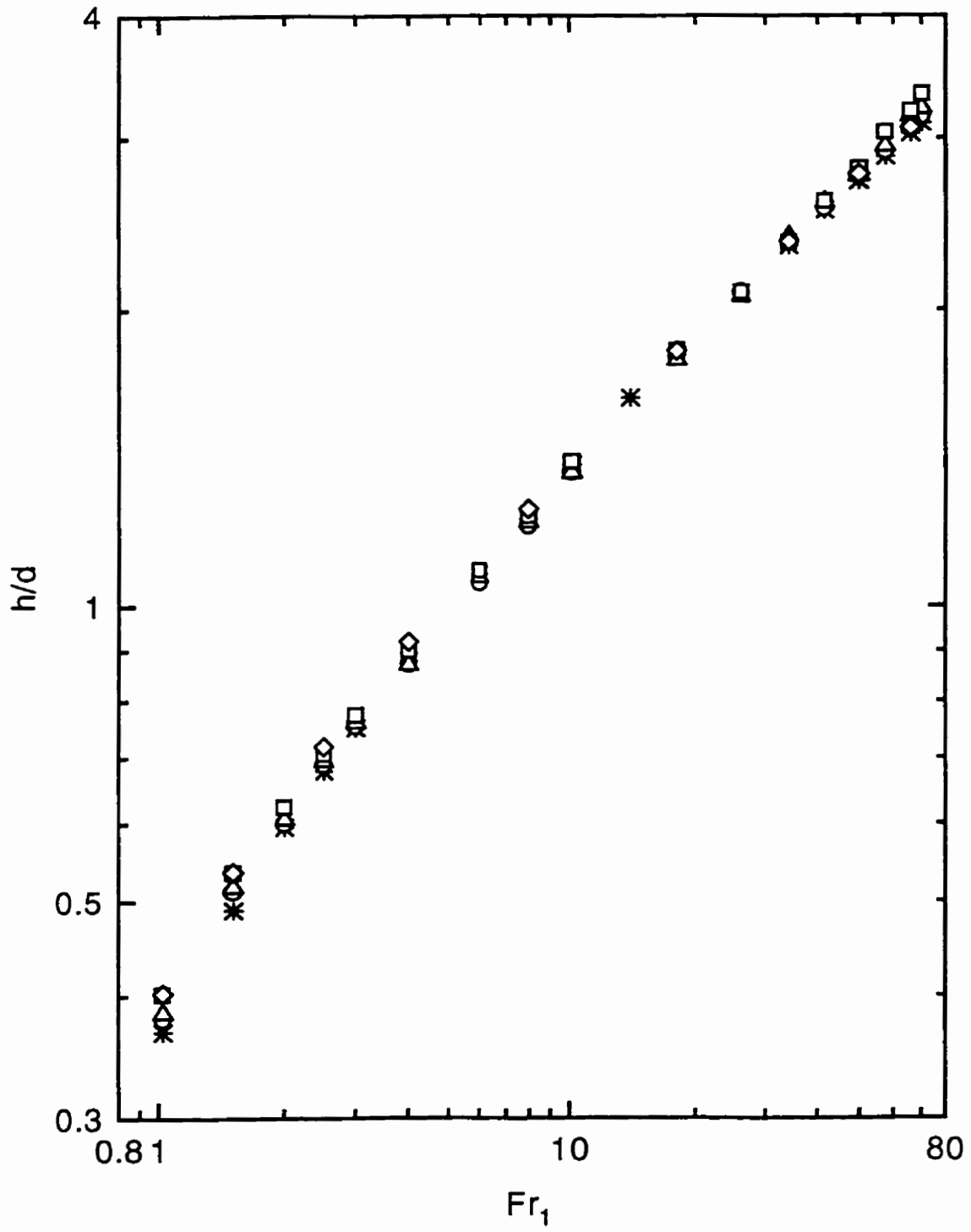

Figure 5.16: Dual-discharge gas entrainment, $l/d = 8.0$ and $\alpha = 30°$; refer to Table 5.4 for symbol notation

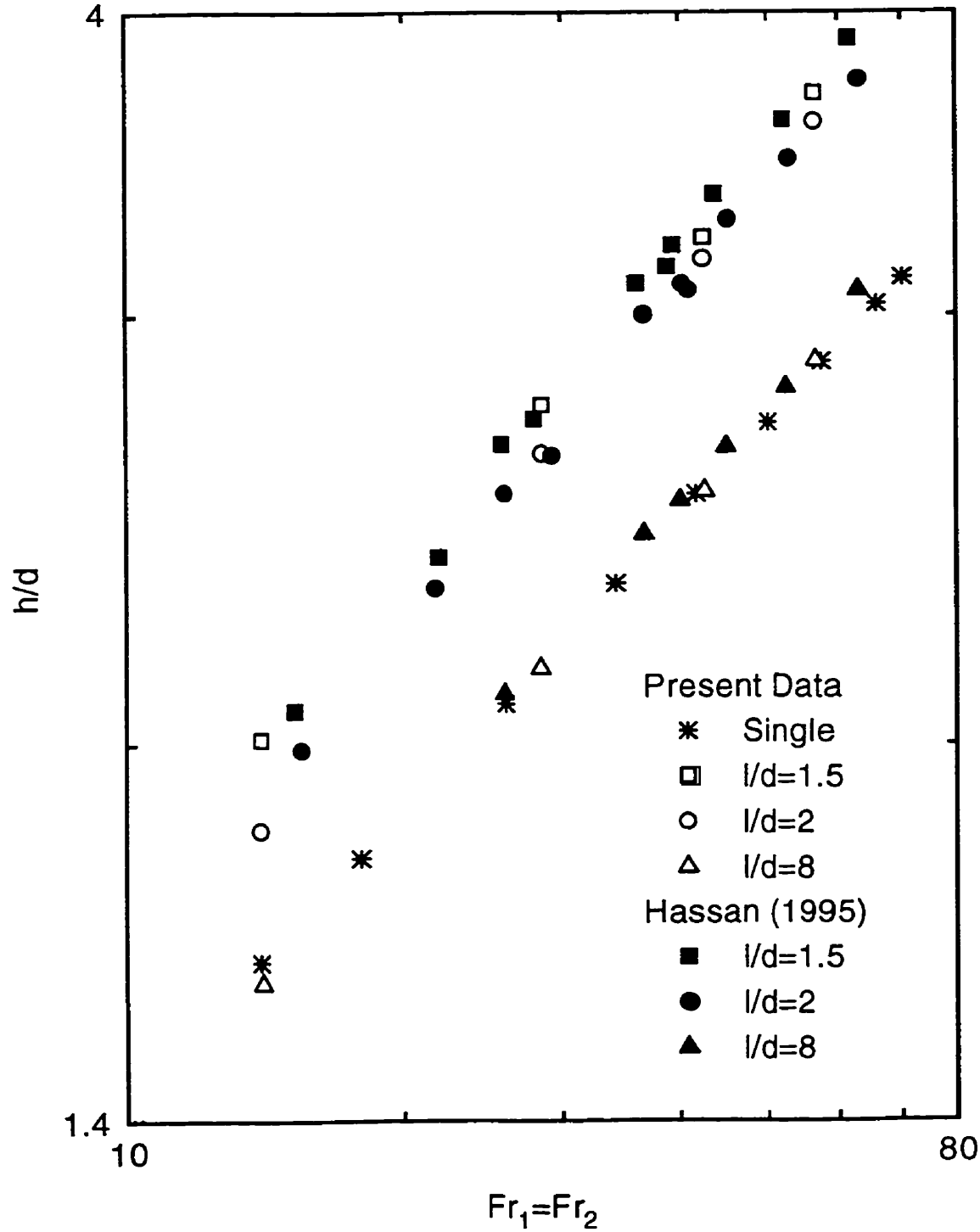

Figure 5.17: Comparison of relevant gas-entrainment results with Hassan (1995) for $Fr_1 = Fr_2$ and $\alpha = 0°$

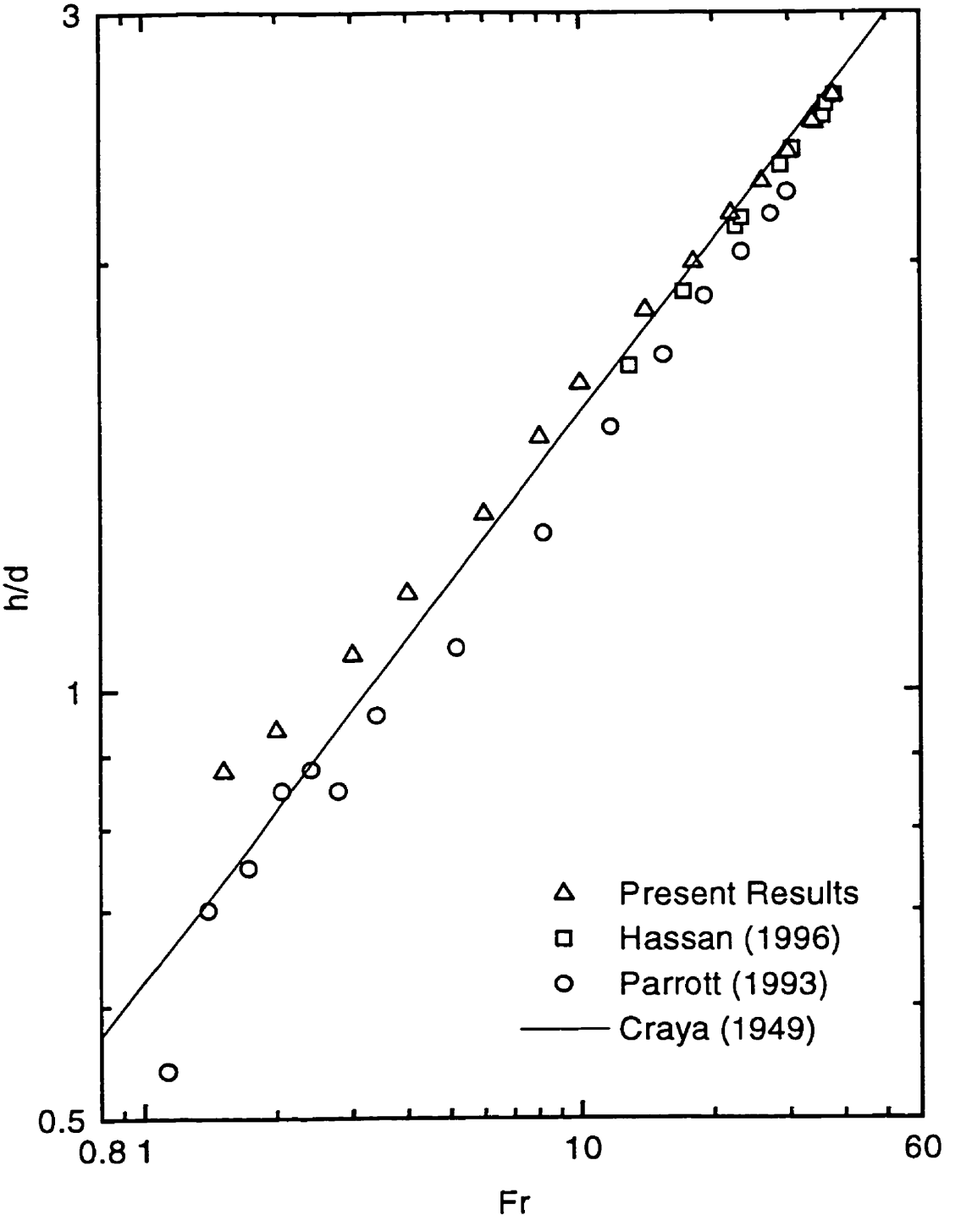

Figure 5.18: Experimental data of liquid entrainment for single discharge

Table 5.5: Liquid-entrainment-data symbols used in Figures 5.19 to 5.29

Fr_2	Symbol	Category
0.0	✱	
9.5	○	1
	⊙	2
	⊕	3
	⊖	4
	●	5
19.0	△	1
	◬	2
	▲	3
	◭	4
	▲	5
28.5	□	1
	⊡	2
	⊞	3
	⊟	4
	■	5
38.0	◇	1
	◈	2
	◆	3
	◆	4
	◆	5

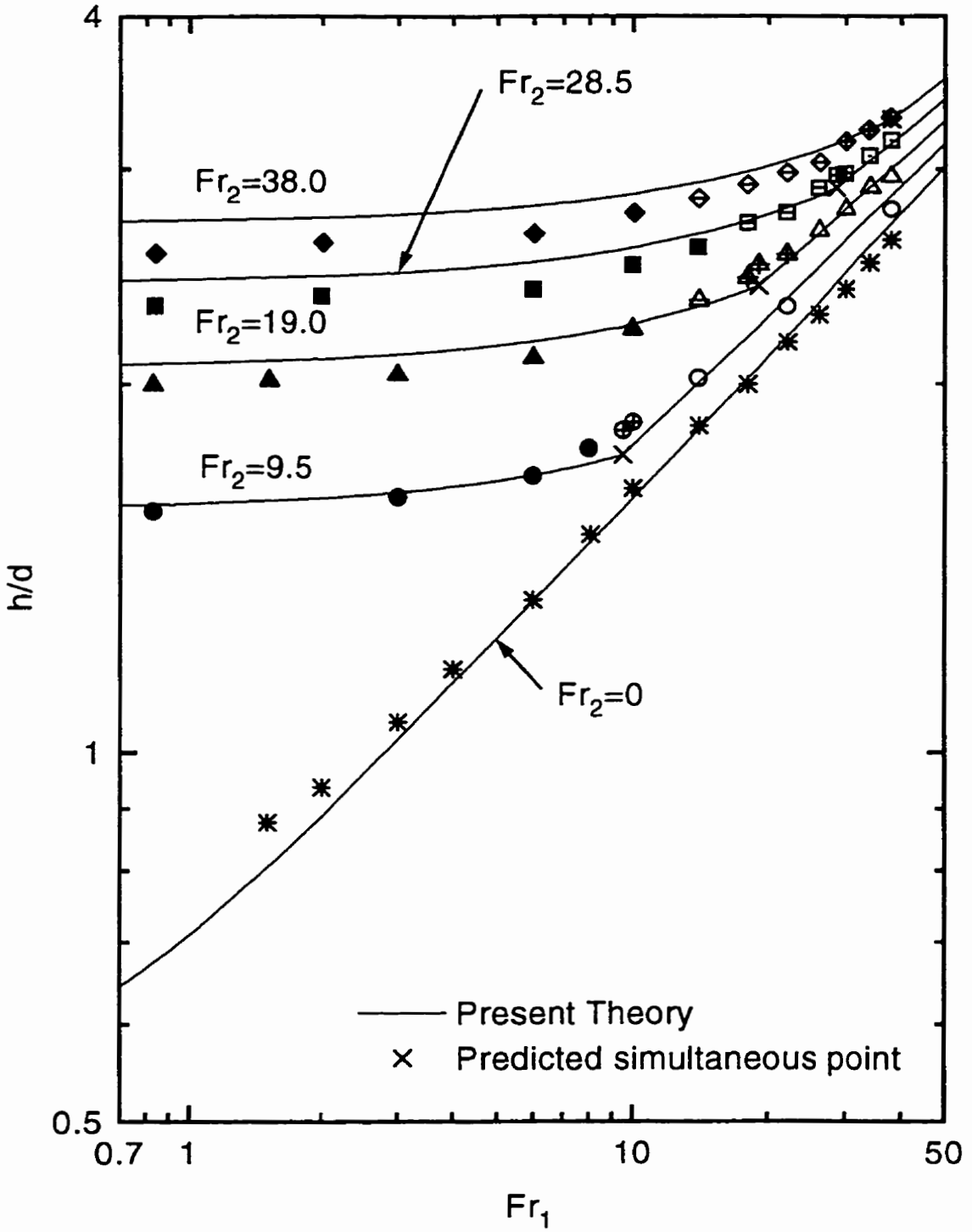

Figure 5.19: Dual-discharge liquid entrainment, $l/d = 1.5$ and $\alpha = 0°$; refer to Table 5.5 for symbol notation

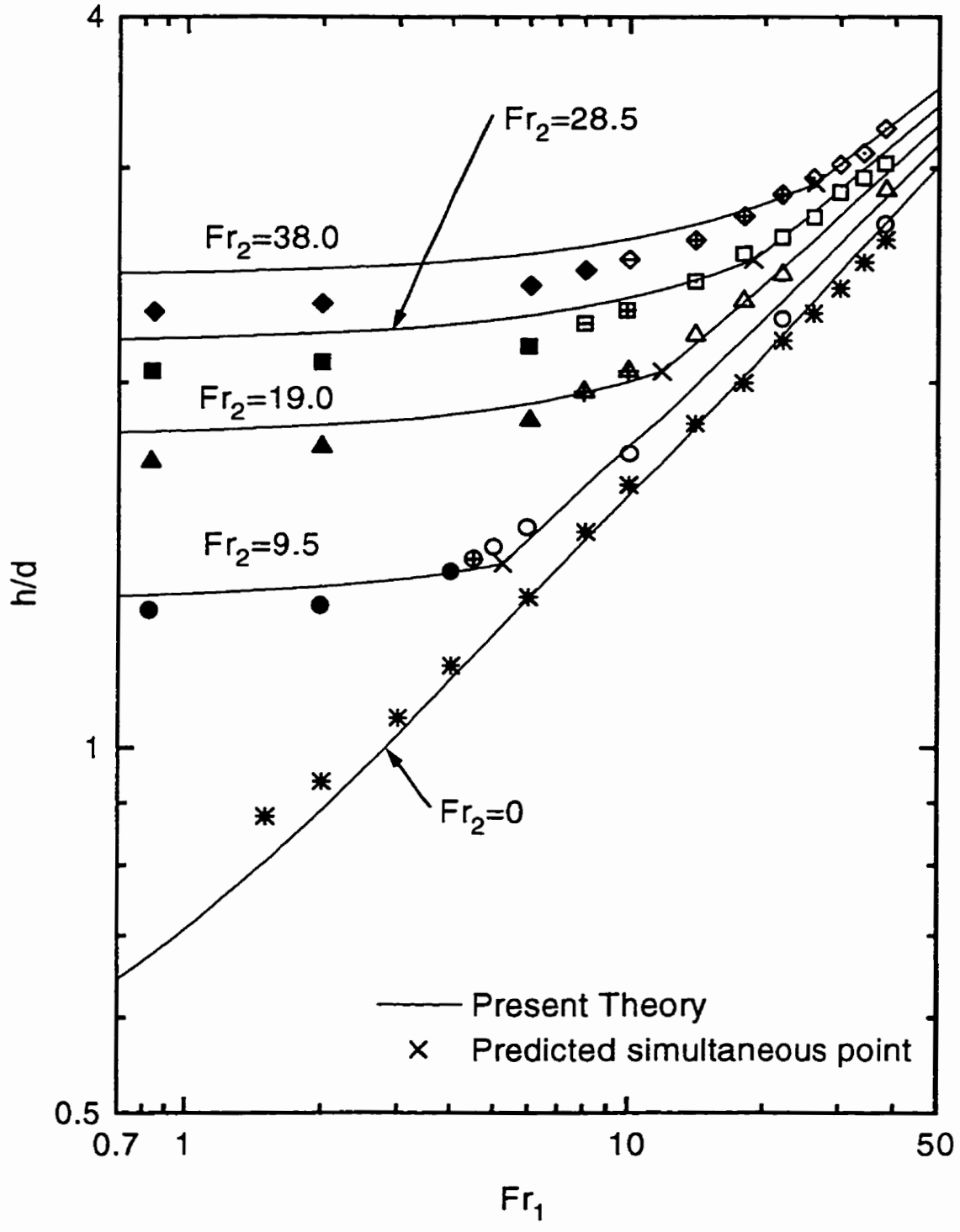

Figure 5.20: Dual-discharge liquid entrainment, $l/d = 1.5$ and $\alpha = 10°$; refer to Table 5.5 for symbol notation

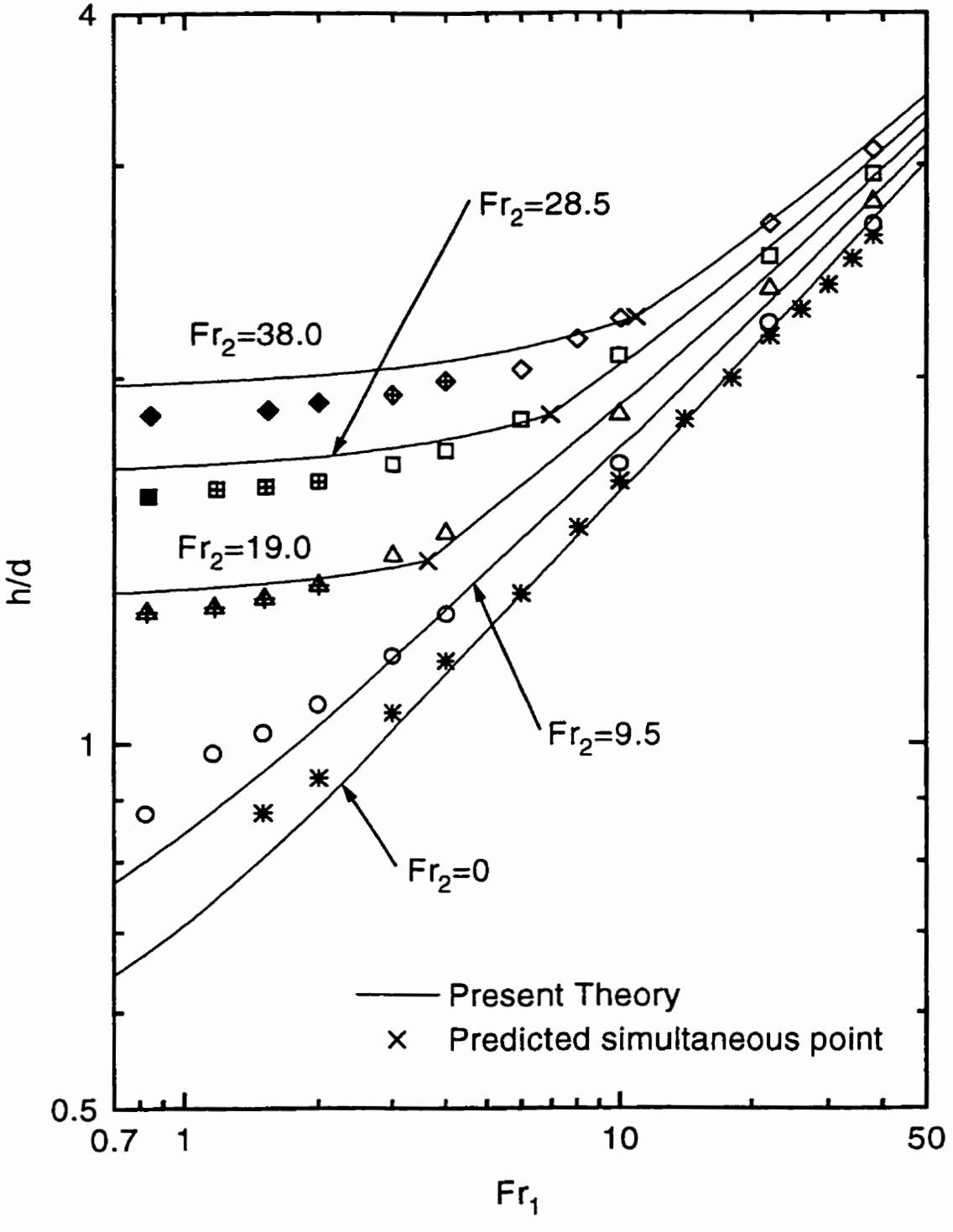

Figure 5.21: Dual-discharge liquid entrainment, $l/d = 1.5$ and $\alpha = 30°$; refer to Table 5.5 for symbol notation

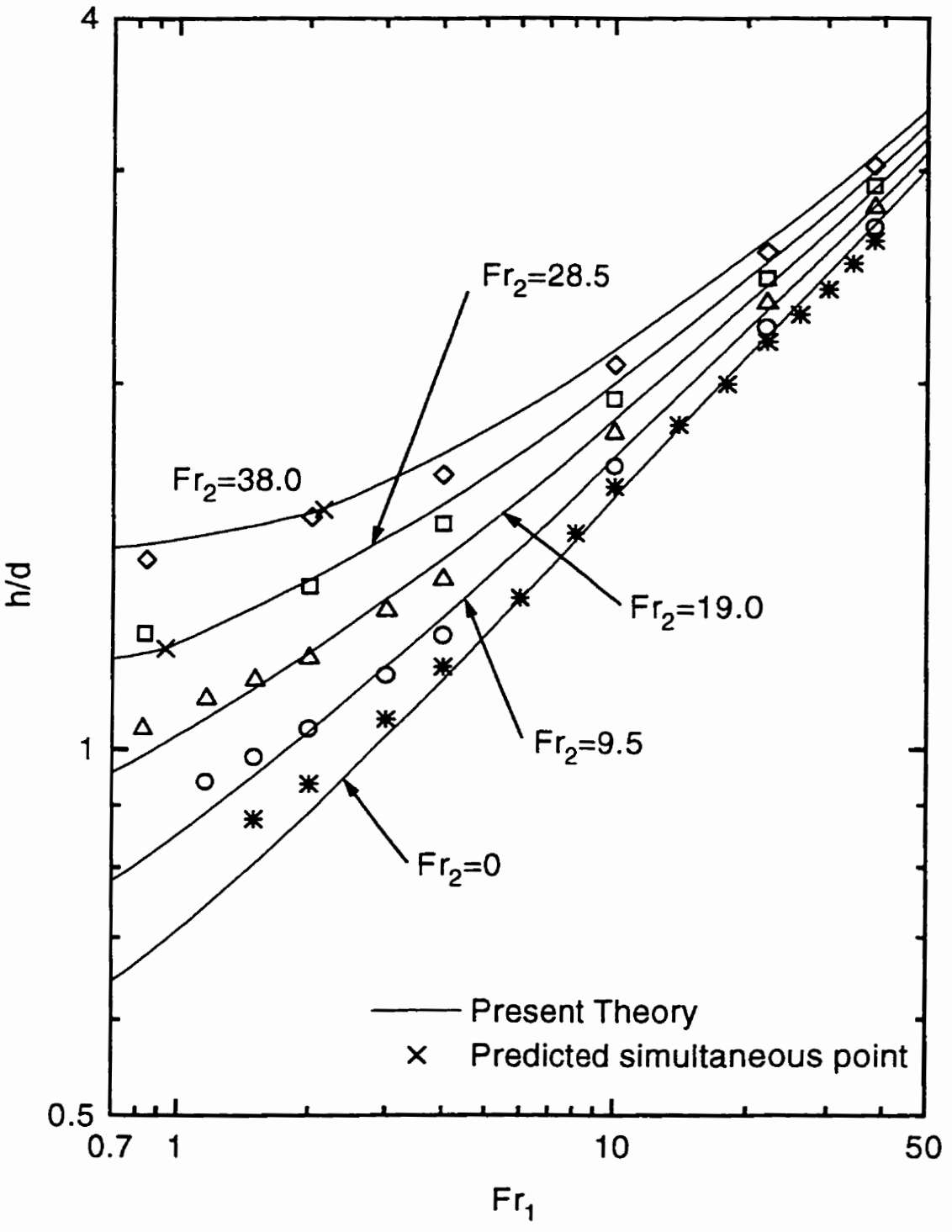

Figure 5.22: Dual-discharge liquid entrainment, $l/d = 1.5$ and $\alpha = 60°$; refer to Table 5.5 for symbol notation

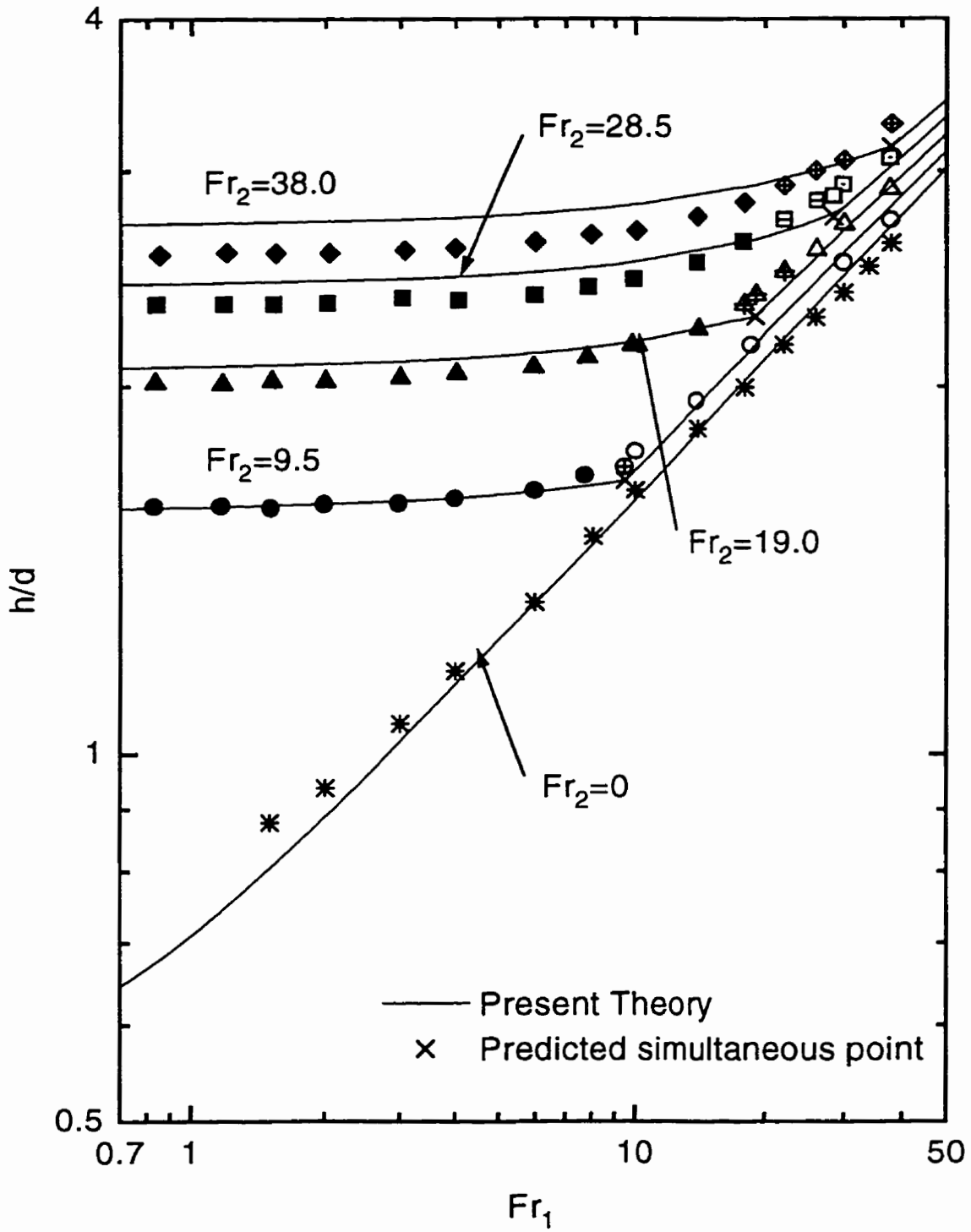

Figure 5.23: Dual-discharge liquid entrainment, $l/d = 2.0$ and $\alpha = 0°$, refer to Table 5.5 for symbol notation

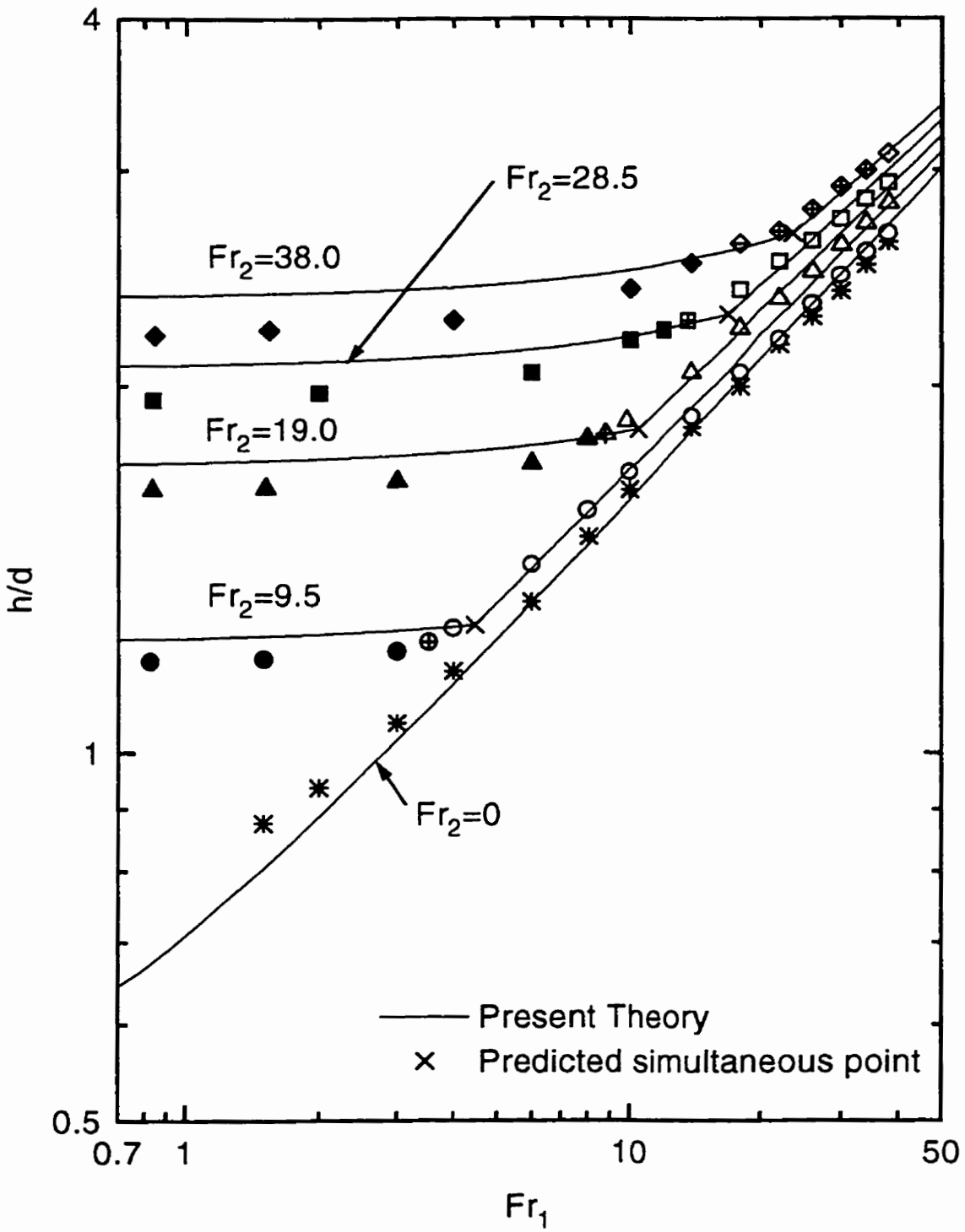

Figure 5.24: Dual-discharge liquid entrainment, $l/d = 2.0$ and $\alpha = 10°$; refer to Table 5.5 for symbol notation

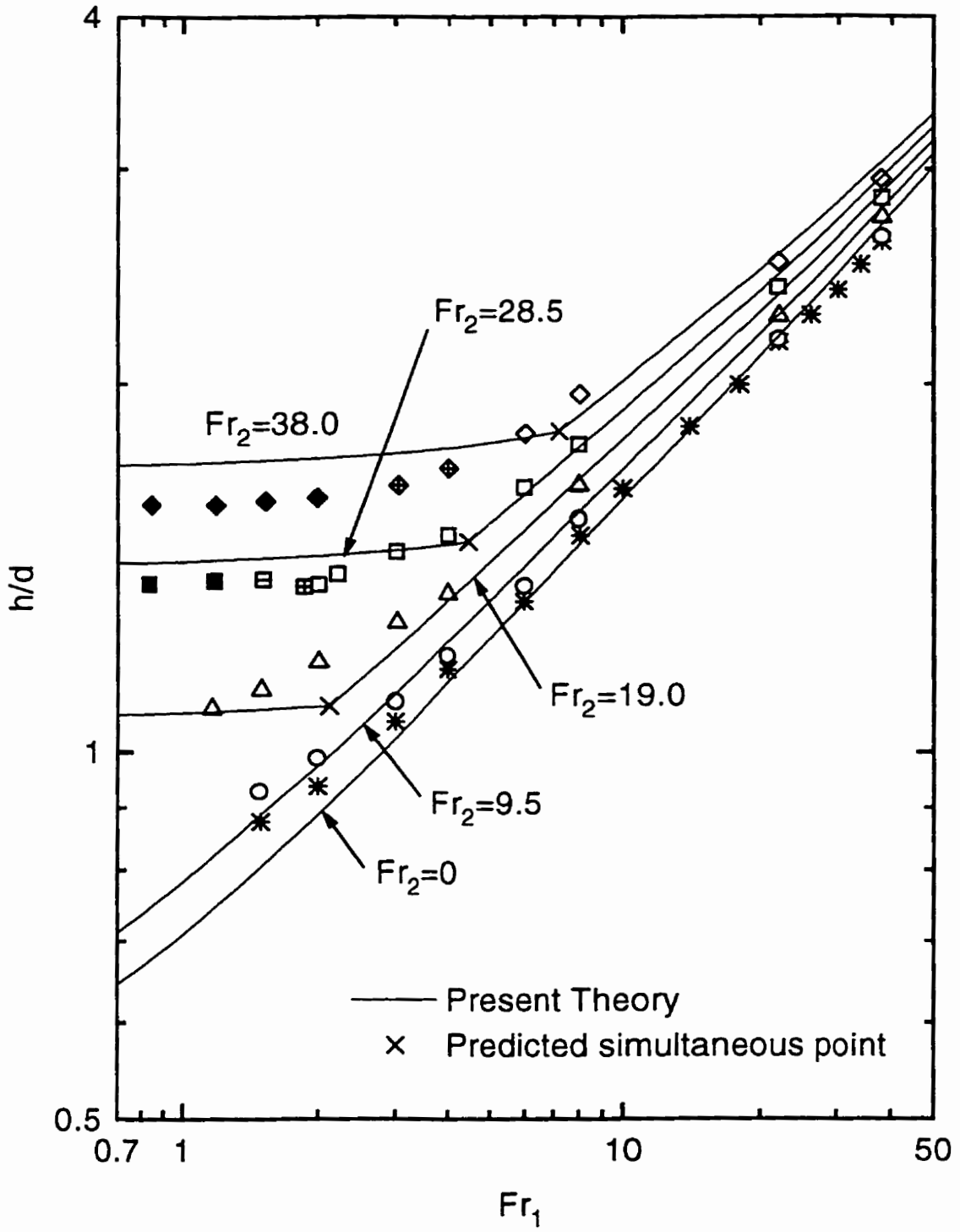

Figure 5.25: Dual-discharge liquid entrainment, $l/d = 2.0$ and $\alpha = 30°$; refer to Table 5.5 for symbol notation

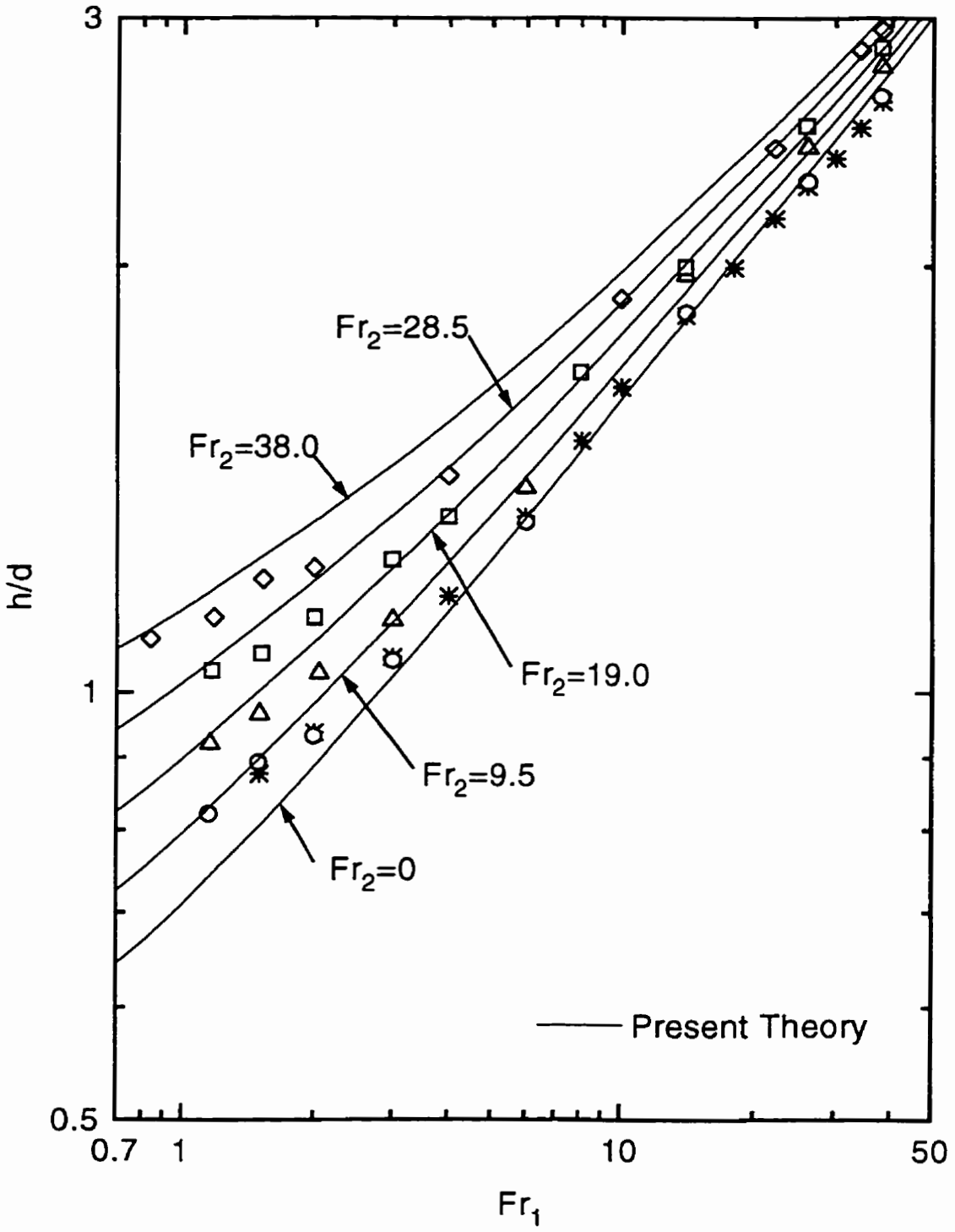

Figure 5.26: Dual-discharge liquid entrainment, $l/d = 2.0$ and $\alpha = 60°$; refer to Table 5.5 for symbol notation

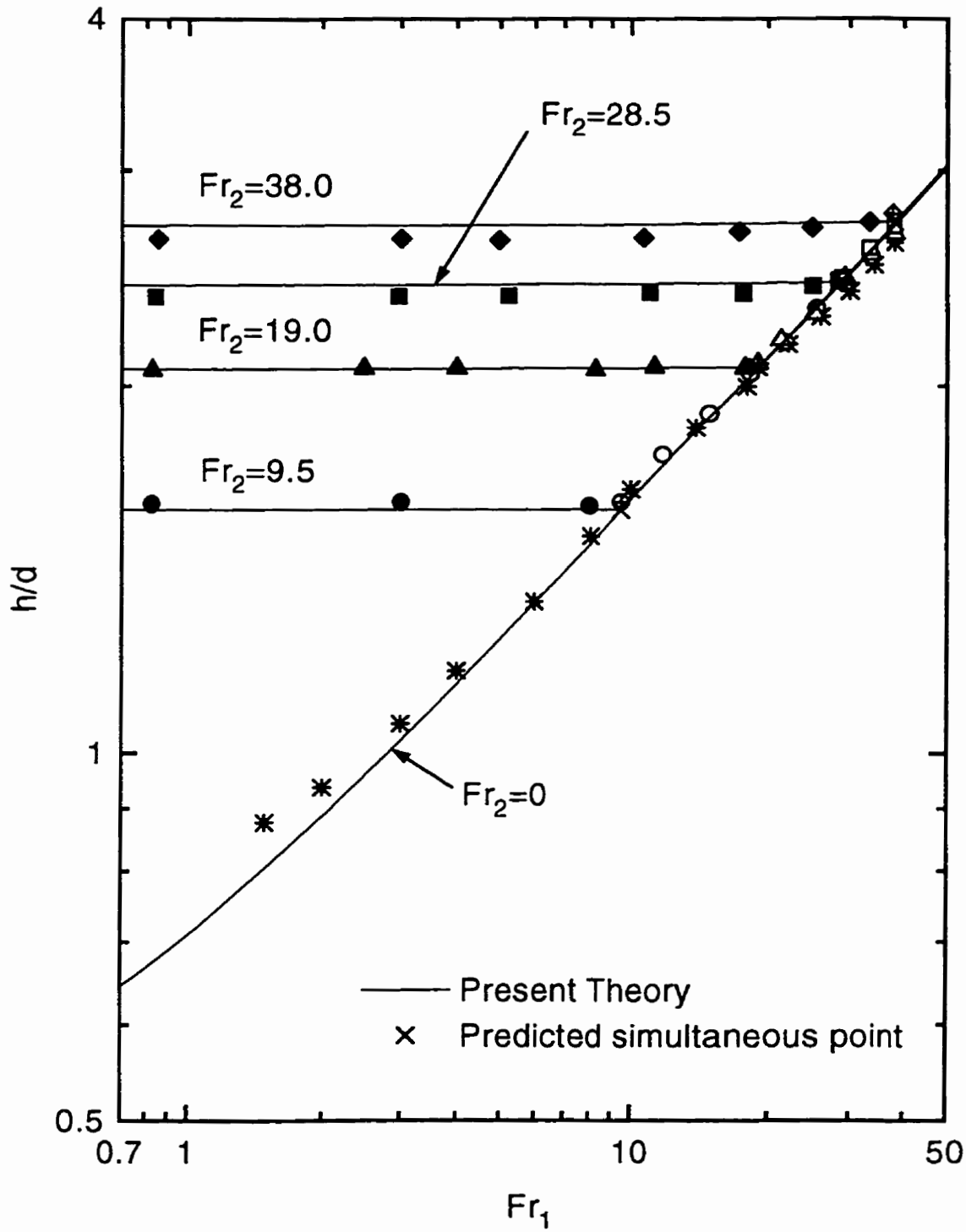

Figure 5.27: Dual-discharge liquid entrainment, $l/d = 8.0$ and $\alpha = 0°$; refer to Table 5.5 for symbol notation

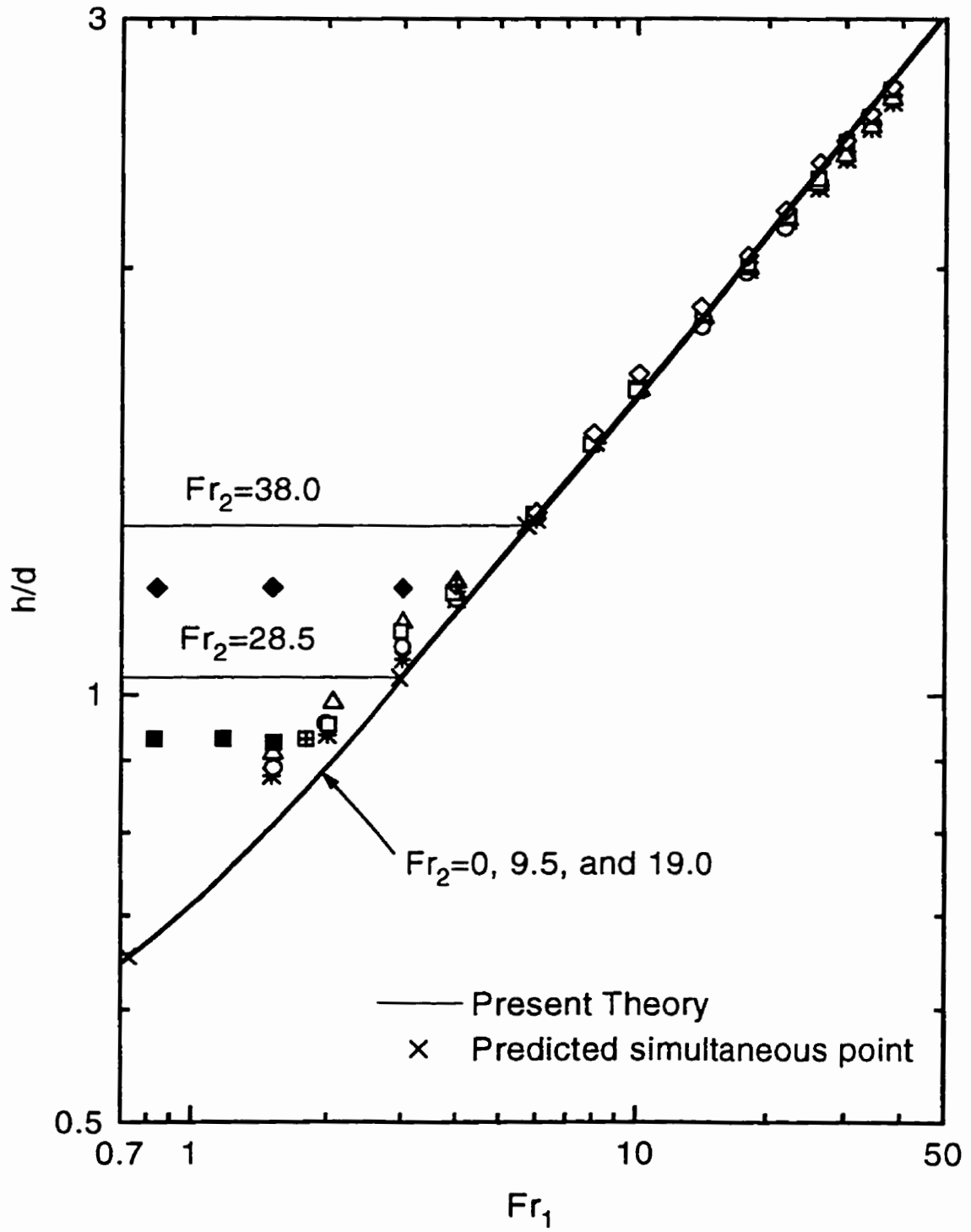

Figure 5.28: Dual-discharge liquid entrainment, $l/d = 8.0$ and $\alpha = 10°$; refer to Table 5.5 for symbol notation

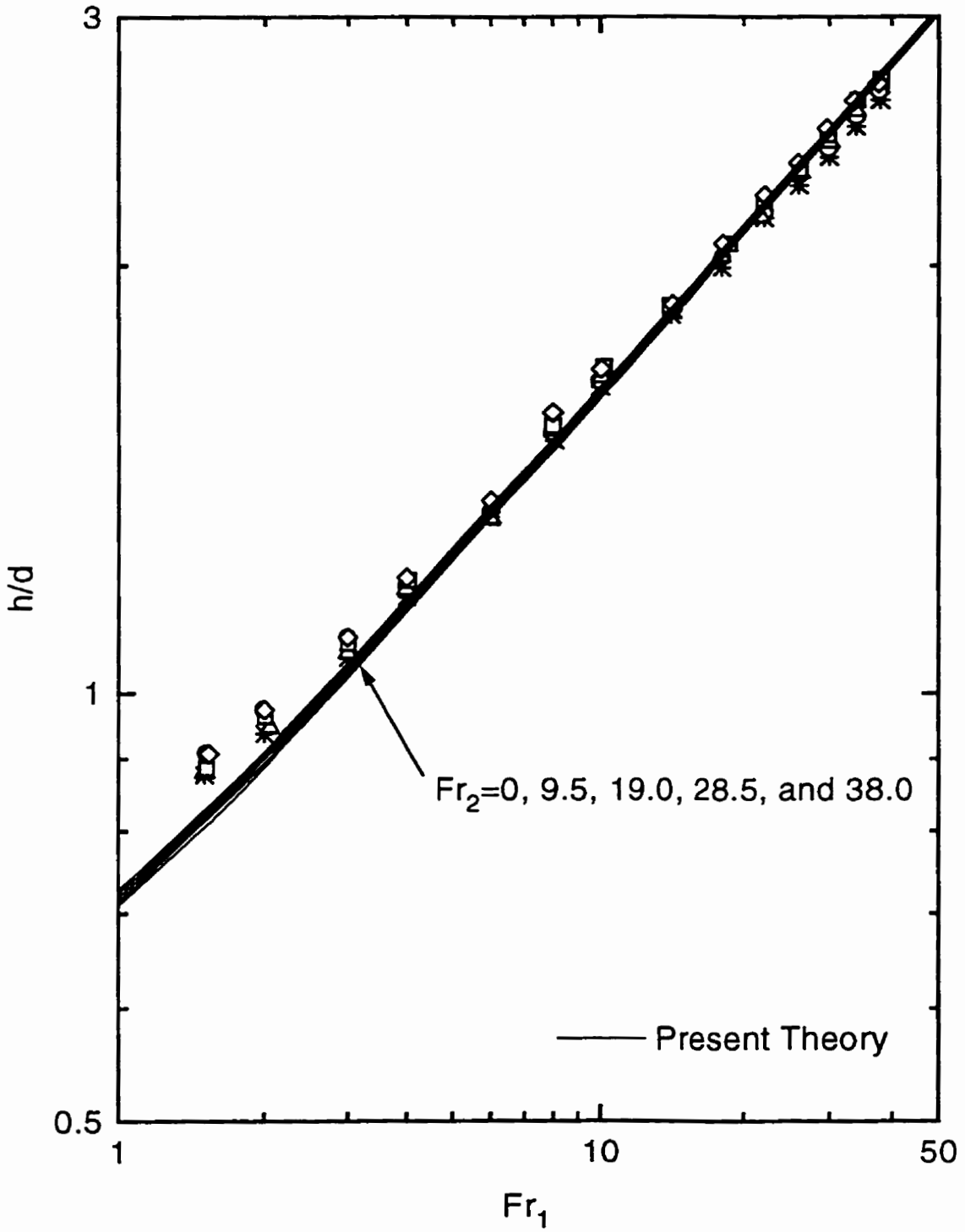

Figure 5.29: Dual-discharge liquid entrainment, $l/d = 8.0$ and $\alpha = 30°$; refer to Table 5.5 for symbol notation

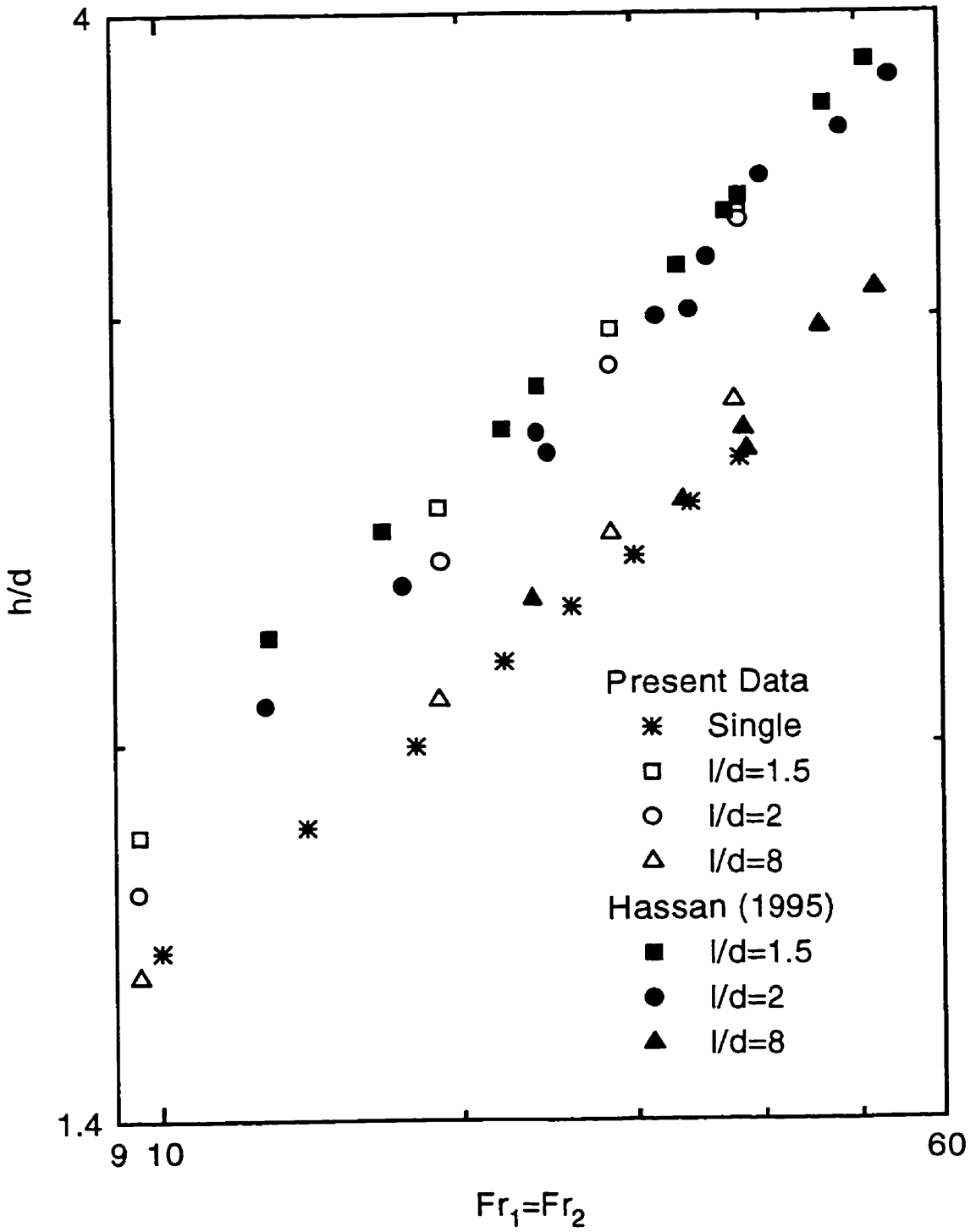

Figure 5.30: Comparison of relevant liquid-entrainment results with Hassan (1995) for $Fr_1 = Fr_2$ and $\alpha = 0$

CHAPTER 6

CONCLUSIONS AND RECOMMENDATIONS

6.1 Conclusions

Experimental data were generated for the onsets of gas and liquid entrainment for the case of two horizontal side circular branches of 6.35 mm diameter discharging from a large reservoir containing a stratified, two-phase mixture of air and water. The independent variables in the investigation included the separation distance l/d, the rate of discharge from each branch, Fr_1 and Fr_2, and the angular alignment of the branch centerlines, α. The dependent variable was the critical height at which the onset occurred, h/d, as measured from the flat, smooth air-water interface. The experimental data were collected at a test section pressure of 510 kPa for gas entrainment and 310 kPa for liquid entrainment. For both the gas and liquid entrainment investigations separation distances of l/d = 1.5, 2.0, and 8.0 were studied and angles of α = 0°, 10°, 30°, and 60° were investigated. Measurements of the critical height were taken over a wide range of Froude numbers from the branches. In addition, a theoretical investigation was conducted for the onset of liquid entrainment. A theoretical model was developed to predict the onset of liquid entrainment and sample results are presented. The following conclusions were drawn:

1. The theoretical model developed in this thesis yields a closed-form solution and can be solved using an iterative technique. The model agreed very well with existing single- and dual-discharge mathematical models as well as with the experimental data collected during this investigation. The assumptions used and the solution method are validated by the successfull comparisons with existing models and data as stated.
2. The experimental data for the onset of gas and liquid entrainment can be classified into five distinct regions.
3. Generally, the critical height increases with an increase in either Fr_1 or Fr_2. An exception to the preceding statement occurs at $l/d = 8$ when entrainment is occurring at branch 2. Then, the critical height is relatively constant. Next, generally, the critical height increases with a decrease in l/d.
4. As the angular alignment of the branches increases the critical height decreases.
5. For the covered range of operating conditions, entrainment at the secondary branch no longer occurred or was limited to very low Fr_1 for: $\alpha = 60°$ with $l/d = 1.5$ and 2.0 and for $\alpha = 30°$ with $l/d = 8.0$ for both gas and liquid entrainment.

6.2 Recommendations for Future Work

The following recommendations are suggested for future work:

1. The present work could be extended to include measurements of the mass flow rate and flow quality in each branch as the interface is lowered from the onset of gas entrainment to the onset of liquid entrainment.
2. The present work could be extended to include studying the onsets of gas and liquid entrainment for three branches with centerlines falling in an inclined plane.
3. The present work could be extended to include studying the onsets of gas and liquid entrainment using steam and water to more closely resemble industrial applications.

REFERENCES

Anderson, J. L., "Steam/Water Entrainment and Pull-Through Phenomena at a Pipe Branch", Presented at the AIChE Annual Meeting, New York, November 15-20, 1987.

Airy, G. B., "Theory of Errors of Observation", Macmillan and Company, London, England, 1879. As referenced from Kline and McClintock (1953).

Armstrong, K. F., "Theoretical Investigation of the Onset of Liquid Entrainment During Dual Discharge From Large Reservoirs", M. Sc. Thesis, University of Manitoba, 1991.

Armstrong, K. F., Parrott, S. D., Sims, G. E., Soliman, H. M. and Krishnan, V. S., "Theoretical and Experimental Study of the Onset of Liquid Entrainment During Dual Dishcharge from Large Reservoirs", International Jounal of Multiphase Flow, Vol. 18, No. 2, pp. 217-227, 1992.

Armstrong, K. F., Soliman, H. M. and Sims, G. E., "The Onset of Liquid Entrainment for a System with Two Parallel Slots", International Communications in Heat and Mass Transfer, Vol. 19, pp. 827-839, 1992.

Bateman, H., "Tables of Integral Transforms", Vol. 1, McGraw-Hill, New York, 1954.

Craya, A., "Theoretical Research on the Flow of Nonhomogeneous Fluids", La Houille Blanche, Vol. 4, pp. 44-55, Jan./Feb. 1949.

Crowley, C. J. and Rothe, P. H., "Flow Visualization and Break Mass Flow Measurements in Small Break Separate Effects Experiments", Small Break Loss-of-Coolant Accident Analysis in LWRs, Report EPRI WS-81-201, No. 4, 1981.

Daggett, L. L. and Keulegan, G. H., "Similitude in Free-Surface Vortex Formations", Journal of the Hydraulics Division, Proceedings of the ASCE, Vol. 100, No.

HYS, Aug. 1974.

Gariel, P., "Experimental Research on the Flow of Nonhomogeneous Fluids", La Houille Blanche, Vol. 4, pp. 56-64, Jan./Feb. 1949.

Hardy, P. G. and Richter, H. J., "Critical Two-Phase Flow in Small Break Loss of Coolant Accident", M. Sc. Thesis, Thayer School of Engineering, Dartmouth College, Hanover, New Hampshire, 1983.

Hassan, I. G., Soliman, H. M., Sims, G. E. and Kowalski, J. E., "Two-Phase Flow from a Large Reservoir Through a Small Side Orifice", ASME FED-Vol. 180, pp. 47-58, Presented at the ASME Fluids Engineering Summer Meeting, Lake Tahoe, Nevada, June 19-23, 1994.

Hassan, I. G., "Single, Dual and Triple Discharge From a Large Stratified, Two-Phase Region Through Small Branches", Ph.D. Thesis, University of Manitoba, 1995.

Kline, S. J. and McClintock, F. A., "Describing Uncertainties in Single-Sample Experiments", Mech. Eng., Vol. 75 pp 3-8, 1953.

Kowalski, J. E. and Krishnan, V. S., "Two-Phase Flow Distribution in a Large Manifold", AIChE Annual Meeting, New York, November 15-20, 1987.

Lubin, B. and M. Hurwitz, "Vapor Pull-Through at a Tank Drain - with and without Dielectrophoretic Baffling," Proc. Conf. Long Term Cryo-Propellant Storage in Space, NASA Marshall Space Center, Huntsville, Ala., pp. 173, October 1966.

Lubin, B. T. and Springer, G. S., "The Formation of a Dip on the Surface of a Liquid Draining from a Tank", Journal of Fluid Mechanics, Vol. 29, Part 2, pp. 385-390, 1967.

Micaelli, J. C. and Memponteil, A., "Two-Phase Flow Behaviour in a Tee-Junction - The Cathare Model", Proceedings of the Fourth International Topical Meeting on Nuclear Reactor Thermal-Hydraulics, Karlsruhe, Germany, Vol. 2, pp. 1024-1030,

October 10-13, 1989.

Parrott, S. D., Soliman, H. M., Sims, G. E. and Krishnan, V. S., "Experiments on the Onset of Gas Pull-Through During Dual Discharge from a Reservoir", International Journal of Multiphase Flow, Vol. 17, pp. 119-129, 1991.

Reimann, J. and Khan, M., "Flow Through a Small Break at the Bottom of a Large Pipe with Stratified Flow", Nuclear Science and Engineering, Vol. 88, pp. 297-310, 1984.

Reimann, J. and Smoglie, C., "Flow Through a Small Pipe at the Top of a Large Pipe with Stratified Flow", Annual Meeting of the European Two-Phase Flow Group, Zurich, Switzerland, June 14-16, 1983.

Rouse, H., "Seven Exploratory Studies in Hydraulics", Proceedings ASCE, Journal of the Hydraulics Division, Vol. 82, Paper No. 1038, 1956.

Schrock, V. E., Revankar, S. T., Mannheimer, R., Wang, C. H., and Jia, D., "Steam-Water Critical Flow Through Small Pipes From Stratified Upstream Regions", Proceedings of the Eighth International Heat Transfer Conference, San Fransico, California, Vol. 5, pp. 2307-2311, August 17-22, 1986.

Smoglie, C. and Reimann, J., "Two-Phase Flow Through Small Branches in a Horizontal Pipe with Stratified Flow", International Journal of Multiphase Flow, Vol. 12, pp. 609-625, 1986.

Soliman, H. M. and Sims, G. E., "Theoretical Analysis of the Onset of Liquid Entrainment for Slots of Finite Width", International Journal of Heat and Fluid Flow, Vol. 12, No. 4, December 1991.

Soliman, H. M. and Sims, G. E., "Theoretical Analysis of the Onset of Liquid Entrainment for Orifices of Finite Diameter", International Journal of Multiphase Flow, Vol. 18, No. 2, pp. 229-235, 1992.

Yonomoto, T. and Tasaka, K., "New Theoretical Model for Two-Phase Flow Discharged from Stratified Two-Phase Region through Small Break", Journal of Nuclear Science and Technology, Vol. 25, No. 5, pp. 441-455, May 1988.

Yonomoto, T. and Tasaka, K., "Liquid and Gas Entrainment to a Small Break Hole from a Statified Two-Phase Region", International Journal of Multiphase Flow, Vol. 17, No. 6, pp. 745-765, 1991.

Zill, D.G., "Differential Equations with Boundary-Value Problems", 2nd Edition, PWS-KENT Publishing Company, 1989.

Zuber, N., "Problems in Modeling of Small Break LOCA", U.S. Nuclear Regulatory Commission, Report NUREG-0724, October 1980.

APPENDIX A

INSTRUMENT CALIBRATION

A.1 Test-Section Pressure Gauge

A Bourdon gauge was used to measure the test section pressure during the experiment. The gauge was calibrated over its entire range, 5 to 100 *psig* (34.47 to 689.46 kPa) using a dead-weight tester. Pressures were imposed by adding weights in 5 *psi* increments. The actual pressure and the pressure reading given by the Bourdon gauge were recorded. After loading to maximum pressure, the weights were removed in 5 *psi* decrements. The gauge showed little hysteresis. The average of the gauge readings was then correlated with the actual pressure. Equation (A.1) shows the results.

$$P_{act} = 0.054 + 0.995 P_g \tag{A.1}$$

A.2 Differential-Pressure Transducer

A Rosemount model 1151 DP pressure transducer was used in the experiment to measure the interface level in the test section. The pressure transducer was calibrated against a micromanometer. The micromanometer had a range of 0 to 254 mm of water pressure and the reading was distinguishable to 0.1 mm of water pressure. The zero point of the transducer was elevated so that the range would span the interface level in the test section. The zero point was adjusted to a 2 V offset by imposing a calibration height of water, D_{cal}, in the high side of the transducer. The high pressure

sides of the transducer and the micromanometer were connected to a common line that was connected to a pressure source. The low pressure sides were connected to a common line that was open to atmosphere. The pressure source was used to apply pressure in 50 mm increments as read by the micromanometer. A digital voltmeter with a resolution of 1 mV was used to record the pressure transducer reading. After loading to maximum pressure, the pressure was decremented in 50 mm of water. The values as read by the digital voltmeter were averaged and then correlated with the micromanometer pressure. Equation (A.2) shows the results.

$$P_{act} = -70.181 + 35.052DPT - 0.006DPT^2 \tag{A.2}$$

A.3 Flow-Meter Calibration

The experimental apparatus used in the present investigation was calibrated during a previous study. Therefore, it was decided to check the calibration of the flow meters against the existing calibration correlations and manufacturer's data (when available). It was found that all flow meters were still characterized by the existing calibration correlations and that recalibration was not necessary.

A.3.1 Water-Flow Meters

The calibration of all water flow meters was checked by flowing a mass of water through each flow meter over a period of time. The water was collected in a weigh tank and the collection time ranged from 5 to 30 minutes. Each flow meter was calibrated between 10 and 100 percent of full scale. The float remained steady for all points. The flow rates were then compared to existing correlations and manufacturer's data. Table A.1 provides the correlations used for each flow meter. The correlations

given are the same as the exiting correlations from previous studies and the intent was to check that they still held for the equipment.

Table A.1: Water-flow-meter correlations

Flow Meter	Correlation, kg/min
Wa1	$\dot{m} = 0.15379 \times 10^{-3} SCALE^2 + 0.38669 SCALE + 1.1342$
Wa2	$\dot{m} = 0.32993 \times 10^{-4} SCALE^2 + 0.34602 \times 10^{-1} SCALE + 0.16278$
Wb1	$\dot{m} = 0.25086 \times 10^{-4} SCALE^2 + 0.391 SCALE + 1.2593$
Wb2	$\dot{m} = 0.41932 \times 10^{-4} SCALE^2 + 0.3411 \times 10^{-1} SCALE + 0.13792$

Table A.2 shows the scale reading and the corresponding flow rate obtained for flow meters Wa1 and Wb1. For flow meters Wa1 and Wb1, manufacturer's data were available for comparison and the results are shown. Table A.3 shows the scale reading and the corresponding flow rate obtained for flow meters Wa2 and Wb2. For flow meters Wa2 and Wb2, comparison was made to the existing correlations given in Table A.1.

Table A.2: Calibration results of the large water flow meters

% Scale	Flow Rate, l/min		Manufacturer	% Difference	
	Wa1	Wb1	l/min	Wa1	Wb1
20	9.05	9.20	8.97	1.19	2.53
40	17.22	17.30	16.96	1.57	1.96
60	24.83	24.98	24.95	-0.53	0.1

80	33.16	32.82	32.97	-0.61	-0.42
100	41.75	41.11	40.96	1.92	0.38

Table A.3: Calibration results of the small water flow meters

% Scale	Flow Rate, l/min		% Difference	
	Wa2	Wb2	Wa2	Wb2
20	0.87	0.87	1.26	3.3
40	1.59	1.59	-0.42	1.16
60	2.35	2.35	-0.21	0.89
80	3.18	3.14	0.54	0.62

A.3.2 Air-Flow Meters

The calibration of all air flow meters was checked using by a combination of two wet test meters and two venturi meters. Both wet test meters were manufactured by Elster Mainz and had maximum capacities of 10 and 250 $SLPM$. The venturi meters were manufactured by Fox Valve Development Corp. and had throat diameters equal to 9.525 and 16.51 mm. Table A.4 provides the correlations used.

Table A.4: Air-flow meter-correlations

Flow Meter	Correlation, $SLPM$
Aa1	$\dot{Q} = 0.56422 \times 10^{1} + 0.11299 \times 10^{2} SCALE + 0.19309 \times 10^{-1} SCALE^{2}$
Aa2	$\dot{Q} = 0.37145 \times 10^{1} + 0.15702 \times 10^{1} SCALE + 0.1493 \times 10^{-2} SCALE^{2}$
Ab1	$\dot{Q} = 0.24863 \times 10^{2} + 0.11049 \times 10^{2} SCALE + 0.2289 \times 10^{-1} SCALE^{2}$
Ab2	$\dot{Q} = 0.38972 \times 10^{1} + 0.15748 \times 10^{1} SCALE + 0.17022 \times 10^{-2} SCALE^{2}$

Table A.5 shows the scale reading and the corresponding flow rate obtained for flow meters Aa1 and Ab1. For flow meters Aa1 and Ab1, manufacturer's data was available for comparison and the results are shown. Table A.6 shows the scale reading and the corresponding flow rate obtained for flow meters Aa2 and Ab2. For flow meters Aa2 and Ab2, comparison was made to the existing correlations given in Table A.1.

Table A.5: Calibration results of the large air flow meters

% Scale	$SLPM$		Manufacturer	% Error	
	Aa1	Ab1	$SLPM$	Aa1	Ab1
20	286.23	285.95	277.17	3.3	3.2
40	537.93	539.63	524.90	2.5	2.8
60	785.94	787.64	772.92	1.7	1.9
80	1009.61	1005.36	1020.65	-1.1	-1.5
100	1246.01	1244.60	1268.66	-1.6	-1.9

Table A.6: Calibration results of the small air flow meters

% Scale	Flow Rate, $SLPM$		% Error	
	Aa2	Ab2	Aa2	Ab2
20	35.70	35.97	1.92	2.76
40	68.19	68.65	0.76	1.49
60	101.84	104.45	0.16	2.52
80	136.04	138.56	-0.79	0.65

APPENDIX B

CALCULATION OF THE INTERFACE HEIGHT

B.1 Calibration of the Pressure Transducer at Atmospheric Pressure

Parrott (1993) developed the method of calculating the interface height using a differential pressure transducer. The method is presented here so that this document remains as complete as possible.

The differential pressure transducer was calibrated at atmospheric pressure as described in Appendix A, Section A.2. Since the experiment was conducted at pressures greater than atmospheric pressure, the increase of the air density in the low side of the transducer required compensation. Figure B.1 provides a sketch and nomenclature of the situation. A column of water of height D_{cal} was placed in the high pressure side of the transducer to elevate the zero. When pressure P_{cal} was applied to the high pressure side, the pressure difference as read by the micromanometer was W_{cal}. The height difference between the water level in the low side of the micromanometer and the water level in the high side of the pressure transducer will be denoted as D_{loc}. Therefore, the pressure difference $P_1 - P_2$ is given by

$$P_1 - P_2 = (P_{cal} - P_{atm}) + D_{cal} g (\rho_L - \rho_{G,atm}) \tag{B.1}$$

The pressure difference read by the micromanometer is

$$P_{cal} - P_{atm} = W_{cal} g (\rho_L - \rho_{G,P_{cal}}) - D_{loc} g (\rho_{G,P_{cal}} - \rho_{G,atm}) \tag{B.2}$$

Substituting Equation (B.2) into Equation (B.1) yields an expression for the pressure difference across the transducer as a function of the manometer reading.

$$P_1 - P_2 = W_{cal} g (\rho_L - \rho_{G,P_{cal}}) - D_{loc} g (\rho_{G,P_{cal}} - \rho_{G,atm}) + D_{cal} g (\rho_L - \rho_{G,atm}) \quad \text{(B.3)}$$

The second term on the right hand side of Equation (B.3) can be neglected since its maximum value cannot be distinguished by the micromanometer. Therefore, the remaining expression can be rearranged as

$$P_1 - P_2 = W_{cal} g (\rho_L - \rho_{G,P_{cal}}) - W_{cal} g (\rho_{G,P_{cal}} - \rho_{G,atm}) + D_{cal} g (\rho_L - \rho_{G,atm}) \quad \text{(B.4)}$$

Now, the second term on the right hand side of Equation (B.4) can be neglected as it cannot be distinguished by the micromanometer. Therefore,

$$P_1 - P_2 = W_{cal} g (\rho_L - \rho_{G,P_{cal}}) + D_{cal} g (\rho_L - \rho_{G,atm}) \quad \text{(B.5)}$$

The differential pressure transducer calibration described in Appendix A Section A.2 was performed with the zero of the transducer elevated a distance D_{cal} above the transducer centerline. The pressure difference as given by correlating Equation (A.2) could be stated as

$$P_{cal} - P_{atm} = -70.181 + 35.052 (DPT - 2.0) - 0.006 (DPT - 2.0)^2 \quad \text{(B.6)}$$

Therefore, $P_{cal} - P_{atm} = W_{cal}$ and by setting $DPT = DPT_{cal}$ gives

$$W_{cal} = -70.181 + 35.052 (DPT_{cal} - 2.0) - 0.006 (DPT_{cal} - 2.0)^2 \quad \text{(B.7)}$$

which can then be substituted into Equation (B.5) to yield an expression for the pressure differential across the transducer as a function of the digital voltmeter reading at atmospheric pressure.

$$P_1 - P_2 = \{-70.181 + 35.052 (DPT_{cal} - 2.0) - 0.006 (DPT_{cal} - 2.0)^2\} g (\rho_L - \rho_{G,P_{cal}}) + D_{cal} g (\rho_L - \rho_{G,atm}) \quad \text{(B.8)}$$

B.1.1 Calibration of the Pressure Transducer with the Primary Branch Centerline

Recall that the method for calculating the interface height depended on knowing the position or height of the primary branch. A general equation will be developed that permits calculation of the primary branch centerline at atmospheric pressure. The notation is given in Figure B.2. In Figure B.2, D_{cl} refers to the interface height at the centerline of the primary branch.

The pressure difference across the transducer with respect to the primary branch centerline is given by

$$P_1 - P_2 = (D_{cl} + D_{cal})\, g\, (\rho_L - \rho_{G,cl}) \tag{B.9}$$

Now, Equations (B.8) and (B.9) were developed at atmospheric pressure. Therefore, they can be equated and by substituting $DPT_{cl,atm}$ in place of DPT_{cal} and noting that $\rho_{G,cl} = \rho_{G,atm}$, an expression for the height of the interface at the centerline of the primary branch is obtained.

$$D_{cl} = -70.181 + 35.052\,(DPT_{cl,atm} - 2.0) - 0.006\,(DPT_{cl,atm} - 2.0)^2 \tag{B.10}$$

B.1.2 Calibration of the Pressure Transducer at Experimental Pressures

When performing the experiment, a pressure greater than atmospheric pressure was inside the test section. Therefore, a general correlation that relates the working pressure inside the test section to the pressure transducer voltage is required. Figure B.3 shows the notation used to calculate the interface height.

With a pressure P inside the test section, the pressure applied to each side of the

transducer at the height of the interface is

$$P_1 = P + (D + D_{cal})\, g\rho_L \quad P_2 = P + (D + D_{cal})\, g\rho_{G,P} \tag{B.11}$$

Therefore, the delta across the transducer was

$$P_1 - P_2 = (D + D_{cal})\, g\,(\rho_L - \rho_{G,P}) \tag{B.12}$$

Now, Equation (B.8) and Equation (B.12) were combined with DPT_D replacing DPT_{cal}.

$$\{-70.181 + 35.052\,(DPT_D - 2.0) - 0.006\,(DPT_D - 2.0)^2\}\, g\,(\rho_L - \rho_{G,P_{cal}}) + D_{cal} g\,(\rho_L - \rho_{G,atm}) = (D + D_{cal})\, g\,(\rho_L - \rho_{G,P}) \tag{B.13}$$

Solving for D yields,

$$D = \{-70.181 + 35.052\,(DPT_D - 2.0) - 0.006\,(DPT_D - 2.0)^2\} \left[\frac{\rho_L - \rho_{G,atm}}{\rho_L - \rho_{G,P}}\right] + D_{cal}\left[\frac{\rho_L - \rho_{G,atm}}{\rho_L - \rho_{G,P}}\right] - 1 \tag{B.14}$$

B.1.3 Method for Calculating Interface Height

1. Calibrate the differential pressure transducer with atmospheric pressure in the low-pressure side. Correlate the calibration to yield an expression similar to Equation (B.6).
2. Find the voltage corresponding to the alignment of the interface height with the primary-branch centerline.
3. Conduct the experiment under the desired test-section pressure to find the voltage corresponding to the desired onset which yields D.
4. Calculate the onset height by,

$$h = D - D_{cl} \tag{B.15}$$

where D is given by Equation (B.14) and D_{cl} by Equation (B.10). By rearranging, a final form is obtained

$$\begin{aligned} h = & \left\{-70.181 + 35.052\,(DPT_D - 2.0) - 0.006\,(DPT_D - 2.0)^2\right\} X \\ & + D_{cal}\,(X - 1) - \left\{-70.181 + 35.052\,(DPT_{cl} - 2.0)\ -0.006\,(DPT_{cl} - 2.0)^2\right\} X \end{aligned} \tag{B.16}$$

where

$$X = \left[\frac{\rho_L - \rho_{G,atm}}{\rho_L - \rho_{G,P}}\right] \tag{B.17}$$

Equation (B.16) was used in the reduction of the experimental data.

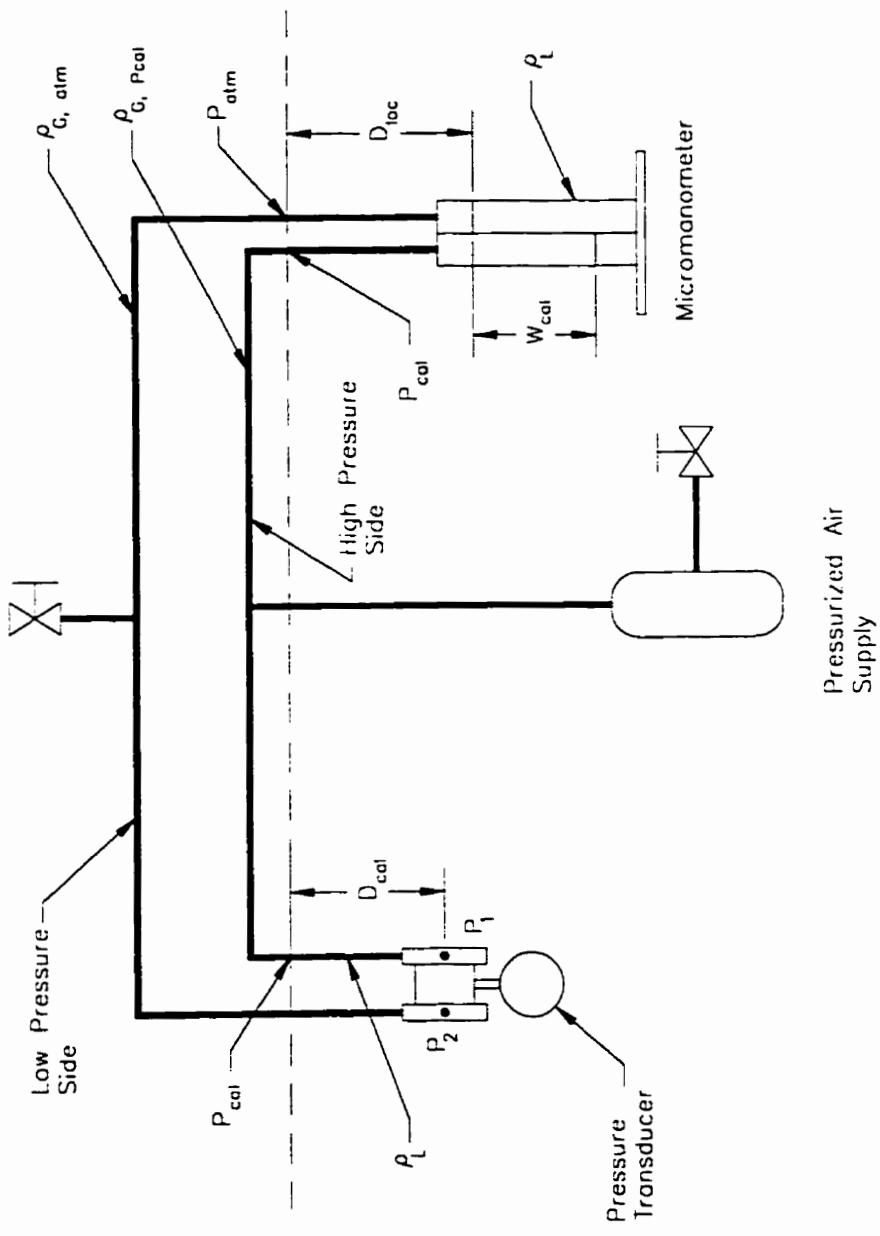

Figure B.1: Setup and nomenclature for calibration of pressure transducer at atmospheric pressure

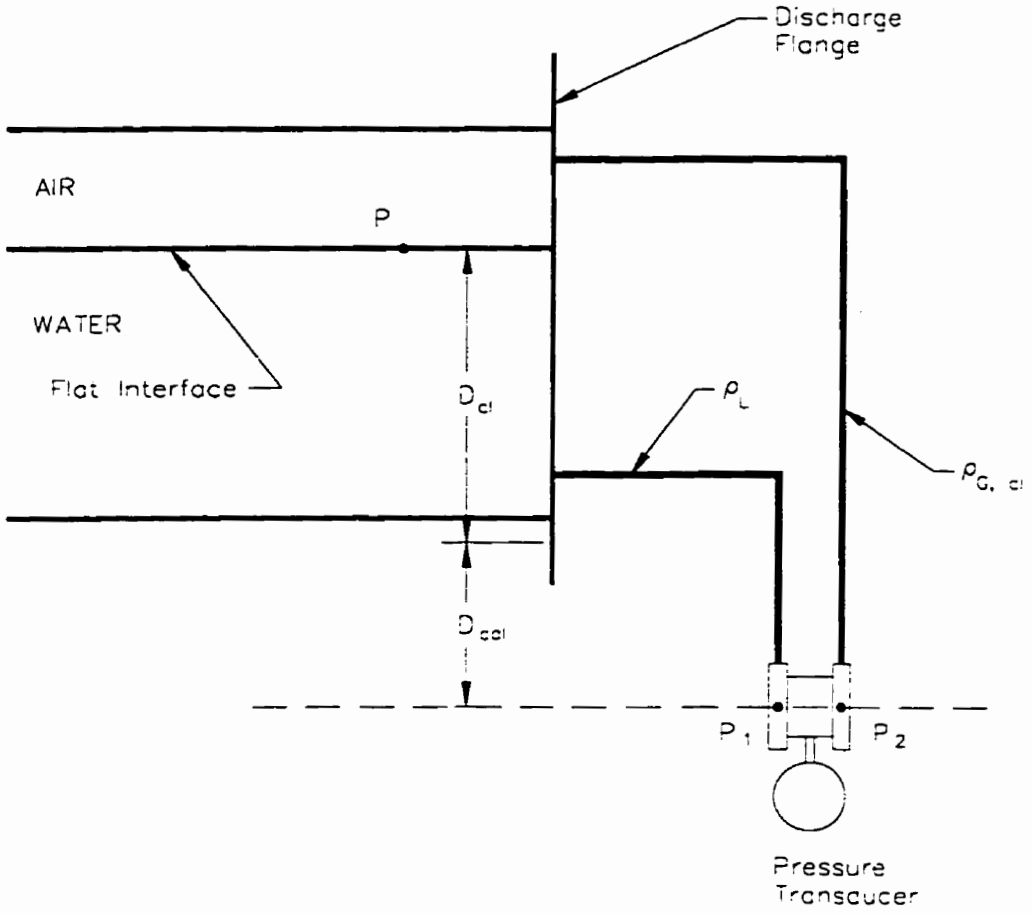

Figure B.2: Nomenclature for calibration of the pressure transducer with primary branch centerline

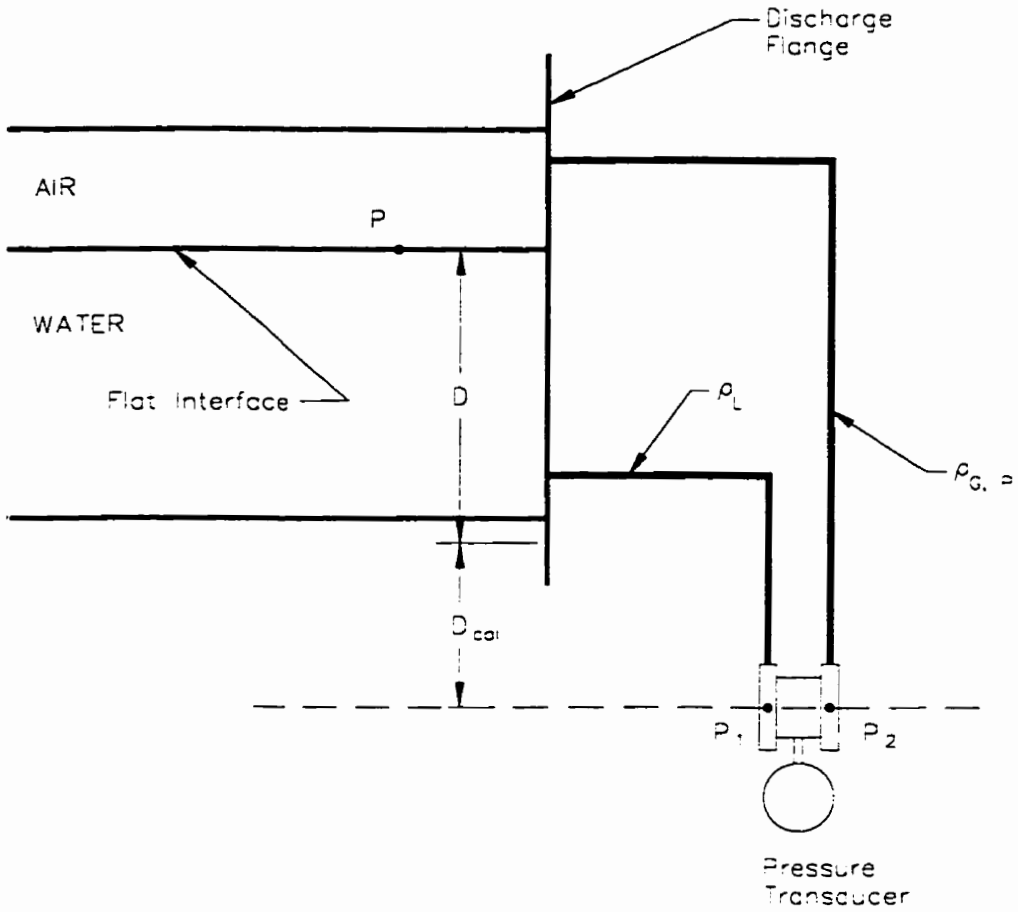

Figure B.3: Nomenclature for calibration of the pressure transducer with test section experimental pressure

APPENDIX C

Experimental Data

C.1 Introduction

This appendix contains the experimental data collected during the course of the investigation. It is divided into two sections. First, the gas entrainment experimental data are given followed by the liquid entrainment experimental data.

C.2 Gas-Entrainment Experimental Data

Table C.1 gives the experimental data for single discharge. The column labelled *Mode* refers to the descriptions given in Table 5.1. For each Froude number, the table contains multiple entries. For example, the first entry in Table C.1 is a Froude number of 70.18. Under the h/d and *Mode* headings, the corresponding values are 3.148 and 3, respectively. This means that at a Froude number of 70.18, the first observed gas entrainment was at $h/d = 3.148$ and it was by mode 3 (Initial Depression Entrainment, IDE, an intermittent mode) in Table 5.1. Still under the Froude number of 70.18 entry, the next row shows an $h/d = 3.109$ that occurred by mode 4 in Table 5.1. Mode 4 corresponds to entrainment by Continuous Depression Entrainment, CDE. Thus, this entry was the entry that appeared in the figures of Chapter 5 since it was the continuous form of entrainment at that Froude number. Therefore, with the Froude number set at 70.18, there were two instances of gas entrainment - one at an $h/d = 3.148$ by mode 3, an intermittent mode, and one at an $h/d = 3.109$ by mode 4, a continuous mode.

Table C.1: Experimental gas-entrainment data - single branch

— Fr —	— h/d —	— Mode —
70.18	3.148	3
	3.109	4
66.00	3.081	1
	3.070	3
	3.032	4
57.64	2.909	1
	2.904	3
	2.871	4
50.11	2.754	1
	2.749	3
	2.710	4
41.77	2.555	3
	2.533	4
34.26	2.356	3
	2.328	4
25.93	2.096	3
	2.079	4
18.03	1.808	3
	1.797	4
13.97	1.627	4
10.14	1.393	4
7.968	1.227	4
6.005	1.078	4
4.011	0.8784	4

Experimental gas-entrainment data - single branch

— Fr —	— h/d —	— Mode —
3.013	0.7507	4
2.505	0.6784	4
2.004	0.5953	4
1.511	0.4899	4
1.025	0.3680	4

Tables C.2 to C.12 give the experimental data for dual discharge. The column labelled *Branch* refers to which branch entrainment occurred. An *S* within the tabulated data in column *Branch* indicates simultaneous entrainment. The column labelled *Mode* refers to the descriptions given in Table 5.1. An asterix, *, given in column *Mode* indicates data for which the information was not available. Early in the program, the method of data collection and categorization was not refined to the degree finally used. Consequently, for some data sets, the detailed information on the mode of entrainment is missing. Finally, the column labelled *Category* refers to the category in which the data point was eventually placed as described in Table 5.2. Similar to Table C.1, there are multiple *Branch*, *Mode*, and *Category* entries for each Fr_1 entry.

Table C.2: Experimental gas-entrainment data for $l/d = 1.5$ and $\alpha = 0°$

a)

$Fr_2 = 14.0$				
Fr_1	h/d	Branch	Mode	Category
70.20	3.421	1	1	
	3.360	1	2	1
41.76	2.852	1	1	
	2.819	1	2	1
18.03	2.200	1	1	
	2.189	1	3	
	2.172	1	4	1
13.97	2.037	S	1	
	2.031	S	3	
	2.009	S	4	3
10.14	1.923	2	3	
	1.901	2	4	5
7.966	1.841	2	3	
	1.818	2	4	5
3.011	1.702	2	3	
	1.691	2	4	5
1.025	1.652	2	4	5

b)

$Fr_2 = 28.5$				
Fr_1	h/d	Branch	Mode	Category
70.19	3.649	1	1	
	3.555	1	3	
	3.533	1	4	1
41.76	3.102	1	1	
	3.052	1	3	
	3.041	1	4	1
34.26	2.936	1	1	
	2.886	1	3	
	2.875	1	4	1
28.51	2.807	S	1	
	2.774	S	3	
	2.757	S	4	3
25.93	2.753	S	1	
	2.725	S	3	
	2.714	S	4	3
18.03	2.582	2	1	
	2.571	2	2	5
10.14	2.399	2	1	
	2.377	2	2	5
6.005	2.305	2	1	
	2.288	2	3	
	2.272	2	4	5
3.012	2.239	2	3	
	2.217	2	4	5
1.025	2.205	2	3	
	2.183	2	4	5

c)

$Fr_2 = 42.5$				
Fr_1	h/d	Branch	Mode	Category
70.25	3.834	1	1	
	3.690	1	3	
	3.668	1	4	1
66.06	3.861	1	1	
	3.634	1	3	
	3.612	1	4	1
57.68	3.668	1	1	
	3.513	1	3	
	3.485	1	4	1
50.14	3.596	1	1	
	3.397	1	3	
	3.397	2	3	
	3.386	1	4	2
	3.386	2	3	2
42.46	3.280	S	1	
	3.242	S	3	
	3.231	S	4	3
34.27	3.215	1	1	
	3.215	2	1	
	3.149	1	3	
	3.149	2	3	
	3.132	1	3	4
	3.132	2	4	4
25.94	3.033	2	1	
	3.011	2	2	5
18.03	2.951	2	1	
	2.890	2	2	5
7.967	2.708	2	1	
	2.702	2	2	5
3.012	2.636	2	1	
	2.619	2	3	
	2.597	2	4	5
1.025	2.597	2	1	
	2.591	2	3	
	2.569	2	4	5

d)

$Fr_2 = 56.6$				
Fr_1	h/d	Branch	Mode	Category
65.99	4.252	1	1	
	3.998	2	1	
	3.904	1	3	
	3.904	2	3	
	3.843	1	4	2
	3.843	2	3	2
56.62	3.859	2	1	
	3.776	1	1	
	3.737	S	3	
	3.704	S	4	3
50.10	3.705	2	1	
	3.699	1	1	
	3.644	1	3	
	3.644	2	3	
	3.616	1	3	4
	3.616	2	4	4
41.75	3.655	2	1	
	3.550	2	3	
	3.522	2	4	5
34.25	3.473	2	1	
	3.423	2	3	
	3.401	2	4	5
18.02	3.207	2	1	
	3.157	2	2	5
7.965	3.025	2	1	
	3.002	2	2	5
3.011	2.953	2	1	
	2.931	2	3	5
1.024	2.914	2	4	
	2.914	2	1	
	2.908	2	3	
	2.886	2	4	5

Table C.3: Experimental gas-entrainment data for $l/d = 1.5$ and $\alpha = 10°$

a)

$Fr_2 = 14.0$				
Fr_1	h/d	Branch	Mode	Category
70.24	3.343	1	1	
	3.288	1	3	
	3.277	1	4	1
41.79	2.812	1	1	
	2.768	1	2	1
18.04	2.121	1	1	
	2.088	1	3	
	2.077	1	4	1
10.14	1.773	1	1	
	1.768	1	3	
	1.751	1	4	1
8.978	1.708	1	3	
	1.691	1	4	1
8.479	1.685	1	3	
	1.669	S	4	3
7.971	1.651	S	3	
	1.634	2	4	5
6.006	1.574	2	3	
	1.563	2	4	5
2.466	1.442	2	3	
	1.431	2	4	5
1.026	1.379	2	4	5

b)

$Fr_2 = 28.5$				
Fr_1	h/d	Branch	Mode	Category
70.20	3.628	1	1	
	3.511	1	3	
	3.495	1	4	1
41.77	3.058	1	1	
	2.997	1	2	1
25.93	2.677	1	1	
	2.644	1	2	1
18.03	2.450	1	1	
	2.439	1	2	1
17.03	2.422	S	1	
	2.378	S	3	
	2.361	S	4	3
14.29	2.350	2	1	
	2.328	2	2	5
10.14	2.217	2	3	
	2.190	2	4	5
6.005	2.090	2	1	
	2.079	2	2	5
2.465	2.002	2	3	
	1.980	2	4	5
1.025	1.956	2	3	
	1.928	2	4	5

c)

$Fr_2 = 42.5$				
Fr_1	h/d	Branch	Mode	Category
70.21	3.837	1	1	
	3.660	1	3	
	3.638	1	4	1
41.77	3.339	1	1	
	3.195	1	3	
	3.173	1	4	1
34.26	3.125	1	1	
	3.075	1	3	
	3.042	1	4	1
28.17	2.970	S	1	
	2.915	S	3	
	2.899	S	4	3
25.93	2.941	1	1	
	2.908	S	1	
	2.886	S	3	
	2.875	S	4	3
18.03	2.743	2	1	
	2.726	2	3	
	2.710	2	4	5
14.29	2.660	2	1	
	2.649	2	3	
	2.633	2	4	5
6.003	2.472	2	1	
	2.467	2	2	5
2.464	2.406	2	1	
	2.401	2	3	
	2.379	2	4	5
1.025	2.378	2	3	
	2.351	2	4	5

d)

$Fr_2 = 56.6$				
Fr_1	h/d	Branch	Mode	Category
65.99	4.032	1	1	
	3.772	1	3	
	3.761	1	4	1
41.76	3.529	1	1	
	3.391	1	3	
	3.369	1	4	1
40.01	3.485	1	1	
	3.369	S	3	
	3.341	1	4	2
34.25	3.341	2	3	
	3.396	1	1	
	3.308	S	1	
	3.264	S	3	
	3.242	S	4	3
25.93	3.164	2	1	
	3.103	2	3	
	3.081	1	3	
	3.081	2	4	4
18.03	2.998	2	1	
	2.976	2	3	
	2.954	2	4	5
6.004	2.754	2	1	
	2.732	2	3	
	2.721	2	4	5
1.025	2.666	2	1	
	2.655	2	3	
	2.627	2	4	5

Table C.4: Experimental gas-entrainment data for $l/d = 1.5$ and $\alpha = 30°$

a)

$Fr_2 = 14.0$				
Fr_1	h/d	Branch	Mode	Category
70.20	3.348	1	1	
	3.292	1	3	
	3.259	1	4	1
34.27	2.540	1	1	
	2.529	1	2	1
13.96	1.855	1	1	
	1.838	1	3	
	1.827	1	4	1
6.006	1.368	1	3	
	1.357	1	4	1
2.466	1.069	1	4	1
2.004	1.030	S	4	3
1.473	0.9915	2	4	5
1.025	0.9583	2	4	5

b)

$Fr_2 = 28.5$				
Fr_1	h/d	Branch	Mode	Category
70.24	3.518	1	1	
	3.412	1	3	
	3.385	1	4	1
34.28	2.743	1	1	
	2.716	1	2	1
13.97	2.130	1	1	
	2.102	1	2	1
6.009	1.743	1	1	
	1.715	1	3	
	1.687	1	4	1
5.508	1.693	S	3	
	1.671	S	4	3
5.006	1.704	1	1	
	1.687	1	1	
	1.682	2	3	
	1.654	2	4	5
4.013	1.632	2	1	
	1.621	2	3	
	1.604	2	4	5
2.005	1.538	2	3	
	1.516	2	4	5
1.025	1.494	2	3	
	1.477	2	4	5

c)

$Fr_2 = 42.5$				
Fr_1	h/d	Branch	Mode	Category
70.23	4.360	1	1	
	3.563	1	2	1
34.28	2.944	1	1	
	2.878	1	2	1
13.97	2.369	1	1	
	2.341	1	2	1
10.14	2.236	1	1	
	2.186	1	2	1
8.981	2.159	1	1	
	2.142	S	1	
	2.131	S	2	3
7.971	2.125	S	1	
	2.098	2	2	5
6.007	2.059	2	1	
	2.042	1	1	
	2.037	2	2	5
4.012	1.982	2	1	
	1.965	2	2	5
2.466	1.921	2	1	
	1.910	2	3	
	1.888	2	4	5
1.025	1.871	2	1	
	1.838	2	4	5

d)

$Fr_2 = 56.6$				
Fr_1	h/d	Branch	Mode	Category
66.04	3.912	1	1	
	3.646	1	3	
	3.580	1	4	1
34.28	3.193	1	1	
	3.032	1	2	1
13.97	2.612	1	1	
	2.557	1	2	1
10.14	2.479	S	1	
	2.452	S	2	3
7.972	2.407	S	1	
	2.385	2	2	5
6.008	2.335	2	1	
	2.319	2	2	5
2.467	2.230	2	1	
	2.214	2	3	
	2.186	2	4	5
1.025	2.192	2	1	
	2.169	2	3	
	2.153	2	4	5

Table C.5: Experimental gas-entrainment data for $l/d = 1.5$ and $\alpha = 60°$

a)

$Fr_2 = 14.0$				
Fr_1	h/d	Branch	Mode	Category
70.20	3.252	1	1	
	3.219	1	3	
	3.186	1	4	1
34.27	2.461	1	1	
	2.450	1	3	
	2.428	1	4	1
18.04	1.929	1	3	
	1.907	1	4	1
7.972	1.370	1	3	
	1.365	1	4	1
3.014	0.9382	1	3	
	0.9327	1	4	1
1.026	0.6445	1	4	1

b)

$Fr_2 = 28.5$				
Fr_1	h/d	Branch	Mode	Category
70.23	3.405	1	1	
	3.250	1	2	1
34.28	2.537	1	1	
	2.514	1	2	1
18.04	2.050	1	1	
	2.022	1	2	1
7.972	1.552	1	1	
	1.524	1	3	
	1.508	1	4	1
3.014	1.181	1	3	
	1.159	1	4	1
1.025	0.9932	1	3	
	0.9821	1	4	1

c)

$Fr_2 = 42.5$				
Fr_1	h/d	Branch	Mode	Category
70.24	3.553	1	1	
	3.432	1	3	
	3.387	1	4	1
34.29	2.746	1	1	
	2.685	1	3	
	2.663	1	4	1
18.04	2.270	1	1	
	2.237	1	2	1
7.974	1.839	1	1	
	1.794	1	2	1
3.014	1.529	1	1	
	1.490	1	2	1
1.026	1.363	1	1	
	1.346	1	2	1

d)

$Fr_2 = 56.6$				
Fr_1	h/d	Branch	Mode	Category
66.04	4.047	1	1	
	3.472	1	3	
	3.433	1	4	1
34.28	3.024	1	1	
	2.852	1	2	1
18.04	2.476	1	1	
	2.421	1	2	1
7.972	2.061	1	1	
	2.000	1	2	1
3.014	1.779	1	1	
	1.768	1	2	1
2.506	1.762	1	1	
	1.740	1	2	1
2.005	1.735	1	1	
	1.713	1	2	1
1.511	1.702	1	1	
	1.674	1	2	1
1.026	1.663	1	1	
	1.651	S	2	3

Table C.6: Experimental gas-entrainment data for $l/d = 2.0$ and $\alpha = 0°$

a)

$Fr_2 = 14.0$				
Fr_1	h/d	Branch	Mode	Category
70.22	3.371	1	1	
	3.277	1	2	1
66.03	3.315	1	1	
	3.199	1	2	1
57.65	3.166	1	1	
	3.061	1	2	1
50.11	2.995	1	1	
	2.901	1	2	1
41.77	2.824	1	1	
	2.735	1	2	1
34.26	2.580	1	1	
	2.548	1	3	
	2.532	1	2	1
25.93	2.410	1	1	
	2.310	1	3	
	2.288	1	4	1
18.03	2.111	1	1	
	2.051	1	3	
	2.039	1	4	1
13.96	1.883	S	3	
	1.844	S	4	3
10.14	1.835	2	1	
	1.780	2	3	
	1.769	2	4	5
7.967	1.741	2	1	
	1.730	2	3	
	1.708	2	4	5
6.004	1.691	2	3	
	1.675	2	4	5
4.010	1.662	2	3	
	1.635	2	4	5
3.012	1.647	2	3	
	1.636	2	4	5
2.504	1.647	2	3	
	1.636	2	4	5
2.003	1.636	2	3	
	1.625	2	4	5
1.510	1.625	2	3	
	1.619	2	4	5
1.025	1.619	2	3	
	1.614	2	4	5

b)

$Fr_2 = 28.5$				
Fr_1	h/d	Branch	Mode	Category
70.21	3.560	1	1	
	3.450	1	3	
	3.417	1	4	1
66.02	3.599	1	1	
	3.372	1	3	
	3.350	1	4	1
57.65	3.394	1	1	
	3.228	1	3	
	3.217	1	4	1
50.13	3.283	1	1	
	3.106	1	3	
	3.062	1	4	1
41.77	3.096	1	1	
	2.935	1	3	
	2.908	1	4	1
34.26	2.803	1	1	
	2.781	1	3	
	2.765	1	4	1
28.52	2.660	S	3	
	2.632	S	4	3
25.93	2.693	2	1	
	2.605	2	3	
	2.577	2	4	5
18.03	2.509	2	1	
	2.448	2	3	
	2.421	2	4	5
10.14	2.366	2	1	
	2.278	2	3	
	2.255	2	4	5
7.969	2.311	2	1	
	2.244	2	3	
	2.239	2	4	5
6.006	2.255	2	1	
	2.222	2	3	
	2.206	2	4	5
4.011	2.217	2	1	
	2.205	2	3	
	2.178	2	4	5
3.013	2.194	2	1	
	2.189	2	3	
	2.167	2	4	5
2.505	2.194	2	1	
	2.194	2	3	
	2.161	2	4	5
2.004	2.189	2	3	
	2.161	2	4	5
1.511	2.184	2	3	
	2.161	2	4	5
1.025	2.178	2	3	
	2.156	2	4	5

c)

$Fr_2 = 42.5$				
Fr_1	h/d	Branch	Mode	Category
70.21	4.130	1	1	
	3.754	2	1	
	3.648	1	3	
	3.604	1	4	1
66.00	3.732	1	1	
	3.660	2	1	
	3.599	1	3	
	3.555	1	4	1
57.63	3.589	1	1	
	3.456	1	3	
	3.428	1	4	1
50.10	3.495	1	1	
	3.335	1	3	
	3.296	1	4	1
42.50	3.226	S	3	
	3.165	S	4	3
41.75	3.307	2	1	
	3.252	1	1	
	3.196	S	3	
	3.169	S	4	3
34.25	3.175	2	1	
	3.070	2	3	
	3.036	2	4	5
25.92	3.015	2	1	
	2.921	2	3	
	2.899	2	4	5
18.02	2.926	2	1	
	2.799	2	3	
	2.788	2	4	5
10.13	2.727	2	1	
	2.689	2	3	
	2.666	2	4	5
7.964	2.700	2	1	
	2.650	2	3	
	2.661	2	2	5
4.009	2.633	2	1	
	2.617	2	2	5
3.011	2.617	2	1	
	2.600	2	3	
	2.578	2	4	5
2.003	2.602	2	3	
	2.567	2	4	5
1.024	2.594	2	3	
	2.561	2	4	5

d)

$Fr_2 = 56.6$				
Fr_1	h/d	Branch	Mode	Category
66.03	4.523	1	1	
	3.936	2	1	
	3.732	1	3	
	3.687	1	4	1
57.67	4.129	1	1	
	3.830	2	1	
	3.614	S	3	
	3.587	S	4	3
56.63	3.771	2	1	
	3.754	1	1	
	3.627	S	3	
	3.605	S	4	3
50.13	3.897	2	1	
	3.731	1	1	
	3.537	2	3	
	3.504	2	4	5
41.77	3.504	2	1	
	3.477	2	4	5
34.26	3.433	2	1	
	3.284	2	4	5
25.93	3.306	2	1	
	3.174	2	3	
	3.157	2	4	5
18.03	3.196	2	1	
	3.091	2	2	5
10.14	3.035	2	3	
	2.975	2	2	5
7.970	3.012	2	1	
	2.934	2	2	5
6.006	2.968	2	1	
	2.929	2	2	5
4.011	2.929	2	1	
	2.896	2	3	
2.003	2.874	2	4	5
	2.896	2	1	
	2.880	2	3	
1.025	2.863	2	4	5
	2.824	2	4	5

Table C.7: Experimental gas-entrainment data for $l/d = 2.0$ and $\alpha = 10°$

a)

$Fr_2 = 14.0$				
Fr_1	h/d	Branch	Mode	Category
70.20	3.410	1	1	
	3.294	1	3	1
57.64	3.123	1	1	
	3.068	1	2	1
50.11	2.968	1	1	
	2.913	1	2	1
41.75	2.792	1	1	
	2.737	1	2	1
34.25	2.598	1	1	
	2.565	1	2	1
25.92	2.372	1	1	
	2.311	1	3	
	2.283	1	4	1
18.03	2.084	1	1	
	2.035	1	3	
	2.007	1	4	1
10.14	1.675	1	1	
	1.648	1	3	
	1.631	1	4	1
7.965	1.554	1	1	
	1.531	1	3	
	1.515	1	4	1
7.081	1.482	S	4	3
6.003	1.471	2	1	
	1.437	2	4	5
4.009	1.399	2	1	
	1.388	2	3	
	1.382	2	4	5
2.003	1.355	2	3	
	1.349	2	4	5
1.024	1.344	2	3	
	1.332	2	4	5

b)

$Fr_2 = 28.5$				
Fr_1	h/d	Branch	Mode	Category
70.21	3.577	1	1	
	3.411	1	2	1
57.65	3.390	1	1	
	3.217	1	2	1
41.77	3.046	1	1	
	2.896	1	3	
	2.874	1	4	1
34.26	2.847	1	1	
	2.725	1	3	
	2.703	1	4	1
25.93	2.676	1	1	
	2.515	1	3	
	2.493	1	4	1
18.03	2.354	1	1	
	2.293	1	3	
	2.266	1	4	1
15.03	2.197	S	3	
	2.175	S	4	3
10.14	2.095	2	1	
	2.067	2	3	
	2.039	2	4	5
7.966	2.068	2	1	
	2.023	2	3	
	1.990	2	4	5
3.011	1.924	2	1	
	1.913	2	3	
	1.896	2	4	5
1.024	1.897	2	3	
	1.869	2	4	5

c)

$Fr_2 = 42.5$				
Fr_1	h/d	Branch	Mode	Category
70.22	3.869	1	1	
	3.609	1	2	1
57.64	3.698	1	1	
	3.388	1	3	
	3.366	1	4	1
50.10	3.544	1	1	
	3.262	1	3	
	3.234	1	4	1
41.75	3.267	1	1	
	3.090	1	3	
	3.074	1	4	1
34.25	3.063	1	1	
	2.958	1	3	
	2.919	1	4	1
25.92	2.831	1	1	
	2.753	1	3	
	2.731	S	3	
	2.715	S	4	3
24.26	2.754	1	1	
	2.726	S	3	
	2.715	S	4	3
23.01	2.787	1	1	
	2.698	2	1	
	2.693	S	3	
	2.682	S	4	3
18.02	2.593	2	1	
	2.582	2	3	
	2.571	2	4	5
10.13	2.466	2	1	
	2.411	2	3	
	2.400	2	4	5
6.002	2.394	2	1	
	2.339	2	2	5
2.503	2.306	2	1	
	2.289	2	3	
	2.278	2	4	5
1.024	2.278	2	1	
	2.278	2	3	
	2.256	2	4	5

d)

$Fr_2 = 56.6$				
Fr_1	h/d	Branch	Mode	Category
66.00	4.405	1	1	
	3.681	1	2	1
57.62	3.798	1	1	
	3.588	1	3	
	3.533	1	4	1
50.14	3.515	1	1	
	3.421	1	3	
	3.399	1	4	1
41.79	3.521	1	1	
	3.277	1	3	
	3.227	1	4	1
34.27	3.344	1	1	
	3.167	1	3	
	3.145	2	3	
	3.123	S	4	3
30.10	3.251	1	1	
	3.102	2	1	
	3.074	S	3	
	3.024	S	4	3
25.94	3.107	1	1	
	3.046	2	1	
	2.991	2	3	
	2.968	2	4	5
18.03	2.930	2	1	
	2.847	2	3	
	2.824	2	4	5
7.968	2.725	2	1	
	2.681	2	2	5
3.012	2.631	2	1	
	2.615	2	2	5
1.025	2.604	2	1	
	2.598	2	3	
	2.576	2	4	5

Table C.8: Experimental gas-entrainment data for $l/d = 2.0$ and $\alpha = 30°$

a)

$Fr_2 = 14.0$				
Fr_1	h/d	Branch	Mode	Category
70.20	3.328	1	1	
	3.262	1	2	1
41.77	2.676	1	1	
	2.664	1	2	1
18.03	1.945	1	1	
	1.929	1	3	
	1.918	1	4	1
7.968	1.387	1	3	
	1.370	1	4	1
2.504	0.8886	1	4	1
1.025	0.6667	1	4	2
	0.6667	2	1	2

b)

$Fr_2 = 28.5$				
Fr_1	h/d	Branch	Mode	Category
70.19	3.506	1	1	
	3.357	1	3	
	3.318	1	4	1
41.76	2.864	1	1	
	2.798	1	2	1
18.03	2.200	1	1	
	2.140	1	2	1
6.005	1.586	1	1	
	1.470	1	3	
	1.448	1	4	1
4.010	1.346	1	3	
	1.287	1	4	1
3.170	1.282	S	3	
	1.260	S	4	3
3.012	1.282	2	3	
	1.276	1	3	
	1.254	2	4	5
2.504	1.254	2	3	
	1.226	2	4	5
1.025	1.193	2	1	
	1.188	2	3	
	1.160	2	4	5

c)

$Fr_2 = 42.5$				
Fr_1	h/d	Branch	Mode	Category
70.24	3.835	1	1	
	3.437	1	2	1
41.80	3.077	1	1	
	2.928	1	2	1
18.04	2.414	1	1	
	2.286	1	2	1
7.972	2.032	1	1	
	1.822	1	3	
	1.794	1	4	1
6.304	1.813	1	1	
	1.763	S	3	
	1.736	S	4	3
6.007	1.828	1	1	
	1.750	2	3	
	1.717	2	4	5
4.012	1.673	2	1	
	1.651	2	3	
	1.634	2	4	5
2.004	1.618	2	1	
	1.601	2	2	5
1.025	1.573	2	3	
	1.534	2	4	5

d)

$Fr_2 = 56.6$				
Fr_1	h/d	Branch	Mode	Category
66.00	3.925	1	1	
	3.505	1	3	
	3.472	1	4	1
57.61	3.666	1	1	
	3.406	1	2	1
34.24	3.113	1	1	
	2.936	1	2	1
18.02	2.655	1	1	
	2.455	1	3	
	2.433	1	4	1
13.96	2.399	1	1	
	2.305	1	3	
	2.255	1	4	1
10.14	2.339	1	1	
	2.179	1	3	
	2.140	S	4	3
8.975	2.228	1	1	
	2.195	2	1	
	2.117	S	3	
	2.084	2	4	5
7.963	2.174	1	1	
	2.129	2	1	
	2.102	2	3	
	2.057	2	4	5
6.002	2.074	2	1	
	2.024	2	3	
	1.991	2	4	5
2.503	1.941	2	1	
	1.919	2	3	
	1.902	2	4	5
1.025	1.888	2	1	
	1.871	2	3	
	1.849	2	4	5

Table C.9: Experimental gas-entrainment data for $l/d = 2.0$ and $\alpha = 60°$

a)

$Fr_2 = 14.0$				
Fr_1	h/d	Branch	Mode	Category
70.22	3.226	1	1	
	3.215	1	3	
	3.176	1	4	1
34.28	2.440	1	1	
	2.429	1	3	
	2.407	1	4	1
7.972	1.333	1	4	1
2.506	0.8011	1	4	1
1.026	0.5294	1	4	1

b)

$Fr_2 = 28.5$				
Fr_1	h/d	Branch	Mode	Category
70.18	3.459	1	1	
	3.354	1	3	
	3.304	1	4	1
34.25	2.563	1	1	
	2.546	1	2	1
7.967	1.506	1	1	
	1.495	1	3	
	1.456	1	4	1
2.504	0.9968	1	3	
	0.9802	1	4	1
1.025	0.7696	1	4	1

c)

$Fr_2 = 42.5$				
Fr_1	h/d	Branch	Mode	Category
70.19	3.503	1	1	
	3.398	1	3	
	3.365	1	4	1
34.26	2.701	1	1	
	2.657	1	2	1
7.966	1.667	1	1	
	1.633	1	3	
	1.600	1	4	1
2.503	1.219	1	3	
	1.174	1	4	1
1.025	1.042	1	4	
	1.020	1	4	1

d)

$Fr_2 = 56.6$				
Fr_1	h/d	Branch	Mode	Category
66.00	3.907	1	1	
	3.414	1	3	
	3.387	1	4	1
41.77	3.087	1	1	
	2.910	1	3	
	2.888	1	4	1
18.04	2.317	1	1	
	2.256	1	2	1
6.009	1.769	1	1	
	1.658	1	2	1
2.506	1.525	1	1	
	1.370	1	3	
	1.343	1	4	1
1.512	1.364	1	1	
	1.281	1	3	
	1.248	1	4	1
1.026	1.310	1	1	
	1.249	1	3	
	1.216	1	4	1

Table C.10: Experimental gas-entrainment data for $l/d = 8.0$ and $\alpha = 0°$

a)

$Fr_2 = 14.0$				
Fr_1	h/d	Branch	Mode	Category
70.17	3.231	1	*	1
65.98	3.154	1	*	1
57.61	2.932	1	*	1
50.09	2.761	1	*	1
41.75	2.561	1	*	1
34.24	2.374	1	*	1
25.92	2.097	1	*	1
18.02	1.819	1	*	1
14.04	1.594	S	*	3
10.13	1.594	2	*	5
7.965	1.593	2	*	5
6.003	1.593	2	*	5
4.009	1.599	2	*	5
3.011	1.599	2	*	5
2.503	1.593	2	*	5
2.003	1.599	2	*	5
1.510	1.599	2	*	5
1.025	1.599	2	*	5

b)

$Fr_2 = 28.5$				
Fr_1	h/d	Branch	Mode	Category
70.19	3.670	1	1	
	3.183	1	3	
	3.105	1	4	1
65.99	3.508	1	1	
	3.105	1	3	
	3.044	1	4	1
57.61	3.233	1	1	
	2.934	1	3	
	2.901	1	4	1
50.08	2.934	1	1	
	2.780	1	3	
	2.741	1	4	1
41.74	2.619	1	1	
	2.586	1	3	
	2.536	1	4	1
34.24	2.371	1	3	
	2.343	1	4	1
28.42	2.165	S	3	
	2.149	S	4	3
25.93	2.169	2	*	5
18.03	2.151	2	*	5
10.14	2.151	2	*	5
7.966	2.151	2	*	5
6.004	2.146	2	*	5
4.010	2.152	2	*	5
3.012	2.152	2	*	5
2.504	2.146	2	*	5
2.003	2.152	2	*	5
1.510	2.152	2	*	5
1.025	2.152	2	*	5

c)

$Fr_2 = 42.5$				
Fr_1	h/d	Branch	Mode	Category
70.20	4.170	1	1	
	3.695	2	1	
	3.191	1	3	
	3.114	1	4	1
65.98	3.966	1	1	
	3.706	2	1	
	3.126	1	3	
	3.059	1	4	1
57.61	3.641	2	1	
	3.574	1	1	
	2.949	1	3	
	2.899	1	4	1
50.10	3.502	2	1	
	3.431	1	1	
	2.794	1	3	
	2.733	1	4	1
42.60	2.848	2	1	
	2.826	1	1	
	2.583	1	3	
	2.566	2	3	
	2.539	S	4	3
34.26	2.865	2	1	
	2.610	1	1	
	2.555	2	3	
	2.516	2	4	5
25.93	2.599	2	1	
	2.555	2	3	
	2.500	2	4	5
18.03	2.555	2	3	
	2.511	2	4	5
10.13	2.574	2	4	5
7.963	2.581	2	4	5
6.001	2.576	2	4	5
4.008	2.580	2	4	5
3.010	2.576	2	4	5
2.502	2.587	2	4	5
2.002	2.581	2	4	5
1.509	2.575	2	4	5
1.024	2.587	2	4	5

d)

$Fr_2 = 56.6$				
Fr_1	h/d	Branch	Mode	Category
66.00	4.283	1	1	
	4.145	2	1	
	3.138	1	3	
	3.077	1	4	1
60.96	4.184	1	1	
	4.184	2	1	
	3.033	1	3	
	2.950	1	4	1
56.78	3.726	1	1	
	3.726	2	1	
	2.935	1	3	
	2.918	2	3	
	2.874	S	4	3
50.11	3.875	2	1	
	3.819	1	1	
	2.901	2	3	
	2.856	2	4	5
41.77	3.741	1	1	
	3.730	2	1	
	2.894	2	3	
	2.839	2	4	5
34.28	3.342	2	1	
	3.292	1	1	
	2.871	2	3	
	2.838	2	4	5
25.94	3.031	2	1	
	2.860	2	3	
	2.838	2	4	5
18.03	2.938	2	1	
	2.866	2	3	
	2.838	2	4	5
10.14	2.866	2	3	
	2.838	2	4	5
7.964	2.891	2	4	5
6.002	2.886	2	4	5
4.008	2.886	2	4	5
3.011	2.886	2	4	5
2.503	2.886	2	4	5
2.003	2.886	2	4	5
1.510	2.891	2	4	5
1.024	2.886	2	4	5

Table C.11: Experimental gas-entrainment data for $l/d = 8.0$ and $\alpha = 10°$

a)

$Fr_2 = 14.0$				
Fr_1	h/d	Branch	Mode	Category
70.18	3.273	1	*	1
65.99	3.079	1	*	1
57.62	2.891	1	*	1
50.10	2.737	1	*	1
41.75	2.549	1	*	1
34.25	2.344	1	*	1
25.92	2.084	1	*	1
18.02	1.791	1	*	1
10.14	1.365	1	*	1
7.966	1.204	1	*	1
6.003	1.049	1	*	1
4.010	0.8603	1	*	1
3.012	0.7388	1	*	1
2.504	0.6610	1	*	1
2.004	0.5834	1	*	1
1.510	0.4948	1	*	1
1.025	0.3731	1	*	1

b)

$Fr_2 = 28.5$				
Fr_1	h/d	Branch	Mode	Category
70.14	3.247	1	*	1
65.97	3.125	1	*	1
57.61	2.947	1	*	1
50.10	2.793	1	*	1
41.76	2.543	1	*	1
34.26	2.332	1	*	1
25.94	2.066	1	*	1
18.04	1.785	1	*	1
10.14	1.357	1	*	1
7.971	1.196	1	*	1
6.007	1.053	1	*	1
4.012	0.8697	1	*	1
3.013	0.7592	1	*	1
2.933	0.7379	S	*	3
2.504	0.7381	2	*	5
2.003	0.7375	2	*	5
1.510	0.7375	2	*	5
1.025	0.7375	2	*	5

c)

$Fr_2 = 42.5$				
Fr_1	h/d	Branch	Mode	Category
70.17	3.694	1	1	
	3.163	1	3	
	3.113	1	4	1
66.00	3.660	1	1	
	3.041	1	3	
	3.030	1	4	1
57.65	3.329	1	1	
	2.880	1	3	
	2.847	1	4	1
50.15	3.028	1	1	
	2.729	1	3	
	2.679	1	4	1
41.80	2.634	1	1	
	2.546	1	3	
	2.496	1	4	1
34.28	2.430	1	1	
	2.325	1	3	
	2.297	1	4	1
25.92	2.115	1	4	1
18.02	1.840	1	4	1
10.13	1.413	1	4	1
7.962	1.242	1	4	1
6.730	1.155	S	4	3
6.000	1.143	2	4	5
4.007	1.148	2	4	5
3.010	1.148	2	4	5
2.502	1.148	2	4	5
2.002	1.149	2	4	5
1.509	1.149	2	4	5
1.024	1.149	2	4	5

d)

$Fr_2 = 56.6$				
Fr_1	h/d	Branch	Mode	Category
66.00	4.181	1	1	
	3.080	1	3	
	3.008	1	4	1
57.64	3.970	1	1	
	2.913	1	3	
	2.858	1	4	1
50.13	3.527	1	1	
	2.747	1	3	
	2.719	1	4	1
41.78	3.001	1	1	
	2.558	1	3	
	2.492	1	4	1
34.26	3.046	1	1	
	2.609	2	1	
	2.382	1	3	
	2.343	1	4	1
25.92	2.157	1	3	
	2.090	1	4	1
18.02	1.847	1	3	
	1.797	1	4	1
13.96	1.612	1	4	1
10.97	1.474	1	3	
	1.469	2	1	
	1.452	1	4	1
10.55	1.452	2	1	
	1.441	1	3	
	1.430	2	3	
	1.408	S	4	3
10.14	1.470	2	1	
	1.426	2	3	
	1.397	2	4	5
7.969	1.420	2	3	
	1.402	2	4	5
6.006	1.424	2	3	
	1.390	2	4	5
3.013	1.391	2	4	5
1.025	1.419	2	4	5

Table C.12: Experimental gas-entrainment data for $l/d = 8.0$ and $\alpha = 30°$

a)

$Fr_2 = 14.0$				
Fr_1	h/d	Branch	Mode	Category
70.18	3.156	1	*	1
65.99	3.063	1	*	1
57.62	2.908	1	*	1
50.10	2.747	1	*	1
41.76	2.544	1	*	1
34.25	2.350	1	*	1
25.93	2.083	1	*	1
18.03	1.790	1	*	1
10.14	1.369	1	*	1
7.969	1.208	1	*	1
6.005	1.055	1	*	1
4.010	0.8711	1	*	1
3.012	0.7551	1	*	1
2.504	0.6888	1	*	1
2.003	0.6003	1	*	1
1.510	0.5118	1	*	1
1.025	0.3791	1	*	1

b)

$Fr_2 = 28.5$				
Fr_1	h/d	Branch	Mode	Category
70.15	3.219	1	*	1
65.96	3.159	1	*	1
57.60	2.943	1	*	1
50.08	2.745	1	*	1
41.73	2.578	1	*	1
34.24	2.379	1	*	1
25.94	2.065	1	*	1
18.03	1.778	1	*	1
10.14	1.368	1	*	1
7.969	1.219	1	*	1
6.005	1.071	1	*	1
4.010	0.8706	1	*	1
3.012	0.7602	1	*	1
2.504	0.6940	1	*	1
2.003	0.6061	1	*	1
1.510	0.5173	1	*	1
1.025	0.3845	1	*	1

c)

$Fr_2 = 42.5$				
Fr_1	h/d	Branch	Mode	Category
70.14	3.331	1	*	1
65.96	3.196	1	*	1
57.59	3.042	1	*	1
50.08	2.792	1	*	1
41.76	2.586	1	*	1
34.26	2.348	1	*	1
25.93	2.083	1	*	1
18.03	1.817	1	*	1
10.14	1.402	1	*	1
7.966	1.236	1	*	1
6.003	1.087	1	*	1
4.009	0.9002	1	*	1
3.011	0.7743	1	*	1
2.503	0.7065	1	*	1
2.002	0.6235	1	*	1
1.510	0.5348	1	*	1
1.024	0.4020	1	*	1

d)

$Fr_2 = 56.6$				
Fr_1	h/d	Branch	Mode	Category
65.97	3.329	1	1	
	3.136	1	3	
	3.075	1	4	1
50.09	2.860	1	1	
	2.794	1	3	
	2.755	1	4	1
34.24	2.418	1	1	
	2.412	1	3	
	2.351	1	4	1
18.02	1.859	1	3	
	1.815	1	4	1
7.964	1.267	1	3	
	1.256	1	4	1
4.009	0.9235	1	3	
	0.9180	1	4	1
2.503	0.7186	1	4	1
1.510	0.5358	1	4	1
1.025	0.4028	1	4	1

C.3 Liquid-Entrainment Experimental Data

Table C.13 gives the experimental data for single discharge.

Table C.13: Experimental liquid-entrainment data - single branch

— Fr —	— h/d —
38.02	2.620
34.02	2.510
29.98	2.388
25.99	2.278
22.05	2.162
18.00	1.996
14.01	1.847
10.00	1.643
8.061	1.506
5.997	1.330
3.999	1.169
3.000	1.059
2.000	0.9375
1.498	0.8768

Tables C.14 to C.24 give the experimental data for dual discharge. The column labelled *Branch* refers to which branch entrainment occurred. An S with in the tabulated data of column *Branch* indicates simultaneous entrainment. Finally, the column labelled *Category* refers to the category in which the data point was eventually placed as described in Table 5.3.

Table C.14: Experimental liquid-entrainment data for $l/d = 1.5$ and $\alpha = 0°$

$Fr_2 = 9.5$				
Fr_1	h/d	Branch	Category	$T°C$
38.11	2.776	1	1	22.1
22.00	2.312	1	1	22.3
13.99	2.020	1	1	22.1
10.02	1.860	S	3	21.9
9.509	1.832	S	3	22.0
8.002	1.771	2	5	22.3
5.994	1.683	2	5	22.6
2.997	1.617	2	5	22.5
0.8295	1.573	2	5	22.4

$Fr_2 = 19.0$				
Fr_1	h/d	Branch	Category	$T°C$
38.05	2.958	1,2	2	22.3
34.20	2.898	1,2	2	22.1
29.98	2.776	1,2	2	21.8
25.99	2.666	1,2	2	21.9
21.97	2.550	S	3	22.0
19.01	2.500	S	3	22.1
17.99	2.439	S	3	22.3
14.02	2.340	1,2	4	22.4
9.983	2.219	2	5	22.5
5.994	2.102	2	5	22.7
2.986	2.036	2	5	22.4
1.508	2.014	2	5	22.3
0.8271	1.997	2	5	22.3

$Fr_2 = 28.5$				
Fr_1	h/d	Branch	Category	$T°C$
38.01	3.168	1,2	2	22.7
34.01	3.074	1,2	2	22.7
29.97	2.974	S	3	22.6
28.51	2.963	S	3	22.5
25.92	2.892	1,2	4	22.4
21.97	2.759	1,2	4	22.2
17.97	2.704	1,2	4	22.1
13.94	2.582	2	5	22.0
9.992	2.499	2	5	21.9
5.981	2.389	2	5	21.9
1.995	2.361	2	5	21.7
0.8345	2.317	2	5	21.8

$Fr_2 = 38.0$				
Fr_1	h/d	Branch	Category	$T°C$
37.96	3.305	S	3	22.1
33.91	3.228	S	3	22.2
29.99	3.161	S	3	22.3
26.08	3.035	1,2	4	22.2
22.02	2.979	1,2	4	22.1
17.97	2.913	1,2	4	22.1
13.99	2.836	1,2	4	22.1
10.07	2.759	2	5	22.2
6.013	2.654	2	5	22.0
2.014	2.609	2	5	21.9
0.8393	2.554	2	5	22.1

Table C.15: Experimental liquid-entrainment data for $l/d = 1.5$ and $\alpha = 10°$

$Fr_2 = 9.5$				
Fr_1	h/d	Branch	Category	$T°C$
37.90	2.699	1	1	22.0
22.00	2.252	1	1	22.1
10.05	1.744	1	1	22.3
5.955	1.518	1	1	22.4
4.998	1.463	1	1	22.5
4.500	1.430	S	3	22.6
3.988	1.396	2	5	22.6
1.984	1.308	2	5	22.7
0.8242	1.297	2	5	22.8

$Fr_2 = 19.0$				
Fr_1	h/d	Branch	Category	$T°C$
38.13	2.876	1	1	22.0
21.99	2.451	1	1	22.1
17.96	2.329	1	1	22.0
14.01	2.186	1	1	21.9
9.965	2.042	S	3	21.9
7.981	1.965	S	3	21.8
6.012	1.860	2	5	22.0
1.999	1.766	2	5	22.1
0.8303	1.717	2	5	22.2

$Fr_2 = 28.5$				
Fr_1	h/d	Branch	Category	$T°C$
37.95	3.025	1	1	23.0
33.97	2.942	1	1	23.0
29.98	2.865	1	1	22.9
26.01	2.732	1	1	22.8
21.98	2.633	1	1	22.8
17.99	2.550	1	1	22.9
14.00	2.418	1,2	2	23.0
9.90	2.291	S	3	23.1
8.002	2.235	1,2	4	23.0
5.979	2.142	2	5	23.1
1.998	2.075	2	5	23.2
0.8365	2.042	2	5	23.0

$Fr_2 = 38.0$				
Fr_1	h/d	Branch	Category	$T°C$
37.92	3.235	1,2	2	26.0
33.94	3.086	1,2	2	25.9
29.99	3.020	1,2	2	25.9
25.93	2.942	1,2	2	25.8
21.91	2.854	S	3	25.7
18.00	2.738	S	3	25.5
14.00	2.617	S	3	25.5
10.01	2.523	1,2	4	25.4
8.032	2.473	2	5	25.4
6.039	2.402	2	5	25.5
1.995	2.319	2	5	25.6
0.8425	2.286	2	5	25.5

Table C.16: Experimental liquid-entrainment data for $l/d = 1.5$ and $\alpha = 30°$

$Fr_2 = 9.5$				
Fr_1	h/d	Branch	Category	$T°C$
38.01	2.676	1	1	22.9
21.99	2.218	1	1	22.9
10.01	1.698	1	1	23.0
4.015	1.279	1	1	22.9
2.995	1.180	1	1	25.5
1.994	1.075	1	1	25.4
1.498	1.019	1	1	25.6
1.159	0.9807	1	1	25.5
0.8236	0.8754	1	1	25.4

$Fr_2 = 19.0$				
Fr_1	h/d	Branch	Category	$T°C$
37.97	2.792	1	1	25.5
22.00	2.367	1	1	25.4
9.991	1.864	1	1	25.3
3.997	1.489	1	1	25.5
3.003	1.428	1	1	25.6
2.000	1.351	S	3	25.4
1.508	1.317	S	3	25.3
1.166	1.295	2	5	25.6
0.8277	1.284	2	5	25.7

$Fr_2 = 28.5$				
Fr_1	h/d	Branch	Category	$T°C$
38.00	2.947	1	1	25.4
22.01	2.521	1	1	25.4
9.990	2.085	1	1	25.3
5.997	1.847	1	1	25.4
4.001	1.742	1	1	25.5
3.002	1.698	1	1	25.4
2.002	1.643	S	3	25.5
1.520	1.626	S	3	25.6
1.182	1.620	S	3	25.4
0.8342	1.599	2	5	25.4

$Fr_2 = 38.0$				
Fr_1	h/d	Branch	Category	$T°C$
37.98	3.085	1	1	26.0
22.07	2.682	1	1	26.0
10.05	2.240	1	1	25.9
8.018	2.151	1	1	25.8
6.001	2.030	1	1	25.8
3.999	1.986	S	3	25.7
3.002	1.936	S	3	25.5
2.003	1.908	2	5	25.5
1.537	1.881	2	5	25.3
0.8434	1.864	2	5	25.4

Table C.17: Experimental liquid-entrainment data for $l/d = 1.5$ and $\alpha = 60°$

$Fr_2 = 9.5$				
Fr_1	h/d	Branch	Category	$T°C$
38.00	2.691	1	1	18.2
21.98	2.222	1	1	18.1
10.01	1.708	1	1	18.3
4.002	1.239	1	1	18.4
2.999	1.151	1	1	18.2
1.998	1.040	1	1	18.3
1.501	0.9851	1	1	18.2
1.161	0.9409	1	1	18.3

$Fr_2 = 19.0$				
Fr_1	h/d	Branch	Category	$T°C$
38.10	2.796	1	1	18.3
22.01	2.327	1	1	18.3
9.990	1.819	1	1	18.4
4.003	1.377	1	1	18.5
3.001	1.300	1	1	18.3
2.001	1.189	1	1	18.4
1.509	1.140	1	1	18.3
1.166	1.101	1	1	18.5
0.8278	1.040	1	1	18.3

$Fr_2 = 28.5$				
Fr_1	h/d	Branch	Category	$T°C$
38.03	2.912	1	1	18.8
22.01	2.437	1	1	18.9
9.990	1.940	1	1	19.1
4.002	1.532	1	1	19.0
2.011	1.361	1	1	19.2
0.8353	1.245	1	1	19.5

$Fr_2 = 38.0$				
Fr_1	h/d	Branch	Category	$T°C$
37.98	3.028	1	1	19.2
22.07	2.564	1	1	19.2
10.03	2.073	1	1	19.4
4.001	1.681	1	1	19.5
2.027	1.554	1	1	19.8
0.8408	1.432	1	1	19.9

Table C.18: Experimental liquid-entrainment data for $l/d = 2.0$ and $\alpha = 0°$

$Fr_2 = 9.5$				
Fr_1	h/d	Branch	Category	$T°C$
37.93	2.736	1	1	20.4
29.94	2.526	1	1	20.2
18.59	2.162	1	1	20.3
13.89	1.946	1	1	20.4
10.00	1.770	1	1	20.5
9.478	1.719	S	3	20.0
7.717	1.691	2	5	20.1
5.975	1.642	2	5	19.9
3.991	1.619	2	5	19.8
2.975	1.603	2	5	19.4
1.990	1.598	2	5	19.6
1.505	1.587	2	5	19.5
1.164	1.593	2	5	19.3
0.8268	1.593	2	5	19.6

$Fr_2 = 19.0$				
Fr_1	h/d	Branch	Category	$T°C$
37.78	2.902	1	1	20.5
30.08	2.714	1	1	20.5
26.10	2.587	1	1	20.3
22.10	2.482	S	3	20.5
19.09	2.377	S	3	20.4
17.94	2.333	S	3	20.1
14.07	2.228	2	5	20.0
9.841	2.162	2	5	19.9
7.807	2.112	2	5	19.8
5.957	2.074	2	5	19.9
4.027	2.051	2	5	19.4
2.994	2.034	2	5	19.7
2.004	2.018	2	5	19.5
1.515	2.018	2	5	19.6
1.172	2.007	2	5	19.5
0.8333	2.013	2	5	19.3

$Fr_2 = 28.5$				
Fr_1	h/d	Branch	Category	$T°C$
37.79	3.079	1,2	2	20.5
29.89	2.924	1,2	2	20.4
28.45	2.863	S	3	20.2
26.16	2.836	1,2	4	20.3
22.10	2.736	1,2	4	20.1
17.87	2.626	2	5	20.0
13.94	2.527	2	5	19.9
9.912	2.448	2	5	20.0
7.856	2.415	2	5	20.1
5.989	2.376	2	5	19.8
4.063	2.355	2	5	19.6
3.026	2.366	2	5	19.7
2.017	2.338	2	5	19.5
1.529	2.333	2	5	19.3
1.180	2.333	2	5	19.5
0.8383	2.333	2	5	19.4

$Fr_2 = 38.0$				
Fr_1	h/d	Branch	Category	$T°C$
38.08	3.283	S	3	19.6
30.10	3.062	S	3	19.8
25.97	3.002	S	3	20.6
22.12	2.919	S	3	20.1
17.98	2.825	2	5	20.3
13.99	2.753	2	5	20.5
10.07	2.681	2	5	19.9
7.982	2.664	2	5	20.1
6.000	2.626	2	5	20.3
3.997	2.598	2	5	20.3
3.064	2.587	2	5	20.2
2.043	2.570	2	5	19.9
1.545	2.570	2	5	20.5
1.197	2.571	2	5	19.9
0.8497	2.560	2	5	20.0

Table C.19: Experimental liquid-entrainment data for $l/d = 2.0$ and $\alpha = 10°$

$Fr_2 = 9.5$				
Fr_1	h/d	Branch	Category	$T°C$
34.06	2.571	1	1	20.9
29.95	2.459	1	1	20.8
26.00	2.333	1	1	20.7
22.03	2.184	1	1	20.4
18.01	2.051	1	1	19.9
14.00	1.886	1	1	19.5
9.984	1.698	1	1	19.6
8.021	1.582	1	1	19.9
6.003	1.427	1	1	20.1
3.997	1.267	1	1	20.3
3.518	1.234	S	3	20.4
3.000	1.212	2	5	20.6
1.504	1.195	2	5	20.5
0.8264	1.190	2	5	20.2

$Fr_2 = 19.0$				
Fr_1	h/d	Branch	Category	$T°C$
38.09	2.819	1	1	20.6
34.00	2.714	1	1	20.5
30.09	2.604	1	1	20.7
26.03	2.477	1	1	20.2
22.03	2.355	1	1	19.9
17.98	2.228	1	1	20.1
13.99	2.051	1	1	19.8
9.836	1.869	1	1	19.6
8.809	1.825	S	3	19.9
7.999	1.809	2	5	20.1
6.005	1.726	2	5	20.4
3.000	1.670	2	5	20.7
1.515	1.648	2	5	20.5
0.8325	1.643	2	5	20.6

$Fr_2 = 28.5$				
Fr_1	h/d	Branch	Category	$T°C$
38.00	2.929	1	1	19.1
33.97	2.841	1	1	19.1
30.01	2.736	1	1	19.2
25.98	2.625	1	1	19.1
22.00	2.526	1	1	19.3
18.02	2.394	1	1	19.4
13.75	2.261	S	3	19.6
12.02	2.222	2	5	19.5
10.02	2.178	2	5	19.7
6.000	2.051	2	5	19.4
2.004	1.974	2	5	19.6
0.8377	1.946	2	5	19.5

$Fr_2 = 38.0$				
Fr_1	h/d	Branch	Category	$T°C$
33.96	3.001	S	3	20.8
30.00	2.907	S	3	20.7
25.97	2.786	S	3	20.8
22.00	2.676	S	3	19.4
17.97	2.614	1,2	4	19.5
13.97	2.520	2	5	19.6
10.03	2.399	2	5	20.0
3.998	2.266	2	5	20.3
1.541	2.222	2	5	20.5
0.8453	2.200	2	5	20.2

Table C.20: Experimental liquid-entrainment data for $l/d = 2.0$ and $\alpha = 30°$

$Fr_2 = 9.5$				
Fr_1	h/d	Branch	Category	$T°C$
38.02	2.643	1	1	25.1
22.01	2.173	1	1	25.0
7.999	1.552	1	1	25.2
6.006	1.370	1	1	24.9
3.996	1.199	1	1	25.1
2.999	1.099	1	1	25.2
1.996	0.9889	1	1	25.0
1.490	0.9282	1	1	25.1

$Fr_2 = 19.0$				
Fr_1	h/d	Branch	Category	$T°C$
38.03	2.742	1	1	22.5
22.04	2.272	1	1	22.3
8.003	1.654	1	1	22.6
4.000	1.350	1	1	22.4
3.020	1.278	1	1	22.5
2.013	1.184	1	1	22.7
1.506	1.124	1	1	22.3
1.165	1.085	1	1	22.4

$Fr_2 = 28.5$				
Fr_1	h/d	Branch	Category	$T°C$
38.03	2.842	1	1	22.1
21.98	2.400	1	1	22.2
8.001	1.786	1	1	22.2
5.999	1.648	1	1	22.1
4.000	1.505	1	1	22.3
3.015	1.460	1	1	23.1
2.223	1.400	1	1	23.2
2.012	1.373	1,2	2	23.4
1.871	1.367	S	3	23.1
1.523	1.386	1,2	4	23.3
1.179	1.381	2	5	23.2
0.8325	1.375	2	5	23.4

$Fr_2 = 38.0$				
Fr_1	h/d	Branch	Category	$T°C$
37.88	2.946	1	1	24.4
21.98	2.521	1	1	24.4
8.028	1.963	1	1	24.2
6.034	1.825	1	1	24.1
4.010	1.709	3	3	24.0
3.041	1.654	3	3	23.9
1.995	1.615	2	5	23.8
1.536	1.604	2	5	23.6
1.187	1.593	2	5	23.2
0.8429	1.594	2	5	22.7

Table C.21: Experimental liquid-entrainment data for $l/d = 2.0$ and $\alpha = 60°$

$Fr_2 = 9.5$				
Fr_1	h/d	Branch	Category	$T°C$
37.82	2.639	1	1	23.6
26.07	2.297	1	1	23.7
14.03	1.855	1	1	23.8
6.014	1.318	1	1	23.7
3.003	1.053	1	1	23.6
1.999	0.9317	1	1	23.5
1.492	0.8931	1	1	23.6
1.154	0.8213	1	1	23.7

$Fr_2 = 19.0$				
Fr_1	h/d	Branch	Category	$T°C$
38.05	2.773	1	1	24.6
26.04	2.430	1	1	24.7
14.02	1.972	1	1	24.8
5.985	1.396	1	1	24.7
2.994	1.125	1	1	24.8
2.053	1.032	1	1	24.6
1.500	0.9653	1	1	24.5
1.160	0.9211	1	1	24.8

$Fr_2 = 28.5$				
Fr_1	h/d	Branch	Category	$T°C$
38.04	2.860	1	1	24.7
25.94	2.518	1	1	24.8
13.99	1.998	1	1	24.9
8.001	1.683	1	1	24.8
3.999	1.330	1	1	24.7
2.999	1.241	1	1	24.6
2.002	1.131	1	1	24.5
1.514	1.065	1	1	24.4
1.171	1.037	1	1	24.5

$Fr_2 = 38.0$				
Fr_1	h/d	Branch	Category	$T°C$
38.12	2.943	1	1	24.2
34.04	2.849	1	1	24.2
22.04	2.428	1	1	24.4
9.987	1.898	1	1	24.5
4.003	1.423	1	1	24.4
2.000	1.225	1	1	24.6
1.528	1.202	1	1	24.5
1.181	1.131	1	1	24.4
0.8387	1.092	1	1	24.5

Table C.22: Experimental liquid-entrainment data for $l/d = 8.0$ and $\alpha = 0°$

$Fr_2 = 9.5$				
Fr_1	h/d	Branch	Category	$T°C$
38.07	2.654	1	1	20.8
33.56	2.549	1	1	20.9
29.40	2.422	1	1	20.8
25.51	2.312	1	1	20.9
21.84	2.168	1	1	20.7
18.35	2.047	1	1	20.6
15.02	1.897	1	1	20.8
11.83	1.754	1	1	20.9
9.506	1.604	S	3	20.5
8.007	1.593	2	5	20.6
3.002	1.604	2	5	20.7
0.8248	1.599	2	5	20.8

$Fr_2 = 19.0$				
Fr_1	h/d	Branch	Category	$T°C$
38.07	2.665	1	1	21.2
33.48	2.560	1	1	21.1
29.25	2.450	1	1	21.0
25.22	2.289	1	1	20.9
21.31	2.178	1	1	20.8
19.00	2.085	S	3	21.0
17.82	2.068	2	5	21.1
11.30	2.073	2	5	21.2
8.246	2.062	2	5	21.3
4.000	2.068	2	5	21.2
2.479	2.068	2	5	21.1
0.8254	2.062	2	5	21.0

$Fr_2 = 28.5$				
Fr_1	h/d	Branch	Category	$T°C$
37.93	2.703	1	1	21.0
33.25	2.593	1	1	20.9
29.02	2.449	1	1	20.8
28.48	2.439	S	3	20.9
25.03	2.412	2	5	20.7
17.67	2.378	2	5	20.6
11.01	2.383	2	5	20.9
5.228	2.367	2	5	21.1
2.961	2.367	2	5	21.2
0.8409	2.366	2	5	21.0

$Fr_2 = 38.0$				
Fr_1	h/d	Branch	Category	$T°C$
37.60	2.766	S	3	21.7
33.10	2.722	2	5	21.8
24.86	2.694	2	5	21.7
17.30	2.675	2	5	21.6
10.64	2.644	2	5	21.5
4.980	2.632	2	5	21.0
2.999	2.643	2	5	21.3
0.8514	2.638	2	5	21.5

Table C.23: Experimental liquid-entrainment data for $l/d = 8.0$ and $\alpha = 10°$

$Fr_2 = 9.5$				
Fr_1	h/d	Branch	Category	$T°C$
37.97	2.633	1	1	19.3
34.21	2.528	1	1	19.2
30.03	2.396	1	1	19.1
26.07	2.286	1	1	19.0
21.84	2.137	1	1	18.8
17.78	1.987	1	1	18.9
13.95	1.816	1	1	18.7
10.04	1.645	1	1	18.8
8.003	1.512	1	1	18.9
6.002	1.335	1	1	19.0
3.997	1.170	1	1	19.3
3.000	1.081	1	1	19.2
1.990	0.9543	1	1	19.2
1.515	0.8881	1	1	19.1

$Fr_2 = 19.0$				
Fr_1	h/d	Branch	Category	$T°C$
37.93	2.634	1	1	19.0
34.04	2.518	1	1	18.9
29.80	2.402	1	1	18.8
25.84	2.291	1	1	18.8
22.12	2.164	1	1	18.7
18.01	1.999	1	1	18.6
14.11	1.844	1	1	18.6
10.12	1.640	1	1	18.7
8.089	1.518	1	1	18.6
5.975	1.342	1	1	18.8
4.001	1.203	1	1	18.9
3.005	1.125	1	1	19.0
2.060	0.9874	1	1	19.1
1.510	0.9101	1	1	19.0

$Fr_2 = 28.5$				
Fr_1	h/d	Branch	Category	$T°C$
37.78	2.677	1	1	19.6
33.85	2.561	1	1	19.6
29.97	2.457	1	1	19.5
25.90	2.313	1	1	19.6
22.14	2.175	1	1	19.7
17.94	2.015	1	1	19.6
14.00	1.855	1	1	19.5
9.97	1.639	1	1	19.4
7.91	1.502	1	1	19.1
5.94	1.341	1	1	19.0
3.93	1.181	1	1	18.9
2.966	1.109	1	1	19.0
2.012	0.953	1	1	19.0
1.792	0.9315	S	3	18.9
1.514	0.9259	2	5	19.1
1.171	0.9314	2	5	19.2
0.8314	0.9314	2	5	19.2

$Fr_2 = 38.0$				
Fr_1	h/d	Branch	Category	$T°C$
37.93	2.688	1	1	19.3
33.95	2.573	1	1	19.0
29.9	2.462	1	1	18.9
26.13	2.374	1	1	18.7
21.89	2.197	1	1	18.5
17.95	2.042	1	1	18.5
13.9	1.876	1	1	18.6
10.09	1.683	1	1	18.7
8.007	1.529	1	1	18.8
6.002	1.345	1	1	18.9
3.994	1.197	S	3	19.0
2.999	1.191	2	5	19.2
1.501	1.191	2	5	19.1
0.8398	1.191	2	5	19.0

Table C.24: Experimental liquid-entrainment data for $l/d = 8.0$ and $\alpha = 30°$

$Fr_2 = 9.5$				
Fr_1	h/d	Branch	Category	$T°C$
37.97	2.658	1	1	18.8
34.13	2.553	1	1	18.8
29.92	2.420	1	1	18.7
26.05	2.321	1	1	18.5
22.06	2.178	1	1	18.6
18.02	2.029	1	1	18.4
14.20	1.869	1	1	18.5
9.992	1.659	1	1	18.3
7.994	1.526	1	1	18.5
5.996	1.338	1	1	18.5
3.991	1.189	1	1	18.6
2.996	1.095	1	1	18.7
1.987	0.9737	1	1	18.8
1.513	0.9075	1	1	18.7

$Fr_2 = 19.0$				
Fr_1	h/d	Branch	Category	$T°C$
37.78	2.691	1	1	19.5
33.98	2.575	1	1	19.2
30.05	2.448	1	1	19.0
26.12	2.327	1	1	18.6
21.69	2.166	1	1	18.5
17.94	2.034	1	1	18.7
14.05	1.852	1	1	18.9
10.05	1.669	1	1	19.0
8.028	1.532	1	1	19.1
5.992	1.327	1	1	19.0
3.990	1.184	1	1	18.9
2.998	1.068	1	1	19.2
2.056	0.9462	1	1	19.1
1.502	0.8799	1	1	19.0

$Fr_2 = 28.5$				
Fr_1	h/d	Branch	Category	$T°C$
38.15	2.708	1	1	19.0
34.29	2.620	1	1	19.1
29.85	2.476	1	1	19.0
26.14	2.338	1	1	19.0
22.04	2.222	1	1	18.8
18.71	2.072	1	1	18.6
13.93	1.874	1	1	18.5
10.18	1.697	1	1	18.6
8.016	1.543	1	1	18.7
6.034	1.355	1	1	18.6
4.036	1.200	1	1	18.7
3.005	1.084	1	1	18.7
2.005	0.9629	1	1	18.6
1.517	0.8856	1	1	18.8

$Fr_2 = 38.0$				
Fr_1	h/d	Branch	Category	$T°C$
37.69	2.692	1	1	19.4
33.72	2.619	1	1	19.4
29.65	2.503	1	1	19.3
25.93	2.365	1	1	19.5
22.07	2.244	1	1	19.4
18.11	2.073	1	1	19.1
14.11	1.880	1	1	19.0
10.05	1.692	1	1	19.2
8.001	1.576	1	1	19.1
6.020	1.366	1	1	19.3
3.998	1.206	1	1	19.4
3.003	1.095	1	1	19.5
2.002	0.9735	1	1	19.4
1.530	0.9073	1	1	19.6

APPENDIX D

REPEATABILITY STUDIES

D.1 Introduction

In order to ensure the quality of the data of the present investigation, a repeatability study was conducted. This appendix provides the results of, and demonstrates the quality of, the experimental data collected.

D.2 Single-Branch Repeatability Study

The single-discharge repeatability studies were at the conclusion of the data collection phase of the current investigation. Data were collected for gas entrainment and liquid entrainment. Table D.1 and D.2 show the results of the repeatability study for gas entrainment and liquid entrainment, respectively. As can be seen, the repeat data are in excellent agreement with the original single-discharge data reported. The maximum differences were -2.0% for gas entrainment and less than 1.0% for liquid entrainment.

Table D.1: Gas entrainment repeatability results for single discharge

Fr	4	42
$h/d_{original\ exp.}$	0.8784	2.533
$h/d_{repeated\ exp.}$	0.8607	2.487
% difference	-2.0	-1.8

Table D.2: Liquid entrainment repeatability results for single discharge

Fr	4	18	30
$h/d_{original\ exp.}$	1.169	1.996	2.388
$h/d_{repeated\ exp.}$	1.158	1.997	2.406
% difference	-0.9	-0.05	+0.75

D.3 Dual-Branch Repeatability Study

The repeated data for dual discharge showed very good agreement with the original reported data. Not only was the onset height, h/d, repeated very well, but also the category of entrainment (as given in Tables 5.2 and 5.3) for gas and liquid entrainments, repectively, was repeated very well.

D.3.1 Gas Entrainment

Table D.3 and D.4 show the repeated data for $l/d = 1.5$ and $\alpha = 10°$ and $30°$, respectively. Table D.3 shows data for Fr_2 of 14.0 and 56.6. Table D.4 shows data for Fr_2 of 14.0, 42.5, and 56.6. As can be seen, the data are in excellent agreement with the reported data. The difference in the repeated points in Table D.3 is -1.6% for $Fr_2 = 14.0$ and -1.2% for $Fr_2 = 56.6$. In Table D.4, the differences are -3.7%, -1.8%, and -0.5% for $Fr_2 = 14.0$, 42.5, and 56.6, respectively.

Table D.3: Gas entrainment repeatability results for $l/d = 1.5$ and $\alpha = 10°$

Fr_2	14.0	56.6
Fr_1	8	34
$h/d_{original\ exp.}$	1.634	3.242
$h/d_{repeated\ exp.}$	1.608	3.202
% difference	-1.6	-1.2

Table D.4: Gas entrainment repeatability results for $l/d = 1.5$ and $\alpha = 30°$

Fr_2	14.0	42.5	56.6
Fr_1	2	9	34
$h/d_{original\ exp.}$	1.03	2.131	3.032
$h/d_{repeated\ exp.}$	1.00	2.093	3.018
% difference	-3.7	-1.8	-0.5

Table D.5 shows the repeated data for $l/d = 2.0$, $\alpha = 30°$, and Fr_2 of 14.0 and 56.6. As can be seen, the data are in excellent agreement with the differences of -3.0% and -1.1% for $Fr_2 = 14.0$ and 56.6, respectively.

Table D.5: Gas entrainment repeatability results for $l/d = 2.0$ and $\alpha = 30°$

Fr_2	14.0	56.6
Fr_1	1.025	34
$h/d_{original\ exp.}$	0.67	2.936
$h/d_{repeated\ exp.}$	0.64	2.903
% difference	-3.0	-1.1

Finally, Table D.6 shows a simultaneous point for $l/d = 8.0$, $\alpha = 10°$, and $Fr_2 = 56.6$. The repeated data are practically coincident with the original point; the difference is 0.4%.

Table D.6: Gas entrainment repeatability results for $l/d = 8.0$ and $\alpha = 10°$

Fr_2	56.6
Fr_1	10.6
$h/d_{original\ exp.}$	1.413
$h/d_{repeated\ exp.}$	1.419
% difference	+0.4

D.3.2 Liquid Entrainment

Table D.7 and Table D.8 give the repeated data for $l/d = 1.5$ and $\alpha = 10°$ and $\alpha = 10°$, respectively. The data are in very good agreement with the original and the maximum difference was 3.6% in Table D.7 and 4.7% in Table D.8.

Table D.7: Liquid entrainment repeatability results for $l/d = 1.5$ and $\alpha = 10°$

Fr_2	28.5			
Fr_1	8	10	14	18
$h/d_{original\ exp.}$	2.235	2.291	2.418	2.550
$h/d_{repeated\ exp.}$	2.293	2.354	2.470	2.641
% difference	+2.60	+2.75	+2.15	+3.6

Table D.8: Liquid entrainment repeatability results for $l/d = 1.5$ and $\alpha = 30°$

Fr_2	9.5	19.0	38.0
Fr_1	1.5	1.17	22
$h/d_{original\ exp.}$	1.019	1.295	2.682
$h/d_{repeated\ exp.}$	1.067	1.349	2.747
% difference	+4.7	+4.17	+2.42

Table D.9 contains a repeated simultaneous point and a data point where entrainment occurred at branch 1 for $l/d = 2.0$, $\alpha = 10°$, and $Fr_2 = 28.5$, respectively.

The data points are in excellent agreement with the reported data with a maximum difference of 2.92%. Table D.10 shows repeated data for $l/d = 2.0$, $\alpha = 30°$, and $Fr_2 = 19.0$. The data are in excellent agreement with a maximum difference less than 2.0%.

Table D.9: Liquid entrainment repeatability results for $l/d = 2.0$ and $\alpha = 10°$

Fr_2	28.5	
Fr_1	14	26
$h/d_{original\ exp.}$	2.261	2.625
$h/d_{repeated\ exp.}$	2.327	2.686
% difference	+2.92	+2.32

Table D.10: Liquid entrainment repeatability results for $l/d = 2.0$ and $\alpha = 30°$

Fr_2	19.0		
Fr_1	1.167	1.5	2.0
$h/d_{original\ exp.}$	1.085	1.124	1.184
$h/d_{repeated\ exp.}$	1.10	1.144	1.194
% difference	+1.38	+1.78	+0.84

Finally, Table D.11 contains repeated data for $l/d = 8.0$ and $\alpha = 10°$. The data are in good agreement with the reported data with a maximum difference of 3.72%.

Table D.11: Liquid entrainment repeatability results for $l/d = 8.0$ and $\alpha = 10°$

Fr_2	28.5	38.0	
Fr_1	2	6	30
$h/d_{original\ exp.}$	0.953	1.345	2.462
$h/d_{repeated\ exp.}$	0.937	1.395	2.538
% difference	-1.68	+3.72	+3.09

APPENDIX E

EXPERIMENTAL UNCERTAINTY ANALYSIS

E.1 Introduction

An uncertainty analysis was performed following the method of Kline and McClintock (1953) for single-sample experiments. Kline and McClintock define error as the difference between the true and observed values. The uncertainty is defined as the possible value the error might have. Thus, error and uncertainty differ since the error is a certain fixed number whereas the uncertainty may vary depending upon the manner in which the observation was taken. Kline and McClintock attribute the important distinction between uncertainty and error to Airy (1879). The following expression was used to perform the uncertainty analysis for each independent variable.

$$\omega_Q = \left(\left[\frac{\partial Q}{\partial x} \omega_x \right]^2 + \left[\frac{\partial Q}{\partial y} \omega_y \right]^2 + \dots \right)^{0.5} \tag{E.1}$$

where Q is the result which is a function of independent variables x, y, ... each of which is normally distributed. The present uncertainty analysis was based on an odds of 20 to 1. The probability that the measured values are within $\pm\omega$ of the true value was approximately 95%.

The uncertainty analysis was performed here for six representative data sets: three for gas entrainment and three for liquid entrainment. The reason for performing an abbreviated uncertainty analysis stems from the fact that the experimental apparatus was used in previous studies. The uncertainty in the data obtained from the experimental rig has been established by Parrott (1993) and Hassan (1995).

E.2 Gas Entrainment

For gas entrainment the uncertainty in each independent variable was assessed. The uncertainty of the separation distance l/d develops from the uncertainty in the ruler used to obtain the values. The uncertainty in l/d was estimated to be $\pm 0.1\ mm$. The uncertainty in the angular inclination of the branches develops from the protractor used to obtain the measurement. The protractor had a resolution of 0.5°. Therefore, the uncertainty in α was estimated to be ± 0.5 °.

E.2.1 Froude Number

The uncertainty in the the Froude number was obtained using Equation (E.1) applied to Equation (E.2). The uncertainty analysis was the same for Fr_1 and Fr_2. Therefore, the analysis was performed for Fr_1 only.

$$Fr = \frac{4\dot{m}}{\pi\sqrt{gd^5\rho\Delta\rho}} \tag{E.2}$$

The resulting expression was

$$\omega_{Fr} = \left(\left[\frac{\partial Fr}{\partial \dot{m}_L}\omega_{\dot{m}_L}\right]^2 + \left[\frac{\partial Fr}{\partial g}\omega_g\right]^2 + \left[\frac{\partial Fr}{\partial d}\omega_d\right]^2 + \left[\frac{\partial Fr}{\partial \rho_G}\omega_{\rho_G}\right]^2 + \left[\frac{\partial Fr}{\partial \rho_L}\omega_{\rho_L}\right]^2 \right)^{0.5} \tag{E.3}$$

The uncertainty in the gravitational constant was considered negligible. The branch diameter was estimated to have an uncertainty $\pm 0.1\ mm$ which was based on the ruler used to obtain the measurement.

The uncertainty in the mass flow rate through the branch was estimated by applying Equation (E.1) to obtain

$$\omega_{\dot{m}_L} = \left(\left[\frac{\partial \dot{m}_L}{\partial \dot{Q}}\omega_{\dot{Q}}\right]^2 + \left[\frac{\partial \dot{m}_L}{\partial \rho_L}\omega_{\rho_L}\right]^2 \right)^{0.5} \tag{E.4}$$

The uncertainty in $\dot{Q}$ was calculated based upon the root-sum-of-squares of the flow meter reading and the uncertainty in the calibration. The uncertainty in the flow meter reading was estimated to be $\pm 0.5\%$ of the full scale reading. The uncertainty in the calibration was estimated to be $\pm 0.4\%$ of the full scale reading. Thus, for the large flow meter the uncertainty was then $\pm 689\ cm^3/s$ and for the small flow meter the uncertainty was $\pm 65.8\ cm^3/s$.

E.2.2 Water Density

The water density was approximated as the density of saturated liquid water at the same temperature. The tolerance for density from the steam tables was $0.2\ kg/m^3$. The uncertainty in the temperature measurement was estimated to be $\pm 0.1°C$. Therefore, the uncertainty in the water density was calculated as the root-sum-of-squares of the steam table tolerance and the temperature measurement. Thus, the uncertainty in the water density measurement was $\pm 0.22\ kg/m^3$.

E.2.3 Air Density

The air density in the test section was calculated assuming the air behaved as an ideal gas. The uncertainty in the air density calculation arose from the uncertainty in the air temperature and pressure measurements. The uncertainty in the ideal gas constant R was assumed negligible. The uncertainty in the temperature was $\pm 0.1°C$ and the uncertainty in the pressure measurement was estimated to be $\pm 3.5\ kPa$. The uncertainty in the air density was calculated by applying Equation (E.1) to the ideal gas law. Equation (E.5) was used to calculate the air density uncertainty.

$$\omega_{\rho_G} = \left(\left[\frac{1}{RT} \omega_P \right]^2 + \left[\frac{P}{RT^2} \omega_T \right]^2 \right)^{0.5} \tag{E.5}$$

E.2.4 Results

Tables E.1 through E.3 provide the results of the uncertainty analysis for gas entrainment. As can be seen, the velocity through the branch was the largest contributor to the uncertainty in the Froude number. For the data sets examined, the uncertainty of the Froude number was not greater than ±4.77%. The tables are arranged in order of decreasing Froude number. Following down a column, the uncertainty in the Froude number increases to a maximum, then the next entry in the table shows a smaller value of the uncertainty in the Froude number. This indicates the change from the large flow meter to the small flow meter. The uncertainty then, steadily increases. The trend in the uncertainty down the column follows from the calibration and use of flow meters where it is generally known that the flow meters are more accurate at the top of the scale.

The uncertainty in the air density and water density were insignificant. The uncertainty in Fr_2 will be identical for the uncertainty in Fr_1 when Fr_1 and Fr_2 are equal.

Table E.1: Gas-entrainment uncertainty analysis for $l/d = 1.5$, $\alpha = 60°$, and $Fr_2 = 28.5$

$\%d$	$\%A$	$\%\dot{Q}$	$\%\dot{m}$	$\%\rho_G$	$\%\rho_L$	$\%Fr$
1.57	3.16	0.80	0.80	0.69	0.02	3.36
1.57	3.16	1.63	1.63	0.69	0.02	3.47
1.57	3.16	3.09	3.10	0.69	0.02	3.67
1.57	3.16	0.67	0.67	0.69	0.02	3.26
1.57	3.16	1.77	1.77	0.69	0.02	3.28
1.57	3.16	3.60	3.60	0.69	0.02	4.77

Table E.2: Gas-entrainment uncertainty analysis for $l/d = 2.0$, $\alpha = 30°$, and $Fr_2 = 14.0$

$\%d$	$\%A$	$\%\dot{Q}$	$\%\dot{m}$	$\%\rho_G$	$\%\rho_L$	$\%Fr$
1.57	3.16	0.80	0.80	0.69	0.02	3.36
1.57	3.16	1.34	1.34	0.69	0.02	3.43
1.57	3.16	3.10	3.10	0.69	0.02	3.67
1.57	3.16	0.67	0.67	0.69	0.02	3.26
1.57	3.16	2.10	2.10	0.69	0.02	3.33
1.57	3.16	3.60	3.60	0.69	0.02	4.77

Table E.3: Gas-entrainment uncertainty analysis for $l/d = 8.0$, $\alpha = 0°$, and $Fr_2 = 56.6$

$\%d$	$\%A$	$\%\dot{Q}$	$\%\dot{m}$	$\%\rho_G$	$\%\rho_L$	$\%Fr$
1.57	3.16	0.85	0.85	0.69	0.02	3.37
1.57	3.16	0.92	0.92	0.69	0.02	3.38
1.57	3.16	0.98	0.98	0.69	0.02	3.39
1.57	3.16	1.11	1.11	0.69	0.02	3.40
1.57	3.16	1.34	1.34	0.69	0.02	3.44
1.57	3.16	1.63	1.63	0.69	0.02	3.47
1.57	3.16	2.15	2.15	0.69	0.02	3.55
1.57	3.16	3.10	3.10	0.69	0.02	3.67
1.57	3.16	0.53	0.53	0.69	0.02	3.26
1.57	3.16	0.67	0.67	0.69	0.02	3.26
1.57	3.16	0.89	0.89	0.69	0.02	3.27

Gas-entrainment uncertainty analysis for $l/d = 8.0$, $\alpha = 0°$, and $Fr_2 = 56.6$

$\%d$	$\%A$	$\%\dot{Q}$	$\%\dot{m}$	$\%\rho_G$	$\%\rho_L$	$\%Fr$
1.57	3.16	1.33	1.33	0.69	0.02	3.27
1.57	3.16	1.77	1.77	0.69	0.02	3.28
1.57	3.16	2.13	2.13	0.69	0.02	3.28
1.57	3.16	2.66	2.66	0.69	0.02	3.29
1.57	3.16	3.15	3.15	0.69	0.02	3.69
1.57	3.16	3.60	3.60	0.69	0.02	4.77

E.3 Liquid Entrainment

The uncertainty in the independent variables l/d and α were the same as in Gas Entrainment.

E.3.1 Froude Number

The uncertainty in the Froude number develops in the same manner as given in the gas entrainment analysis. However, in Equation (E.2), the mass flow rate and density of the lighter phase were now the properties through the branch inlet. The uncertainty analysis was the same for Fr_1 and Fr_2. Therefore, the analysis was performed for

Fr_1 only. The expression to calculate the uncertainty in the Froude number was,

$$\omega_{Fr} = \left(\left[\frac{\partial Fr}{\partial \dot{m}_G} \omega_{\dot{m}_G} \right]^2 + \left[\frac{\partial Fr}{\partial g} \omega_g \right]^2 + \left[\frac{\partial Fr}{\partial d} \omega_d \right]^2 + \left[\frac{\partial Fr}{\partial \rho_{G,i}} \omega_{\rho_{G,i}} \right]^2 + \left[\frac{\partial Fr}{\partial \rho_L} \omega_{\rho_L} \right]^2 \right)^{0.5} \quad \text{(E.6)}$$

The values of ω_d and ω_{ρ_L} were the same as estimated for gas entrainment. The uncertainty in the gravitational constant was assumed negligible. The values of $\omega_{\dot{m}_G}$ and $\omega_{\rho_{G,i}}$ were calculated using Equation (E.1).

Branch Mass Flow Rate

The uncertainty in the mass flow rate was evaluated from the following equation.

$$\omega_{\dot{m}} = \left([\rho_{G,fm} \omega_{ALPM}]^2 + [ALPM \omega_{\rho_{G,fm}}]^2 \right)^{0.5} \quad \text{(E.7)}$$

The uncertainty in $ALPM$ in the mass flow uncertainty calculation was estimated by applying Equation (E.1) to Equation (4.3). The resulting equation was:

$$\omega_{ALPM} = \left(\left[\left(\frac{\rho_{G,ST}}{\rho_{G,fm}} \right)^{0.5} \omega_{SLPM} \right]^2 + \left[0.5 SLPM \frac{\rho_{G,ST}^{0.5}}{\rho_{G,fm}^{1.5}} \omega_{\rho_{G,fm}} \right]^2 \right)^{0.5} \quad \text{(E.8)}$$

The uncertainty in $SLPM$ was calculated based upon the root-sum-of-squares of the flow meter reading and the uncertainty in the calibration. The uncertainty in the flow meter reading was estimated to be $\pm 0.5\%$ of the full scale reading. The uncertainty in the calibration was estimated to be $\pm 0.4\%$ of the full scale reading. Thus, for the small flow meter the uncertainty was then 1.07 l/min and the uncertainty for the large flow meter was 8.02 l/min.

The uncertainty in the density of the air in the flow meter stems from assuming the air behaved as an ideal gas. The equation used to calculate the uncertainty was

$$\omega_{\rho_{G,fm}} = \left(\left[\frac{1}{RT} \omega_P \right]^2 + \left[\frac{P}{RT^2} \omega_T \right]^2 \right)^{0.5} \tag{E.9}$$

The uncertainty in the temperature was the same as for gas entrainment. The uncertainty in the pressure measurement was calculated as the root-sum-of-squares of the uncertainty in the mercury manometer used to measure the pressure and the barometer used to measure the atmospheric pressure. The uncertainty in the mercury manometer was $\pm 0.05\ inHg$ and the uncertainty in the barometer was $\pm 0.1\ mmHg$. Therefore, the uncertainty in the pressure was $\pm 0.170\ kPa$.

E.3.2 Branch Inlet Air Density

The uncertainty in the branch inlet air density develops by assuming the air behaved as an ideal gas and by assuming the expansion from stagnant conditions to the branch inlet was isentropic. The following equation was used to calculate the uncertainty in the air density at the branch inlet.

$$\omega_{\rho_{G,i}} = \left(\left[\frac{1}{RT_{G,i}} \omega_{P_{G,i}} \right]^2 + \left[\frac{P_{G,i}}{RT_{G,i}^2} \omega_{T_{G,i}} \right] \right)^{0.5} \tag{E.10}$$

Thus, based on the assumptions, the calculations of the pressure and temperature at the branch inlet propogated uncertainty to the density calculation. The uncertainty in calculating the pressure and temperature was estimated based upon the assumption of isentropic expansion. If isentropic expansion was considered to be the upper limit on n, the polytropic exponent, then an isothermal expansion would represent the lower limit on n with the gas still behaving ideally. Therefore, for this uncertainty analysis a median exponent of 1.2 was used to calculate the temperatures and pressures for the expansion process. The uncertainty of each property was then taken as the difference between the two process calculations.

E.3.3 Results

Tables E.4 through E.6 provide the results of the uncertainty analysis for liquid entrainment. As can be seen, the gas density in the branch throat and the branch mass flow rate were the largest contributors to the uncertainty in the Froude number. By examining the volume flow rate column, $\dot{Q}$, the uncertainty is seen to increase down the column. This follows from the use and calibration of flow meters where it is known that at lower scale readings the uncertainty is greater. However, by examining the gas density in the branch throat the opposite occurs down the column. That is, the uncertainty decreases down the column. This occurs because of the assumptions used in data reduction. The assumption used in the data reduction was isentropic expansion with k=1.4. The assumption used to assess the uncertainty was an adiabatic, polytropic process with n=1.2. The two differing exponents will produce two curves that are close at low values and diverge at high values. Thus, at low flow rates, the two assumptions produce similar gas densities with similar uncertainties. At higher flow rates, the two assumptions produce gas densities that are increasingly diverging and therefore, the uncertainties are diverging. Therefore, the uncertainties in the branch-throat gas density given in the table are as expected.

The uncertainty in the flow meter air density and water density were insignificant. The uncertainty in Fr_2 will be identical for the uncertainty in Fr_1 when Fr_1 and Fr_2 are equal.

Table E.4: Liquid-entrainment uncertainty analysis for $l/d = 1.5$, $\alpha = 0°$, and $Fr_2 = 38.8$

$\%d$	$\%A$	$\%\dot{Q}$	$\%\dot{m}$	$\%\rho_L$	$\%\rho_{G,fm}$	$\%\rho_{G,i}$	$\%Fr$
1.57	3.16	1.05	1.06	0.02	0.15	15.24	8.67
1.57	3.16	1.15	1.16	0.02	0.15	11.78	7.20
1.57	3.16	1.28	1.29	0.02	0.15	8.90	6.09
1.57	3.16	1.45	1.45	0.02	0.15	6.97	5.47
1.57	3.16	1.68	1.69	0.02	0.16	5.68	5.15
1.57	3.16	2.04	2.05	0.02	0.16	3.67	4.81
1.57	3.16	2.59	2.59	0.02	0.17	2.27	4.86
1.57	3.16	3.56	3.57	0.02	0.16	1.27	5.36
1.57	3.16	5.91	5.91	0.02	0.17	0.66	7.12
1.57	3.16	2.25	2.29	0.02	0.17	0.23	4.71
1.57	3.16	5.38	5.38	0.02	0.17	0.00	6.67

Table E.5: Liquid-entrainment uncertainty analysis for $l/d = 2.0$, $\alpha = 10°$, and $Fr_2 = 19.0$

$\%d$	$\%A$	$\%\dot{Q}$	$\%\dot{m}$	$\%\rho_L$	$\%\rho_{G,fm}$	$\%\rho_{G,i}$	$\%Fr$
1.57	3.16	1.02	1.03	0.02	0.16	12.01	7.27
1.57	3.16	1.12	1.13	0.02	0.16	8.90	6.07
1.57	3.16	1.25	1.26	0.02	0.16	7.18	5.49
1.57	3.16	1.42	1.43	0.02	0.16	5.79	5.10
1.57	3.16	1.65	1.66	0.02	0.16	3.74	4.67
1.57	3.16	2.00	2.01	0.02	0.16	2.31	4.58

Liquid-entrainment uncertainty analysis for $l/d = 2.0$, $\alpha = 10°$, and $Fr_2 = 19.0$

$\%d$	$\%A$	$\%\dot{Q}$	$\%\dot{m}$	$\%\rho_L$	$\%\rho_{G,fm}$	$\%\rho_{G,i}$	$\%Fr$
1.57	3.16	2.55	2.56	0.02	0.17	1.33	4.75
1.57	3.16	3.60	3.60	0.02	0.17	0.63	5.35
1.57	3.16	4.01	4.01	0.02	0.17	0.50	5.63
1.57	3.16	4.41	4.42	0.02	0.17	0.41	5.92
1.57	3.16	0.76	0.77	0.02	0.17	0.23	4.02
1.57	3.16	1.50	1.51	0.02	0.17	0.06	4.22
1.57	3.16	2.96	2.96	0.02	0.17	0.01	4.93
1.57	3.16	5.38	5.38	0.02	0.17	0.00	6.68

Table E.6: Liquid-entrainment uncertainty analysis for $l/d = 8.0$, $\alpha = 10°$, and $Fr_2 = 38.0$

$\%d$	$\%A$	$\%\dot{Q}$	$\%\dot{m}$	$\%\rho_L$	$\%\rho_{G,fm}$	$\%\rho_{G,i}$	$\%Fr$
1.57	3.16	1.02	1.03	0.02	0.15	12.01	7.27
1.57	3.16	1.12	1.13	0.02	0.15	8.90	6.07
1.57	3.16	1.25	1.26	0.02	0.15	7.18	5.49
1.57	3.16	1.42	1.43	0.02	0.15	5.79	5.10
1.57	3.16	1.65	1.66	0.02	0.15	3.74	4.67
1.57	3.16	2.00	2.01	0.02	0.16	2.31	4.58
1.57	3.16	2.55	2.56	0.02	0.16	1.33	4.75
1.57	3.16	3.60	3.60	0.02	0.16	0.63	5.35
1.57	3.16	4.01	4.01	0.02	0.16	0.50	5.63
1.57	3.16	0.57	0.60	0.02	0.16	0.41	3.99

Liquid-entrainment uncertainty analysis for $l/d = 8.0$, $\alpha = 10°$, and $Fr_2 = 38.0$

$\%d$	$\%A$	$\%\dot{Q}$	$\%\dot{m}$	$\%\rho_L$	$\%\rho_{G,fm}$	$\%\rho_{G,i}$	$\%Fr$
1.57	3.16	0.76	0.77	0.02	0.16	0.23	4.02
1.57	3.16	1.50	1.51	0.02	0.16	0.06	4.22
1.57	3.16	2.96	2.96	0.02	0.16	0.01	4.93
1.57	3.16	5.38	5.38	0.02	0.16	0.00	6.68

E.4 Uncertainty in the Critical Height

The uncertainty in the critical height was calculated using Equation (E.11).

$$\omega_{h/d} = \left(\left[\frac{\partial h/d}{\partial h} \omega_h \right]^2 + \left[\frac{\partial h/d}{\partial d} \omega_d \right]^2 \right)^{0.5} \tag{E.11}$$

The uncertainty in the branch diameter was the same as for the previous analyses at $\pm 0.1\ mm$. The uncertainty in the calculation of the interface height h was found by applying Equation (E.1) to Equation (B.16). The following was obtained,

$$\omega_h = \left(\left[\frac{\partial h}{\partial DPT_D} \omega_{DPT_D} \right]^2 + \left[\frac{\partial h}{\partial X} \omega_X \right]^2 + \left[\frac{\partial h}{\partial DPT_{cl}} \omega_{DPT_{cl}} \right]^2 + \left[\frac{\partial h}{\partial D_{cal}} \omega_{D_{cal}} \right]^2 + \left[\frac{\partial h}{\partial a} \omega_a \right]^2 + \left[\frac{\partial h}{\partial b} \omega_b \right]^2 + \left[\frac{\partial h}{\partial c} \omega_c \right]^2 + \right)^{0.5} \tag{E.12}$$

where $a = -70.18$, $b = 35.05$, and $c = -0.006$ from Equation (B.16). The uncertainty in a, b, and c arise from the uncertainty in the pressure transducer calibration. Thus, the estimated uncertainties were 0.1 mm for a, 0.03 mm/V for b, and 0.0004 mm/V^2 for c. The uncertainty in the voltage at the onset, DPT_D, was estimated from the

digital voltmeter. The voltmeter had a resolution of 1 mV and therefore, the uncertainty in DPT_D was taken as 1 mV. The uncertainty in the zero offset height of the pressure transducer, D_{cal} was estimated from the ruler used to measure the height. As well, due to the arrangement of the equipment further uncertainty was added. Therefore, the uncertainty in D_{cal} was estimated as 2 mm. The uncertainty in the branch centerline distance, represented by the voltage reading, was the root-sum-of-squares of the voltage reading with the interface at the top of the branch and at the bottom of the branch. Therefore, the uncertainty in the voltage with the interface at the branch centerline was estimated as 4 mV.

The uncertainty in parameter X was calculated by applying Equation (E.1) to Equation (B.17).

$$\omega_X = \left(\left[\frac{\partial X}{\partial \rho_L} \omega_{\rho_L} \right]^2 + \left[\frac{\partial X}{\partial \rho_{G,o}} \omega_{\rho_{G,o}} \right]^2 + \left[\frac{\partial X}{\partial \rho_{G,atm}} \omega_{\rho_{G,atm}} \right]^2 \right)^{0.5} \tag{E.13}$$

The uncertainties in ρ_L and $\rho_{G,o}$ were the same as presented previously. The uncertainty in the atmospheric air density was calculated by applying Equation (E.1) to the ideal gas law.

$$\omega_{\rho_{G,atm}} = \left(\left[\frac{1}{RT} \omega_P \right]^2 + \left[\frac{P}{RT^2} \omega_T \right]^2 \right)^{0.5} \tag{E.14}$$

The uncertainty in the temperature was the same as previously discussed. The uncertainty in the atmospheric pressure was estimated from the barometer. The barometer had a resolution of 0.1 $mmHg$ and therefore, the uncertainty was estimated as 0.1 $mmHg$.

Tables E.7 through E.9 provide the results of the uncertainty analysis for gas entrainment and Tables E.10 through E.12 provide the results for liquid entrainment. As can be seen in all cases the greatest contributor to the uncertainty in the critical

height was ρ_G and h. The uncertainties in ρ_L and X were insignificant. The uncertainty in d remained unchanged from the Froude number analyses. The uncertainty in the critical height for gas entrainment was approximately $\pm 1.86\%$ to $\pm 5.36\%$ for most of the data points examined. For liquid entrainment the values were in the range of $\pm 1.85\%$ to $\pm 3.09\%$.

Table E.7: Gas-entrainment uncertainty analysis for $l/d = 1.5$, $\alpha = 60°$, and $Fr_2 = 28.5$

$\%\rho_G$	$\%\rho_L$	$\%X$	$\%DPT_D$	$\%h$	$\%h/d$
0.69	0.02	0.01	0.01	1.00	1.86
0.69	0.02	0.01	0.01	1.29	2.03
0.69	0.02	0.01	0.01	1.59	2.24
0.69	0.02	0.01	0.01	2.11	2.64
0.69	0.02	0.01	0.01	2.75	3.17
0.69	0.02	0.01	0.01	3.24	3.60

Table E.8: Gas-entrainment uncertainty analysis for $l/d = 2.0$, $\alpha = 30°$, and $Fr_2 = 14.0$

$\%\rho_G$	$\%\rho_L$	$\%X$	$\%DPT_D$	$\%h$	$\%h/d$
0.69	0.02	0.01	0.01	0.98	1.86
0.69	0.02	0.01	0.01	1.20	1.98
0.69	0.02	0.01	0.01	1.66	2.29
0.69	0.02	0.01	0.01	2.33	2.81

Gas-entrainment uncertainty analysis for $l/d = 2.0$, $\alpha = 30°$, and $Fr_2 = 14.0$

$\%\rho_G$	$\%\rho_L$	$\%X$	$\%DPT_D$	$\%h$	$\%h/d$
0.69	0.02	0.01	0.01	3.59	3.92
0.69	0.02	0.01	0.01	5.12	5.36

Table E.9: Gas-entrainment uncertainty analysis for $l/d = 8.0$, $\alpha = 0°$, and $Fr_2 = 56.6$

$\%\rho_G$	$\%\rho_L$	$\%X$	$\%DPT_D$	$\%h$	$\%h/d$
0.69	0.02	0.01	0.01	1.04	1.89
0.69	0.02	0.01	0.01	1.09	1.91
0.69	0.02	0.01	0.01	1.12	1.93
0.69	0.02	0.01	0.01	1.12	1.93
0.69	0.02	0.01	0.01	1.13	1.94
0.69	0.02	0.01	0.01	1.13	1.94
0.69	0.02	0.01	0.01	1.13	1.94
0.69	0.02	0.01	0.01	1.13	1.94
0.69	0.02	0.01	0.01	1.13	1.94
0.69	0.02	0.01	0.01	1.11	1.93
0.69	0.02	0.01	0.01	1.11	1.93
0.69	0.02	0.01	0.01	1.11	1.93
0.69	0.02	0.01	0.01	1.11	1.93
0.69	0.02	0.01	0.01	1.11	1.93
0.69	0.02	0.01	0.01	1.11	1.93
0.69	0.02	0.01	0.01	1.11	1.93

Gas-entrainment uncertainty analysis for $l/d = 8.0$, $\alpha = 0°$, and $Fr_2 = 56.6$

$\%\rho_G$	$\%\rho_L$	$\%X$	$\%DPT_D$	$\%h$	$\%h/d$
0.69	0.02	0.01	0.01	1.11	1.93

Table E.10: Liquid-entrainment uncertainty analysis for $l/d = 1.5$, $\alpha = 0°$, and $Fr_2 = 38.0$

$\%\rho_G$	$\%\rho_L$	$\%X$	$\%DPT_D$	$\%h$	$\%h/d$
1.13	0.02	0.00	0.01	0.96	1.85
1.13	0.02	0.00	0.01	0.99	1.86
1.13	0.02	0.00	0.01	1.01	1.87
1.13	0.02	0.00	0.01	1.05	1.89
1.13	0.02	0.00	0.01	1.07	1.90
1.13	0.02	0.00	0.01	1.09	1.92
1.13	0.02	0.00	0.01	1.12	1.93
1.13	0.02	0.00	0.01	1.15	1.95
1.13	0.02	0.00	0.01	1.20	1.98
1.13	0.02	0.00	0.01	1.22	1.99
1.13	0.02	0.00	0.01	1.24	2.01

Table E.11: Liquid-entrainment uncertainty analysis for $l/d = 2.0$, $\alpha = 10°$, and $Fr_2 = 19.0$

$\%\rho_G$	$\%\rho_L$	$\%X$	$\%DPT_D$	$\%h$	$\%h/d$
1.13	0.02	0.00	0.02	1.13	1.94
1.13	0.02	0.00	0.02	1.17	1.96
1.13	0.02	0.00	0.02	1.22	1.99
1.13	0.02	0.00	0.02	1.28	2.03
1.13	0.02	0.00	0.02	1.35	2.07
1.13	0.02	0.00	0.02	1.43	2.12
1.13	0.02	0.00	0.02	1.55	2.21
1.13	0.02	0.00	0.02	1.70	2.32
1.13	0.02	0.00	0.02	1.74	2.35
1.13	0.02	0.00	0.02	1.76	2.36
1.13	0.02	0.00	0.02	1.84	2.42
1.13	0.02	0.00	0.02	1.90	2.47
1.13	0.02	0.00	0.02	1.93	2.49
1.13	0.02	0.00	0.02	1.93	2.49

Table E.12: Liquid-entrainment uncertainty analysis for $l/d = 8.0$, $\alpha = 10°$, and $Fr_2 = 38.0$

$\%\rho_G$	$\%\rho_L$	$\%X$	$\%DPT_D$	$\%h$	$\%h/d$
1.13	0.02	0.00	0.02	1.18	1.97
1.13	0.02	0.00	0.02	1.24	2.00
1.13	0.02	0.00	0.02	1.29	2.04

Liquid-entrainment uncertainty analysis for $l/d = 8.0$, $\alpha = 10°$, and $Fr_2 = 38.0$

$\%\rho_G$	$\%\rho_L$	$\%X$	$\%DPT_D$	$\%h$	$\%h/d$
1.13	0.02	0.00	0.02	1.34	2.07
1.13	0.02	0.00	0.02	1.45	2.14
1.13	0.02	0.00	0.02	1.56	2.21
1.13	0.02	0.00	0.02	1.69	2.31
1.13	0.02	0.00	0.02	1.89	2.46
1.13	0.02	0.00	0.02	2.08	2.61
1.12	0.02	0.00	0.02	2.36	2.84
1.13	0.02	0.00	0.02	2.65	3.08
1.13	0.02	0.00	0.02	2.66	3.09
1.13	0.02	0.00	0.02	2.66	3.09
1.13	0.02	0.00	0.02	2.66	3.09

IMAGE EVALUATION TEST TARGET (QA-3)

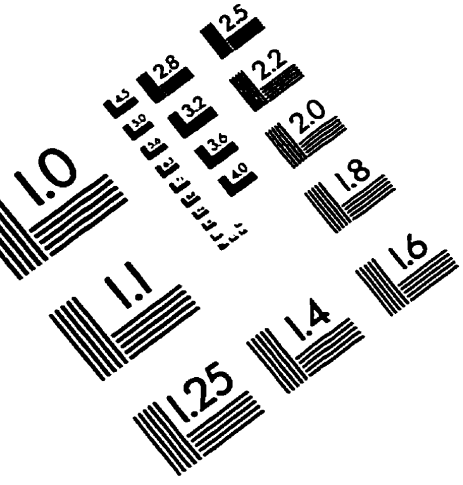

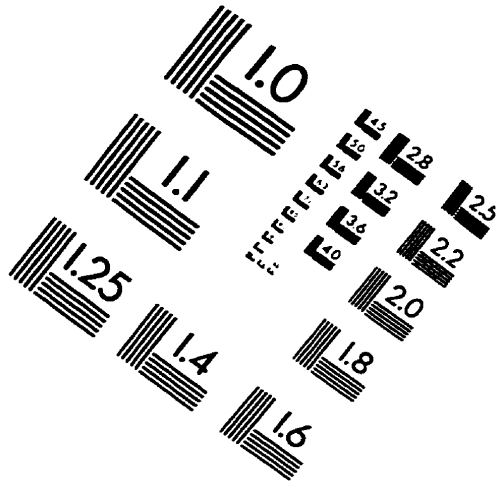

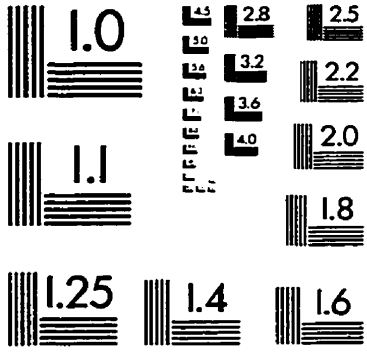

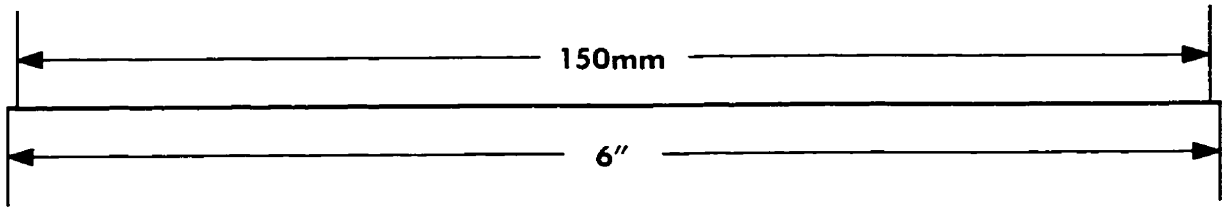

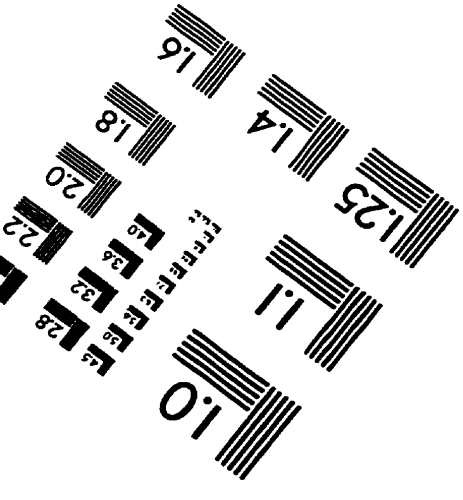

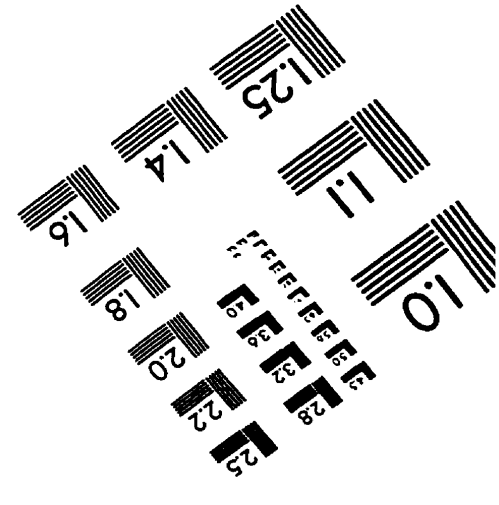

APPLIED IMAGE, Inc
1653 East Main Street
Rochester, NY 14609 USA
Phone: 716/482-0300
Fax: 716/288-5989